Search for a
Permanent Electric Dipole Moment of ^{129}Xe
with a He/Xe Clock-Comparison Experiment

Dissertation

zur Erlangung des Grades
"Doktor der Naturwissenschaften"
am Fachbereich Physik, Mathematik und Informatik
der Johannes Gutenberg-Universität
in Mainz

vorgelegt von

Stefan Zimmer

geboren in Koblenz

Mainz, März 2018

Tag der mündlichen Prüfung: 19. Juni 2018

Abstract

The search for sources that violate the combined symmetry of charge conjugation (C) and parity transformation (P) is one of the main concerns of high-precision experiments in fundamental physics. The evidence of a CP-violation beyond the Standard Model of particle physics would be a profound indication for the origin of matter-antimatter asymmetry in the early universe [1]. Possible candidates for this are permanent electric dipole moments of fundamental particles (EDMs), which would cause a breakdown of both parity transformation and time reversal symmetry (T). Through the CPT-theorem, this is directly corresponding to a CP-violation.
In the last decades, various experiments have been performed in order to lower the limits of EDMs with more and more precise measurements. The methodical approach of most of these experiments is the same: According to Pauli's exclusion principle [2], a finite EDM of a fundamental particle is always coupled to the spin of the particle. The existence of an EDM leads to an additional - although extremely small - energy splitting in the presence of an electrical field, besides the Zeeman splitting induced by a magnetic field. Measuring the resulting tiny frequency shifts of the Larmor precession is an extreme experimental challenge.

In this thesis our experiment for the search of a permanent electric dipole moment of ^{129}Xe (Xe-EDM) is presented. For these kinds of high-precision experiments the method of comagnetometry is a convenient tool. Our approach is to detect the free spin precession of the two hyperpolarized spin samples ^{3}He and ^{129}Xe in the same measurement volume. We are able to measure frequency shifts of the spin precession of the co-located species with a statistical sensitivity in the order of $\delta\omega \approx 6 \cdot 10^{-10}\,\mathrm{rad/s}$. To achieve this excellent value, numerous experimental challenges had to be mastered. For example, the design and development of an exceptionally homogeneous magnetic environment was an important step in order to obtain long coherence times of several hours and to achieve high signal-to-noise ratios. The construction of the experimental setup, the elaboration of experimental procedures, along with particular checks and optimizations are discussed in detail in this work.
With first measurements and a preliminary evaluation we were able to lower the upper limit of the Xe-EDM from a current value of $|d_{\mathrm{Xe}}| < 7.3 \cdot 10^{-27}\,e\mathrm{cm}$ (95% CL) [3] to $|d_{\mathrm{Xe}}| < 1.0 \cdot 10^{-27}\,e\mathrm{cm}$ (95% CL). The continuous development of the experimental conditions and operating procedures will allow us to further improve the achievable sensitivity.

Kurzfassung

Die Suche nach einer Verletzung der kombinierten Symmetrie von Ladungskonjugation (C) und Raumspiegelung (P) ist ein Hauptanliegen vieler Hochpräzisionsexperimente im Bereich der fundamentalen Physik. Der Nachweis einer solchen CP-Verletzung über das Standardmodell der Elementarteilchen hinaus wäre ein fundierter Hinweis hinsichtlich des Ursprungs der Materie-Antimaterie-Asymmetrie im frühen Universum [1]. Permanente elektrische Dipolmomente (EDMs) von Elementarteilchen führen in diesem Zusammenhang zu einer Verletzung der Raumspiegelungs- sowie der Zeitumkehrsymmetrie T. Über das CPT-Theorem ist dies direkt mit einer CP-Verletzung verknüpft.
In den letzten Jahrzehnten wurden zahlreiche Experimente durchgeführt um die Obergrenzen von EDMs mit immer genaueren Messungen herabzusetzen. Der methodische Ansatz vieler dieser Experimente ist dabei der Gleiche: Entsprechend des Pauli-Prinzips [2] ist ein endliches EDM eines Elementarteilchens immer an seinen Spin gekoppelt. Existiert ein EDM, so kommt, abgesehen von der Zeeman-Aufspaltung in einem magnetischen Feld, eine zusätzliche - wenn auch extrem geringe - Energieaufspaltung durch ein elektrisches Feld hinzu. Die Messung von solch resultierender kleiner Frequenzverschiebungen der Larmorpräzession ist eine erhebliche experimentelle Herausforderung.

In dieser Arbeit wird unser Experiment zur Suche eines permanenten elektrischen Dipolmoments von ^{129}Xe (Xe-EDM). Für diese Art von Hochpräzisionsexperiment hat sich die Methode der Komagnetometrie als nützliches Werkzeug etabliert. Die Herangehensweise ist dabei die Spinpräzession der zwei hyperpolarisierten Spin-Spezies ^{3}He und ^{129}Xe, die sich im gleichen Messvolumen befinden, zu detektieren. Damit ist es uns möglich Frequenzänderungen der Spinpräzession beider Spezies mit einer statistischen Sensitivität von etwa $\delta\omega \approx 6 \cdot 10^{-10}\,\mathrm{rad/s}$ zu messen. Um diesen exzellenten Wert zu erreichen, mussten zahlreiche experimentelle Aufgaben gemeistert werden. So war beispielsweise die Entwicklung und Gestaltung einer außergewöhnlich homogenen magnetischen Umgebung ein wichtiger Schritt, um lange Kohärenzzeiten von mehreren Stunden und um hohe Signal-zu-Rausch Verhältnisse zu erreichen. Der experimentelle Aufbau, die Erarbeitung experimenteller Prozeduren, ebenso wie systematische Tests und die Optimierung experimenteller Parameter sind in dieser Arbeit detailliert diskutiert.
Mit ersten Messungen und einer vorläufigen Analyse konnten wir die bisherige Obergrenze des Xe-EDMs von $|d_{\mathrm{Xe}}| < 7.3 \cdot 10^{-27}\,e\mathrm{cm}$ (95% CL) [3] auf einen Wert von $|d_{^{129}\mathrm{Xe}}| < 1.0 \cdot 10^{-27}\,e\mathrm{cm}$ (95% CL) herabsetzen. Im Bezug auf gewonnene Erkenntnisse bei experimentellen Bedingungen und Vorgängen werden laufende Optimierungen die erreichbare Sensitivität weiter verbessern.

Table of Contents

1

Motivation

Nature provides innumerable mysteries and puzzles scientist with unresolved and complex questions - today in the same way as ever. The list of unsolved problems in physics appears to grow from day to day. To get more specific, one of these problems arises by interpreting Dirac's famous equation, predicting that every particle has a corresponding antiparticle, with the CPT-theorem, describing the symmetry for this correspondence:

Why is the observable universe dominated by matter over antimatter?

Based on a symmetry between particles and antiparticles - matter and antimatter - and a balance as an initial condition after the Big Bang, this very question is of profound significance for the understanding of nature, both from a physical and philosophical point of view. Numerous experiments all over the world aim to come a little closer to solve this problem - among others experiments in the field of research of permanent electric dipole moments (short: EDMs) of fundamental particles. The search for EDMs of compound particles like atoms and molecules offers insights of these fundamental EDMs.

This thesis presents our experiment to search for the permanent electric dipole moment of ^{129}Xe with He/Xe clock-comparison in a magnetically shielded room at the research center Jülich. The experiment is the prime concern of our MIXed$\vec{}$-collaboration[1].

MIXed

Measurement and Investigation of the Xenon-129 electric dipole moment

[1]Collaboration partners:
Institut für Physik at the Johannes Gutenberg-Universität Mainz
Physikalisches Institut at the Ruprecht-Karls-Universität Heidelberg
Van Swinderen Institute at the University of Groningen
Peter Grünberg Institut at the Forschungszentrum Jülich

After introducing the mostly theoretical motivation within this chapter, the following chapter 2 establishes the methodical and conceptual framework. Since this work sets its priority on the experimental realization, the developed experimental setup is presented in detail in chapter 3 and the principle of measurement is illustrated in chapter 4. Both, systematic considerations and a critical interpretation of first results are unveiled in chapter 5 and 6. The thesis is concluded with a summary and an experimental outlook in chapter 7.

1.1. Baryogenesis

The abundance of baryonic matter in our present universe can be scaled by the baryon-asymmetry parameter [4]

$$\eta = \frac{n_{\mathrm{B}}}{n_{\gamma}} \quad . \tag{1.1}$$

This quantity relates the baryon number density $n_{\mathrm{B}} = n_{\mathrm{b}} - n_{\bar{\mathrm{b}}}$ with the number of baryons n_{b} and antibaryons $n_{\bar{\mathrm{b}}}$ per unit of volume. The existence of large clusters of antimatter within a distance of approximately light years can be excluded by the observation of antihelium nuclei in space [5] and the detection of the derivation of cosmic gamma rays. Antimatter dominated regions in a "patchwork universe" would lead to annihilation processes along the boundaries of matter and antimatter regions [6]. From this it follows that $n_{\mathrm{b}} - n_{\bar{\mathrm{b}}} \approx n_{\mathrm{b}}$. By astronomical observations of light element occurrences (^{2}H, D, ^{3}He, ^{4}He, ^{7}Li) [7] the baryon number density can be estimated [8, 9] to

$$n_{\mathrm{B}} \approx n_{\mathrm{b}} \approx 2.5 \cdot 10^{-7}\,\mathrm{cm}^{-3} \quad . \tag{1.2}$$

If matter and antimatter would have been completely annihilated after the Big Bang, this value should be zero ($n_{\mathrm{b}} = n_{\bar{\mathrm{b}}}$). The photon number density can be calculated by means of the temperature $T = 2.7\,\mathrm{K}$ of the cosmic microwave background (CMB) photons [10]. Since the CMB shows the thermodynamic properties of blackbody radiation, the number density of the photon gas [11] is

$$n_{\gamma} = 16\,\zeta(3)\left(\frac{kT}{hc}\right)^3 \approx 413\,\mathrm{cm}^{-3} \tag{1.3}$$

where $\zeta(3) \approx 1.202$ is Apéry's constant [12]. As a result, the asymmetry parameter can be deduced [7, 13] to

$$\eta = (6.14 \pm 0.25) \cdot 10^{-10} \quad . \tag{1.4}$$

Assuming the universe was not created in such an asymmetric way, a possible explanation for this deviation, and for our existence and the reason why we can puzzle over this fundamentally existential value of η, is the so-called baryogenesis in the early universe, which was proposed by Andrei Sakharov in 1967. The three required conditions for a baryon-generating process are known as the Sakharov criteria [1]:

- Violation of the baryon number B
- Violation of C- and CP-symmetry
- Departure from thermal equilibrium

The first criterion is automatically fulfilled if the initial situation of the universe was symmetric ($n_{\mathrm{b}} = n_{\bar{\mathrm{b}}}$). Therefore, the baryon number cannot have been constant, if the universe is not symmetric ($\eta \neq 0$) at the present time.

The second criterion regards the transformation between baryons and antibaryons. To get a global excess of baryonic matter, a process which generates more baryons than antibaryons (net $B > 0$) has to be preferred, compared to the opposing process which generates more antibaryons than baryons (net $B < 0$). Because the baryon number operator $\mathbf{B}$ is odd under C and CP, this can only be the case if the symmetry in C and CP is violated, resulting in $[\mathbf{B}, \mathbf{H}] \neq 0$.
In the standard model the CP violation is primarily embedded in the complex phase of the CKM matrix [14] in the theory of weak interactions. However, this CP violating contribution of the Standard Model of particle physics is insufficient by about ten to twelve orders of magnitude [15] to explain the observable baryon-asymmetry [16].
Thus, much experimental and theoretical effort is put in the investigation of additional CP violating sources *beyond the Standard Model* (short: BSM). An evidence for CP violating BSM-physics would be a permanent electric dipole moment (EDM) of fundamental particles, as per statement below in section 1.2.

The third criterion demands that the baryon-asymmetry generating process has to occur in a period in the early universe, where the rate of the baryogenesis is less than the expansion rate of the universe. Consider a hypothetical baryon-asymmetry generating process $X \to Y + B$, where X and Y are the initial and final state with vanishing baryon number, and B are the excess baryons produced. In thermal equilibrium, the rate of the inverse process $Y + B \to X$ is equal by definition. Therefore, no net baryon-asymmetry is produced. If the decays occur out of thermal equilibrium, and if X is the heavier particle, the baryon-generating process $X \to Y + B$ has a higher probability than the inverse process.

1.2. Permanent Electric Dipole Moment of Particles

Classically, an electric dipole moment $\vec{d}$ exists when either a) the centers of a positive $+q$ and a negative charge distribution $-q$ are separated by a distance $\vec{l}$, so it is $\vec{d} = q \cdot \vec{l}$, or b) the center of mass does not coincide with the charge center. A charge distribution $\rho(\vec{r})$ with the location $\vec{r}$ results in an EDM of

$$\vec{d} = \int_V \rho(\vec{r}) \cdot \vec{r}\, d^3r \tag{1.5}$$

which is unequal zero if the charge distribution is not symmetrical to the origin.
Taking the water molecule H_2O as an example, the intrinsic electric dipole moment of $d_{H_2O} = 3.8 \cdot 10^{-9}\, e\text{cm}$ results from the distance $r = 95.84 \cdot 10^{-10}\,\text{cm}$ between the hydrogen atoms (charge δ^+) and the oxygen atom (charge δ^-) [17]. The existence of such an intrinsic electric dipole moment is not related to a symmetry breaking, since the ground state has two degenerate states of opposing parity; the orbitals show an sp^3-hybridization [18].
In the non-classical case of fundamental or composed particles, for example the neutron, the EDM vector is always aligned with the axial spin vector $\vec{S}$, since the spin is the only vector that characterizes a quantization axis in the inertial frame. Otherwise an additional quantum number is needed, which would be in disagreement with the Pauli principle [2]. So it is

$$\vec{d} = d \cdot \frac{\vec{S}}{|\vec{S}|} \quad . \tag{1.6}$$

The Hamiltonian of such a system describes the interaction of the spin, or rather the magnetic moment $\vec{\mu}$, with a magnetic field $\vec{B}$, and of the EDM $\vec{d}$ with an electric field $\vec{E}$:

$$\hat{H} = -\hat{\vec{\mu}} \cdot \vec{B} - \hat{\vec{d}} \cdot \vec{E} \tag{1.7}$$

Considering a parity transformation P (reversed spatial configuration), both axial vectors, the magnetic moment as well as the magnetic field, do not change their direction, hence their term in the Hamiltonian remains the same. Furthermore, the EDM vector stays aligned with the spin vector, whereas the polar vector of the electric field changes the direction; the particular term in the Hamiltonian changes sign. On the other hand, a time reversal T leads to a change of the direction of the axial vectors of the magnetic field and the magnetic moment, and therefore of the EDM since it is coupled to the spin. The direction of the polar vector of the electric field remains the same. Again, the

term of the magnetic interaction stays the same and the term of the electric interaction changes sign. This behavior is illustrated in figure 1.1.

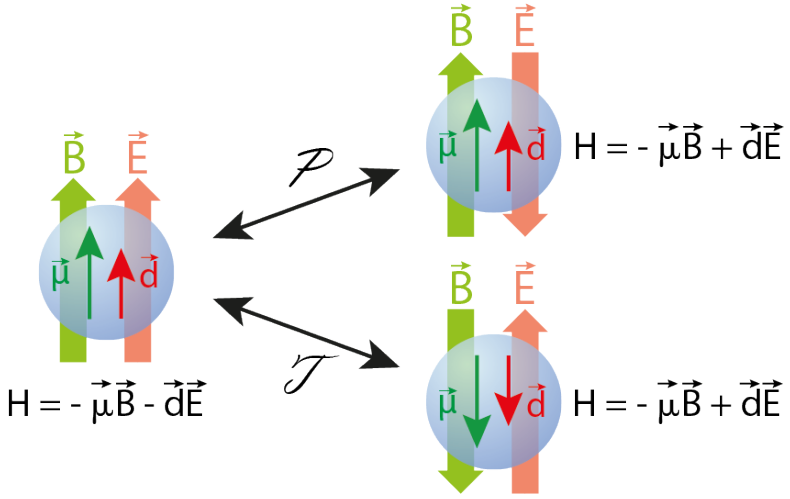

Figure 1.1.: Illustration of the behavior of the magnetic moment $\vec{\mu}$ and the electric dipole moment $\vec{d} = d \cdot \vec{S}/|\vec{S}|$ of a particle under P and T transformation.

In conclusion, a finite (non-zero) permanent electric dipole moment has to violate parity, as well as time reversal symmetry. Because of the CPT-theorem - the combined symmetry of charge-, parity- and time reversal - this equates a violation of the combined CP-symmetry.

1.2.1. Impact of a Permanent EDM on CP Violation

In the sector of weak interactions, CP-violation is well predicted by the standard model and experimentally confirmed, for example by studies of the 2π-decay of the K_L meson [19]. This CP-violating contribution stems from the complex phase of the CKM matrix, describing the weak interaction of the three generations of quarks [14]. With regard to EDMs, the prediction by this CP-violating process is far below current experimental sensitivities (cf. section 1.2.2). For example, the Standard Model prediction for the electron EDM [20]

$$d_e \sim 10^{-38}\, e\text{cm} \tag{1.8}$$

is extremely small.

Another potential contribution to the Standard Model CP-violation has its origin in the so-called Θ-term of the QCD-Lagrangian

$$\mathcal{L}_\Theta = -\Theta \frac{\alpha_S}{8\pi} \tilde{G}^a_{\mu\nu} G^a_{\mu\nu} \tag{1.9}$$

where $G^a_{\mu\nu}$ is the gauge invariant gluon field strength tensor (analogous to the electromagnetic field strength tensor $F_{\mu\nu}$ in QED) and α_S is the gluon coupling constant, analogous to the fine-structure constant α for electromagnetic interactions. It is possible to relate this CP-violating parameter Θ with an EDM. For example, the neutron EDM depending on Θ was calculated by [21] to

$$d_n = 8 \cdot 10^{-16} \cdot \Theta \, e\text{cm} \quad . \tag{1.10}$$

The current best (direct[2]) upper limit of the neutron EDM was experimentally determined [22] to

$$|d_n| < 3 \cdot 10^{-26} \, e\text{cm} \ (90\% \ CL) \quad . \tag{1.11}$$

The experimental history of the neutron EDM measurements, shown in figure 1.2, proves nicely the persistence of the researchers to steadily improve the experimental upper limit with more and more sensitive measurements.

However, the very small result for the phase $\Theta < 3 \cdot 10^{-10}$ leads to a conflict known as the *Strong CP Problem*[3]. There is no obvious reason for the very small result, which can naively be expected to be in the order of 1.

At this point it can be said that the non-observation of EDMs with current experiments is (still) consistent with the CP violation predicted by the Standard Model. Therefore, other CP violating sources in BSM-scenarios, expressed as an additional term of the CP violating Lagrangian

$$\mathcal{L}_{\text{CPV}} = \mathcal{L}_{\text{CKM}} + \mathcal{L}_{\bar{\Theta}} + \mathcal{L}^{\text{CPV}}_{\text{BSM}} \quad , \tag{1.12}$$

are of interest in modern physics to find an explanation for the cosmic matter-antimatter-asymmetry. A prospective candidate for BSM-physics is given by a super-symmetric (SUSY) extension of the Standard Model. In SUSY models, bosons and fermions are related by the introduction of super-symmetric partners, only differing in their spin. For instance, fermions have the super-symmetric partner *sfermions*, featured with a bosonic integer spin. Numerous additional CP violating phases in the mixing matrix could lead

[2] From measurements of the EDM of ^{199}Hg, an indirect upper limit for the neutron EDM of $|d_n| < 1.6 \cdot 10^{-26} \, e\text{cm}$ (95% CL) is determined.

[3] As a further reading for this issue the interested reader may refer to [23].

to new sources of EDMs. Nevertheless, and as mentioned before, until today the constantly improved experimental findings and upper limits are still consistent with the Standard Model predictions but they are putting profound constraints on certain SUSY models in some instances [24].

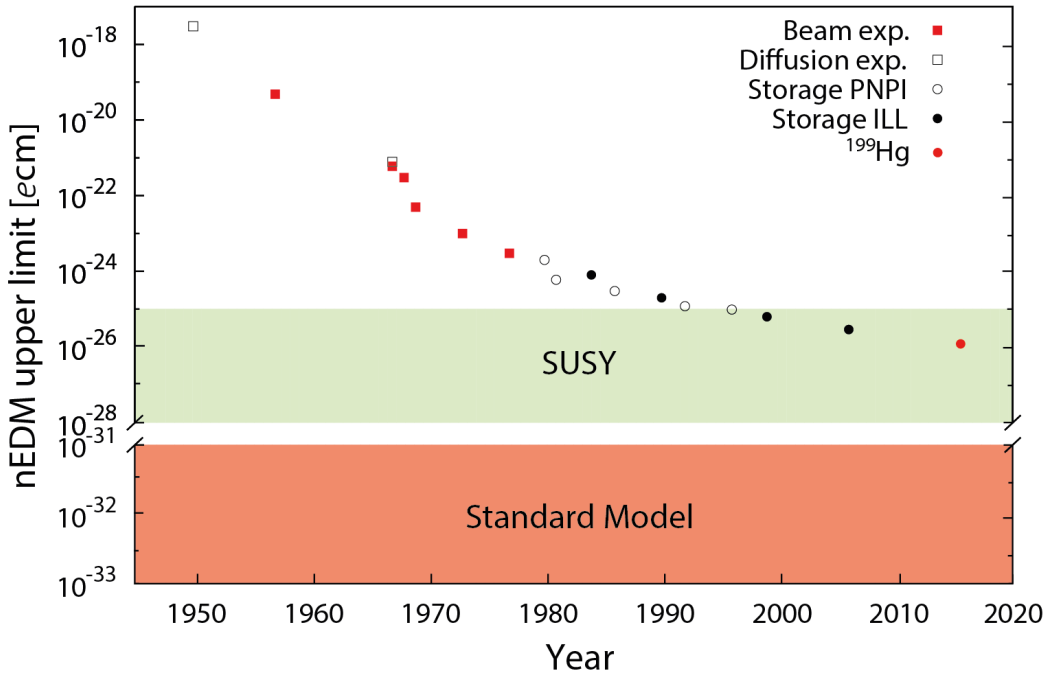

Figure 1.2.: Experimental history of the upper limit measurements of the neutron EDM. Since the 1950s and ongoing until today, much effort is put in the field of research to continuously improve the achievable sensitivity; SUSY (light green) is getting more and more constrained. Although the predicted regime by the Standard Model (light red) is a long way away - from the experimental point of view - the investigations are still going on, with the aspiration to find an indication for BSM-physics. Adapted from [25]. Updated with [26, 27]

1.2.2. Approach and Phenomenology of Permanent EDMs

The Hamiltonian $\hat{H}$ of a pure magnetic interaction of the magnetic moment $\vec{\mu} = \gamma\hat{\sigma}$ in a magnetic field $\vec{B}_0$ is given by

$$\hat{H} = -\gamma\hat{\sigma} \cdot \vec{B}_0 \quad . \tag{1.13}$$

More general with an additional non-magnetic interaction $\hat{H}_1$ the Hamiltonian gets

$$\hat{H} = -\gamma\hat{\sigma} \cdot \vec{B}_0 + \hat{H}_1 \quad . \tag{1.14}$$

Such an additional interaction of type $\hat{H}_1 = -\vec{a}\hat{\sigma}$ can be for example a Lorentz invariance violating background field, an axion field, or - in this case of a coupling to an electric dipole moment - an electric field. Phenomenologically, an EDM leads to a splitting of the energy level of a particle system, in addition to the Zeeman splitting due to the magnetic moment. Therefore, it has to be included in the Hamiltonian

$$\hat{H} = -\left(\hat{\vec{\mu}} \cdot \vec{B} + \hat{\vec{d}} \cdot \vec{E}\right) \tag{1.15}$$

with a magnetic moment $\vec{\mu}$ coupled to a magnetic field $\vec{B}$ and an electric dipole moment $\vec{d}$ coupled to an electric field $\vec{E}$. The resulting energy splitting becomes

$$\mathrm{E} = \hbar\omega = 2\mu B \pm 2dE \quad , \tag{1.16}$$

where $\omega = \omega_L \pm \omega_E$ is the transition frequency due to the magnetic field (ω_L) and the electric field (ω_E), as illustrated in figure 1.3.

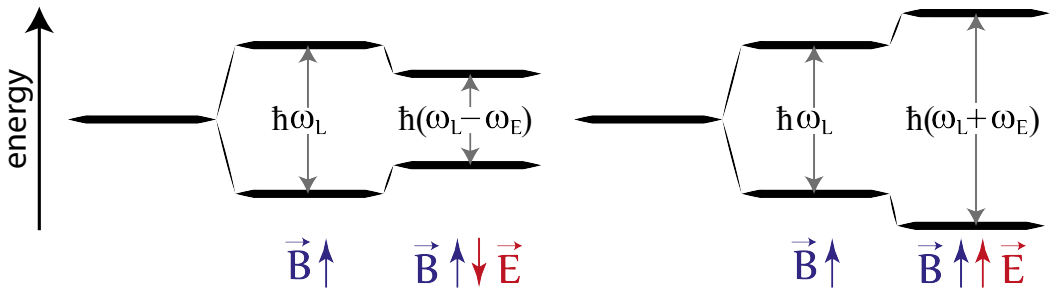

Figure 1.3.: Splitting of a spin 1/2-system due to the magnetic field $\vec{B}$ and the electric field $\vec{E}$. Depending on the alignment of $\vec{B}$ and $\vec{E}$ the transition frequency $\omega = \omega_L \pm \omega_E$ changes in the presence of an EDM.

To be sensitive to an EDM effect very small frequency changes - depending on the electric field $\vec{E}$ - have to be detected. The experimental method with focus on ^{3}He-^{129}Xe-comagnetometry is described in detail in chapter 2.

A reasonable choice for EDM experiments is an electric neutral[4] system with a non-vanishing total angular momentum, mostly $F = 1/2$. Systems with a higher F, for example atoms with a nuclear spin $I \geq 1$, have an electric quadrupole moment, which is technically more complicated to detect via electric field gradients.
Looking particularly at composite, electrostatically bound systems, e.g. atoms or molecules, it has to be considered that an external electric field is shielded inside the system. In case of a neutral atom with non-relativistic particles, the effective electric field inside the atom is zero, because of a rearrangement of the charged components - the external field is exactly compensated by the counteracting internal field at the nucleus

$$\begin{aligned} \vec{E}_{\text{eff}} &= \vec{E}_{\text{ext}} + \vec{E}_{\text{int}} \\ &= \varepsilon \cdot \vec{E}_{\text{ext}} \\ &= 0 \end{aligned} \tag{1.17}$$

where ε can be regarded as the shielding factor of the system. Consequently, the effect on a possible EDM, relating to equation 1.16, vanishes, as it is pointed out by Schiff [31]. However, exceptions from Schiff's theorem lead to mechanisms that could generate atomic EDMs[5]. The fundamental Lagrangian $\mathcal{L}^{\text{CPV}}_{\text{BSM}}$ from equation 1.12 can be expressed by a set of Wilson coefficients from effective field theory [34, 35]. A set of low energy parameters (LEPs) connects these Wilson coefficients to the electron (leptonic) EDM, electron-nucleon (semi-leptonic) contributions and nucleon (hadronic) EDMs [36]. In the following it is explained how these LEPs contribute to an atomic EDM, depending on the atomic structure:

Despite the nuclear shielding, **paramagnetic atoms** can have large enhancement factors to the intrinsic electron EDM d_e and in second order to electron-nucleon (eN) CP violating interactions C_S. In fact the actual EDM sensitivity of the bound and unpaired electron of a paramagnetic atom can be many orders of magnitude better than

[4] Electric charged systems, e.g. electrons, protons, ions, etc. would be accelerated inside of an electric field. Exceptions confirm this rule: examples are the searches for the EDM of light ions proton, deuteron [28] or the muon [29, 30] in storage rings.

[5] Because of the high complexity of this theoretical framework, this paragraph gives only a short overview of the mandatory informations. The interested reader is recommended to have a comprehensive insight with [32, 33].

the pure experimental sensitivity of the particular particle system. The reason for this enhancement

$$K = \frac{d_{\text{atom}}}{d_{\text{e}}} \gg 1 \tag{1.18}$$

is the relativistic motion of an unpaired electron. A relativistic treatment of the electronic wave function leads to a dependency of the enhancement factor with the atomic number, Z, which scales like [37, 38]

$$K \propto Z^3 \quad . \tag{1.19}$$

In addition, polar molecules - or rather molecules with a highly electronegative and with a heavy element - can have enhancement factors orders of magnitudes larger than atoms [39]. Here the enhancement stems from the molecule's orientation with an applied external electric field. The intermolecular field, seen by the nuclei and electrons, can differ drastically from zero. The enhancement factor K relates now to the effective internal electric field ε_{eff}, which can be in the order of several GV/cm. The molecule thorium monoxide (ThO), which was used to set the current best upper limit of the electron EDM (cf. table 1.2), has an effective internal electric field on the unpaired electron of $\varepsilon_{\text{eff}} \approx 84\,\text{GV/cm}$ [40].

Nuclear spin polarized **diamagnetic atoms** in the ground state $^1S_0$ have no unpaired electron. Nevertheless, a relativistic treatment shows that in the case of a finite size nucleus, the nucleus is not completely shielded. The degree to which a nuclear EDM is unscreened is traditionally characterized by the Schiff moment S. Besides contributions from finite nucleon EDMs (neutron d_n, proton d_p), the nuclear EDM can also have contributions from CP violating pion-nucleon interactions (isoscalar g_0, isovector g_1, isotensor g_2). These LEPs are summed up in a dimensionless parameter η [6] which characterizes the strength of the CP violating nuclear potential [41], or rather the Schiff moment

$$S = a \cdot \eta \quad . \tag{1.20}$$

The nuclear spin-dependent CP violating eN interaction C_T contributes in second order. Both, the C_T- and $\eta-$contribution to the atomic EDM have a Z^2 dependency [42]. Furthermore, diamagnetic atoms are still sensitive to d_e and C_S due to hyperfine interaction, although strongly suppressed compared to C_T - it holds: $K \ll 1$. Examples of enhancement/suppression factors of different atoms are given in the following table 1.1 [32].

[6] not to be confused with the baryon-asymmetry parameter, eq. 1.1.

	atom	enhancement factor K
paramagnetic	Rb	≈ 22
paramagnetic	Cs	≈ 120
paramagnetic	Tl	≈ -600
diamagnetic	Hg	≈ -0.014
diamagnetic	Xe	≈ -0.0008

Table 1.1.: Enhancement/suppression factors for different paramagnetic and diamagnetic atoms [32]. The enhancement of Tl towards Xe is 750000.

Because of the Z^2 dependency, the EDM of ^{3}He can be neglected in comparison to the much heavier ^{129}Xe in the context of ^{3}He/^{129}Xe comagnetometry, where ^{3}He essentially serves as a normalization for magnetic field drifts. For the investigation of the neutron EDM in ultra cold neutron (UCN) experiments [43–45] it was found that the ^{3}He-EDM is orders of magnitudes smaller than the neutron EDM [46].

Although paramagnetic systems can have very large enhancement factors, it has to be taken into account that a high achievable spin coherence time of diamagnetic systems is made up for the suppressing shielding, keeping in mind that the unpaired electron in a paramagnetic system can easily interact with its environment[7]. For example for ThO there are interaction times in the order of $\tau \approx 1\,\mathrm{ms}$ [40]. In contrast to this, diamagnetic systems can have $\tau \approx 100\,\mathrm{h}$. Assuming the same signal-to-noise ratio, the EDM sensitivity can thus be high in diamagnetic systems in spite of the Schiff suppression.

However, because there are only three stable diamagnetic isotopes in ground state with $I = 1/2$ that are convenient for optical pumping experiments at room temperature - ^{3}He, ^{129}Xe and ^{199}Hg, which can have long spin coherence times τ - the variety of different experiments is limited.

[7] For example interaction with the containment vessel. Also, in the case metastable systems, the excited states can easily be destroyed by an external high electric field.

Summing up the findings from above leads to a universal expression for an EDM which includes the electron EDM contribution and the contributions from the particular LEPs.

$$d = \alpha_{d_e} d_e + \alpha_{C_S} C_S + \alpha_{C_T} C_T + \alpha_\eta \eta \tag{1.21}$$

where α_x quantifies the strength of the electron EDM (d_e), electron-nucleon ($C_{S,T}$), and nuclear (η) contribution[8]. From theoretical models and calculations it is possible to extract these parameters from experimental studies of EDMs of composite particles, such as atoms or molecules. The present best limits and their origins are collected in table 1.2.

	parameter	current limit (95 % CL)	source
leptonic	d_e	$1.1 \cdot 10^{-28}\, e\text{cm}$	ThO [40]
semi-leptonic	C_S	$7.2 \cdot 10^{-9}$	ThO [40]
semi-leptonic	C_T	$1.5 \cdot 10^{-10}$	^{199}Hg [27]
hadronic	η	$1.1 \cdot 10^{-5}$	^{199}Hg [27] and [47, 48]

Table 1.2.: Current best limits of the electron EDM d_e and the CP violating parameters C_S, C_T and η. The 95% confidence level of the electron was calculated from the experimental value, listed in table 1.3. The limits of C_S and C_T were directly extracted from the particular publications. The limit of η was recalculated from the experimental value of mercury, listed in table 1.3, and the theoretical framework of [47, 48].

Experimental and theoretically extracted limit of the ^{129}Xe-EDM

This thesis sets its focus on the EDM of ^{129}Xe (from now on short: Xe-EDM). For this case, the coefficients of the parameters can be calculated [32, 36, 48][9] to

$$d_{\text{Xe}} = 0.8 \cdot 10^{-3} \cdot d_e + 5.6 \cdot 10^{-23}\, e\text{cm} \cdot C_S + 5.2 \cdot 10^{-21}\, e\text{cm} \cdot C_T + 6.7 \cdot 10^{-26}\, e\text{cm} \cdot \eta \tag{1.22}$$

It is easy to see that the electron EDM contribution to the atomic EDM is strongly suppressed, since ^{129}Xe is a diamagnetic atom.

[8] The parameter η, in turn, can be expressed by the nucleon EDMs and CP violating pion-nucleon interactions.

[9] It has to be mentioned that the calculated factors are strongly depending on the theoretical model.

Using this equation and the current best limits of the parameters that are presented in the previous table 1.2, an indirect upper limit for the Xe-EDM can be estimated to $|d_{\mathrm{Xe}}| < 2.0 \cdot 10^{-30}\, e\mathrm{cm}$ (95% CL). Compared to the current best experimental upper limit [3] of $|d_{\mathrm{Xe}}| < 7.3 \cdot 10^{-27}\, e\mathrm{cm}$ (95% CL) it is clearly evident that the experimental sensitivity has to be enhanced to improve present theoretical constraints, or rather the upper limits of the LEPs.

The following table 1.3 shows the latest experimental results of some EDM experiments. A comparison with SUSY and Standard Model predictions is presented in figure 1.4. It is evident from both expositions that until today all experimental results are consistent with zero within the measuring uncertainty.

	experimental value	year and reference
neutron	$d_n = (-0.21 \pm 1.82) \cdot 10^{-26}\, e\mathrm{cm}$	2006 [49] (rev. 2015 [22])
^{129}Xe	$d_{\mathrm{Xe}} = (-0.70 \pm 3.3_{\mathrm{stat}} \pm 0.1_{\mathrm{sys}}) \cdot 10^{-27}\, e\mathrm{cm}$	2001 [3]
^{199}Hg	$d_{\mathrm{Hg}} = (-2.20 \pm 2.75_{\mathrm{stat}} \pm 1.48_{\mathrm{sys}}) \cdot 10^{-30}\, e\mathrm{cm}$	2016 [27]
^{255}Ra	$d_{\mathrm{Ra}} = (-0.5 \pm 2.5_{\mathrm{stat}} \pm 0.2_{\mathrm{sys}}) \cdot 10^{-22}\, e\mathrm{cm}$	2015 [50]
ThO	$d_{\mathrm{e}} = (-2.1 \pm 3.7_{\mathrm{stat}} \pm 2.5_{\mathrm{sys}}) \cdot 10^{-29}\, e\mathrm{cm}$	2013 [40]
muon	$d_{\mu} = (0.0 \pm 0.9_{\mathrm{stat}}) \cdot 10^{-19}\, e\mathrm{cm}$	2009 [29]

Table 1.3.: Comparison of some latest EDM experiments with the measured experimental value.

Based on the theoretical motivation of this chapter, the following chapter 2 introduces the methodical framework of our experiment for the search of the Xe-EDM with ^{3}He/^{129}Xe-comagnetometry.

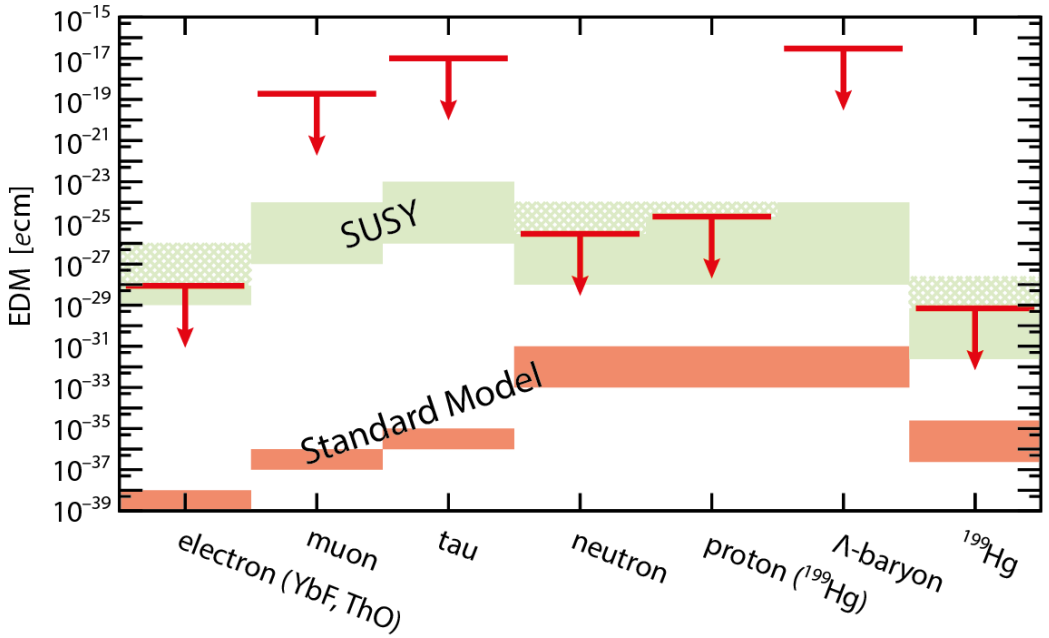

Figure 1.4.: Comparison of some latest EDM upper limits. There are already some significant constraints of SUSY predictions (light green), especially from measured EDM upper limits of the neutron, the electron and of ^{199}Hg. Adapted from [26].

2

Comagnetometry with ^{3}He and ^{129}Xe

This chapter gives a theoretical and conceptional introduction of the method of comagnetometry with ^{3}He and ^{129}Xe. The principle of the so-called clock-comparison makes it possible to investigate non-magnetic spin couplings that are indicating new physics. In the case of the Xe-EDM experiment the aim is to set new limits on the electric dipole moment of ^{129}Xe associated with the coupling of its nuclear spin to an applied electric field. Co-located ^{3}He serves as a magnetometer for magnetic field normalization. Earlier experiments of our collaboration proved the advantage of ^{3}He/^{129}Xe comagnetometry, to set new sensitivity limits on non-magnetic spin couplings. Examples are the new limits on Lorentz Invariance violation in the matter sector for the bound neutron [51] and the investigation of short-range interactions mediated by axion-like particles [52].

2.1. Nuclear Spin in a Magnetic Field

The nuclear magnetic moment $\vec{\mu}$ of an atom arises from its nuclear spin $\vec{I}$:

$$\vec{\mu} = g\mu_N \vec{I} = \gamma\hbar\vec{I} \quad . \tag{2.1}$$

Here $\mu_N = \frac{e\hbar}{2m_P} = 3.1524512550(15) \cdot 10^{-8}\,\mathrm{eV{\cdot}T^{-1}}$ [53] is the nuclear magneton with the proton mass m_P, the elementary charge e and the reduced Planck constant $\hbar = 6.582119514(40) \cdot 10^{-16}\,\mathrm{eV{\cdot}s}$ [54]. The nuclear g-factor g and the gyromagnetic ratio γ vary for different atomic species. ^{3}He [53] and ^{129}Xe [55] have the following values[1]:

$$\begin{aligned} g_{^3\mathrm{He}} &= -4.255250616(50) \\ \gamma_{^3\mathrm{He}} &= -20.380167993(311) \cdot 10^7\,\mathrm{rad \cdot s^{-1} \cdot T^{-1}} \\ g_{^{129}\mathrm{Xe}} &= -1.544978008(100) \\ \gamma_{^{129}\mathrm{Xe}} &= -7.399733421(505) \cdot 10^7\,\mathrm{rad \cdot s^{-1} \cdot T^{-1}} \end{aligned} \tag{2.2}$$

[1]The values for γ were calculated from g with μ_N and $\hbar$, with respect to the particular uncertainties.

A magnetic moment $\vec{\mu}$ in a magnetic field has an energy given by

$$\mathrm{E} = -\vec{\mu} \cdot \vec{B} \quad . \tag{2.3}$$

Since both isotopes are spin $I = 1/2$-particles, the projection of their nuclear spin on the z-axis can have the values $m_I = \pm\frac{1}{2}$. If the magnetic field is $\vec{B} = B\hat{e}_z$ without loss of generality, the Zeeman effect leads to a splitting in the energy levels with a difference

$$\Delta\mathrm{E} = \mathrm{E}_{+\frac{1}{2}} - \mathrm{E}_{-\frac{1}{2}} = -\gamma\hbar B_0 \quad . \tag{2.4}$$

The exerting torque of the magnetic field on the angular momentum results in the so called Larmor precession of a species S with the angular frequency

$$\omega_L = \frac{|\Delta\mathrm{E}|}{\hbar} = \frac{|g_\mathrm{S}|\mu_N}{\hbar} B_0 = \gamma_\mathrm{S} B_0 \quad . \tag{2.5}$$

2.2. Polarization of ^{3}He and ^{129}Xe

Spin states can be described with the populations of Zeeman levels. In this context, polarization P is an unequal population of different spin states i with the quantum number m_i and the population number $N(m_i)$. It holds

$$P = \frac{1}{F} \frac{\sum_i m_i \cdot N(m_i)}{\sum_i N(m_i)} \tag{2.6}$$

where $F = I + J$ is the total angular momentum with the nuclear spin I and the total electronic angular momentum J. For a species S with a vanishing total electronic angular momentum in ground state and a nuclear spin of $I = 1/2$ (which is the case for both ^{3}He and ^{129}Xe) this equation can be simplified to

$$P = \frac{N_{+\frac{1}{2}} - N_{-\frac{1}{2}}}{N_{+\frac{1}{2}} + N_{-\frac{1}{2}}} \quad , \tag{2.7}$$

because in this two-state quantum system the magnetic quantum number can only be $m = \pm\frac{1}{2}$. In thermal equilibrium at the temperature T the population of the energy levels are given by the Boltzmann statistics

$$\frac{N_{-\frac{1}{2}}}{N_{+\frac{1}{2}}} = e^{-\frac{\Delta\mathrm{E}}{kT}} \quad , \tag{2.8}$$

with the Boltzmann constant k and where - in case of ^{3}He and ^{129}Xe - the spin state $m = -\frac{1}{2}$ is the lower energy level due to the negative g-factor. According to equation 2.7 this results in the so-called Boltzmann polarization

$$P_B = \frac{e^{-\frac{\Delta E}{kT}} - 1}{e^{-\frac{\Delta E}{kT}} + 1} > 0 \quad . \tag{2.9}$$

Due to the very small Zeeman splitting of the energy levels in comparison to the kinetic energy kT at room temperature ($T = 300\,\mathrm{K}$) the resulting Boltzmann polarization is merely in the order of $P \approx 10^{-6}$ at a magnetic field of $B = 1\,\mathrm{T}$. [56]

Optical pumping is a convenient method to obtain a higher polarization than the thermal Boltzmann polarization, which is usually called hyperpolarization. The following sections 2.2.1 and 2.2.2 give an introduction in two well-established methods:
2.2.1) **M**etastability **E**xchange **O**ptical **P**umping, (MEOP), used to hyperpolarize ^{3}He
2.2.2) **S**pin **E**xchange **O**ptical **P**umping, (SEOP), used to hyperpolarize ^{129}Xe.

2.2.1. Metastability Exchange Optical Pumping of ^{3}He

For the method of MEOP ^{3}He gas atoms is excited with laser light and the resulting angular momentum is transferred to the nucleus via metastable exchange collisions. The quantization axis is provided by a homogeneous magnetic field of a few Gauss. The method is briefly explained hereinafter.

By means of a weak gas discharge in ^{3}He gas at about 1 mbar, atoms are excited from ground state $1^1\mathrm{S}_0$ to the metastable state $2^3\mathrm{S}_1$, resulting in a concentration of about 1 ppm. The relevant energy levels for optical pumping of ^{3}He are shown in fig. 2.1. From this state, resonant laser light at around 1083 nm induces different hyperfine transitions to the 2^3P-states. Nine transitions in total can be identified, termed C1-9. For optical pumping the transitions C8 ($2^3\mathrm{S}_1(F = 1/2) \rightarrow 2^3\mathrm{P}_0$) and C9 ($2^3\mathrm{S}_1(F = 3/2) \rightarrow 2^3\mathrm{P}_0$) are the most efficient ones. Because of Doppler-broadening, which is about 2 GHz at room temperature [57], the closely spaced transitions C1 to C7 are partly overlapping and can not be resolved. Since some of these transitions even result in an opposing nuclear spin polarization, the C8 or C9 transitions are used, which are separated by about 6 GHz. C8 and C9 have their resonance at the wavelengths $\lambda_{\mathrm{C8}} = 1083.06\,\mathrm{nm}$ and $\lambda_{\mathrm{C9}} = 1083.03\,\mathrm{nm}$. For efficient pumping, the spectral line width of the resonant laser is matched to the Doppler-broadening.

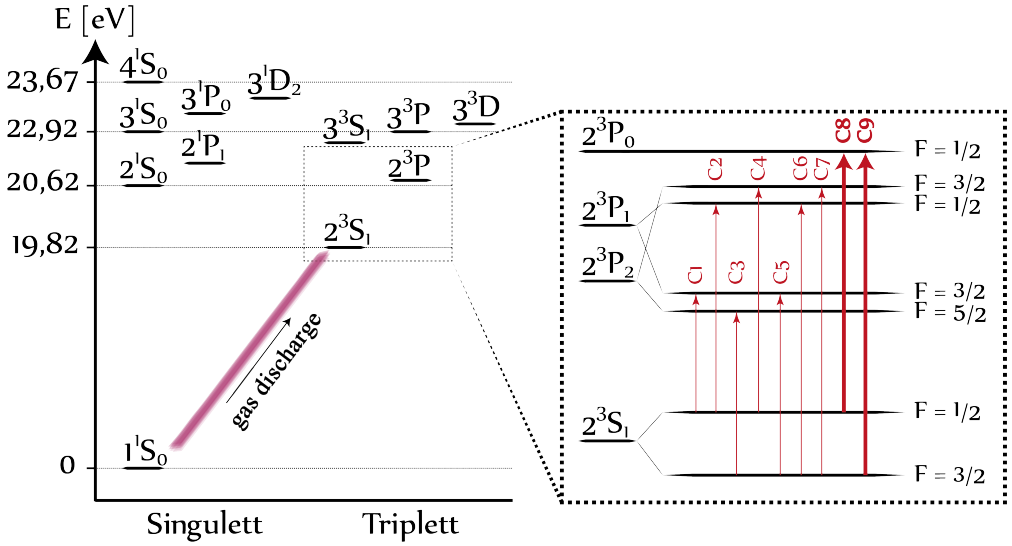

Figure 2.1.: Relevant energy levels for optical pumping of ^{3}He. The atoms are excited with a weak gas discharge to the metastable state 2^3S_1. By means of circular polarized laser light the transitions C8 and C9 are used to pump to the state 2^3P_0.

During the lifetime of the 2^3P_0-state of about $\tau_P \approx 10^{-7}$ s, gas kinetic collisions provide an equal population among the 2^3P-states which is known as collisional mixing. Afterwards they decay back to the 2^3S_1-states by isotropic light emission. By using σ^--polarized light the magnetic quantum number m_F changes by $\Delta m_F = -1$. The subsequent isotropic reemission to the metastable 2^3S_1-state does not change the net angular momentum. The atomic system has gained an angular momentum of $-\hbar$. Continuing resonant absorption of σ^--light and reemission increases the population number towards the negative m_F states in the 2^3S_1-state [58].

Due to hyperfine interaction part of the angular momentum of the absorbed laser photon is transferred to the nuclear spin almost instantaneously since the hyperfine coupling is strong and has a typical exchange time of $\tau_{HF} = 2.23 \cdot 10^{-10}$ s [59]. As a result, the ^{3}He in the metastable state gets nuclear spin polarized. By means of metastability exchange collisions the nuclear polarization of the metastable atom is transferred to the nuclear spin of the ground state atoms. During such a binary collision a molecule with a short lifetime of $\tau_{bin} \approx 10^{-12}$ s is formed. Since the nuclei of these molecules are indistinguishable, there is a probability that after dissociation both nuclei have changed their places. The former unpolarized nucleus of the ground state atom has gained a polarization. Only S-states are involved in this process, which conserves the angular momentum, i.e. no angular momentum leaks out in translational momenta:

$$^3\mathrm{He}^*(m_F) \; + \; ^3\mathrm{He}(\downarrow) \; \rightleftharpoons \; ^3\mathrm{He}^*(m_F - 1) \; + \; ^3\mathrm{He}(\uparrow) \tag{2.10}$$

This process is reversible, but it is more likely going from the right to the left because the states with lower m_F are more populated as a result of the optical pumping. The time constant of this metastable exchange is in the order of seconds [58]. The whole process is illustrated in figure 2.2.

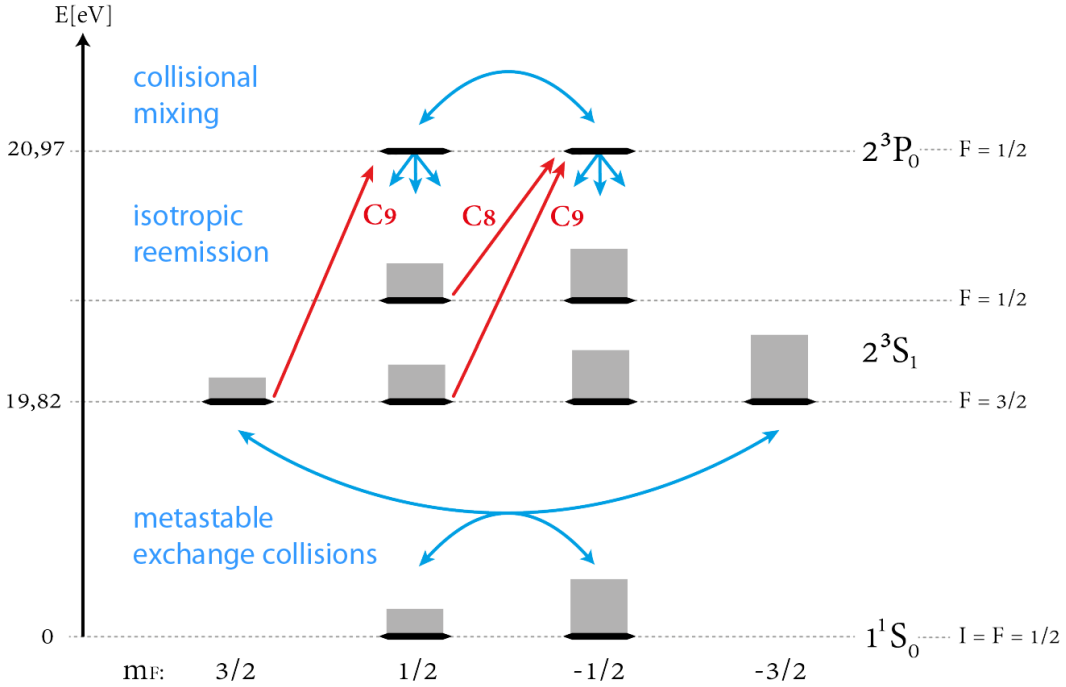

Figure 2.2.: The process of optical pumping of ^{3}He by using the C8- or C9-line with σ^--light and metastable exchange collisions to transfer the polarization to the ground state atoms: States with higher m_F are depopulated compared to the ones with lower m_F. Acc. [60]

Under standard conditions MEOP works very efficiently at a ^{3}He pressure of about 1 mbar. In order to reach higher gas pressures[2], the polarizer in Mainz, that is in use for the Xe-EDM experiment, is equipped with a non-magnetic compressor unit and an intermediate storage volume, which allows the polarized gas to be compressed into a storage cell in a second step. The process scheme of this polarizer is sketched in figure 2.3. A detailed insight into the method of operation can be found in [57].

[2] A high pressure $p \gg 1$ mbar is required for the storage and transport of the gas to avoid losses due to gradient relaxation, c.f. section 2.3.2. Furthermore, for our experiment we need a ^{3}He pressure in the order of 100 mbar in the transport cell.

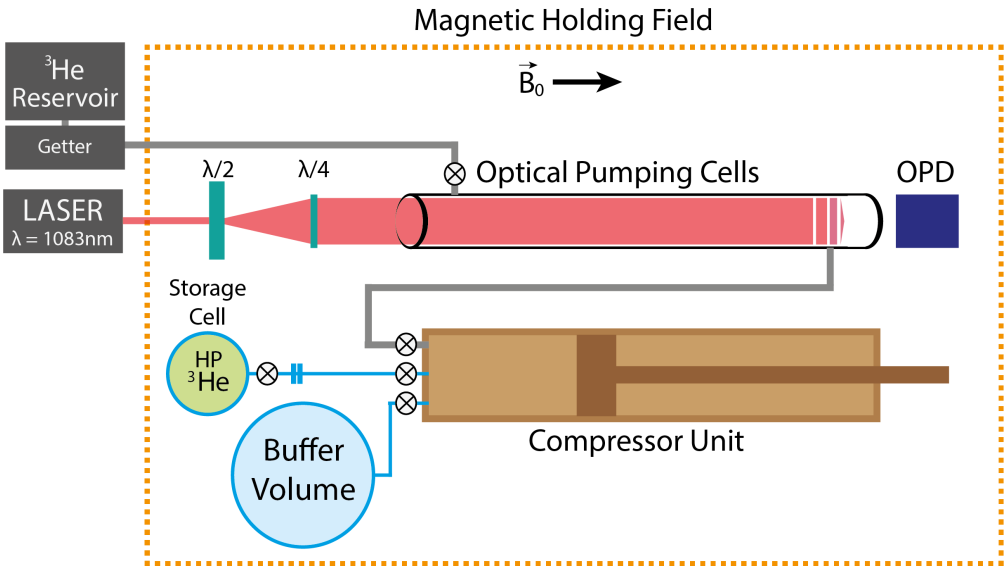

Figure 2.3.: Scheme of the compact ^{3}He MEOP polarizer in Mainz, used for the Xe-EDM experiment: Starting from a ^{3}He reservoir, the gas is purified by an SAES Getter (impurities < 1 ppb [61], in experimental conditions < 1 ppm) and afterwards it is filled into the optical pumping cells (OPC) up to a pressure of about 1 mbar. The six OPCs are glass cylinders with a length of ≈ 1.2 m and a diameter of ≈ 6 cm, each terminated with optical windows and connected in series. The length of the OPCs is adapted to the absorption length of the laser light at that given gas pressure and discharge strength. The laser light with $\lambda = 1083$ nm and a power of 15 W is linear polarized by a half-wave plate and expanded to match the diameter of the OPCs. Beam splitters (not shown) divide the light into six separate beams which pass through the respective OPCs. Quarter-wave plates provide circular polarization (σ^-) of the pumping light. Behind the OPCs, optical polarization detectors (OPD) monitor the polarization of the ^{3}He by observing the polarization of the $\lambda = 668$ nm fluorescent light of the gas discharge, which is proportional to the nuclear polarization of the ^{3}He [57]. After a polarization time of about ten seconds, a valve at the outlet of the last OPC is opened to let the gas flow from the outlet into a compressor unit. Afterwards the polarized gas is compressed into a buffer volume. Then the cycle is repeated until a sufficient amount of polarized gas is collected in the buffer cell. Finally it can be filled into a storage/transport cell and transported to the experiment inside a polarization conserving magnetic field.

The maximum achievable polarization is depending on different factors like the gas pressure, the purity of the gas, the strength of the gas discharge, as well as the goodness and adjustment of the σ^--laser-light. Polarization degrees higher than 90% have already been measured [60]. The compact polarizer in Mainz has a production rate of about 1.0 bar·l/h with an achievable polarization in the transport cell of $P \geq 60\%$ [57]. For the EDM measurements in Jülich, the hyperpolarized ^{3}He was transported from Mainz inside a special transport box with a polarization conserving magnetic field [62] (cf. section 4.3) in time intervals of two to three days.

2.2.2. Spin Exchange Optical Pumping of ^{129}Xe

^{129}Xe can be hyperpolarized by spin exchange optical pumping. This two step process is explained in this section. A more detailed description, as well as the method of operation can be found in [63].

In a first process the valence electron of alkali atoms (in our case rubidium vapor at a pressure of $p_{\mathrm{Rb}} \approx 0.1\,\mathrm{mbar}$) is spin polarized due to the absorption of circular polarized light inside a cylindrical glass cell [64]. The quantization axis is provided by a magnetic field $B_0 \simeq 1\,\mathrm{mT}$ which is parallel to the cylindrical axis of the cell and the laser beam. For optical pumping the D1 transition at $\lambda = 794.7\,\mathrm{nm}$ is used. Applying e.g. σ^+-light, atoms from the $5^2\mathrm{S}_{-\frac{1}{2}}$ ground state are excited into the $5^2\mathrm{P}_{+\frac{1}{2}}$ level. With a lifetime of $\tau_{\mathrm{P}} = 27.75\,\mathrm{ns}$, the excited state decays back to the ground state $5^2\mathrm{S}_{-\frac{1}{2}}$ with a probability of $\approx 2/3$ or to $5^2\mathrm{S}_{+\frac{1}{2}}$ with a probability of $\approx 1/3$. According to equation 2.7, the resulting polarization of rubidium after n absorption-and-emission cycles is

$$P_{\mathrm{Rb}} = \frac{N(m_S = +\frac{1}{2}) - N(m_S = -\frac{1}{2})}{N(m_S = +\frac{1}{2}) + N(m_S = -\frac{1}{2})} = 1 - \left(\frac{2}{3}\right)^n \quad . \tag{2.11}$$

In order to optimize this process, nitrogen at about 100 mbar is added as a buffer gas. This leads to a collisional mixing of the excited 5^2P levels. Furthermore, the additional N_2 quenches the emission of fluorescence light and the lifetime of the excited states is reduced to about $\tau_{\mathrm{P}} \approx 1\,\mathrm{ns}$. The unpolarized fluorescence light could otherwise be reabsorbed by the rubidium atoms, leading to a strongly reduced polarization. In combination with collisional mixing, the non-radiative decay of the 5^2P-states causes an even more efficient polarization build-up:

$$P_{\mathrm{Rb}} = 1 - \left(\frac{1}{2}\right)^n \quad . \tag{2.12}$$

Moreover, helium is added to the gas mixture to increase the total pressure inside the optical pumping cell. The resulting pressure broadening of the absorption line of the rubidium is adjusted to match the spectral line width of the laser[3] [63].
After the process of optical pumping, the rubidium atoms are spin polarized, with the spin quantization axis defined by the magnetic field $\vec{B}_0$.

[3] In our case, the spectral line width of the laser is about 0.15 nm. That requires to use buffer gases at a total pressure of about $p \approx 3 - 4\,\mathrm{bar}$ in order to match the pressure broadened absorption line to the spectral width of the laser.

In a second process, the polarized spin of the valence electron of a Rb atom is transferred to a ^{129}Xe nucleus in angular momentum conserving exchange collisions, like

$$\mathrm{Rb}(\uparrow) + \mathrm{Xe}(\downarrow) \longleftrightarrow \mathrm{Rb}(\downarrow) + \mathrm{Xe}(\uparrow) \quad . \tag{2.13}$$

The spin exchange is induced by the Fermi contact interaction of the Rb spin with the nuclear spin of the ^{129}Xe. Here the efficiency is strongly dependent on the interaction time of the collision process. Besides binary collisions with an interaction time of $\tau_{\mathrm{bin}} \approx 10^{-12}\,\mathrm{s}$, the Rb and Xe atoms can form van der Waals (vdW) molecules with an interaction time of $\tau_{\mathrm{vdW}} \approx 10^{-11} - 10^{-7}\,\mathrm{s}$ [63]. The formation of such vdW molecules is provided by three body collision process of type [65]

$$\mathrm{Rb} + \mathrm{Xe} + \mathrm{B} \rightleftarrows \mathrm{RbXe} + \mathrm{B} \quad , \tag{2.14}$$

as it is illustrated in figure 2.4. The third collision partner B - in this case a buffer gas atom (He or N_2) - is necessary to conserve energy and momentum in the collision process. Due to the longer interaction time, the spin exchange rate γ_{SE} of vdW interactions is higher than of binary collisions; $\gamma_{\mathrm{SE}}^{\mathrm{vdW}} \approx 3 \cdot \gamma_{\mathrm{SE}}^{\mathrm{bin}}$ [63].

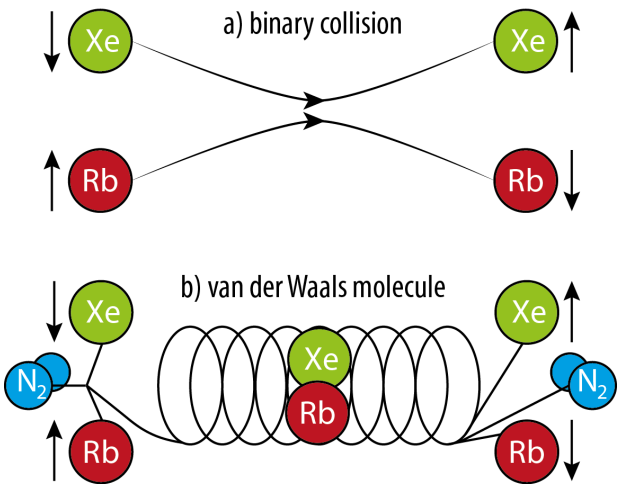

Figure 2.4.: Illustration of the spin exchange of Rb-Xe: a) due to binary collisions b) via van der Waals molecules (in this case with nitrogen as a buffer gas).

After the polarization procedure, the hyperpolarized ^{129}Xe is separated cryogenically [66] from the buffer gases: [Xe] : [B] $\approx 1 - 2\%$ [63]. By cooling the gas mixture - which is flowing out of the optical pumping cell - with a liquid nitrogen trap ($T = 77\,\mathrm{K}$), the only part that is freezing is the xenon with a freezing temperature of 161 K [67].

Once a sufficient amount of Xe-ice is accumulated, the buffer gases are pumped out, the remaining Xe is heated quickly to room temperature, and the sublimated gas is filled into a storage cell. The polarization process is schematically illustrated in figure 2.5.

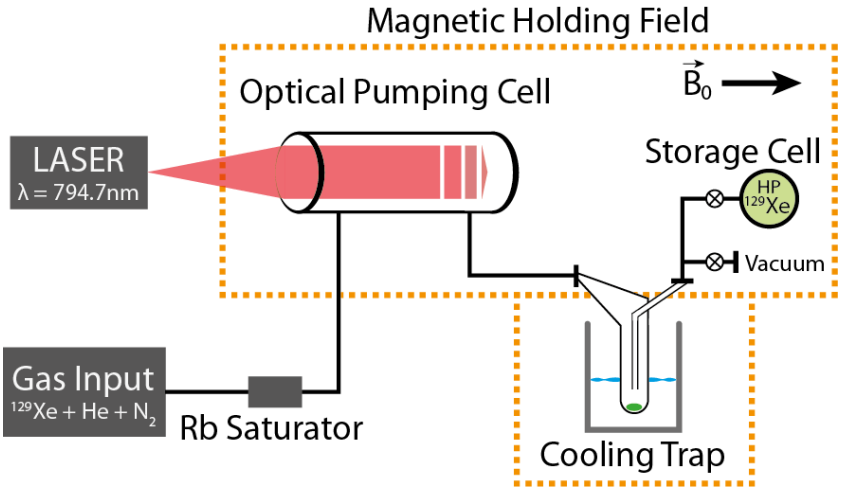

Figure 2.5.: Scheme of the ^{129}Xe SEOP polarizer used in the Xe-EDM experiment: The enriched ^{129}Xe[4] is mixed with the buffer gases He and N_2. Saturated with Rb, the gas mixture is filled into the optical pumping cell. A laser with $\lambda = 794.7\,\text{nm}$ and a power of about 50 W is used for the optical pumping of the rubidium. Via spin exchange, the xenon gets nuclear polarized and the gas mixture is flowing to a cooling trap. In this trap the Xe freezes and the buffer gases are pumped out. Once enough hyperpolarized Xe is accumulated, the Xe-ice is getting thawed and the sublimated Xe gas is stored in a storage cell. This cell can be detached and transported to the experiment. The whole process takes place in a magnetic holding field, provided by a Helmholtz-coil configuration and by permanent magnets[5].

The production rate of the polarizer is about 400 mbar·l/h [63]. Regarding the van der Waals relaxation (cf. section 2.3.2.1), the polarizer provides the possibility to mix the pure xenon again with a buffer gas, for example CO_2. Afterwards the storage cell can be detached and transported to the EDM experiment with a special transport box or a battery operated transport coil, providing a homogeneous magnetic guiding field for the hyperpolarized sample, as it will be introduced in section 4.3.2. The polarization in the transport cell was measured to $P \approx 20\%$.
For the Xe-EDM experiment the ^{129}Xe-polarizer was moved to the research center in Jülich. A transport of the hyperpolarized xenon from Mainz to Jülich - similar to the transport of hyperpolarized helium (cf. section 2.2.1) - was tested [69], but losses due to the high wall relaxation (compared to helium) were substantial.

[4] Isotopically enriched xenon with a ^{129}Xe content of 85%
[5] Halbach array [68] for the freezing/thawing unit

2.3. Magnetic Field of Spin Polarized Atoms

The magnetization $\vec{M}$ of an ensemble of nuclear polarized atoms is their total nuclear magnetic moment $\vec{m}$ per sample volume V

$$\vec{M} = \frac{\mathrm{d}\vec{m}}{\mathrm{d}V} \quad . \tag{2.15}$$

The total nuclear magnetic moment $\vec{m}$ in turn is the sum of the nuclear magnetic moments of the spin sample, or rather their expectation value $\langle\vec{\mu}\rangle$

$$\vec{m} = \sum\langle\vec{\mu}\rangle \quad . \tag{2.16}$$

Considering a degree of polarization P of a spin I with a gyromagnetic ratio γ, the macroscopic magnetization of the sample is given by

$$M = \frac{1}{V} \cdot m = \frac{1}{V} \cdot N \cdot P \cdot \gamma \cdot I \cdot \hbar \tag{2.17}$$

with the total number of atoms $N = \dfrac{pV}{kT}$ (pressure p, volume V, temperature T and Boltzmann constant k).

The resulting magnetic field of a spherical spin sample of polarization P can directly be linked to its magnetization $\vec{m}$. Outside of the sample volume the magnetic field is an ideal magnetic dipole field [70]

$$\vec{B}(\vec{r}) = \frac{\mu_0}{4\pi}\frac{3\vec{r}(\vec{r}\cdot\vec{m}) - \vec{m}}{r^3} \tag{2.18}$$

where $\vec{r}$ is the distance vector between the magnetic moment $\vec{m}$, concentrated in the center of the magnetized sphere, and a position outside of the sphere. If the magnetic moment is pointing in z-direction (without loss of generality), the resulting magnetic field component in this direction is

$$B_z(r) = \frac{\mu_0}{4\pi}\frac{m(3\cos^2\Theta - 1)}{r^3} \tag{2.19}$$

where Θ is the angle between the axis of the magnetic moment (z-axis) and $\vec{r}$.

2.3.1. Spin Precession

The equations of motion of a magnetization $\vec{M}$ in a magnetic field $\vec{B}$ can be described by the Bloch equations [71]

$$\frac{d}{dt}\vec{M}(t) = \gamma\vec{M}(t) \times \vec{B}(t) \tag{2.20}$$

with the gyromagnetic ratio γ of a particular atomic species.
Assuming that the magnetic moment is aligned with the magnetic field it is possible to flip the magnetic moment (or rather the spins) to the transversal plane. The magnetic moment starts to precess freely with the Larmor frequency ω_{L} (according to equation 2.5) around the axis (z-axis, without loss of generality) of the static magnetic field $\vec{B} = (0, 0, B_{\mathrm{z}})$.

A spin flip can be performed by different methods. Well known from classical NMR is the application of a resonant alternating magnetic field $\vec{B}_1(t)$, a so-called RF-pulse

$$\vec{B}_1(t) = B_1(\hat{e}_{\mathrm{x}} \cos(\omega_{\mathrm{RF}} \cdot t) + \hat{e}_{\mathrm{y}} \cos(\omega_{\mathrm{RF}} \cdot t)) \tag{2.21}$$

with the resonant frequency $\omega_{\mathrm{RF}} = \omega_{\mathrm{L}}$. The duration $0 \leq t \leq \tau_{\mathrm{RF}}$ and the amplitude B_1 define the resulting flip angle α of the RF-pulse

$$\alpha = \gamma B_1 \tau_{\mathrm{RF}} \quad . \tag{2.22}$$

If the magnetization is completely flipped from the longitudinal direction ($\vec{M} \parallel \vec{B}$) to the transversal direction ($\vec{M} \perp \vec{B}$) it is called a 90°- or $\pi/2$-pulse. Then the precession in the transversal plane is described by

$$\vec{M}(t) = \begin{pmatrix} M \cdot \cos(\omega_{\mathrm{L}} \cdot t) \\ M \cdot \sin(\omega_{\mathrm{L}} \cdot t) \\ 0 \end{pmatrix} \quad . \tag{2.23}$$

An alternative method of spin flip requires a distinction between adiabatic and non-adiabatic field rotation: If the external magnetic field $\vec{B}$ is rotated slowly out of the z-axis ($t_{\mathrm{rotation}} \gg 2\pi/\omega_{\mathrm{L}}$, adiabatic field change), the magnetic moment follows the magnetic field change and stays parallel to the current field axis. On the other hand, if $\vec{B}$ is rotating fast enough ($t_{\mathrm{rotation}} \ll 2\pi/\omega_{\mathrm{L}}$, non-adiabatic field change), the magnetic moment does not follow the field rotation and starts to precess around the actual B-field axis.

In the context of the Xe-EDM experiment with the spin species ^{3}He and ^{129}Xe, both methods are beneficial. The resonant excitation allows to select and to flip only one species at a predefined time ($\omega_{\mathrm{RF}} = \omega_{\mathrm{He\ (Xe)}}$), whereas it is possible to flip both species with the non-adiabatic field rotation simultaneously and even more under identical conditions, concerning the spin-flipped state.

2.3.2. Relaxation Mechanisms

Generally, the return of a system to the ground state - not in thermal equilibrium into its equilibrium state - is called relaxation. Considering a polarization P of a spin 1/2-state it has to be distinguished between two different mechanisms: the longitudinal component of the magnetization $\vec{M}$, parallel to the magnetic guiding field $\vec{B}_0$, decays exponentially with a characteristic decay time (relaxation time) T_1 into its value $M_{\mathrm{z,th}}$ at thermal equilibrium [71]. The transverse component, perpendicular to $\vec{B}_0$, decays exponentially with a transverse relaxation time T_2^*. This decay time T_2^* determines the envelope of the free decay of a free spin precession signal A, as shown in figure 2.6.

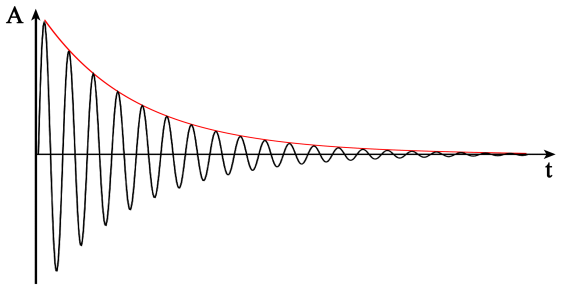

Figure 2.6.: Free decay of a spin precession, detected for example by an atomic magnetometer [72] or - as in our case - a SQUID system. The relaxation time T_2^* is represented by the envelope (red) of the decaying signal with $\sim \exp(-1/T_2^*)$. In nuclear magnetic resonance (NMR), this mechanism is called *free induction decay*; after a resonant excitation the precessing magnetization induces a decaying AC voltage to the NMR circuit.

To get the extended equations of motion, the relaxation terms have to be considered in the Bloch equations (cf. equation 2.20)

$$\frac{d}{dt}\vec{M}(t) = \gamma\vec{M}(t) \times \vec{B}(t) + \begin{pmatrix} -M_{\mathrm{x}}/T_2^* \\ -M_{\mathrm{y}}/T_2^* \\ (M_{\mathrm{z,th}} - M_{\mathrm{z}})/T_1 \end{pmatrix} \quad . \tag{2.24}$$

Both processes of relaxation are explained in the following paragraphs 2.3.2.1 and 2.3.2.2.

2.3.2.1. Longitudinal Relaxation

A decay of the longitudinal component M_z, and thus of the polarization P, can be described by

$$P(t) = (P_0 - P_\mathrm{B}) \cdot e^{-\frac{t}{T_1}} + P_\mathrm{B} \approx P_0 \cdot e^{-\frac{t}{T_1}} \quad , \tag{2.25}$$

where the approximation $P_0 \gg P_\mathrm{B}$ can be assumed, since we work with hyperpolarized gases. The time constant T_1 , the characteristic decay time for the polarization converging the Boltzmann polarization P_B in thermal equilibrium, is called longitudinal relaxation time. Different mechanisms contribute to T_1. Within the framework of the Xe-EDM experiment, the most relevant mechanisms are:

a) the relaxation due to magnetic field gradients (gradient relaxation) $T_{1,\mathrm{grad}}$,

b) the relaxation due to the interaction between the hyperpolarized samples and the wall of their container (wall relaxation) $T_{1,\mathrm{wall}}$,

c) the relaxation due to interaction between the atoms of the sample among each other, caused by binary collisions with $T_{1,\mathrm{bin}}$ and dimerization (van der Waals molecules) with $T_{1,\mathrm{vdW}}$,

d) as well as the relaxation due to paramagnetic gases - usually oxygen - $T_{1,\mathrm{O_2}}$.

All contributions add reciprocally to the total longitudinal relaxation time

$$\frac{1}{T_1} = \frac{1}{T_{1,\mathrm{grad}}} + \frac{1}{T_{1,\mathrm{wall}}} + \frac{1}{T_{1,\mathrm{bin}}} + \frac{1}{T_{1,\mathrm{vdW}}} + \frac{1}{T_{1,\mathrm{O_2}}} \quad . \tag{2.26}$$

Hereafter, the individual contributions are discussed in detail for both ^{3}He and ^{129}Xe.

a) Gradient Relaxation

To maintain the polarization after the actual polarization process a holding magnetic field $\vec{B}_0 = B_0 \cdot \hat{e}_z$ is still required. Naturally, such a magnetic field has gradients. In case of the longitudinal relaxation, transversal gradients located at the position of the gas sample - $\nabla B_{1,x} = \left(\frac{\partial B_{1,x}}{\partial x}, \frac{\partial B_{1,x}}{\partial y}, \frac{\partial B_{1,x}}{\partial z}\right)$ and analogously $\nabla B_{1,y}$ - result in a variation of the magnitude of the magnetic field which is seen by each atom. While the atom is diffusing inside the cell it perceives a fluctuating magnetic field in its rest frame. If the Fourier transform of this fluctuation contains frequency components at or close to the resonant frequency ω_L, it leads to a spin flip, according to equation 2.22 and causes the gradient induced $T_{1,\mathrm{grad}}$ relaxation.

For a spherical sample volume the general expression for the longitudinal gradient relaxation is given by [73]

$$\frac{1}{T_{1,\mathrm{grad}}} = 2D\frac{|\nabla B_{1,x}|^2 + |\nabla B_{1,y}|^2}{B_0^2} \times \sum_n \frac{1}{|x_{1,n}^2 - 2| \cdot (1 + D^2 x_{1,n}^4 (\gamma B_0)^{-2} R^{-4})} \quad . \tag{2.27}$$

Here R is the radius of the sphere and D is the diffusion coefficient of the gas species. $x_{1,n}$ with $n = 1, 2, 3, ...$ are the zeros of the derivative of the spherical Bessel function, $\frac{d}{dx} j_1(x_{1,n}) = 0$.

For the Xe-EDM experiment, gas mixtures with different additional buffer gases, i.e. CO_2, SF_6, ^{4}He and N_2, are used, for example to optimize the overall relaxation time (cf. appendix A.3). The diffusion coefficients of the gases of interest are listed in table 2.1.

diff. coeff.	[cm^2/s]	temp. [K]	ref.	diff. coeff.	[cm^2/s]	temp. [K]	ref.
D_{He}	1.85	294	[74]	D_{Xe}	0.058	294	[74]
$D_{\mathrm{He\ in\ Xe}}$	0.61	294	[74]	$D_{\mathrm{Xe\ in\ He}}$	0.790	294	[74]
$D_{\mathrm{He\ in\ CO2}}$	0.60	298	[75]	$D_{\mathrm{Xe\ in\ CO2}}$	0.085	298	[75]
$D_{\mathrm{He\ in\ SF6}}$	0.48	294	[74]	$D_{\mathrm{Xe\ in\ SF6}}$	0.046	293	[76]
$D_{\mathrm{He\ in\ N2}}$	0.77	294	[74]	$D_{\mathrm{Xe\ in\ N2}}$	0.21	353	[77]

Table 2.1.: Self diffusion coefficients of He and Xe and binary diffusion coefficients of He and Xe - mutually and in CO_2, SF_6 and N_2 at a pressure of 1 bar. For ^{3}He and ^{4}He the same values can be assumed.

The diffusion coefficient of a species i in a particular gas mixture GM can be calculated with

$$\frac{1}{D_i^{\mathrm{GM}}} = \left(\frac{p_i}{D_i} + \frac{p_{j1}}{D_{i\ \mathrm{in\ j1}}} + \frac{p_{j2}}{D_{i\ \mathrm{in\ j2}}} + \frac{p_{j3}}{D_{i\ \mathrm{in\ j3}}} + \cdots \right) \cdot \frac{1}{p_0} \cdot \frac{T_0^{3/2}}{T^{3/2}} \tag{2.28}$$

where p_i is the partial pressure of the species of interest with the corresponding self diffusion coefficient D_i and $p_{\mathrm{j1,2,3}}$ are the partial pressures of the additional gas components with the corresponding binary diffusion coefficients $D_{i\ \mathrm{in\ j1,2,3}}$.

Regarding the gradient relaxation and the denominator in equation 2.27 it is convenient to define the relation [73, 77]

$$\frac{\tau_d}{\tau_p} = \frac{R^2 \cdot \omega_{\mathrm{L}}}{D} \propto pB_0 \quad . \tag{2.29}$$

Here $\tau_d = R^2/D$ is the diffusion time and $\tau_p = 1/\omega_\mathrm{L}$ is the spin precession time. It can be distinguished between two different cases:

i) $\tau_d/\tau_p \ll 1$: The diffusion time throughout the sample cell is much smaller than the spin precession time. For a given radius R this is the so-called low pressure regime. In this case the gradient relaxation time $T_{1,\mathrm{grad}}$ is inversely proportional to the square of **absolute** transverse field gradients

$$\frac{1}{T_{1,\mathrm{grad}}} \approx \frac{8R^4\gamma^2}{175D}\left(|\vec{\nabla}B_x|^2 + |\vec{\nabla}B_y|^2\right) \quad . \tag{2.30}$$

ii) $\tau_d/\tau_p \gg 1$: The diffusion time is much larger than the spin precession time. For a given radius R this is the so-called high pressure regime. In this case the gradient relaxation time $T_{1,\mathrm{grad}}$ is inversely proportional to the square of **relative** transverse field gradients

$$\frac{1}{T_{1,\mathrm{grad}}} \approx \frac{D}{B_0^2}\left(|\vec{\nabla}B_x|^2 + |\vec{\nabla}B_y|^2\right) \quad . \tag{2.31}$$

During the transport and storage of the hyperpolarized gases, as well as for the measurements, that are presented in this thesis, the settings are altogether stated in the high pressures regime. The gas samples in the storage/transport cells ($R \approx 6\,\mathrm{cm}$ for He and $R \approx 3\,\mathrm{cm}$ for Xe) after the polarization processes have a pressure of about 1 bar (for both He and Xe, cf. sections 2.2.1 and 2.2.2). The gas handling of the experimental procedure, as it will be introduced in section 4.3, requires transport and storage of the gases and the possibility to mix them together with buffer gases. A special magnetic transport box and a transport coil, as well as a mixing station provide magnetic fields in the order of several G. Furthermore, the gas mixture in the EDM cell ($R \approx 5\,\mathrm{cm}$) during EDM production runs has a total pressure of about 100 mbar (cf. section 4.3.1) with a magnetic field of $B_0 \approx 400 - 500\,\mathrm{nT}$ (cf. section 4.2). In all cases $\tau_d/\tau_p \gg 1$ applies and the $T_{1,\mathrm{grad}}$ relaxation time is limited by the relative magnetic field gradients.

b) Wall Relaxation

The polarized gas samples are always stored in glass cells. Because of Fermi contact interaction with para- and ferromagnetic centers, gas collisions with the wall of the storage cell lead to another contribution of relaxation. Especially ferromagnetic impurities on the inner surface of the glass cells cause spin flips during the short binary collision time. To reduce this influence a special glass is used which shows low relaxivity, even for hyperpolarized Xe gas. This aluminosilicate glass GE-180 [78] is remarkably helium-tight and prevents the atoms to diffuse into the glass matrix due to its high impermeability.

Consequently the interaction time with the wall is reduced to the binary interaction time of $\tau_{\text{bin}} \approx 10^{-12}\,\text{s}$ (for ^{3}He). For ^{129}Xe, its polar character leads to a longer sticking time with the wall, resulting in a higher wall relaxation rate. As a result, ^{129}Xe is much more sensitive to the wall relaxation than ^{3}He. A universal expression for the wall relaxation is given by

$$\frac{1}{T_{1,\text{wall}}} = \eta \cdot \frac{S}{V} \quad . \tag{2.32}$$

The relaxation time is therefore linearly depending on the respective volume V to surface S ratio. Therefore, the wall relaxation in spherical cells is proportional to the radius of the cell $T_{1,\text{wall}} \propto R$. The relaxivity η is depending on the microscopic surface structure of the cell's wall, as well as on the previously mentioned magnetic impurities of the wall material and its permeability. A thorough cleaning procedure of the cell is mandatory to wash out possible contaminations. In addition a degaussing procedure [79,80] is used to demagnetize residual ferromagnetic impurities. For spherical glass cells made out of GE 180, wall relaxation times for He of $T_{1,\text{wall}} > 100\,\text{h}$ and for Xe $T_{1,\text{wall}} \approx 18\,\text{h}$ [81] can be achieved in cells with a radius of $R \approx 5\,\text{cm}$.

c) Binary and van der Waals Relaxation

The spin polarized ^{3}He and ^{129}Xe atoms inside the glass cell can form molecules with a short lifetime via covalent bonds, caused by binary collisions. These molecules have additional degrees of freedom due to vibration and rotation. If the spin of a quasi-bound atom couples to the rotational angular momentum of the molecule, the angular momentum from the spin system leaks out into external momenta after the collision, causing another contribution to the relaxation called binary relaxation with the relaxation time $T_{1,\text{bin}}$. Since the probability of forming such covalent bonds is linearly dependent on the pressure of the gas mixture, the relaxation time is inversely proportional to the pressure. For helium and xenon there are the relations

$$T_{1,\text{bin}}^{\text{He}} \approx \frac{p_0}{p_{\text{He}}} \frac{T}{T_0} \cdot 754\,\text{h} \qquad \text{and} \tag{2.33a}$$

$$T_{1,\text{bin}}^{\text{Xe}} \approx \frac{p_0}{p_{\text{Xe}}} \frac{T}{T_0} \cdot 56\,\text{h} \tag{2.33b}$$

with the standard pressure $p_0 = 1.013\,\text{bar}$ and the standard temperature $T_0 = 273.15\,\text{K}$. Within the range of several $10 - 100\,\text{mbar}$ it can easily be estimated that the binary relaxation $T_{1,\text{bin}}$ is negligible for this experiment, compared for example with $T_{1,\text{wall}}$.
Another enhanced relaxation mechanism for heavy atoms like xenon is induced due to the formation of van der Waals molecules with a longer lifetime than covalent bonds (cf.

section 2.2.2). This longer lifetime leads to a longer interaction between the nuclear spin and the rotational angular momentum, resulting in an increased spin relaxation. The so-called van der Waals relaxation time $T_{1,\mathrm{vdW}}$ for pure xenon (isotopic enrichment of ^{129}Xe to 85%) is determined from experimental studies [81] to

$$T_{1,\mathrm{vdW}}^{\mathrm{Xe}} = (4.6 \pm 0.1)\,\mathrm{h} \quad . \tag{2.34}$$

An admixture of appropriate buffer gases - such as SF_6, N_2, CO_2 or ^{4}He - to the gas reduces the van der Waals relaxation rate. These additional collision partners break up the Xe-Xe dimers and shorten the relaxing interaction. The efficiency of this mechanism is described by

$$T_{1,\mathrm{vdW}}^{\mathrm{Xe\ in\ B}} = T_{1,\mathrm{vdW}}^{\mathrm{Xe}} \left(1 + r_{\mathrm{B}} \frac{[\mathrm{B}]}{[\mathrm{Xe}]}\right) \quad , \tag{2.35}$$

where the destruction rate coefficient r_{B} quantifies the suppression of the van der Waals relaxation by a buffer gas B in ^{129}Xe, depending on the ratio of the partial pressures of both species [82]. Table 2.2 shows the respective destruction rate coefficients of the buffer gases that are mentioned above. With the highest destruction rate CO_2 is the most expedient buffer gas to minimize the van der Waals relaxation.

item	value	reference
r_{N_2}	0.46 ± 0.05	[81]
r_{SF_6}	0.70 ± 0.09	[81]
r_{CO_2}	1.40 ± 0.22	[81]
$r_{^4\mathrm{He}}$	0.25 ± 0.08	[82]

Table 2.2.: Destruction rate coefficients for different buffer gases in xenon.

d) O_2 Relaxation

In their ground state, paramagnetic atoms and molecules have a magnetic momentum caused by their spin and angular momentum. Similar to the mechanisms mentioned above concerning the intrinsic effects of binary and van der Waals relaxation, the relaxation by paramagnetic gases also occurs during collisions between the species and the coupling of their spin to the polarized nuclear spin. The most common contribution in experimental conditions arises from oxygen impurities[6] in the gas. Due to the vacuum

[6] O_2-molecules have a total angular momentum of $J = 1$

conditions during the provision of the polarized gases, their transport and mixing with buffer gases, and the final filling of the mixture, this contaminant is inevitable to a greater or lesser extent. Hence, for long relaxation times it is mandatory to reduce the O_2/air content to a tolerable level.
The relaxation time induced by oxygen in polarized ^{3}He was measured to be

$$T_{1,O_2}(^3\mathrm{He}) = 2.5\,\mathrm{s} \cdot \frac{\mathrm{bar}}{p_{O_2}} \tag{2.36}$$

at a temperature of 299 K [83]. For polarized ^{129}Xe T_{1,O_2} was measured to be

$$T_{1,O_2}(^{129}\mathrm{Xe}) = 2.1\,\mathrm{s} \cdot \frac{\mathrm{bar}}{p_{O_2}} \tag{2.37}$$

at a temperature of 300 K [84]. Clearly, the partial pressure of oxygen p_{O_2} has to be as low as possible to be not limited by T_{1,O_2}. At partial pressures of oxygen smaller than for example 10^{-3} mbar, the corresponding relaxation time is longer than 500 h and consequently this contribution can be neglected. The experimental setup, with the vacuum components in particular (cf. chapter 3), was planned and tested with the functional requirement of keeping oxygen/air contaminations as low as possible.

2.3.2.2. Transverse Relaxation

If the magnetic moment is not parallel or anti-parallel to the magnetic guiding field, the transverse component is precessing with the Larmor frequency (cf. equation 2.23). The amplitude of this transverse component of the magnetic moment decays with the characteristic time constant T_2^*, referred to as transverse relaxation time.
Besides the longitudinal relaxation time T_1 (cf. equation 2.26), T_2^* is also depending on the ∇B_z-contribution of the magnetic guiding field gradients

$$\frac{1}{T_2^*} = \frac{1}{T_1} + \frac{1}{T_{2,\mathrm{grad}(B_z)}} \quad . \tag{2.38}$$

The contribution $T_{2,\mathrm{grad}(B_z)}$ quantifies the loss of phase coherence between the spins of the sample. The spins are dephasing because each polarized atom of a sample sees a different magnetic field due to inevitable magnetic field gradients (∇B_z). Therefore, each spin precesses with a slightly different Larmor frequency $\omega_\mathrm{L}(r) = \gamma \cdot |\vec{B} + \Delta B_z \cdot r|$[7], depending on its local position r inside the sample volume.

[7] Compared to NMR of solids or liquids (almost static case), this process is irreversible since the atoms of the gas are fast diffusing inside the vessel and cannot be recovered, e.g. by a spin-echo pulse [85].

Together with $T_{1,\mathrm{grad}}$, as introduced in the previous section (equation 2.27), the total transverse gradient relaxation $T_{2,\mathrm{grad}}$ for a sample in a spherical volume is given by

$$\begin{aligned}\frac{1}{T_{2,\mathrm{grad}}} &= \frac{1}{T_{1,\mathrm{grad}}} + \frac{1}{T_{2,\mathrm{grad}(B_z)}} \\ &= \frac{8R^4\gamma^2}{175D}\left(a(\lambda)\cdot\left(|\nabla B_x|^2 + |\nabla B_y|^2\right) + |\nabla B_z|^2\right)\end{aligned} \tag{2.39}$$

where the factor

$$a(\lambda) = \frac{175}{8}\lambda \cdot \sum_n \frac{1}{|x_{0,n}^2 - 2| \cdot (1 + x_{0,n}^4\lambda)} \tag{2.40}$$

with

$$\lambda = \frac{D^2}{\gamma^2 B_0^2 R^4} \tag{2.41}$$

describes the contribution of the transversal magnetic field gradients $|\nabla B_x|$ and $|\nabla B_y|$ [73]. As before, R is the radius of the spherical volume, γ is the gyromagnetic ratio of the gas species and $D \propto 1/p$ [86] is its diffusion coefficient in the gas mixture (see table 2.1 for He and Xe and equation 2.28). In the high pressure regime $\tau_d/\tau_p = 1/\sqrt{\lambda} \ll 1$ (cf. equation 2.29) the factor $a(\lambda)$ vanishes. Accordingly $T_{2,\mathrm{grad}}$ is only depending on the gradients in z-direction; the corresponding $T_{1,\mathrm{grad}}$-contribution from equation 2.31 gets negligible. In the low pressure regime $\tau_d/\tau_p \gg 1$ the factor $a(\lambda)$ gets 0.5 (in accordance with equation 2.30) and therefore $T_{2,\mathrm{grad}}$ is also depending on the transverse gradients of the magnetic field [87].
As stated earlier in section 2.3.2.1, the EDM measurements are operated in the high pressure regime. Only for special tests, for the gradient optimization via T_2^* of ^{3}He in particular (cf. section 4.2.2), the pressure is set to smaller values on purpose, to be also sensitive on transversal gradients. For example, with a pressure of 1 mbar of ^{3}He in a $R = 5\,\mathrm{cm}$ cell and a magnetic field of $B_0 = 400\,\mathrm{nT}$ we get $\tau_d/\tau_p = 1.1$ and $a(\lambda) \neq 0$.

To conclude, the magnetic field gradients should be as low as possible to maximize the transverse relaxation time T_2^*. For the Xe-EDM experiment gradients in the order of several pT/cm are aspired to be mainly dependent on the wall relaxation time and the van der Waals relaxation of ^{129}Xe. As a result, with a gas mixture of $p_{\mathrm{Xe}} \approx 100\,\mathrm{mbar}$ and $p_{\mathrm{He}} \approx 50\,\mathrm{mbar}$ and the relaxation times $T_{1,\mathrm{wall,Xe}} \approx 8\,\mathrm{h}$ and $T_{1,\mathrm{vdW,Xe}} \approx 4.6\,\mathrm{h}$ we can achieve transverse relaxation times of $T_{2,\mathrm{Xe}}^* > 2\,\mathrm{h}$. This corresponds to a gradient relaxation time $T_{2,\mathrm{grad,Xe}} > 6\,\mathrm{h}$. An optimization of the achievable sensitivity of the Xe-EDM δd_{Xe} - regarding the gas mixture composition - is presented in appendix A.3. Here, the dependencies on the relevant contributions $T_{1,\mathrm{wall}}$, $T_{1,\mathrm{vdW}}$ and $T_{2,\mathrm{grad}}$ are taken into account concerning the particular limitations.

2.3.3. Readout of the Spin Precession with SQUIDs

A sophisticated device for the detection of spin precession in particular in low magnetic fields ($< 100\,\mu$T) is the so-called SQUID[8] magnetometer. A major advantage over other techniques, for example readout via atomic magnetometers, is especially the low noise level in the order of $\rho \sim \mathrm{fT}/\sqrt{\mathrm{Hz}}$. A low noise level is mandatory to obtain a high signal-to-noise ratio (SNR). For the Xe-EDM experiment we aspire an SNR of $\sim 10000 : 1$, with signal amplitudes in the order of $10 - 100\,$pT (cf. chapter 6).
This section gives a brief overview on the fundamental principle of DC-SQUID magnetometers, as they are used for the Xe-EDM experiment. A more profound discussion of the theory, technical functionality and operational implementation of SQUIDs can be found in "The SQUID Handbook" [88,89]. A detailed description of the setup - including the SQUID-system - is presented in chapter 3.

All SQUID-detectors are based on the principle of magnetic flux quantization in superconducting rings. Due to the quantization with the flux quantum [90]

$$\Phi_0 = \frac{h}{2e} = 2.067833831(13) \cdot 10^{-15}\,\mathrm{Vs} \tag{2.42}$$

an induced current in such a ring is always compensating the magnetic flux through the ring in multiples of the flux quantum. Furthermore, the method of construction provides a superconducting ring divided by one (RF-SQUID) or two (DC-SQUID) thin insulating or resistive layer/s (weak links). The Josephson effect describes a supercurrent via Cooper pairs across such tunneling barriers, the so-called superconducting tunnel junctions or Josephson junctions [91].

In case of a DC-SQUID with two parallel Josephson junctions and no external magnetic field, an input current I splits up in two equal parts, as illustrated in figure 2.7, left. A small change of the external magnetic field leads to a circulating current in the loop, the so called screening current I_s, compensating the flux through the ring. The screening current is consequently parallel to the input current in one of the arms of the ring (total current: $I/2 + I_s$) and antiparallel to the one in the other arm (total current: $I/2 - I_s$). If one of both arms exceeds a critical current I_c in the junction, a quantifiable voltage drop occurs.

[8] short for: Superconducting QUantum Interference Device

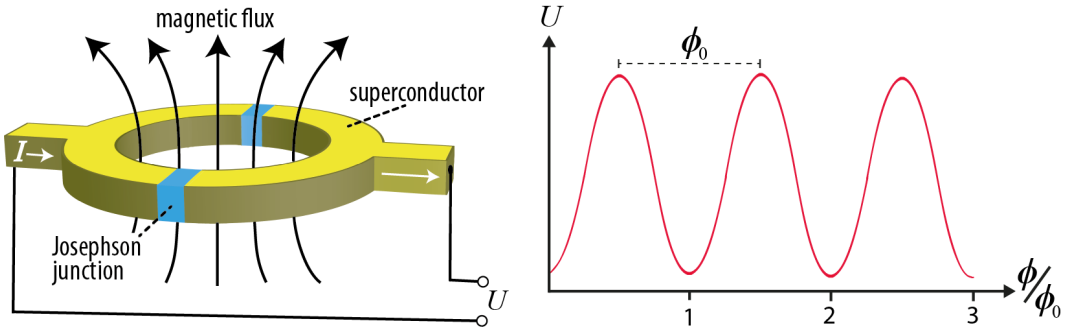

Figure 2.7.: Principle of a DC-SQUID working as a flux-to-voltage converter, acc. [88].

If the external flux through the ring surpasses $\Phi_0/2$, the screening current changes direction to increase the enclosed flux of the loop to Φ_0. Analogous for a higher magnetic flux, the screening current always provides an integer multiple of the magnetic flux quantum through the loop. Therefore, the voltage across the junctions is periodically modulated by the magnetic flux with a periodicity of Φ_0, as illustrated in figure 2.7, right). Amplified and integrated, this flux-to-voltage behavior provides a measurable function of the external magnetic flux through the SQUID.

To improve the signal of a device such as described above, it is possible to use an additional pickup-loop, basically a single superconducting loop, coupled to the SQUID with a coil next to it, shown schematically in figure 2.8. The signal improves due to the larger surface of the pickup-loop compared to the actual SQUID-loop, whereas the intrinsic noise of the SQUID (e.g. Johnson-Nyquist noise of the Josephson junctions) stays the same. Hence a higher signal-to-noise ratio is achievable. Additionally, if two compensating pickup-loops are used - connected in series and separated by a baseline length b - the system works as a gradiometer. The effective flux induced to the SQUID by the input coil gets zero, if the magnetic field is the same at both loops. This is the case for a homogeneous field and homogeneous (non-local) field changes, so called common-mode field drifts. "Global" influences - for example environmental-related mechanical vibrations of the system (building, setup, etc.) relative to the local magnetic field - do not generate a signal in first order. For the practical implementation of such additional pickup-loops, the SQUID itself has to be magnetically shielded to prevent signal distortions[9]. The net signal S of the spin precession of a spherical spin sample, recorded by the gradiometer is given by

$$S \propto \frac{1}{d^3} - \frac{1}{(d+b)^3} \tag{2.43}$$

[9] In our case the sensor unit is mounted inside a niobium capsule.

with the baselength b and the distance d from the center of the sample to the first gradiometer loop next to it, as it is illustrated in figure 2.8. With an appropriate choice of the baselength b, compared to the sample distance d, the benefits of the gradiometer configuration in terms of magnetic noise reduction can significantly outweigh the resulting signal reduction. If we compare the signal of the gradiometer setup with a single-loop configuration we get a reduction of

$$\eta = 1 - \left[\left(\frac{1}{d^3} - \frac{1}{(d+b)^3} \right) : \left(\frac{1}{d^3} \right) \right] \quad . \tag{2.44}$$

In our case we have a signal reduction of about $\eta \approx 17.5\%$ (cf. section 3.1.2).

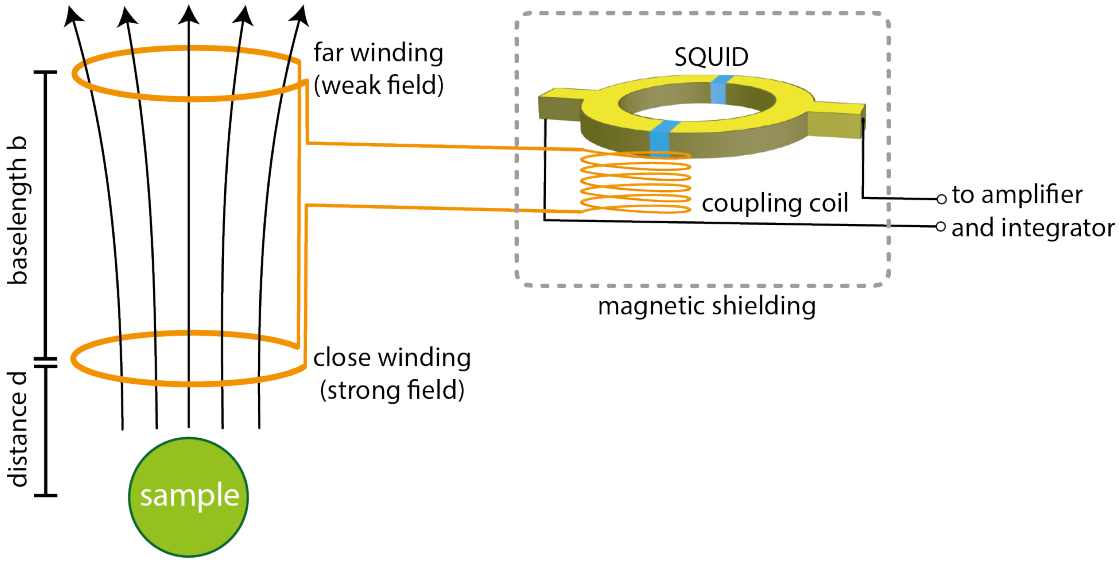

Figure 2.8.: Principle of a DC-SQUID with gradiometer windings. The two pickup-loops are connected in series in a compensating mode with a coupling coil next to the SQUID. The effective signal is the difference between the magnetic flux through the close and distant gradiometer loops with respect to the position of the spin sample. Common-mode drifts do not contribute. The magnetic field of the sample is thereby transformed by the pickup-loops into a current which in its part induces a magnetic field in the coupling coil. This coupling field is detected by the SQUID and can be read out with an amplifier and integrator. Because the SQUID and the coupling coil are magnetically shielded, the signal detected by the SQUID relates exclusively to the gradiometer configuration.

A deeper look into the design of our SQUID system, as well as the description of its further components (such as the cooling system), and characterizing measurements are presented in the next chapter 3, especially in section 3.1.1.

2.4. Methodical Approach of the ^{129}Xe-EDM Experiment

Before introducing the experimental setup in the next chapter 3, this section presents the principle idea behind the measurement of our proposed Xe-EDM experiment.

The basic idea for this experiment is to put a glass cell with hyperpolarized ^{3}He and ^{129}Xe in a magnetic holding field $\vec{B}_0$ and an electric field $\vec{E}$, and observe the spin precession of both species with a SQUID gradiometer. The polarity of a plate capacitor can be changed so that the electric field is switched between a parallel and antiparallel orientation relative to $\vec{B}_0 = B_0 \cdot \hat{e}_z$. To start the precession of the nuclear spins, at first the magnetic field has to be changed adiabatically from $\vec{B}_0$ to $\vec{B}_x \parallel \hat{e}_x$. The orientation of the magnetization of the sample follows this slow rotation. A non-adiabatic field change back to $\vec{B}_0$ will finally start the spin precession for both species (cf. section 2.3.1). The precessing magnetization of ^{3}He and ^{129}Xe can then be detected and evaluated. A schematic illustration of this method is presented in figure 2.9. As it will be shown later, the precession frequency of ^{3}He is used as a (co-)magnetometer to normalize on magnetic field drifts and fluctuations.

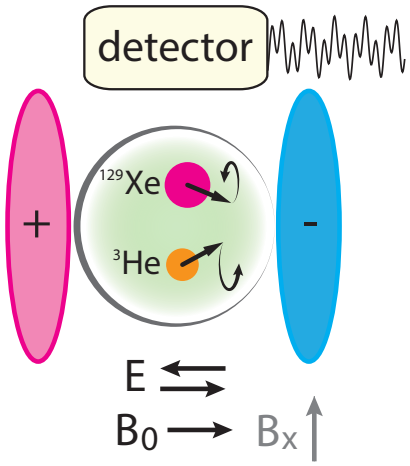

Figure 2.9.: Schematic figure of the functional principle of the Xe-EDM experiment. A glass cell filled with hyperpolarized ^{3}He and ^{129}Xe is placed below a SQUID gradiometer (detector) and in between a plate capacitor with its electric field pointing parallel or antiparallel to the applied magnetic field $\vec{B}_0$. After initializing the spin precession around $\vec{B}_0$ the signal is detected by the SQUID gradiometer. The effective signal is a superposition of the precession signals of ^{3}He and ^{129}Xe, which differ in frequency by the ratio $\gamma_{\mathrm{He}}/\gamma_{\mathrm{Xe}}$. The technique of comagnetometry allows an almost ideal compensation of any magnetic field drifts and fluctuations. The possible change of the precession frequency resulting from a finite electric dipole interaction ($\propto \vec{d} \cdot \vec{E}$) can be detected by comparing the spin precession frequencies with an applied electric field parallel and antiparallel to $\vec{B}_0$.

2.4.1. Comagnetometry

The term *comagnetometry* describes the simultaneous observation of the spin precession of a sample of two co-located (occupying the same volume) polarized spin species - in this experiment ^{3}He and ^{129}Xe with their respective Larmor frequencies ω_{He} and ω_{Xe}. The advantage of this method is that the magnetic interaction with the Hamiltonian (cf. equation 1.13) drops out in the weighted frequency difference

$$\begin{aligned} \Delta\tilde{\omega} &= \omega_{\mathrm{Xe}} - \frac{\gamma_{\mathrm{Xe}}}{\gamma_{\mathrm{He}}} \cdot \omega_{\mathrm{He}} \\ &= \gamma_{\mathrm{Xe}} \cdot B_0 - \frac{\gamma_{\mathrm{Xe}}}{\gamma_{\mathrm{He}}} \cdot \gamma_{\mathrm{He}} \cdot B_0 \\ &= 0 \quad . \end{aligned} \tag{2.45}$$

This means that the observable $\Delta\tilde{\omega}$ is not depending on the magnetic Zeeman splitting, i.e. magnetic field drifts and fluctuations should drop out almost completely. Even inside the magnetically shielded room of our experiment (introduced in section 3.2.1), magnetic field drifts of several pTesla(pT)/h are observable. That corresponds to frequency drifts in the order of 10^{-5} to 10^{-4} Hz/h. An example of such a field drift, measured with the precession frequency of ^{3}He, is plotted in figure 2.10.

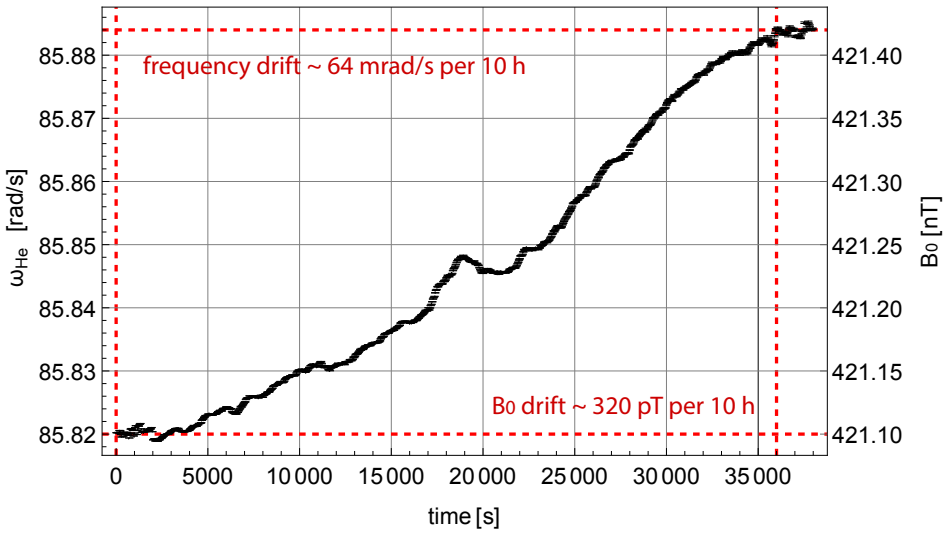

Figure 2.10.: Example of a magnetic field drift in a magnetically shielded environment, monitored by the spin precession frequency of ^{3}He. This measurement was taken in the magnetically shielded room at the research center in Jülich in July 2017 with the EDM setup. The magnetic field B_0 drifts from ~ 421.10 nT to ~ 421.42 nT within ten hours.

Since the measurement sensitivity in terms of EDM-related frequency shifts can reach pHz/day, these much stronger temporal field drifts/fluctuations have to be normalized to a high degree by comagnetometry. For this we use the ^{3}He precession, since it does not contribute to a detectable EDM signal, in contrast to ^{129}Xe (cf. section 1.2.2).

Based on equations 1.15 and 1.16 and considering a non-vanishing EDM the weighted frequency difference of the He/Xe spin clock is

$$\Delta\tilde{\omega} = \omega_{1,\mathrm{Xe}} - \frac{\gamma_{\mathrm{Xe}}}{\gamma_{\mathrm{He}}} \cdot \omega_{1,\mathrm{He}} \neq 0 \quad . \tag{2.46}$$

With respect to the orientation of the electric field to the magnetic field (parallel $E \uparrow\uparrow B$ and antiparallel $E \uparrow\downarrow B$ configuration), the difference of the particular weighted frequency differences ($\Delta\tilde{\omega}_{\uparrow\uparrow}$ and $\Delta\tilde{\omega}_{\uparrow\downarrow}$) is proportional to the electric dipole moment

$$\hbar\Delta\omega = \hbar\left(\Delta\tilde{\omega}_{\uparrow\uparrow} - \Delta\tilde{\omega}_{\uparrow\downarrow}\right) = 4d_{\mathrm{Xe}}E \quad . \tag{2.47}$$

The EDM of ^{3}He can be neglected compared to the one of ^{129}Xe, which simplifies the expressions for the weighted frequency differences to

$$\Delta\tilde{\omega}_{\uparrow\uparrow} = \omega_{\uparrow\uparrow}^{\mathrm{Xe,\ EDM}} - \frac{\gamma_{\mathrm{Xe}}}{\gamma_{\mathrm{He}}} \cdot \omega_{\uparrow\uparrow}^{\mathrm{He,\ EDM}} \approx \omega_{\uparrow\uparrow}^{\mathrm{Xe,\ EDM}} \tag{2.48}$$

and

$$\Delta\tilde{\omega}_{\uparrow\downarrow} = \omega_{\uparrow\downarrow}^{\mathrm{Xe,\ EDM}} - \frac{\gamma_{\mathrm{Xe}}}{\gamma_{\mathrm{He}}} \cdot \omega_{\uparrow\downarrow}^{\mathrm{He,\ EDM}} \approx \omega_{\uparrow\downarrow}^{\mathrm{Xe,\ EDM}} \quad . \tag{2.49}$$

Summarizing these considerations in equation 2.47, the resulting EDM of ^{129}Xe is

$$\begin{aligned} d_{\mathrm{Xe}} &= \frac{\hbar}{4E}\left(\omega_{\uparrow\uparrow}^{\mathrm{Xe,\ EDM}} - \omega_{\uparrow\downarrow}^{\mathrm{Xe,\ EDM}}\right) \\ &= \frac{\hbar}{4E} \cdot \Delta\omega \quad . \end{aligned} \tag{2.50}$$

For the data analysis it is convenient to examine the accumulated weighted phase difference

$$\Delta\tilde{\Phi} = \Phi_{1,\mathrm{Xe}} - \frac{\gamma_{\mathrm{Xe}}}{\gamma_{\mathrm{He}}} \cdot \Phi_{1,\mathrm{He}} \tag{2.51}$$

instead of the weighted frequency difference (cf. [92]). The resulting difference of the weighted phase differences $\Delta\Phi$ is the integration of $\Delta\omega$ over the total measurement time T

$$\Delta\Phi = \Phi_{\uparrow\uparrow}^{\mathrm{Xe,\ EDM}} - \Phi_{\uparrow\downarrow}^{\mathrm{Xe,\ EDM}} = \int \Delta\omega \, dt \quad . \tag{2.52}$$

2.4.2. Sensitivity Estimation

The Heisenberg energy-time uncertainty principle $\delta E \times T = \hbar$ [93] corresponds in an uncertainty of a single frequency measurement of an oscillating signal over a period T:

$$\delta\omega = \frac{1}{T} \quad . \tag{2.53}$$

If the coherence is not destroyed during or after a measurement the oscillating signal can be recorded with a sampling rate r_s during the measurement period T. A further statistical factor enters in the accuracy of the frequency determination which scales $\propto 1/\sqrt{N} = 1/\sqrt{r_s \cdot T}$. Therefore, the overall sensitivity of a frequency measurement of an oscillating signal scales like $T^{-3/2}$. The resulting accuracy of the frequency determination is assessed in the estimation by the Cramér-Rao Lower Bound (CRLB) [94]. Assuming a constant frequency, the achievable frequency sensitivity is given by the variance

$$\sigma_\omega^2 = \frac{12}{\mathrm{SNR}^2 \cdot T^3} \cdot C(T, T_2^*) \tag{2.54a}$$

$$\Rightarrow \quad \sigma_\omega = \sqrt{12} \cdot \frac{\tilde{\rho}}{A} \cdot T^{-3/2} \cdot \sqrt{C(T, T_2^*)} \tag{2.54b}$$

depending on the signal(A)-to-noise($\tilde{\rho}$) ratio $\mathrm{SNR} = A/\tilde{\rho}$ and the total measurement time T [95]. The square of the noise is defined as integration of the square of the power spectral density ρ

$$\tilde{\rho}^2 = \int_0^{f_{\mathrm{bw}}} \rho^2 \, d\nu \quad . \tag{2.55}$$

within a certain sampling rate limited bandwidth f_{bw}, i.e. the Nyquist frequency. In the special case of pure white noise, the noise is $\tilde{\rho} = \rho \cdot \sqrt{f_{\mathrm{bw}}}$. The dimensionless parameter $C(T, T_2^*)$ comprises the influence of the exponential damping of the sinusoidal signal. For $T \ll T_2^*$, this parameter gets 1, reproducing the frequency estimation of a pure sinusoidal signal. Depending on the ratio r of the characteristic transverse relaxation time T_2^* and the total observation time of the free spin precession T

$$r := \frac{T}{T_2^*} \quad , \tag{2.56}$$

the parameter $C(T, T_2^*) = C(r)$ can be calculated according to [72] by

$$C(r) = \frac{(e^{2r} - 1)r^3}{3\cosh(2r) - 3(1 + 2r^2)} \quad . \tag{2.57}$$

The resulting plot of $\sqrt{C(r)}$ against r is presented in figure 2.11.

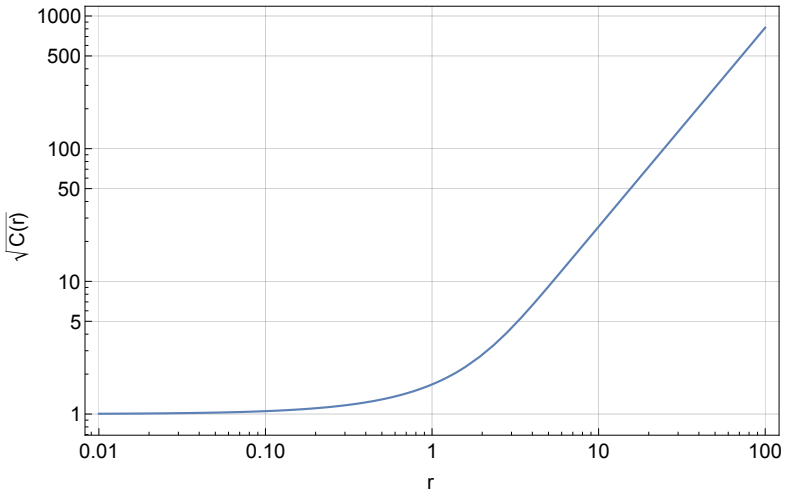

Figure 2.11.: The exponential damping parameter $\sqrt{C(T, T_2^*)} = \sqrt{C(r)}$ of the CRLB plotted against $r = T/T_2^*$

If the total observation time T in equation 2.54 is substituted by $r \cdot T_2^*$, the achievable sensitivity is proportional to

$$\delta d_{\mathrm{Xe}} \propto f(r) \quad \text{with} \quad f(r) := r^{-3/2} \cdot \sqrt{C(r)} \quad . \tag{2.58}$$

Figure 2.12 shows a normalized plot of this function $f(r)$. Here the values for each $f(r)$ are divided by the limit of infinite long observation times ($\lim_{r\to\infty} f(r) = \sqrt{2/3} = 0.816$).

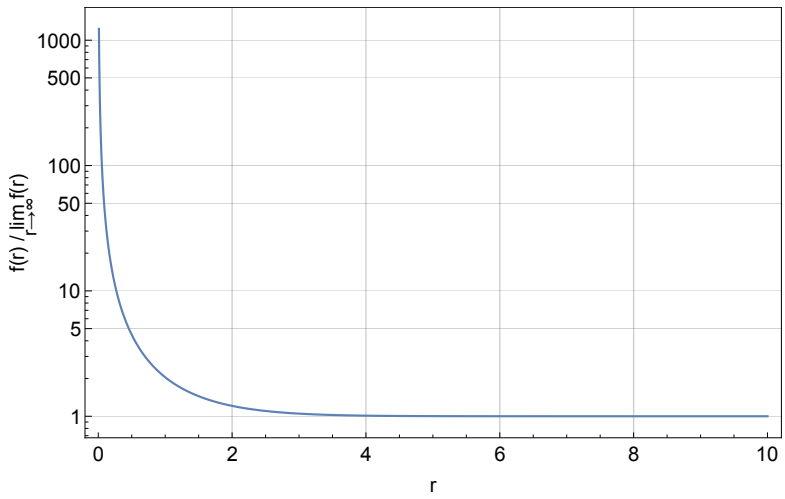

Figure 2.12.: The normalized proportionality function $f(r)/\lim_{r\to\infty} f(r)$ of the CRLB depending on r. The best achievable sensitivity of δd_{Xe} is approximately reached at $r = 3$ ($f(3)/\lim_{r\to\infty} f(r) = 1.049$).

The best achievable sensitivity is more or less reached after an observation time $T = 3 \cdot T_2^*$ ($f(3) = 0.857$). In other words: an observation time longer than three times T_2^* does not significantly improve the sensitivity. Using equation 2.50, the achievable sensitivity for the Xe-EDM δd_{Xe} after N individual measurement runs is

$$\delta d_{\mathrm{Xe}} = \frac{\hbar}{4E} \cdot \sigma_\omega \cdot \frac{1}{\sqrt{N}} \quad . \tag{2.59}$$

Considering values from former experiments ($T = 24\,\mathrm{h} = 3 \cdot T_2^* = 3 \cdot 8\,\mathrm{h}$, $\rho = 3\,\mathrm{fT}/\sqrt{\mathrm{Hz}}$, $A = 10\,\mathrm{pT}$) [51, 52], an uncertainty in the frequency of about $\sigma_\omega \approx 100\,\mathrm{picorad/s}$ is obtainable after a single measurement of 24 h. The achievable EDM sensitivity gets $\delta d_{\mathrm{Xe}} \approx 1 \cdot 10^{-29}\, e\mathrm{cm}\,/\sqrt{N}$, assuming an electric field of $E = 2\,\mathrm{kV/cm}$.
Please note that this is only a theoretical consideration. To be metrologically sensitive on frequency changes due to an EDM, the electric field has to be altered - reversed in polarity - during one measurement to differ between deterministic frequency shifts. An elaborate discussion of these effects and their potential correlation is presented in chapter 5. Furthermore, for these considerations, the measurement time T is completely decoupled from the number of the measurement runs N. In reality the total time for the experiment T_{tot} is only available to a limited extend, for example within a window of two weeks. Further issues, like that ideal experimental conditions (e.g. low system noise) are not available at all times, limit the overall measurement time. Therefore, there is an (always different) optimum between the choice of the measurement time of one individual run and the amount of runs in total: $N = T_{\mathrm{tot}}/T$. In this regard, there are several criteria to consider, as stated in the appendix section A.3, where a detailed analysis of a CRLB-optimization for a single measurement is presented. The different parameters in equation 2.54 are taken into account, mainly including the partial pressures of the gases and their mixing ratio, which affect both the signal amplitude A and the relaxation time T_2^*.

The CRLB power law describes the dependency of the achievable sensitivity on the measurement time. As introduced in equation 2.54 the frequency sensitivity scales with $T^{-3/2}$ and accordingly the phase sensitivity scales with $T^{-1/2}$. Deviations from this behavior, for example due to non-statistical noise sources, can be identified by the Allan Standard Deviation (ASD) [96]. This method is a convenient and established measure to study temporal characteristics of clocks and oscillators, such as the spin precession signal - in our case of ^{3}He-^{129}Xe comagnetometry. The ASD $\sigma_\Phi(\tau)$ of the phase Φ, depending

on the integration time τ, is the square root of the Allan Variance, which is defined as

$$\sigma_\Phi^2(\tau) = \frac{1}{2(N-1)} \sum_{i=1}^{N-1} \left[\overline{\Delta\Phi}_{i+1}(\tau) - \overline{\Delta\Phi}_i(\tau)\right]^2 \quad . \tag{2.60}$$

The integration time τ is given by the total measurement time T which is divided into N data sets, so that $\tau = n \cdot T/N$ for $n = 1, 2, 3, ..., N$. $\overline{\Delta\Phi}_i$ are the determined mean phase differences for each data set $i = 1, 2, 3, ..., N-1$.

If the noise of the clock system is statistical, the ASD is in accordance to the classical standard deviation and the phase sensitivity follows the CRLB power law $\sigma_\Phi(\tau) \propto \tau^{-1/2}$. Furthermore, the log-log plot of the ASD is a graphic tool to analyze the data, regarding possible deviations from white noise and their origins. As an example, the ASD of the phase of one of our precedent experiments [92] is presented in figure 2.13. The linear slope confirms the CRLB power law for $\sigma_\Phi(\tau)$ and it can be concluded that the sensitivity of the He/Xe comagnetometer is not limited by non-statistical noise. Another example in figure 2.14 shows deviations from the statistical behavior.

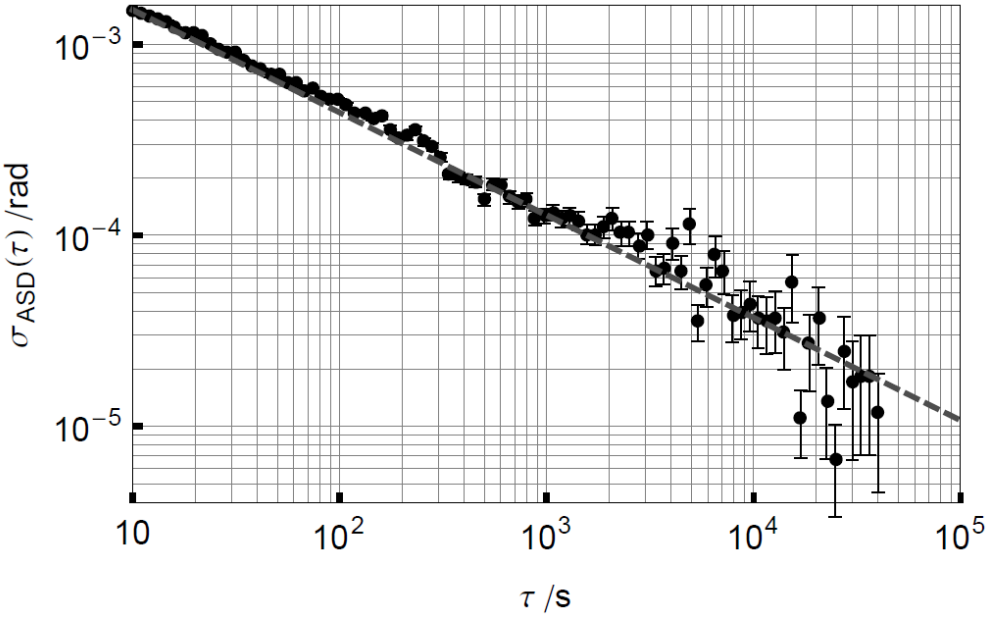

Figure 2.13.: Example of an ASD plot of phase residuals from a precedent experiment during an observation time of $T \approx 24\,\text{h}$. The uncertainty in the phase decreases with $\tau^{-1/2}$, indicated by the dashed line, which is in accordance with the CRLB power law. Non-white noise or an improper fit model would cause a non-conformity of this behavior and a higher minimum of the accessible uncertainty, as it is evident in figure 2.14. From [92].

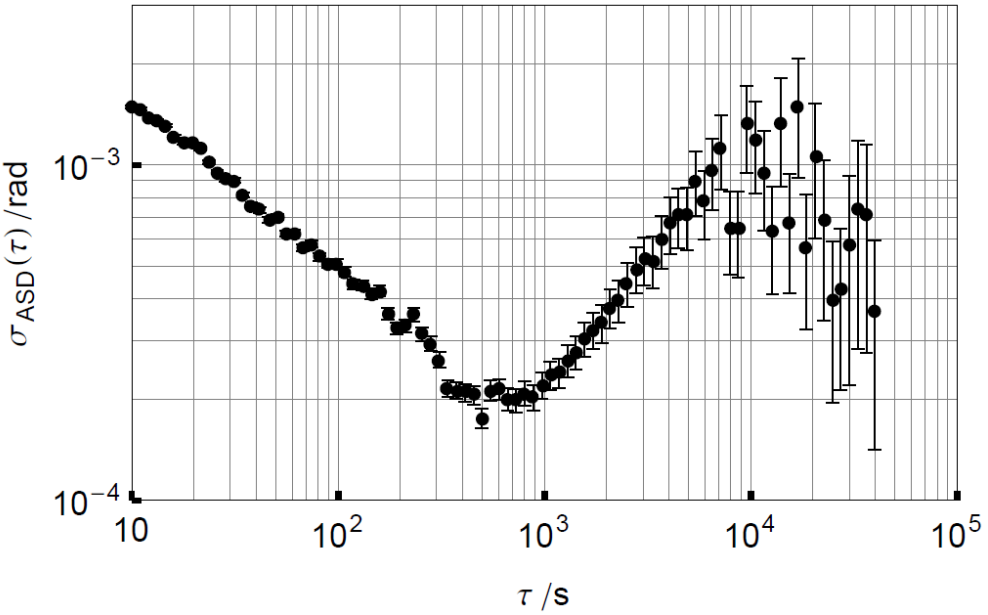

Figure 2.14.: Example of an ASD plot of phase residuals from another precedent experiment. From $\tau \approx 500\,\mathrm{s}$ on there are significant deviations from the statistical $\tau^{-1/2}$-behavior. From [92].

From the given example in figure 2.13, the achievable phase sensitivity of this precedent measurement can be estimated to $\sigma_\Phi \approx 10\,\mu\mathrm{rad}$ after about $T = 24\,\mathrm{h}$ of measurement. According to

$$\sigma_\omega = \frac{\sigma_\Phi}{T} \tag{2.61}$$

this relates to a frequency sensitivity of $\sigma_\omega \approx 100\,\mathrm{picorad/s}$, which is consistent with the estimation from the CRLB.

3

Experimental Setup

This chapter offers a comprehensive overview of the experimental setup, based on the theoretical and methodical insights of chapter 1 and 2. Relating to figure 3.3, the experiment consists of two groups of main components:

- the actual EDM setup including the SQUID system,
- the magnetic environment.

The design and realization of both aspects is strongly coupled. For a greater part of the following considerations, the starting point were the preceding experiments of the collaboration, namely the search for a Lorentz Invariance violation in the matter section for the bound neutron [51] and the investigation of short-range interactions mediated by axion-like particles [52]. To re-emphasize, we want to measure the precession frequency of the nuclear polarized spins of ^{3}He and ^{129}Xe with best possible sensitivity. Keeping in mind equation 2.54, for this purpose we need a) a high signal-to-noise ratio and b) long coherence times. The train of thought of the decision process for building up the experiment is schematically illustrated by the following flowchart 3.1.

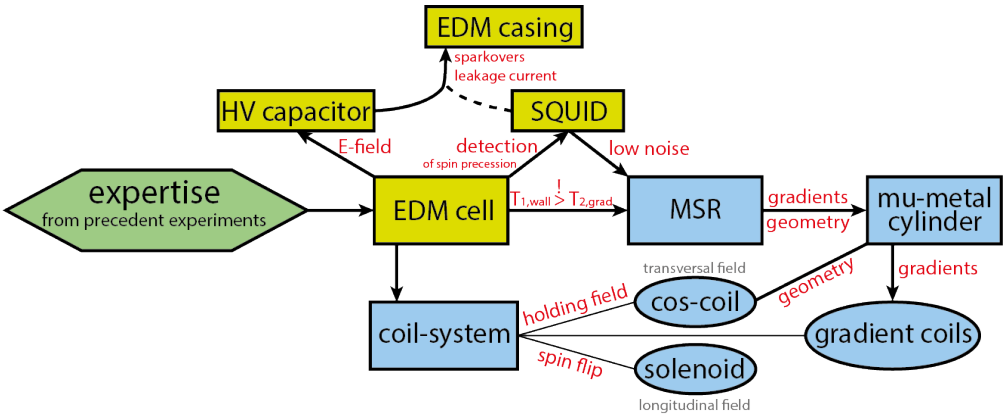

Figure 3.1.: Flowchart of the decision process regarding the experimental setup. The particular issues that led to the respective component are colored in red.

At the beginning of the decision process is the choice of the EDM cell, regarding long $T_{1,\mathrm{wall}}$ relaxation times for both He and Xe. As mentioned before, the detection of the spin precession with a SQUID gradiometer is the option of choice, since these kind of magnetometers show a minimum of intrinsic noise. To generate a high electric field, the EDM cell has to be located inside a capacitor with an applied high voltage. To protect the SQUID system and to prevent sparkovers and leakage currents, the cell and the capacitor have to be located inside a conductive casing, which contains a protective atmosphere.
Concerning the aspired long coherence times, the ambition is to be mostly limited by the wall relaxation time of the EDM cell. By experience, glass cells made out of GE-180 have adequately long $T_{1,\mathrm{wall}}$ times, both for He and Xe. The diameter of the cell is chosen to about 10 cm, which is a compromise of several aspects, like the wall relaxation time itself ($\propto$ volume/surface ratio, cf. eq. 2.32), the signal strength ($\propto$ volume) and the magnetic field gradients in the occupied volume. In this regard of the gradient relaxation time $T_{2,\mathrm{grad}}$, the magnetic field gradients of the magnetic holding field have to be as small as possible. A reasonable environment for such a condition is a magnetically shielded room (MSR). In such a room, the earth magnetic field is shielded by several orders of magnitude and furthermore the residual field inside is much more stable than the field in a non-shielded laboratory. Our experiment takes place inside the MSR of the research center in Jülich, which has two layers of mu-metal and a layer of aluminum to reduce electromagnetic noise (RF-shield). Still, the magnetic field gradients inside this room are not sufficiently small to fulfill the previously mentioned condition. Therefore, an additional shield is required; due to symmetry reasons in the particular case a cylinder of mu-metal. Because of practical reasons, the dimensions of the cylinder are chosen in a way, that it is small enough to fit through the door of the shielded room. Also, the cylinder has to stand upright because the dewar of the SQUID system has to be filled with liquid helium. The magnetic field for the experiment is provided inside the cylinder with a special coil system: The magnetic holding field for the spin precession is generated by a transversal Cosine-Θ-coil (from now on short: cos-coil) due to the upright geometry of the setup. An additional solenoid is required for the spin flip. With several gradient coils the field gradients in the cell's occupied volume can be actively improved further on. This technique of the so called T_2^*-optimization is presented in section 4.2.2. Figure 3.3 gives an overview of the setup with the previously introduced components, which will be discussed in the following sections.
Now it is self-evident, that the gas mixture of ^{3}He and ^{129}Xe, together with required buffer gases, has to be prepared outside of the MSR. Furthermore, the door of the MSR

has to be closed during the experimental operation, because the mu-metal of the room and the cylinder has to be demagnetized to reach small field gradients. Field intrusions through the door would magnetize the material again. A transfer system was installed to externally fill in the gas mixture into the EDM cell, which can be opened and closed with a pneumatic valve. Among others, these experimental procedures are introduced in the subsequent chapter 4 with focus on the functionality of the several (collaborating) components and their characteristics.

The main frame of the setup is a tube of glass fiber reinforced plastic (GRP). It has a length of 210 cm, an outer diameter of 75 cm and a wall thickness of 10 mm, and carries/supports all the setup components. In this way natural vibrations of individual parts relative to the detector (SQUID) are strongly suppressed. Otherwise, for example the coil, generating the magnetic holding field, could oscillate against the SQUIDs, and the electromagnetic noise level would be increased. Moreover, resonances of vibrational modes could sit in the worst case on/near the relatively narrow spectral lines of ^{3}He/^{129}Xe (13 Hz/5 Hz), leading to a variable and enhanced noise in that spectral range. The GRP tube holds a rail system made out of POM[1]. The EDM setup including the cryostat of the SQUID system is mounted on a POM-carriage, movable on this rail. This facilitates assembling and disassembling as well as the maintenance of inner components. The picture in figure 3.2 gives an impression of the mechanism inside the setup.

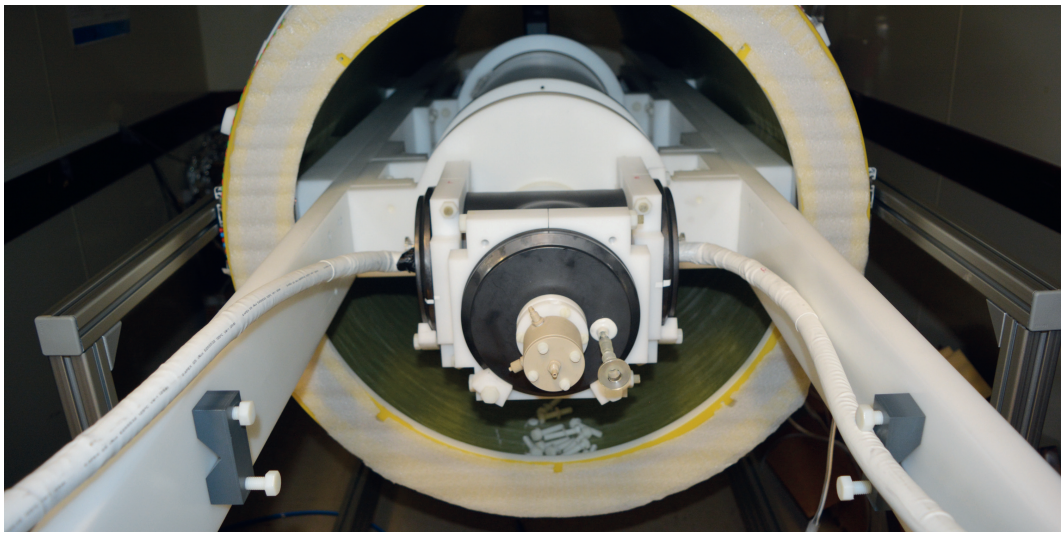

Figure 3.2.: Picture of the fully assembled EDM setup with view from the bottom of the setup. The rail system is attached to the GRP tube; the EDM casing (black) is mounted below the SQUID cryostat on the carriage. For the picture the carriage is partially moved out of the GRP tube.

[1]POM: Polyoxymethylene, characterized by its high strength, rigidity and its low friction value [97].

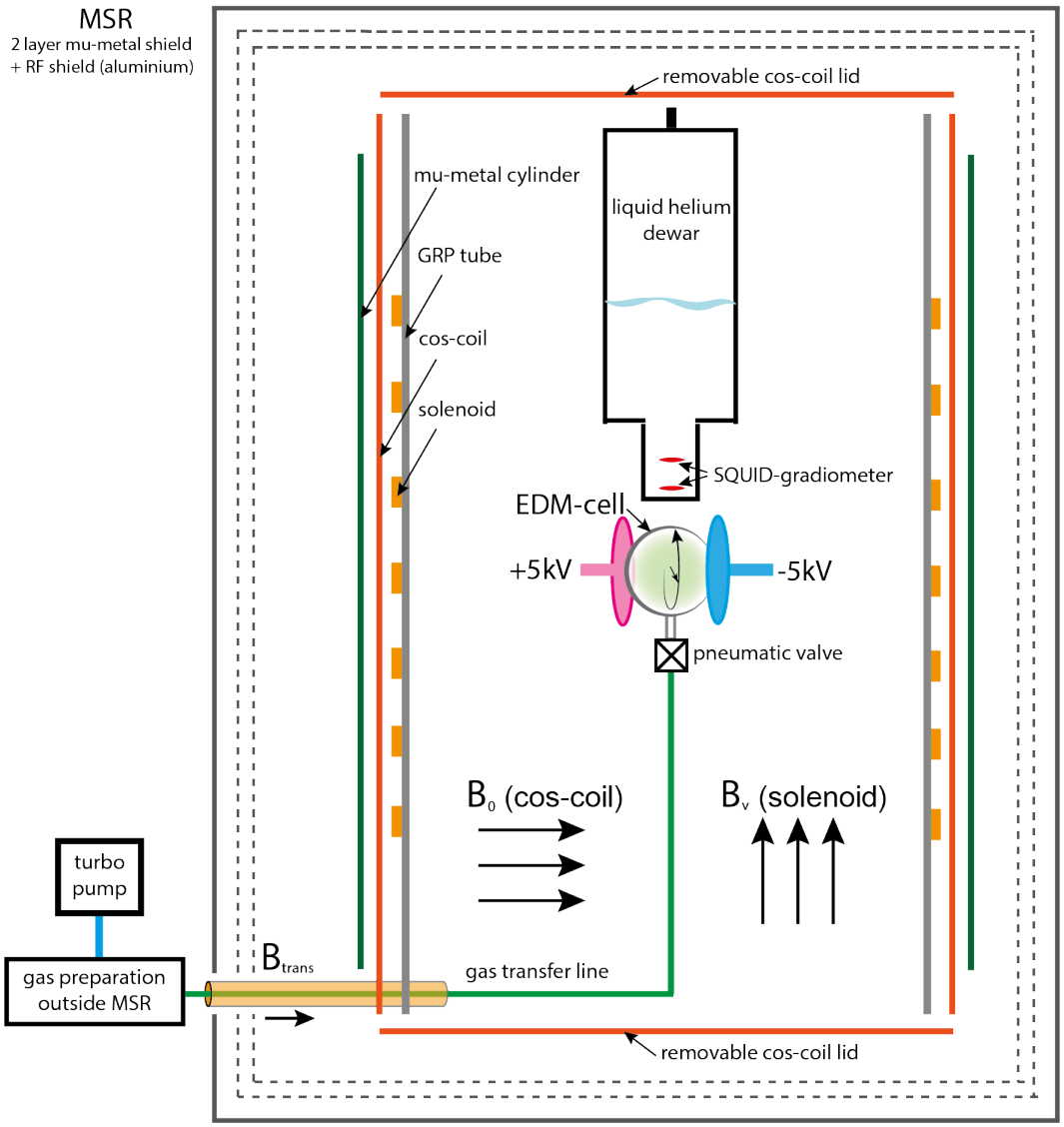

Figure 3.3.: Schematic overview of the experimental setup: The centerpiece of the experimental setup is the EDM cell, located in the center of the setup and surrounded by two plate electrodes. The gas mixture can be filled via a transfer line. During the transfer the polarization is conserved by use of additional transfer coils. For that purpose the EDM cell can be opened and closed by a pneumatically controlled valve.
The magnetic holding field is generated by a cos-coil in the transverse direction of the cylindrical setup. A spin flip can be initiated by switching the field between the cos-coil and the additional solenoid. The whole setup is shielded by a mu-metal cylinder inside the MSR. An additional aluminum layer serves as an RF-shield.
The spin precession is observed with a SQUID gradiometer system which is cooled by liquid helium inside a cryostat.
Not illustrated are the EDM casing - containing the EDM cell - and the supporting carriage with the rail system, which is attached to the GRP tube.

3.1. EDM Setup

This section focuses on the actual central EDM setup. This includes the SQUID-detectors, the EDM cell, the valve for opening and closing the cell, the high voltage connection and the EDM casing providing a safety atmosphere (considering the high voltage), as it is sketched in the figures 3.4 and 3.5.
The whole setup is mounted inside the "magnetic environment" (cf. section 3.2) on the previously mentioned POM-carriage. The EDM casing, holding the EDM cell, is attached right below the cryostat containing the SQUID gradiometers.
To stress it once again: because of the constricted and limited access to the inside of the coil system, it is necessary for the system to be fully operable from outside the magnetically shielded room.

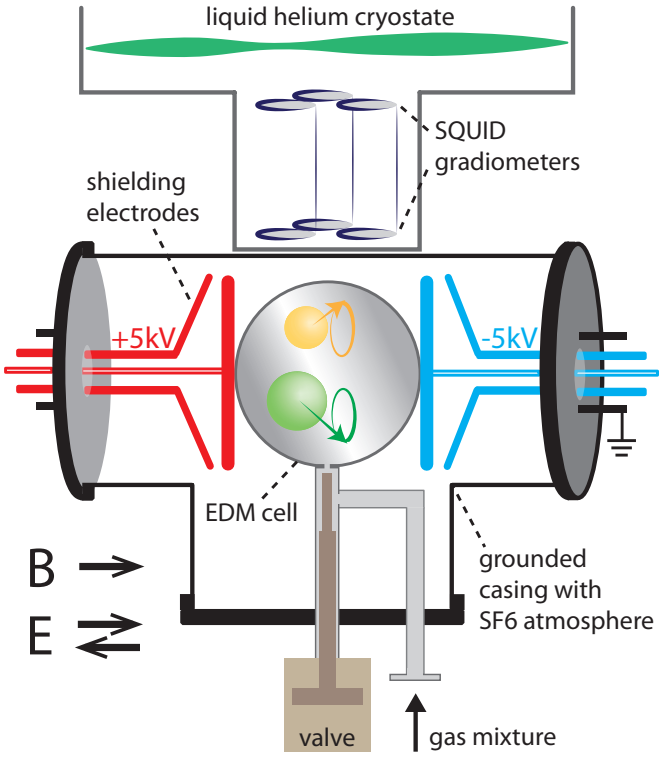

Figure 3.4.: Schematic overview of the EDM setup: The EDM cell is located inside a grounded, conductive casing, which contains an atmosphere of SF_6. The electrodes surrounding the spherical EDM cell are connected to a high voltage. The symmetry axis of this cylindrical plate capacitor (and therefore of the electrical field) is aligned with the magnetic holding field, provided by a cos-coil (not shown). A desired gas mixture can be filled in from the outside by a pneumatically controlled valve. The SQUID gradiometers inside the liquid helium cooled cryostat detect the free spin precession of the gas sample.

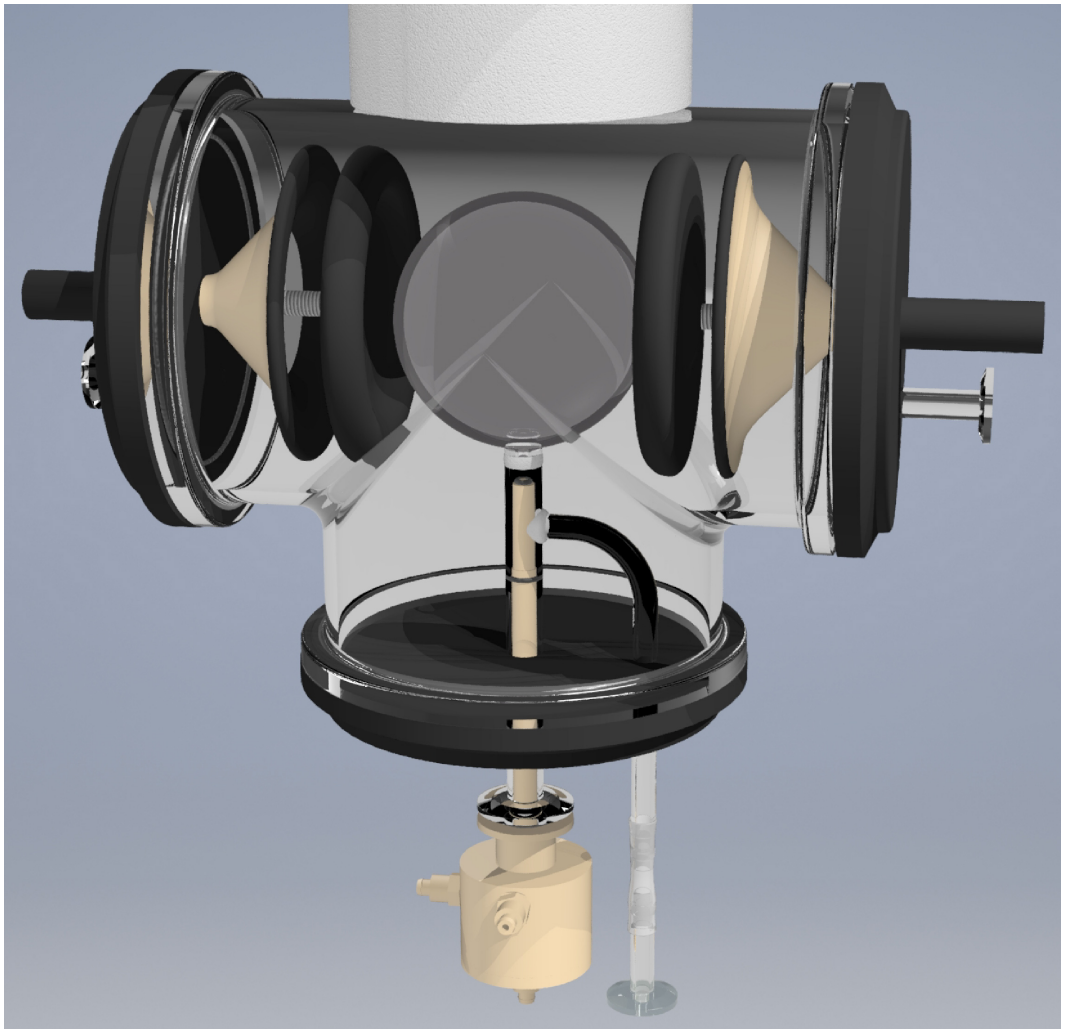

Figure 3.5.: Illustrative rendering of the EDM setup analogous to the scheme in figure 3.4. The EDM casing is rendered transparent to have a look at the electrodes and the shielding electrodes (funnels). The realization is painted with a conductive black paint. The holding mechanism for the casing, made out of POM, is not shown in this illustration.

3.1.1. SQUID System

The SQUID system serves as a detector for the magnetization of the precessing nuclear spins. It consists of three separate SQUID modules, each provided with gradiometer windings. Together with the corresponding electronics, they are mounted on a support made out of glass fiber reinforced plastics. This so called "Probenstab" with all its components was developed and manufactured by Magnicon [98].
To cool down the SQUIDs below the critical temperature, the Probenstab is mounted inside a non-magnetic liquid helium cryostat manufactured by Cryoton [99]. The cylindrical dewar has a length of 900 mm and a diameter of 307 mm. The slimmer end on the bottom side with a diameter of about 127 mm encases the SQUIDs with their electronic and the gradiometer windings. The distance between the lower windings and the bottom outside of the dewar is about $d_1 = 14\,\text{mm}$ at room temperature. The baselength between both gradiometer windings is $b = 70\,\text{mm}$. The windings are made out niobium wire.
As previously mentioned, the cryostat is mounted on the POM-carriage inside the main framing cylinder. The cryostat holds about 16 liters of liquid helium. The duration after all the helium is evaporated - or rather until the SQUIDs are no more superconducting - is about seven days. After this period of time, the cryostat has to be refilled with liquid helium. The data acquisition system was developed within the dissertation of F. Allmendinger [92].

A first measurement of the power density spectrum acquired with this SQUID system inside the magnetically shielded room in Jülich is presented later on in figure 3.13.

3.1.2. EDM Casing

The EDM casing was developed and manufactured to provide several features that are mandatory for operating a free spin precession experiment with an applied high voltage. First of all it serves as a framing for the other EDM components, such as the EDM cell with the valve, the gas filling line and the high voltage connection. Similar to the EDM cell, it cannot be made out of metal or a good conducting material (due to the Johnson-Nyquist noise [100]), nor of a magnetic or magnetizable material (due to the magnetic field gradients). Nevertheless, it should be somehow slightly conducting and electrically grounded to protect the sensitive SQUID electronics in case of sparkovers from the high voltage.
The casing, as depicted in figure 3.6, is realized as a glass T-piece made out of Duran. A flange connection on each opening allows an easy mounting of the components such as

the HV connections and the cell itself. The length from flange to flange is 250 mm and the height from flange to the opposing outer side is 235 mm. The inner diameter of the openings is 140 mm with a wall thickness of the glass of 5 mm. The flanges, also made out of duran, have a thickness of 20 mm.
For a certain electrical conductivity the whole casing (including the flanges) is coated from inside and outside with Aquadag[2]. The sheet resistance of a layer of Aquadag is about $R_{\square,\text{Aquadag}} \approx 500\,\Omega/\square$ [101], whereas metals have a much smaller resistivity, resulting in $R_{\square,\text{metal}} < 10^{-3}\,\Omega/\square$ [102].[3]

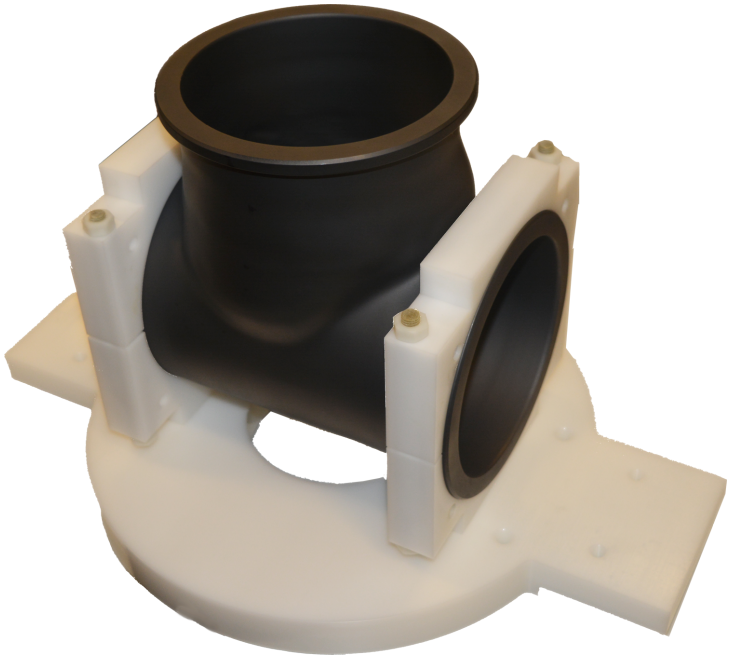

Figure 3.6.: Picture of the glass EDM casing without the flange connections, mounted on a support made out of POM. The black paint (inside and outside) is an electro-conductive Aquadag coating.

The coated glass T-piece is suspended on a support made out of POM (same as the main frame). A hole in the support allows the casing to be placed right below the cryostat (the SQUIDS) to minimize the distance between the EDM cell and the SQUID sensors to maximize the signal. The EDM cell is placed centrally inside the casing. The resulting distance between the center of the cell and the and the cryostat is $d_2 = 140\,\text{mm}/2{+}5\,\text{mm}$. Together with the distance d_1 from the outside of the dewar to the lower windings of the SQUIDs the total distance gets $d = d_1 + d_2 = 89\,\text{mm}$. With the baselength b (cf.

[2] Aquadag AGG303 by Agar Scientific Ltd. [101], short for Aqueous Deflocculated Acheson Graphite: a water-based colloidal graphite. Applicated by airbrushing on the pre-heated glass.
[3] $R_\square$ [ohms per square]: unit equally to ohm, but exclusively used for sheet resistance.

previous section 3.1.1), the reduction η of the signal S due to the gradiometer setup (equation 2.43) compared to a single-loop configuration gets $\eta \approx 17.5\%$.

The two flanges on the side feature a KF-connection to evacuate the casing and to flush it with SF_6. Also, they hold a feed through for the high voltage. These feedthroughs and the necessity of SF_6 as an inert gas are explained in section 3.1.4.
The flange on the bottom side of the casing serves as a base for fixing the EDM cell with the valve and the transfer line for the gas mixture/vacuum.

3.1.3. EDM Cell

The EDM cell is the most essential part of the Xe-EDM experiment. Since it contains the gaseous samples for the measurements, the cell has to satisfy the requirement of a high precision experiment.

A first consideration has to be taken into the dimensions of such a container:
According to equation 2.18, the magnetic field, or rather the signal, on the surface of a magnetized sphere S_0 is not depending on the radius R. The field outside decreases with the distance $d \geq R$ from the center of the cell to the SQUID detector, like $S(d) = S_0 \cdot (R/d)^3$. The minimum distance is $d = 89\,\text{mm}$ (cf. previous section 3.1.2). The logical conclusion would be to make the cell as large as possible to hold $[R/(R/d)]^3 \approx 1$. The fact that the wall relaxation is proportional to the cell radius for a spherical symmetry, $T_{1,\text{wall}} \propto R$ (cf. equation 2.32), also suggests to have a cell as large as possible. However, there is a natural spatial limitation of the experimental setup. But more than that, the gradient relaxation time has the dependency $T_{2,\text{grad}} \propto R^{-4}$ (cf. equation 2.39).
Cells with an outer diameter[4] of 10 cm that were used and investigated in previous experiments [92] revealed a good compromise to the aspects said above. Due this reason, these cells were also used in our Xe-EDM experiments.

For these cells the $T_{1,\text{wall}}$ relaxation time was measured for ^{3}He to about 100 h and for ^{129}Xe to about 10 h. After about three months, the wall relaxation time for Xe (which is the limiting factor, compared to He) dropped to about 8.4 h. To recover the cells (especially for Xe), the construction allows to remove the cell with the cell's flange to perform a cleaning procedure when needed [81].

[4] The wall thickness of these cells is about 2-3 mm.

3.1.3.1. Cell Valve

Containing a polarized gas sample inside a cell makes a valve for opening and closing necessary. Because the cell is not accessible whilst mounted in the experimental environment (EDM casing inside the main frame cylinder) it has to be controlled externally. Hence, a manual solution as it was used in earlier experiments [23, 92] cannot be used. Therefore, the easiest non-magnetic realization is a pneumatically controlled valve.
Such a valve has to be designed concerning several requirements:

- Although it was already mentioned before, it should again be emphasized: Working with polarized gases requires to use only non-magnetic and non-magnetizable materials.
- Because the achievable EDM sensitivity is strongly depending on the signal-to-noise ratio SNR (cf. section 2.4.2, equation 2.54) it is important to keep the electromagnetic noise level as low as possible. Hence, it is improper to use any kind of metal or conducting material for the valve, because of the Johnson-Nyquist noise.
- It has to be ensured that the valve has good vacuum conditions. Oxygen leaks (from the outer atmosphere or from compressed air) would decrease the effective relaxation time (cf. paragraph 2.3.2.1, equation 2.37).
- The wall relaxation mechanism depends on the surface-to-volume ratio of the container of the polarized gases. Therefore, the appendix between cell and valve has to be as small as possible [81, 103].

From earlier experiments [104] PEEK[5] turned out to be a good bulk material for valves because of its magnetic, electric and mechanical properties [105]. It is non-magnetic and non-magnetizable[6], it has a very low electric conductivity and it is lightweight[7] and sturdy towards deformation and wear due to rubbing. Furthermore, its low rate of outgassing testifies its good vacuum property.
According to the necessity of a small appendix between the cell and the valve, is has to be designed as a poppet valve so that the tappet operates close to the cell, respectively the cell's connection. The valve can be operated with compressed nitrogen to prevent

[5] Polyether ether ketone, an organic thermoplastic polymer
[6] Tests were performed with a SQUID magnetometer in the way that a piece of PEEK was moved below the detector and no signal was detected.
[7] Little weight is important in a way that it has to be somehow connected to the glass cell with glue. With a density of $1.31\,\mathrm{g\,cm^{-3}}$ it is more than three times lighter than titanium

the ingress of air, or rather oxygen from the pneumatic movement. Vacuum tests proved the suitability of the construction. A strain relieved glass flange provides a connection for the gas filling line, which is reasonable because the whole setup has to be rotated occasionally. An illustration of the cell with the connected valve and the filling line for the gas mixture is shown in figure 3.7.

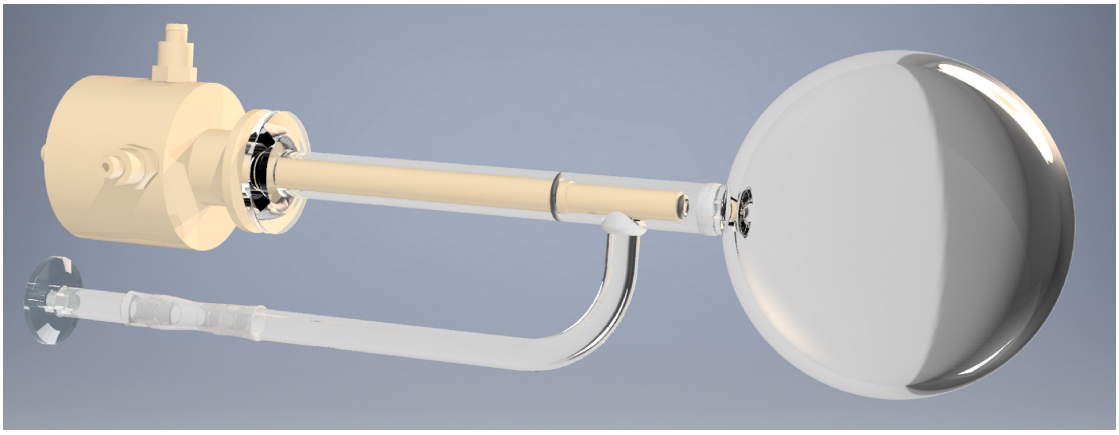

Figure 3.7.: Illustration of the EDM cell with the connected pneumatic valve and the filling line for the gas mixture.

3.1.4. High Voltage

To generate the electric field for the EDM experiment, the electrodes surrounding the EDM cell have to be connected to a high voltage. The high voltage is provided by a two channel high precision high voltage supply NHQ 246L 0n1 by iseg [106]. To maintain a symmetrical setup inside the grounded casing, one electrode is connected to the positive output voltage (0 to +6 kV) and the other one is connected to the negative output voltage (0 to −6 kV). The voltage can remotely be set and changed in polarity. The ramp of the voltage is usually set to 25 V/s.
The electrodes are also made out of PEEK and painted with an electro-conductive Aquadag coating (same as the EDM casing). A simulation of the electrical field was used to determine a special optimized shape of the electrodes. The result is presented in the next paragraph 3.1.4.1.
The battery powered HV-supply is located outside of the MSR inside a box made out of copper plates. The line through the MSR is a cable with an additional high resistance to minimize noise from the outer environment and the HV-supply to the inside of the MSR. A detailed technical discussion of this supply can be found in [92].

3.1.4.1. Simulation of the electric field

An important aspect of the high voltage is the homogeneity of the electrical field. Inhomogeneities, especially at the edge of the plate capacitor electrodes, lead to a non-zero angle between the electric and the magnetic field. As it will be discussed more detailed in 5.2.5, it is reasonable to keep this angle small.

The following figure 3.8 shows a cylindrically symmetric simulation[8]. The T-shaped glass casing, coated with aquadag and set at ground potential, is approximated by a conducting cylinder with a radius of 70 mm. The spherical cell has an inner radius of 46 mm and a wall thickness of 3 mm. The capacitor electrodes have a radius of $R_c = 58\,\mathrm{mm}$, which provides a sufficient distance of 12 mm to the grounded cylinder. The potential of the electrodes is set to $\pm 5\,\mathrm{kV}$. The shape of the electrodes is optimized in a way to maintain a preferably homogeneous electric field inside the EDM cell. Other components like the shielding electrodes and the the wiring are not considered for this simulation.

The calculations show that the electric field varies between $0.95\,\mathrm{kV/cm}$ and $1.1\,\mathrm{kV/cm}$ (mainly at the poles and the equatorial area). The angle between the electrical field and the magnetic field due to transverse components of the electric field can be estimated to about $\Theta_{\mathrm{EB}} \approx 1 - 2°$. A similar accuracy we have for the alignment of the EDM casing and the cos-coil (magnetic field). The electrical field in between the electrodes and the grounded casing can reach $2 - 3\,\mathrm{kV/cm}$. The dielectric strength of dry air is about $E^{(\mathrm{air})} \approx 30\,\mathrm{kV/cm}$ at standard conditions [107]. Nevertheless we use SF_6 as HV protective atmosphere at 1 atm inside the casing. Apart from high vacuum, SF_6 with a dielectric strength of $E^{(\mathrm{SF_6})} > 80\,\mathrm{kV/cm}$ [108] is the natural choice for high voltage applications. Additionally, SF_6 has a lower effective ionization coefficient (respecting dielectric leakage) compared to air [109]. For the same reason, the edges electric components (EDM casing, electrodes, connections) are rounded to prevent point discharges. These issues become even more crucial if - in future - the experiment should be operated with an even higher voltage (cf. outlook, chapter 7).

[8] Simulation performed with Finite Element Method Magnetics FEMM 4.2

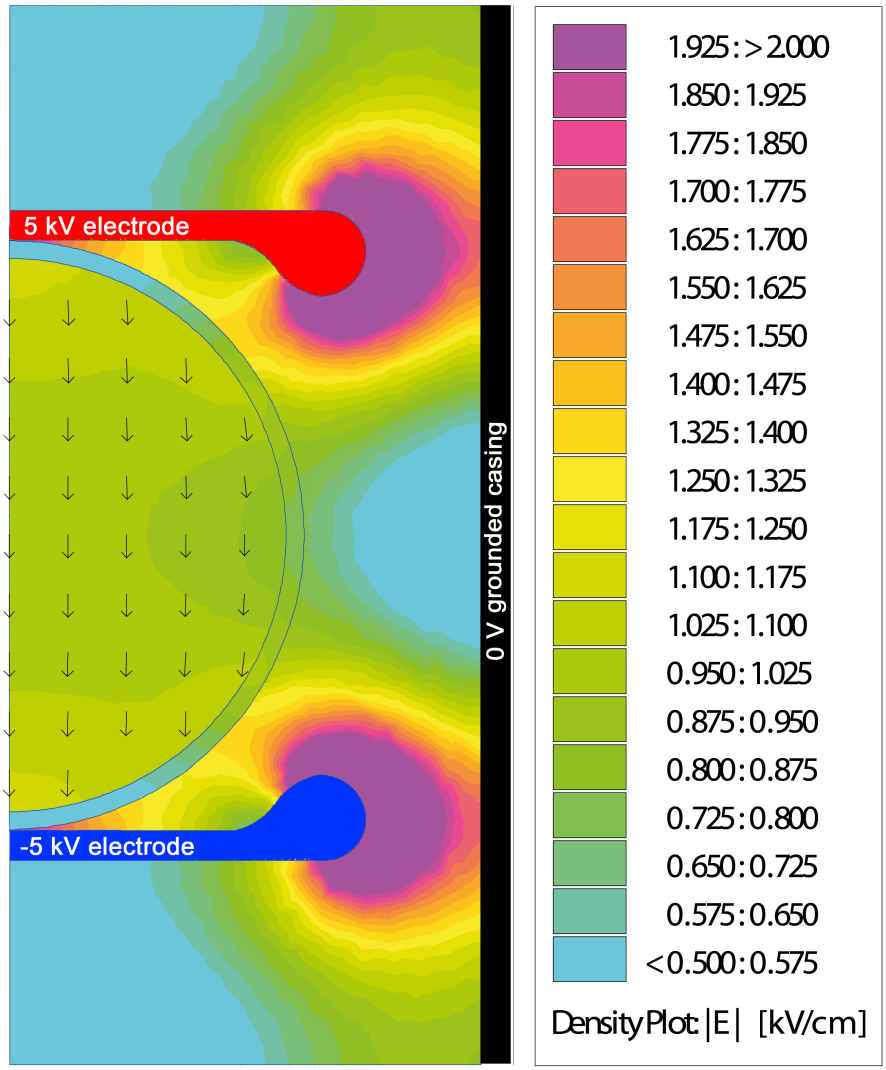

Figure 3.8.: This figure shows a cylinder symmetrical simulation of the electric field generated by the electrodes which are applied to a high voltage of $\pm 5\,\mathrm{kV}$. The distance between the electrodes is the cell's outer diameter $d = 10\,\mathrm{cm}$. The electric field inside the glass cells varies between $0.95\,\mathrm{kV/cm}$ and $1.1\,\mathrm{kV/cm}$. A determining factor for the behavior of the electric field is the surrounding grounded ($0\,\mathrm{V}$) casing. Technically the distance between the cell and the wall of the casing could be chosen larger, but only at the expense of signal strength. The high electric fields between the rounded electrodes and the casing show clear evidence for the necessity of a safety atmosphere inside the casing with an inert gas.

3.1.4.2. High Voltage Connection: Detection of Leakage Currents

Leakage currents, which are correlated to the electric field polarity, flowing through or around the EDM cell could result in a false EDM effect. Systematic effects due to the applied high voltage will be discussed in chapter 5. This paragraph describes how the connection of the high voltage is realized and how the occurring leakage currents, which are in the order of pA, are ascertained and quantified.
The main problem of determining such small currents is that the currents through the insulator of a cable at high voltages are in general much larger. The actual flowing leakage currents can not be distinguished. Therefore, the technique of a double shielded HV connection is the method of choice. A description of the technical realization is presented in following. For a better understanding, an illustration of the HV connection is shown first in figure 3.9.

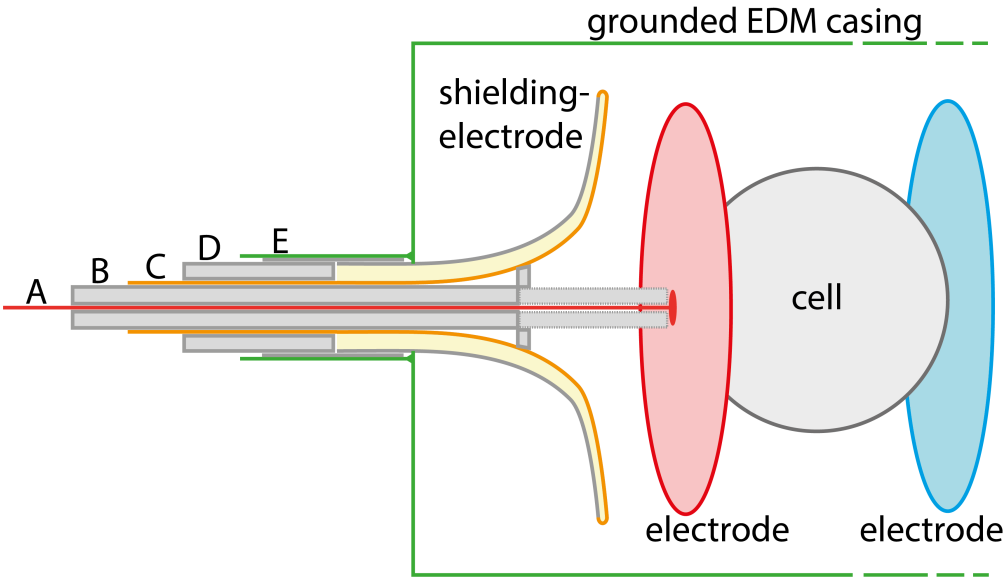

Figure 3.9.: Schematic drawing of the double shielded connection of the electrodes of the EDM cell. All insulators are gray-colored. The innermost conductor A (red) is directly connected to the electrode. Insulated by a layer B, the shielding conductor C (orange) is connected to the shielding electrode. Insulated by a layer D, the outermost grounded shielding E (green) is connected to the EDM casing.

The electrode of the EDM cell is connected to the high potential of the HV power supply. An additional conductive shielding around this conductor is set to the same potential. An outermost conductor is set to ground potential. So there are three (concentric) conductors: A core A at high potential, a sheath C at the same high potential and

a grounded shielding E outside. A and C, as well as C and E are separated by the insulators B and D. In this way, the voltage between A and C is always zero, and as a result there is no leakage current through the insulator B. An occurring current through the innermost conductor A, which is connected to the electrode, is the leakage current from the particular electrode. The high voltage between C and E, on the other hand, leads to a leakage current through the insulator D. However, this current is not associated to the electrode. The shielding C merges into a shielding electrode behind the actual HV electrode. The reason for this shielding electrode is to prevent currents to the electrode from ionized gas inside the conductive EDM casing, which in turn is grounded by the shielding E. Since this method is used for both electrodes we can determine if the current flows from one electrode to another. The double shielding is provided throughout from the electrodes to the pico-amperemeters which measure the current through the innermost conductor A. A detailed discussion of these pA-meters can be found in [92]. A principle drawing of the double shielded HV connection and the pA-meters is presented in figure 3.10.

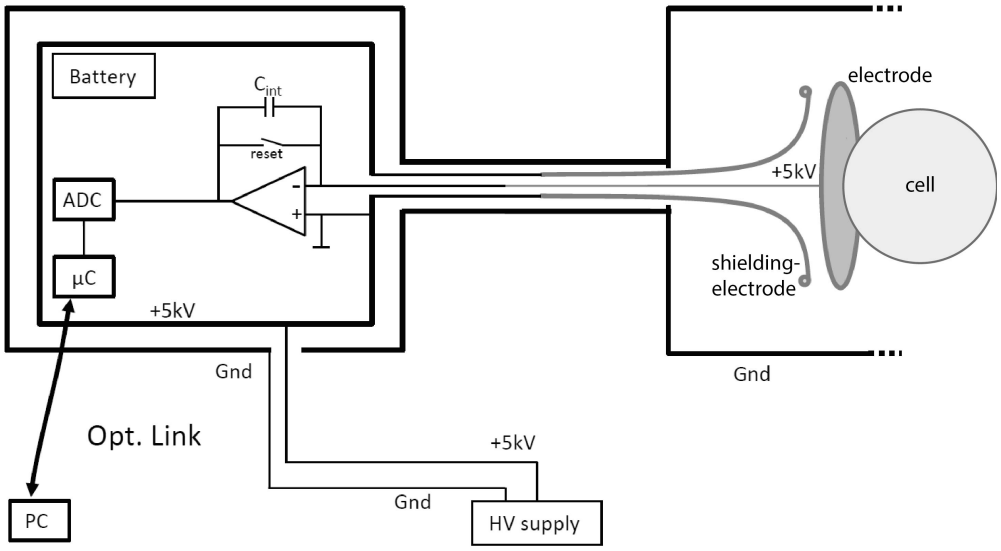

Figure 3.10.: Principle of the double shielded HV connection and the leakage current detection, illustrated for one electrode. For the other electrode the setup is the same. The pA-meter is kept at high potential of the HV supply and is connected to the inner shielding C. The innermost conductor A connects the electrode of the cell with the input of the pA-meter. The surroundings as well as the outermost shielding E and the conductive EDM casing are kept at ground potential of the HV supply. Basically, the pA-meters are integrator ICs with a low bias-current precision op-amp and a capacitor. The output of the integrator is digitalized by an ADC which is read out by a micro-controller that is linked with the measurement computer outside the MSR by an optical fiber. From [92].

At last an overview of the used materials and an annotation of the assembling of the components is presented:

The high voltage cable is a self made threefold coaxial cable, shown in figure 3.11. The conductive components A, C & E are flexible mesh tubes made out of carbon and the insulators B and D are tubes made out of silicone with a volume resistivity of $\rho_{\text{silicone}} \approx 10^{13}\,\Omega\cdot\text{m}$ [110]. The inner tube B has an inner diameter of 2 mm and an outer diameter of 8 mm. The outer tube D has an inner diameter of 10 mm an outer diameter of 20 mm. We choose carbon mesh as the conductors, because of its resistivity $\rho_{\text{C}} \approx 1.6 \cdot 10^{-5} \cdot \Omega\cdot\text{m}$ [111], which is high, compared to copper wires with $\rho_{\text{Cu}} \approx 1.7 \cdot 10^{-8} \cdot \Omega\cdot\text{m}$ [112]. This is relevant in terms of the Johnson noise to be minimized.

Figure 3.11.: Picture showing the composition of the HV cable. The conductors A, C & E are carbon mesh tubes, the insulators B & D are silicone tubes.

The shielding electrodes are funnels made out of PEEK. These funnels are coated with Aquadag from the inside to make it conductive, just as the EDM casing. It is important that they are not conductive from the outside. Otherwise there could be electric contact between C and E. The innermost conductor A and its insulator B go straight through the funnel. The conductor C has contact to the conductive inside of the funnel, as it can be deduced from figure 3.9. The outermost conductor E slides across the additionally insulated contact between the end of the funnel and the insulator D.
The funnels are glued to the two lateral glass flanges of the EDM casing. The innermost wire is connected by an insulating threaded rod (nylon) to the electrode plate. Thereby the carbon mesh of this conductor is crimped with the threaded rod into a thread in the plastic electrode.

3.2. Magnetic Environment

The magnetic environment is an additional limiting factor for the achievable sensitivity of the experiment: magnetic field gradients decrease the spin coherence time; the signal-to-noise ratio is linearly dependent on the electromagnetic noise (cf. chapter 2.4.2, equation 2.54). In the following sections the particular elements of the magnetic environment are discussed.

3.2.1. Magnetically Shielded Room (MSR)

The measurements within the framework of the Xe-EDM experiment take place inside the magnetically shielded room at the research center in Jülich, which is shown in figure 3.12. It is placed inside a laboratory of the Peter Grünberg Institute. Previously, the MSR, constructed by the company **amuneal**, was used for low field MCG[9] measurements.

Figure 3.12.: Status of the MSR in Jülich at the beginning of the Xe-EDM initiative: inside of the room is an examination couch for a test person and a liquid nitrogen cooled SQUID system mounted on a gantry that was used for low field MCG measurements.

[9]Magnetocardiography, a non-invasive method for detecting the electromagnetic heart activity via SQUID magnetometers [113].

The room has an inner base area of 2.50 m × 3.00 m and a height of 2.35 m. A door with a width of 1.00 m and a height of 2.00 m is on a smaller side of the room. The shielding has two mu-metal layers (1.27 mm thickness each) with a distance of around 10 cm in between. Also, an outer layer of 10 mm aluminum serves as a high frequency shield.
In this section the main focus is on the characterization of the MSR with regard to the electromagnetic noise and the magnetic gradients inside. For our tests and measurements we completely removed the setup from earlier experiments (MCG and low field NMR) in order to install the Xe-EDM related equipment.

3.2.1.1. Noise inside the MSR

One of the first investigations was the measurement of the magnetic noise inside of the MSR. As mentioned before and explained in section 2.4.2, the system noise is a decisive factor for the achievable sensitivity. The measurement was performed with our SQUID-system presented in section 3.1.1. The following plot 3.13 shows the amplitude density spectrum of the SQUID gradiometers where the cryostat with the SQUIDs was placed on a wooden frame in the center of the room with the door closed. All other components were removed for this measurement.
The amplitude spectral density at 10 Hz is $\rho(10\,\mathrm{Hz}) \approx 1.5\,\mathrm{fT}/\sqrt{\mathrm{Hz}}$. For frequencies below 10 Hz the spectral density is dominated by the 1/f noise. Concerning the frequencies of the spin samples (as they are determined in section 4.2) at around 5 Hz for ^{129}Xe and 13.8 Hz for ^{3}He the resulting noise level is $\rho \approx 3\,\mathrm{fT}/\sqrt{\mathrm{Hz}}$ for xenon and $\rho \approx 1.5\,\mathrm{fT}/\sqrt{\mathrm{Hz}}$ for helium. The peak located at 50 Hz is caused by the influence of the power grid. Compared to preceding experiments [51, 52] at the BMSR-2 in Berlin, which has a much better shielding factor (seven layer mu-metal shield) [114], the MSR in Jülich fulfills the requirement of sufficiently low noise, thanks to the much lower environmental noise as compared to the site in Berlin.
For the sake of completeness and for understanding the characteristics of the MSR a similar measurement was performed with the SQUID system located in the lab outside of the MSR, resulting in the spectrum shown in figure 3.14. It is clearly evident that the amplitude spectral density is globally much higher than inside of the MSR. A shielding factor of the MSR of about $S = 1000$ for frequencies at around 10 Hz can be estimated. The additional peak at 100 Hz is the feedback of the first harmonic of the power grid, whereas the peak at around 16 Hz has its origin most likely in the 16.7 Hz AC overhead line of an industrial train track, about four kilometers air-line distance away from the MSR (at 50°52′41.2″ N + 6°29′41.5″ E).

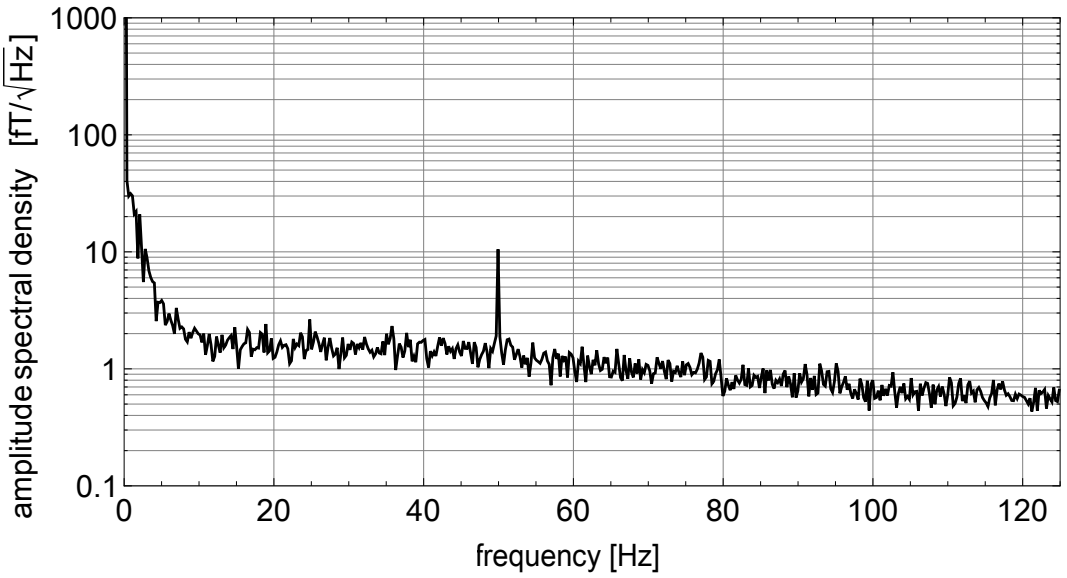

Figure 3.13.: Amplitude density spectrum inside the MSR, measured with our low T_c-SQUID system, as introduced in section 3.1.1. A peak at 50 Hz is clearly evident.

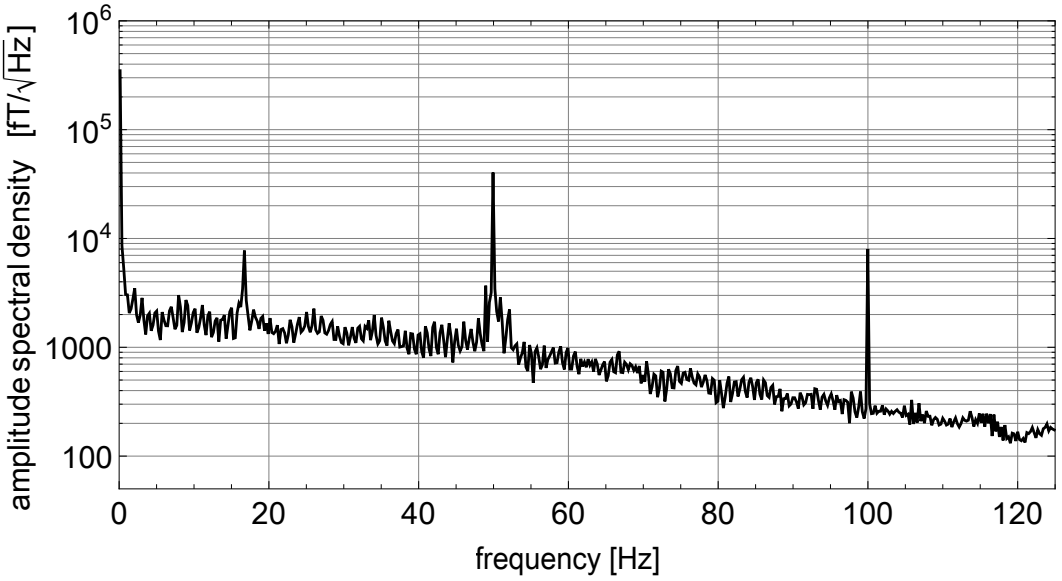

Figure 3.14.: Amplitude density spectrum outside the MSR (but in the same lab), measured with the same low T_c-SQUID system. The peak at 50 Hz is now much more prominent. Also, additional peaks at $\approx$ 16 Hz and 100 Hz appeared.

For comparison, the actual achievable noise with the entire, fully assembled EDM setup is shown in figure 4.2. The obtained noise level there is elevated to $\rho \approx 10\,\mathrm{fT}/\sqrt{\mathrm{Hz}}$ in the frequency region of interest.

3.2.1.2. Field Gradients inside the MSR

An important requirement for a magnetically shielded room is the quality of the residual field inside and its gradients. The residual field and in particular its gradients set constraints for the geometry of the experiment. According to this, the field has to be as low as possible, resulting in small absolute gradients, as well. Absolute field gradients $\nabla B \leq 10\,\mathrm{pT/cm}$ are demanded for preserving long spin coherence times (T_2^*).
The residual field inside the MSR was measured with a fluxgate magnetometer[10]. The measurement setup with the specific axes is sketched in figure 3.15. Axis x is defined from the back of the room (0 cm) to the door (300 cm). Axis y is defined from the right side (0 cm) to the left side (250 cm) of the room and axis z is defined from the floor (0 cm) to the ceiling (236 cm). Accordingly, the center of the room is at $x = 150\,\mathrm{cm}$, $y = 125\,\mathrm{cm}$ and $z = 118\,\mathrm{cm}$. For the measurement, all axes are arranged at the center of each wall and the x-y-plane is located 120 cm above the floor. In this way, all positions were measured in steps of 10 cm and in $x-$, $y-$ and z-direction of the sensor. The door of the MSR was closed for the measurement.

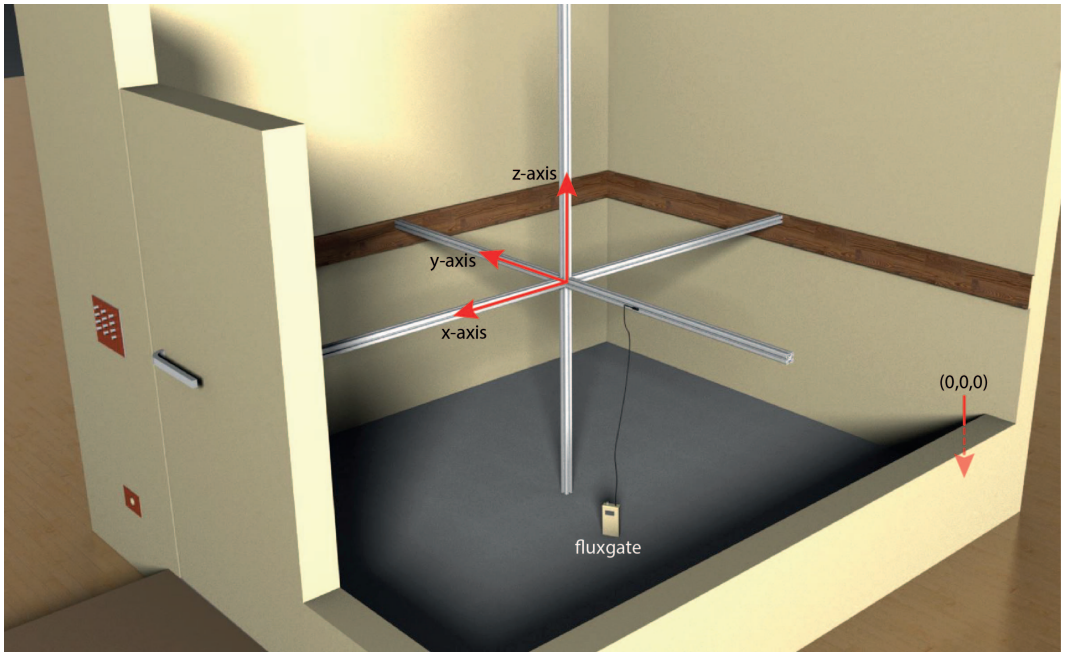

Figure 3.15.: Illustration of the measurement of the MSR residual field with a fluxgate magnetometer.

[10] Fluxgate Magnetometer FLUXMASTER by Stefan Mayer Instruments. Measurement range 0.1 nT to 200 μT, Offset $< 5\,\mathrm{nT}$, DC to 1 kHz. [115]

The following plot 3.16 shows the measurement of the residual field

$$B(x, y, z) = \sqrt{B_x^2 + B_y^2 + B_z^2} \tag{3.1}$$

for the three different axes, where B_x is the magnetic field component measured by the fluxgate sensor when pointing in x-direction, and so on. For clarity the data is intentionally plotted as a line without any error bars. By moving the sensor from the back of the room to the direction of the door (x-movement, black line) the influence of the door is prominent. The residual field is increasing rapidly from $B(x \approx 125\,\text{cm}) \approx 10\,\text{nT}$ in the center of the room to $B(x \approx 275\,\text{cm}) > 100\,\text{nT}$ close to the door. The sensor movement along the other axes y and z does not show such a strong field increase towards the walls. A possible explanation is that every time the door is opened the inner shield is exposed to the Earth magnetic field and it is getting magnetized. Moreover the door itself disturbs the symmetry of the MSR (mu-metal overlaps and additional air-gaps), even if it is closed. Because there was no working demagnetization routine for the MSR at that time[11], it was not possible to get rid of this effect without further ado.

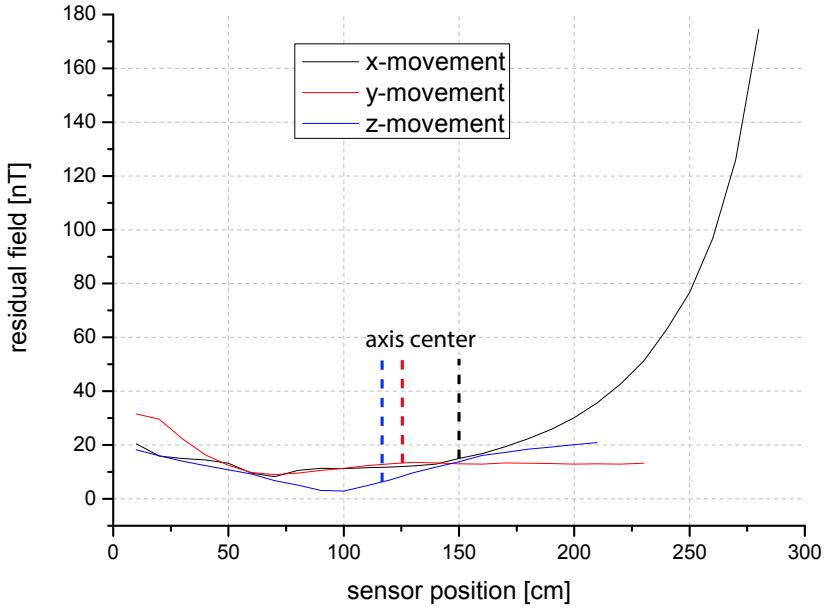

Figure 3.16.: Measurement of the residual magnetic field inside the MSR with a fluxgate magnetometer for the three different axes x,y,z. The center of each axis is indicated by a dashed line. At each point, the total field B was determined from the components B_x, B_y and B_z, according to equation 3.1.

[11] The demagnetization system was again ready for operation two years after these first measurements. Unfortunately there was no possibility to compare the residual fields of the MSR after the demagnetization process, because the EDM setup was already (and still is) installed inside.

The plot 3.17 shows the derivative of the residual field which corresponds to the field gradients. This was calculated by averaging the slopes of two adjacent data points of the vectorial residual field measurement, for example for dB_x/dx

$$\frac{dB_x}{dx} = \frac{1}{2}\left(\frac{B_{x,i+1} - B_{x,i}}{x_{i+1} - x_i} + \frac{B_{x,i} - B_{x,i-1}}{x_i - x_{i-1}}\right) \quad . \tag{3.2}$$

The behavior of the calculated absolute gradients, especially close to the door (dB/dx), is in accordance to the trend of the residual field. The results from these measurements lead to the conclusion, that the shielding and especially the homogeneity of the MSR at the research center in Jülich are in principle not sufficient for the purpose on performing the Xe-EDM experiment. Gradients in the order of 200 pT/cm are too large to achieve meaningful transverse relaxation times.

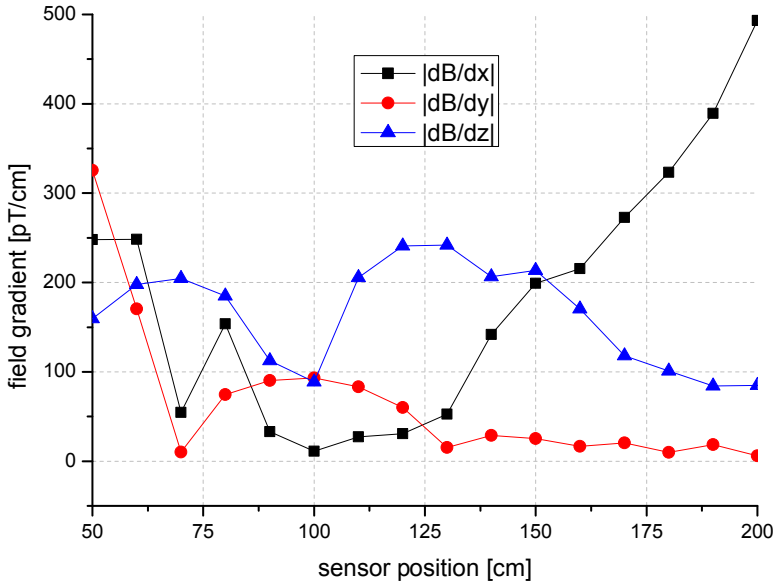

Figure 3.17.: Calculation of the total residual field gradients in x,y and z-direction $|dB/dx, y, z|$ from the field measurement shown in figure 3.16 via equation 3.2. The gradients in the center of the MSR exceed values over 200 pT/cm.

Another issue can be linked to the measurement shown in figure 3.18. The comparison between two measurements of the residual field inside the MSR (plotted is only a movement of the sensor in x-direction) - one measurement with the door closed and one with the door opened - illustrates clearly the shielding behavior of the MSR.

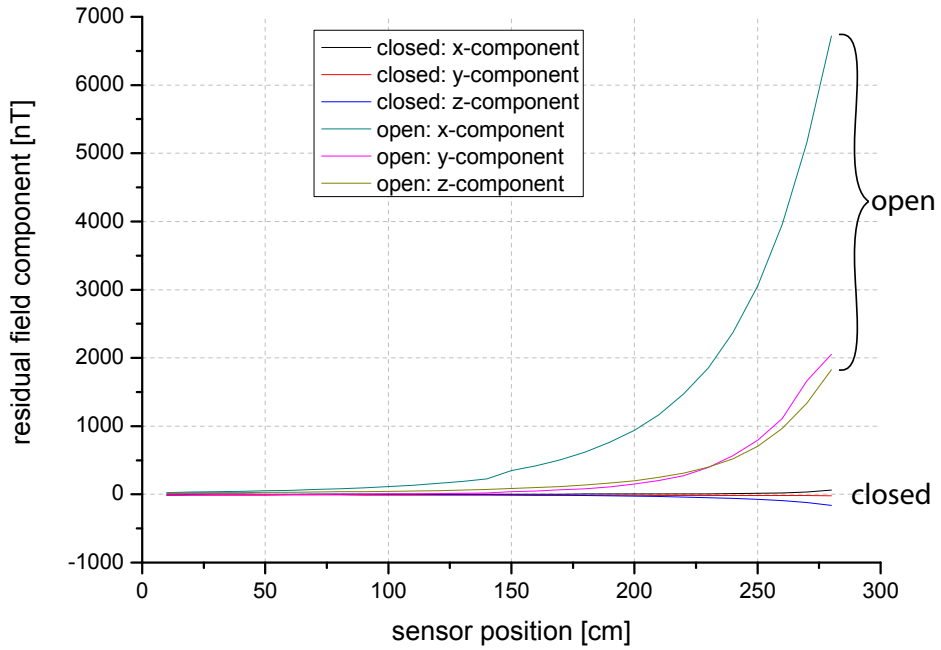

Figure 3.18.: Comparison of the residual field inside the MSR in x-direction with the door of the MSR closed (as before in figure 3.16) and opened. The enhancement of the magnetic field is conspicuous.

The extraordinary large residual field up to several μT could lead to significant magnetization of the mu-metal every time the door is opened (for example to re-fill liquid helium into the cryostat, cf. section 4.1). For this reason a supplementary mu-metal cylinder, introduced in the next section 3.2.2 is implemented in the setup. To solve the problem of magnetization effects, the cylinder can be demagnetized (degaussed).

3.2.2. Additional Mu-Metal Cylinder

To further suppress the residual field and decrease the gradients inside the MSR, as well as to have the option of demagnetization, an additional mu-metal cylinder is required. This particular cylinder[12], shown later on in figure 3.23, has a diameter of $D = 85\,\text{cm}$, a height of $L = 190\,\text{cm}$ and a thickness of $t = 1.5\,\text{mm}$. It consists of an 80 % NiFe alloy with a relative permeability $\mu_r \approx 50000$ @ 50 Hz [116].
The shielding factor S of such a cylinder depends its orientation towards the magnetic

[12] MUMETALL®, manufactured by SEKELS GmbH [116] in 2013

field. It has to be distinguished between the transversal shielding factor S^T and the axial shielding factor S^A [117]:

$$S^T = \frac{\mu_r t}{D} \tag{3.3a}$$

$$S^A = \frac{\mu_r t\sqrt{2D}}{L^{3/2}} \tag{3.3b}$$

The resulting shielding factors, using the given dimensions, are $S^T \approx 90$ and $S^A \approx 30$. In the end, the specified μ_r strongly depends on the condition of the mu-metal, and therefore, the ultimate shielding factor can not be treated as constant. For example a magnetization of the mu-metal decreases the effective μ_r[13]. Consequently the mu-metal has to be demagnetized (degaussed) after it was exposed a high magnetic flux[14], for example when the door of the MSR is opened.
The cylinder is provided with a degaussing-coil. It consists of four loops of 2.5 mm copper wire which is axially wound around the cylinder, each loop displaced by 90°. The degaussing coil is connected to a 10 Hz and 500 VA isolating transformer which is fed with an amplified signal of a digital-to-analog converter. The form of this signal and the degaussing routine is presented in section 4.2.1.
The efficiency of a degaussing coil for a cylindrical mu-metal cylinder with four loops, in terms of residual field gradients, was thoroughly investigated in the context of an assisting bachelor thesis [119].

3.2.3. Coil System

The development of the magnetic field system inside the mu-metal cylinder was one of the main challenges of the Xe-EDM experiment. Several requirements had to be taken into account: First of all, a magnetic holding field, that points in a transversal direction inside the mu-metal cylinder, is required. The main reason for this is the fact that the SQUID system with the cryostat can only be mounted centrically inside the cylinder and it has to be operated while being upright, which allows the gradiometers to only detect spin precession around a transversal magnetic field axis. A coil system that provides such a field is a so-called Cosine-Θ-coil, or short cos-coil. Additional gradient coils are required to suppress the residual gradients from the mu-metal and artificial gradients of

[13] Another example that decreases the effective μ_r is the heating of the material - ultimately to the Curie temperature, where the material loses its magnetic properties [118].
[14] In this context, "high" means magnetic fields higher than the residual field of the MSR or rather the magnetic holding field of the experimental setup.

the setup, especially of the magnetic holding field. Furthermore a field perpendicular to the one of the cos-coil is required to adiabatically and non-adiabatically flip the spins. For this a sequence of coils was put along the axis of the cylindrically shaped cos-coil configuration. The individual coil windings and respective distances are optimized to provide a sufficiently homogeneous magnetic field along the cylinder. The current sources for the individual coils provide a relative stability of 10^{-4} [120].

3.2.3.1. Cosine-Θ-Coil

A perfectly homogeneous transverse magnetic field can be generated by a Cosine-Θ-coil. The distribution of wires follows the relation

$$\Theta_J = \arctan \frac{1}{\sqrt{\frac{N^2}{(2J-1)^2} - 1}} \tag{3.4}$$

with $x_J = R \cdot \sin \Theta_J$ and $y_J = R \cdot \cos \Theta_J$. Here, R is the radius of the cos-coil, N is the amount of loops and $J = 1, 2, ..., N/2$. A distribution of wires with $N = 80$ loops ($2N = 160$ wires) and a diameter of 80 cm is shown in figure 3.19, which corresponds to the actual realization.

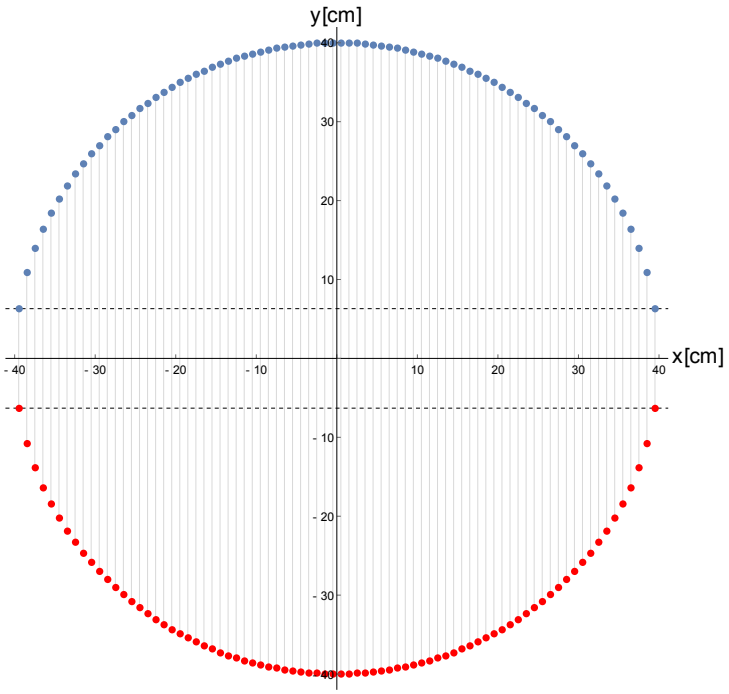

Figure 3.19.: Cosine-Θ-distribution with 80 loops and a diameter of 80 cm. The x-distance between each loop position is 10 mm. The gap (dashed horizontal lines) is 126 mm.

The term "loop" is visualized by the negative current density $\vec{j}$ of the upper wires ($y > 0$, blue dots, pointing inside the drawing plane) and the positive one of the lower wires ($y < 0$, red dots, pointing out of the plane of projection). Then the resulting magnetic field for a sufficiently long cylinder points along the x-axis.
Two features of cos-coils get evident: First, the wires are placed at equal distances of 10 mm along the x-axis which is an important fact for manufacturing such a coil. Second, it can be seen that there is a relatively wide gap of about 126 mm between the outer wires along the y-axis (at $x = \pm 40$ cm). This is an important feature because since the wires have to be connected to loops, there are straight[15] connections between them at the ends of the cylinder, as indicated by the vertical gray lines in figure 3.19. Consequently, during operation these gaps on both sides of the coil are the only accesses to the inside of the coil - for example for the gas filling (cf. 4.3.3) or for other components such as the high voltage cables.

The coil-system has to be placed inside the mu-metal cylinder with its diameter of 85 cm, hence the distance between the wires and the mu-metal is about 25 mm. The main frame of the coil-system is the initially mentioned sturdy cylindrical tube made out of GRP. The wires are tightly attached on distance rings made out of POM, firmly mounted on the GRP tube[16]. At both ends of the cylinder, the connections between the wires to form loops are realized by printed circuit boards. The boards are cut to rings and the printed tin contacts serve as bypass connections for each loop. This realization as bypass-rings is required to provide access from top and bottom to install the further setup on the previously mentioned rail system. A photo of such a bypass-ring is presented in figure 3.20. Because the magnetic field of this design would not be as homogeneous as with straight wires for each loop, as drawn in figure 3.19, additional compensation lids with straight lines for each loop are also realized by printed circuit boards. The bypass lines are additionally compensated. These removable lids on top and bottom of the coil allow access to the inner setup, such as the cryostat of the SQUID gradiometers and the EDM cell. During experimental operation the lids are closed. The resulting height of the cylindrical coil system is approximately 210 cm.
Photographs of the fully assembled coil-system are shown in figures 3.22a and 3.22b. The working principle and the mechanics of the removable lids can be seen in figure 3.23, showing a picture of the fully assembled setup.

[15] The connections have to be straight because of homogeneity reasons.
[16] The worst case of such a high precision coil would be fluttering wires. During the construction it was taken care of an exact and permanent placement of the wires with meticulous precision.

Figure 3.20.: Picture of a bypass ring of the cos-coil system. The wires are connected to loops by bypass lines, which are printed on a circuit board.

A sufficient homogeneity of the holding field of the cos-coil is an indispensable requirement to achieve long relaxation times. Simulations of the magnetic field of the cos-coil placed inside the mu-metal cylinder (cf. section 3.2.2) show that the relative field gradients in the area of the EDM cell with $10^{-3}\,\mathrm{cm}^{-1}$ at a field of $B_{\cos} = 400\,\mathrm{nT}$ are too high to obtain gradients in the order of $10\,\mathrm{pT/cm}$. The main reason for these inhomogeneities are the large gaps between the wires on the x-axis, which lead to large magnetic multipoles. Therefore, a set of gradient coils was developed and designed [121] to reduce the absolute gradients inside the EDM setup, including the additional gradients from the residual field. The magnetic field in x-direction, which is generated by the coil is about $B_{\cos}/I_{\cos} = 115\,\mathrm{nT/mA}$ [120].

3.2.3.2. Gradient Coils

In principle, the gradient (correction) coils are used to produce gradients that go in the opposite direction as the existing gradients and therefore lead to smaller effective gradients at the position of the EDM cell. Besides the possibility of gradient optimization, for some purposes the gradients - or rather the currents of the gradient coils - can intentionally be set in a way to increase the resulting gradients to actively destroy the transverse magnetization on purpose[17]. An illustration of the arrangement of the gradient coils around the GRP cylinder is presented in figure 3.21.

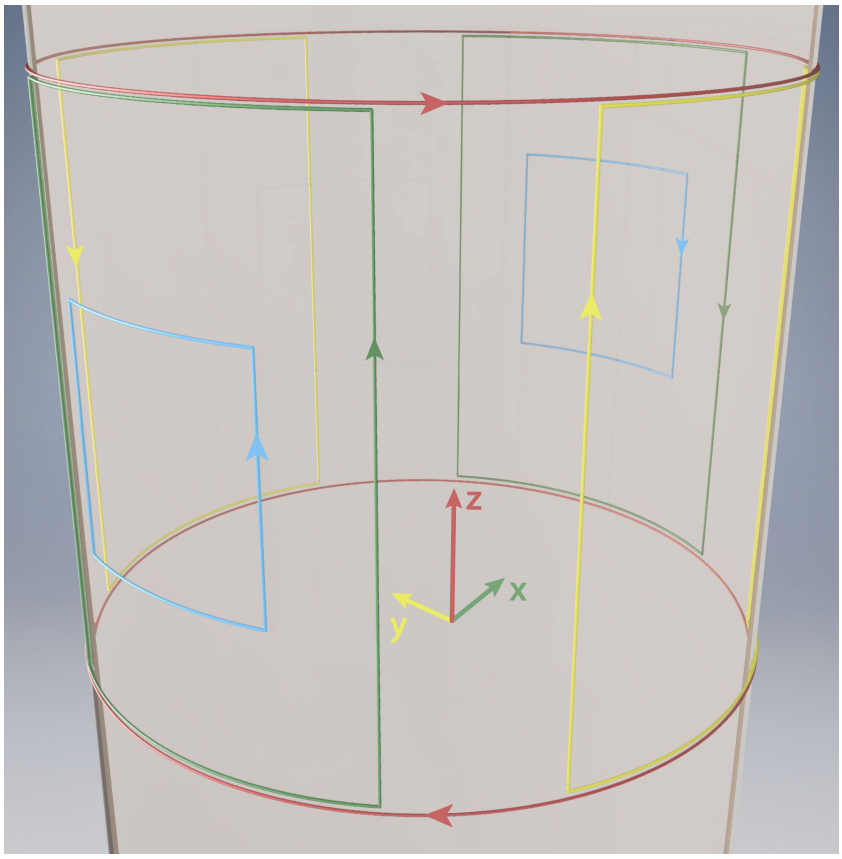

Figure 3.21.: Arrangement of the four gradient coils around the GRP cylinder. All four gradient coils are essentially coil pairs in anti-Helmholtz configuration (see indicated current flow). The coils are placed symmetrically to the midplane (half of the height at 105 cm) of the cylinder. Two saddle coils (green and yellow) produce gradients in x- and y-direction. An anti-Helmholtz coil (red) generates a gradient in z-direction. The smaller saddle coil in x-direction (blue) improves the homogeneity of the cos-coil ($\vec{B}_{\cos} \parallel \hat{e}_x$).

[17] This is known as the principle of so-called spoiler gradients [122].

The design and simulations of these coils were performed by O. Grasdijk [121]. In total, the set of gradient coils consists of two pairs of saddle coils (x- and y-direction) and a Helmholtz-coil (z-direction) complimented by an additional smaller pair of saddle coil (x-direction) for optimizing the magnetic field of the cos-coil. The latter is designed and steadily adjusted in a way to permanently support the cos-coil. The current of this coil, depending on the current of the cos-coil has to be set to $I_{\mathrm{grad,cos\text{-}corr}} = 1/26.455 \cdot I_{\mathrm{cos}}$. As a result, the simulation of the relative field gradients shows an improvement of about one order of magnitude, from $\nabla B/B \approx 10^{-3}\,\mathrm{cm}^{-1}$ to $\nabla B/B \approx 10^{-4}\,\mathrm{cm}^{-1}$. In contrast, the other gradient coils - or rather the corresponding currents - can be varied and optimized as required. The individual gradient coils each have one winding of 1 mm copper wire. The connection wires are twisted to reduce unintended gradients.
According to Gauss's law for magnetism ($\mathrm{div}\vec{B} = 0$) the coils do not generate gradients in only one direction. For example, simulations showed that the saddle coil in x-direction produces a gradient in x-direction of $G_x \approx 87\,\mathrm{pT/cm}$ per mA and also gradients in y- and z-direction of $G_y \approx -59\,\mathrm{pT/cm}$ per mA and $G_z \approx -28\,\mathrm{pT/cm}$ per mA [121]. A technique that is used for optimizing the setting of the coils to improve the T_2^* relaxation time is presented in section 4.2.2.

3.2.3.3. Helmholtz-like Solenoid

A magnetic field in axial direction of the cylindrical symmetry of the setup is produced by a set of ring coils in Helmholtz-like configuration. Seven individual segments (with 33, 15, 13, 12, 13, 15 and 33 windings) made out of 1 mm copper wire are axially arranged on the GRP tube; the distances between each one is optimized to produce a magnetic field as homogeneous as possible. The solenoid with a diameter of 70 cm generates a magnetic field of about $B_{\mathrm{sol}}/I_{\mathrm{sol}} = 100\,\mathrm{nT/mA}$ at the position of the EDM cell.
The axial field is required to perform adiabatic and non-adiabatic spin flips, according to section 2.3.1. The relative magnetic field gradients of the solenoid inside the mu-metal cylinder was calculated to about $\nabla B/B \approx 10^{-4}\,\mathrm{cm}^{-1}$ [121]. For the purpose of rotating the field and flipping the magnetization, this value is sufficient, regarding the gradient relaxation during a flip/rotation.
In figures 3.22a and 3.22b, the seven individual windings of the solenoid can be easily identified.

(a) Coil system: front-view **(b)** Coil system: side-view

Figure 3.22.: Front- (a) and side-view (b) of the coil system mounted on the GRP cylinder. The thin vertical wires form the loops of the cos-coil. These bow-taut wires are hold in place by four well-aligned white rings made out of POM. Openings on top and bottom of the cylinder, clearly recognizable in the front-view picture (a) are used as a passage for the gas filling line, cables and other supply lines. Furthermore, the seven ring coil segments of the solenoid configuration, which are directly glued onto the GRP tube, are discernible. More difficult to recognize are the windings of the gradient coils. The wires forming a two-tines fork-like shape in picture (a) are the supply-lines of the individual coils, twisted in pairs with opposite current directions to prevent interfering fields.

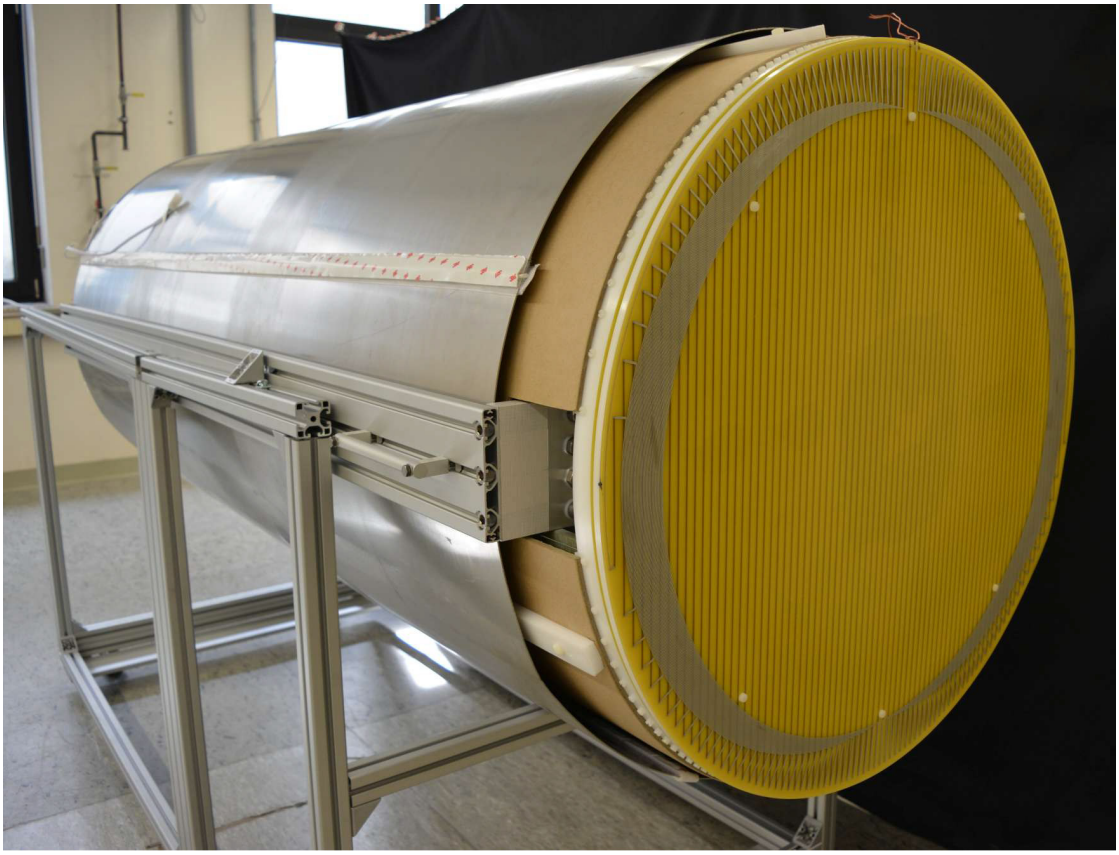

Figure 3.23.: A picture of the fully assembled magnetic field system: The mu-metal cylinder is surrounding the coil system which is protected by two half-shells of cardboard. The removable lids of the cos-coil are attached with plastic screws. An access on the side for the several connections and the gas filling is clearly visible, just below the lid in front. The setup with a height of $\approx 210\,\mathrm{cm}$ is pivoted on a movable cart made out of aluminum that fits through the door of the MSR. If necessary for maintenance, the whole setup can be moved out of the MSR without disassembling. When moved and turned in its final position, the (magnetic) wheels of the cart can be exchanged by non-magnetic and vibration-damped legs.

4

Experimental Procedure

This chapter gives an overview of the necessary steps to perform the Xe-EDM experiment. The particular issues are kept in the order of their application during a standard measurement period, as illustrated in figure 4.1.

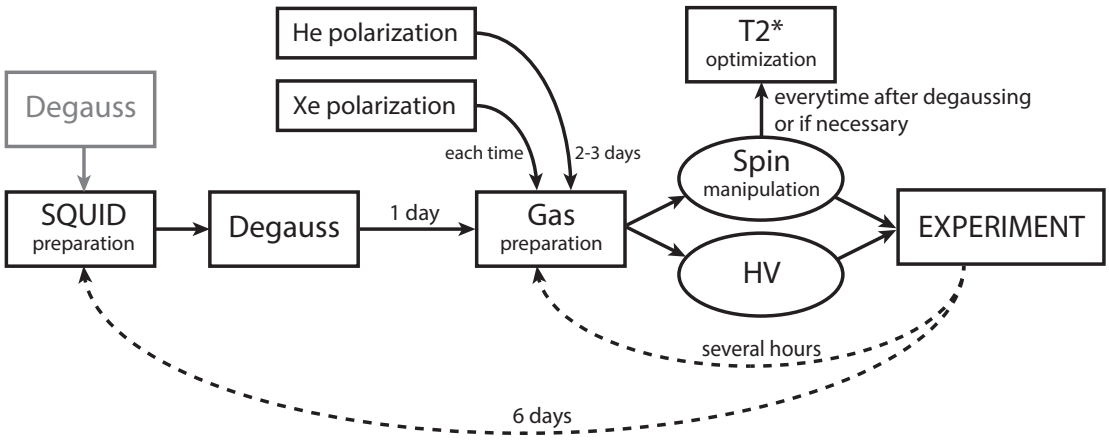

Figure 4.1.: Standard operating procedure for a long term period of measurement. The particular steps and the corresponding time specifications will be explained in the following sections.

This sequence of operational steps represents the current procedure. It is designed for measurement campaigns of one week. The liquid helium for the cryostat of the SQUIDs must then be refilled and the procedure can start from the beginning again. The development is still ongoing (since first test measurements in the MSR in Jülich in 2014) based on the experiences gained in our individual measurement runs. Further enhancements are scheduled to improve the achievable sensitivity. An important step will be the automation of the whole procedure as much as possible. This would be a huge advantage for long term measurements. An outline for this is provided in the outlook of this thesis in the concluding chapter 7.

4.1. SQUID Preparation and Noise Optimization

Before starting the experiment, the SQUID system has to be prepared. Since the low T_c-SQUIDs are working at $T < 9$ Kelvin[1], the cryostat of the system has to be cooled with liquid Helium (ℓHe). A demagnetized filling line for ℓHe can be attached to the dewar without removing parts from the whole setup. Once cooled down, the SQUIDs are ready for operation for about seven days. After this period of time the procedure has to be repeated.

Right after the ℓHe filling procedure the electromagnetic noise in the SQUID signal is considerably increased. Several reasons contribute to this behavior:
First of all an increased noise is caused by mechanical vibrations of the system. When the system is recently filled, the evaporating ℓHe in the dewar causes micro-vibrations. These disturbances are damped if the cryostat system achieves a steady state condition in thermal equilibrium. This process can take up to several hours.
A further factor is the magnetic environment. Before cooling the SQUIDs it is necessary to demagnetize the cylindrical mu-metal shield in order to minimize the residual magnetic field seen by the niobium capsules that shield the SQUIDs. Otherwise the residual magnetic flux would be captured by the capsules in the superconducting state, giving rise to an increased system noise.
In addition it is necessary to demagnetize the mu-metal shield again after filling the cryostat with ℓHe because the door of the MSR has to be open during this procedure. After the degaussing process, expounded in the following section 4.2.1, the mu-metal needs to magnetically relax for several hours into a steady state, without spontaneous domain flips that would also cause an increased noise.
Furthermore, it is required to have an adequate isolating vacuum in the cryostat. Only if the vacuum is sufficient ($< 10^{-3}$ mbar), the amount of ℓHe of one filling lasts for about one week. Otherwise the bad isolation vacuum would lead to a high thermal conductivity in the super-insulation which would cause a faster evaporation, resulting again in an increased noise level. The cryostat can be evacuated within two days to a pressure of $\sim 10^{-5}$ mbar. If it is not cooled permanently with ℓHe, the vacuum has to be restored after a certain time (depending on the resting time).
Figure 4.2 reveals the difference between the resulting amplitude density spectra with the fully assembled setup right after cool down (red) and after the cryostat has relaxed to thermal equilibrium (green).

[1]The critical temperature of niobium is $T_c = 9.26$ K [123].

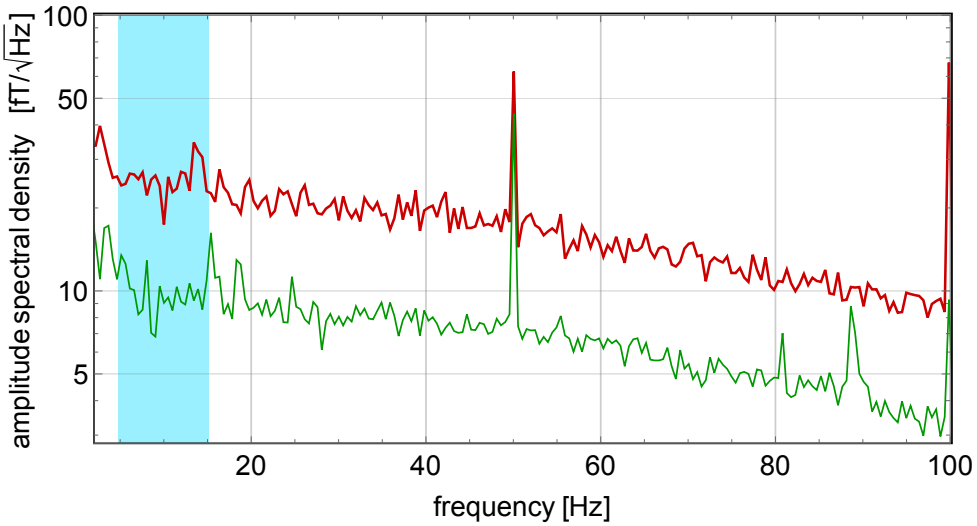

Figure 4.2.: Comparison of the amplitude spectral density of a measurement right after cooling the cryostat down with liquid helium (red) with a measurement when the cryostat is in thermal equilibrium (green). After usually several hours up to one day the system is thermally and magnetically stabilized. The resulting noise level is then reduced by a factor of about two to three in the region of interest (blue shading). As before, the peak which is evident at 50 Hz stems from the power grid.

The observed noise level in the region of interest between 5 Hz and 15 Hz (blue shading) drops to about $\rho \approx 10\,\mathrm{fT}/\sqrt{\mathrm{Hz}}$. At this point it should be mentioned, that the achievable noise strongly depends on external (environmental) electromagnetic sources, i.e. laboratory activities, car traffic outside of the building or running electric equipment like for instance the air conditioning system. Generally, the lowest noise level is reached during night; even a minimum value of $\rho \approx 5\,\mathrm{fT}/\sqrt{\mathrm{Hz}}$ was achieved during a measurement run with the fully assembled setup. As a reminder: Without the additional EDM equipment, e.g. the mu-metal cylinder, a noise level of $\rho \approx 1.5\,\mathrm{fT}/\sqrt{\mathrm{Hz}}$ could be achieved (cf. section 3.13). It can be assumed that the elevation is mainly due to the increased Johnson noise of the particular components.

To briefly summarize: if all the mentioned requirements are taken into account, the noise level of the full setup can be optimized to less than $10\,\mathrm{fT}/\sqrt{\mathrm{Hz}}$ in the region of interest at around 10 Hz. This is a factor of about five higher than under ideal conditions with only the cryostat system installed inside the MSR, as it is presented in figure 3.13. Possible sources are the mu-metal cylinder as well as the coil system (micro-vibration of the SQUIDs through residual magnetic field gradients) and the conductive EDM casing and the high voltage connections (Johnson noise).

4.2. Optimization of the Magnetic Field

The magnetic holding field which ensures the spin precession is one of the most crucial factors of the experiment. At first there is the question for the choice of the magnetic field strength. It is improvident to choose it in an arbitrary way since there are boundaries that should be taken into account: First of all the field, giving a constant magnetic field gradient, should be as low as possible, since the transverse relaxation time depends quadratically on the absolute field gradients (cf. equation 2.39). Ways to reduce these gradients are subsequently described. However, the field cannot be arbitrarily small as well (or negligibly small compared to the residual field inside the MSR). The Larmor frequency depends linearly on the applied magnetic field. For Larmor frequencies in the sub-Hz region the $1/f$-noise of the system dominates and the resulting signal-to-noise ratio would be reduced (cf. figure 4.2). Considering the achievable sensitivity, it is therefore reasonable to adjust the magnetic field strength in such a way that the frequency of xenon ($\gamma_{\mathrm{Xe}} < \gamma_{\mathrm{He}}$) is just above these 5 Hz margin. A quick calculation via equation 2.5 shows that a field of $B_0 = 420\,\mathrm{nT}$ leads to $\nu_{\mathrm{Xe}} = 5.0\,\mathrm{Hz}$ and $\nu_{\mathrm{He}} = 13.8\,\mathrm{Hz}$.

4.2.1. Degaussing

As seen before in figure 3.18 the magnetic flux inside the MSR is huge if the door of the room is opened. To avoid/cancel magnetization effects it is inevitable to have a sufficient degaussing routine. A suitable degaussing routine was found by monitoring the residual field inside the cylinder with a fluxgate. In accordance with preparatory studies of a test-cylinder [119] the most efficient degaussing procedure for the mu-metal cylinder consists of two sequences. The current of the degaussing coil (cf. section 3.2.2) of each sequence is oscillating with an exponentially decaying sine

$$f(t) = A_0 \cdot \exp(-\frac{t}{\tau}) \cdot \sin(\nu \cdot t) \quad . \tag{4.1}$$

The first sequence is set to a frequency $\nu = 3\,\mathrm{Hz}$ and a duration of $T = 300\,\mathrm{s}$ (900 oscillations). The characteristic decay time is set to $\tau = T/10 = 30\,\mathrm{s}$. The second sequence is set to $\nu = 1\,\mathrm{Hz}$, $T = 300\,\mathrm{s}$ (300 oscillations) and $\tau = T/10 = 30\,\mathrm{s}$. For an efficient demagnetization the difference between two adjacent amplitudes ΔA of the decaying sine should be small, as stated in [124] ($\Delta A/A_0 \approx 0.02\,\%$, where A_0 is the initial amplitude). Due to the exponentially decaying envelope, $\Delta A/A_0 \approx 0.01\,\%$ is very small at the end of both sequences.

The resulting small magnetic field gradients inside the mu-metal cylinder - indicating a proper demagnetization - confirm these considerations. A comparison of different residual magnetic field conditions of the mu-metal cylinder is presented in figure 4.3. For this, the magnetic field was measured with a fluxgate in the center (regarding z) of the cylinder, which is located inside the MSR with the door closed. The fluxgate is oriented in radial direction with a distance of about 10 cm from the cylindrical axis, then the sensor is rotated around this axis. A homogeneous field in the transversal plane inside the cylinder leads to a sinusoidal signal measured by the sensor, since the sensor only sees the respective projection. The plots in figure 4.3 show the measured field minus a fitted sine function with one period. The values can be interpreted as the magnetic field gradients $dB_\phi/d\phi$, where ϕ is the rotation angle. Due to $\mathrm{div}\,\vec{B} = 0$ we expect the gradients - or rather the residual field - in other directions to be similar.

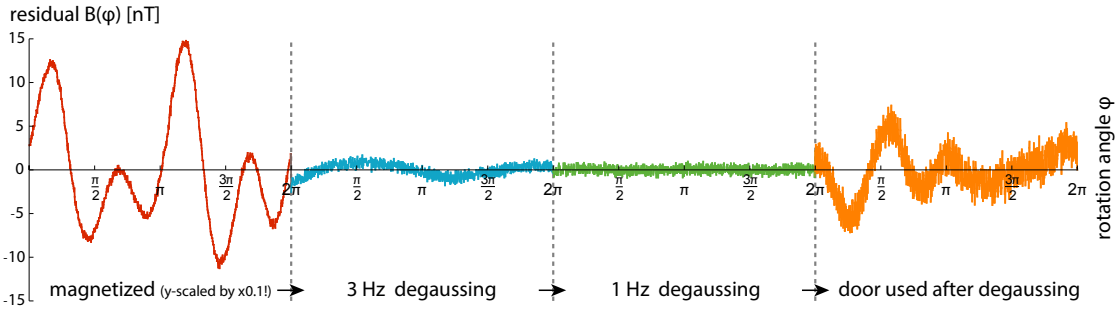

Figure 4.3.: A comparison of different residual magnetic field conditions of the mu-metal cylinder - after the cylinder was magnetized (red), degaussed with $\nu = 3\,\mathrm{Hz}$ (blue), subsequently degaussed with $\nu 1\,\mathrm{Hz}$ (green) and after the door of the MSR was opened and closed again (orange). The residual magnetic field $B(\phi)$ as a function of the rotation angle ϕ of the sensor varies strongly between the different conditions. The red data is y-scaled by 0.1, which means that the y-axis for this measurement goes from $-150\,\mathrm{nT}$ to $150\,\mathrm{nT}$.

It is clearly evident that after the mu-metal is magnetized (red), the first part of the degaussing routine with $\nu = 3\,\mathrm{Hz}$ (blue) already improves the residual field significantly. The second sequence with $\nu = 1\,\mathrm{Hz}$ (green) right after the $\nu = 3\,\mathrm{Hz}$ part reduces the residual field below the digital resolution of the sensor. At this point it is not necessary to determine the gradients quantitatively. A qualitative evaluation indicates the efficiency of the degaussing routine. However, conservatively estimating a field change of about $\delta B_\phi = 1\,\mathrm{nT}$ after a half rotation of the sensor (e.g. between $\phi = 0$ and π), the resulting gradients in the order of about $1\,\mathrm{nT}/20\,\mathrm{cm} = 50\,\mathrm{pT/cm}$, where in this case 20 cm is the distance between both (antiparallel aligned) sensor positions. The most important insight is gained from the residual field condition after opening (for a few minutes) and closing the door again (orange). Clearly, the mu-metal has to be degaussed each time after having access to the MSR by opening the door.

4.2.2. Adjustment of the Gradient Coils: T_2^*-Optimization

According to equation 2.39, the gradient component of the transverse relaxation time $T_{2,\mathrm{grad}}$ is proportional to the square of the absolute magnetic field gradients. To achieve transversal relaxation times as long as possible it is necessary to minimize the magnetic field gradients in close vicinity of the EDM cell. The gradients in the EDM setup stem primarily from two different sources: first from the residual field gradients of the mu-metal shielding (MSR and mu-metal cylinder) and second from the coil system:

- The magnetic holding field to maintain the hyperpolarization of the gaseous spin sample is provided by a cos-coil with a magnetic field of about $B_0 \approx 420\,\mathrm{nT}$ and a simulated homogeneity of about $\Delta B_0/B_0 \approx 10^{-4}\,\mathrm{cm}^{-1}$ [121], leading to gradients in the order of about $\Delta B_0 \approx 50\,\mathrm{pT/cm}$.
- The gradients of the residual field of the mu-metal cylinder after the degaussing routine can be conservatively estimated to be in the same order of magnitude (cf. previous section 4.2.1).

The total gradient is the superposition of both contributions. To reduce these gradients, the gradient coils as described in section 3.2.3 can be adjusted. As mentioned before in the sections 2.3.2.1 and 2.3.2.2 the transverse spin relaxation T_2^* can depend either solely on the longitudinal magnetic field gradients (high pressure regime) or additionally also on the transversal gradients (low pressure regime).
The optimization of the gradients is automated by means of a downhill simplex algorithm. This is a common method to minimize a non-linear function in a multidimensional space [125]. In our case we minimize the function $1/T_2^*$, depending on the currents of the gradient coils. In other words, the T_2^* time of a sample is measured while the currents of the three different gradient coils (cf. section 3.2.3.2) are changed - typically in the order of $I_{\mathrm{grad}} = 0.5 - 1.0\,\mathrm{mA}$. For this we use preferably ^{3}He because of its longer T_1 relaxation time, compared to ^{129}Xe. Accordingly, T_2^* depends more on the gradient relaxation (cf. equation 2.38) and the gradients can be improved more efficiently.
As an example of the T_2^*-, or basically $T_{2,\mathrm{grad}}$-optimization: With hyperpolarized ^{3}He at a pressure of $p = 45.6\,\mathrm{mbar}$ (high pressure regime) we started with $T_2^* \approx 36.000\,\mathrm{s}$. After 22 optimization steps within about four hours we ended up with $T_2^* = 195.000\,\mathrm{s}$, an improvement of about 5.4. The gradient relaxation time $T_{2,\mathrm{grad}}$ is given by equation 2.38 to

$$T_{2,\mathrm{grad}} = \left(\frac{1}{T_2^*} - \frac{1}{T_1}\right)^{-1} \approx 118\,\mathrm{h} \tag{4.2}$$

where T_1 is essentially the wall relaxation time $T_{1,\text{wall}} \approx 100\,\text{h}$. By use of equation 2.39 the total magnetic field gradients after this optimization procedure - integrated over the cell volume - are $\nabla B_0 \approx 9.0\,\text{pT/cm}$; calculated with the pressure-adapted diffusion coefficient of helium, with reference to equation 2.28 and table 2.1. Usually, the gradients after the optimization process are between $\nabla B_0 \approx 10\,\text{pT/cm}$ and $15\,\text{pT/cm}$.

4.3. Gas Preparation

In this section it will be discussed how the gas mixture of polarized ^{3}He and ^{129}Xe and additive buffer gases can be filled into the EDM cell. Since the gas sample can only be filled/applied from the outside of the MSR (cf. figure 3.3), several steps are required:

- Gas Polarization: The hyperpolarized gas samples are provided by the two polarizers built at the Institute of Physics at the University of Mainz.
  The He-polarizer, which was constructed as part of the dissertation of C. Mrozik [57], is located at the University of Mainz. Thus, the polarized helium has to be transported to Jülich using a magnetized transport box with a polarization conserving magnetic field. A detailed description of these boxes is presented in [62].
  The Xe-polarizer, which was constructed as part of the dissertation of M. Repetto [63], was moved from Mainz to Jülich and installed in a lab next to the lab housing the MSR. Although it has been demonstrated that even hyperpolarized ^{129}Xe can be transported from Mainz to Jülich in a magnetized transport box, the polarization losses during transport[2] were not negligible, simply due to the fact that the T_1 relaxation time is much shorter compared to ^{3}He [69]. Due to the relocation of the polarizer, the hyperpolarized Xe can be provided on site as required.

- Gas Mixing: To have the right partial quantities of the gases inside the EDM cell, the different gases gave to be mixed and filled into a transport cell. With the mixing system, described in section 4.3.1, it is possible to mix the gases without significant polarization losses.

- Gas Transport: Once filled into a transport cell, the gas mixture has to be transported to the filling system at the MSR, as described in section 4.3.2.

- Gas Filling: The filling system of the experiment is required to fill a gas sample from the outside of the MSR into the EDM cell. This system, constructed as part of the masters thesis of M. Doll [126], is explained in section 4.3.3.

[2] Driving by car within $\sim 2-3\,\text{h}$ from Mainz to Jülich with a T_1 relaxation time of $\sim 8-10\,\text{h}$ results in a polarization loss of $\sim 25\,\%$.

4.3.1. Gas Mixing

Figure 4.4 shows a photograph of the gas mixing system. The arrangement of valves and glass tubes provides KF glass connections to attach the respective glass vessels and vacuum components:

a) A transport/storage cell ($V_{\text{storage}} \approx 1.3\,\text{l}$) with the ^{3}He gas, polarized in Mainz and transported to Jülich with a magnetic transport box, shown in figure 4.6.

b) A storage cell with the polarized ^{129}Xe gas from the on-site polarizer

c) A cell containing the buffergases

d) A smaller transport cell where the gas mixture is finally stored

e) A non-magnetic pressure sensor[3], used to set the partial pressures of the gases in the mixture

f) A connection for a pumping station to evacuate the whole system

The operational method is described in detail below.

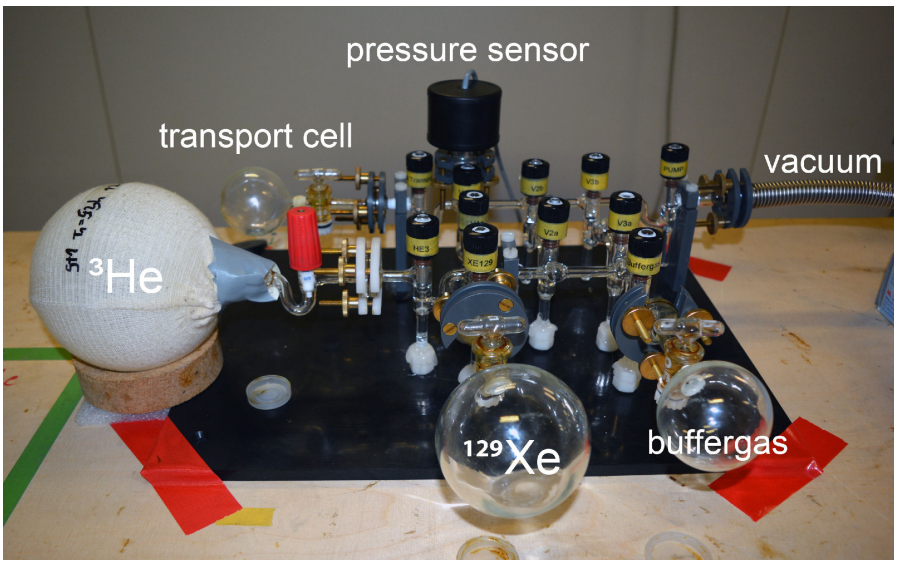

Figure 4.4.: Photograph of the mixing system with the attached glass vessels for ^{3}He, ^{129}Xe, buffergas and the transport cell.

[3]Vacuum gauge set DCP 3000 + VSK 3000 from Vacuubrand. Lower measuring limit: 0.1 mbar; Sensitivity: 0.1 mbar [127]

The mixing system is placed inside a polarization conserving magnetic field [128], which is provided by a pair of Helmholtz coils with a diameter of 140 cm. With a current of 5 A these coils generate a magnetic field of $B_0 \approx 8.5\,\mathrm{G}$. The relative magnetic field gradients are $\nabla B_0/B_0 \approx 10^{-4}$ to $10^{-3}\,\mathrm{cm}^{-1}$ in the center of the coil system. Using equation 2.31, the relaxation time due to gradients can be calculated to $T_{1,\mathrm{grad}}(^3\mathrm{He}) > 150\,\mathrm{h}$ and $T_{1,\mathrm{grad}}(^{129}\mathrm{Xe}) > 4800\,\mathrm{h}$, having pressures in each storage cell of $p_{\mathrm{storage}} \approx 1\,\mathrm{bar}$. Therefore the storing time of the polarized samples in the mixing system is not significantly limited by the homogeneity of the magnetic field.
The whole setup, located about ten meters away from the MSR, is shown in figure 4.5.

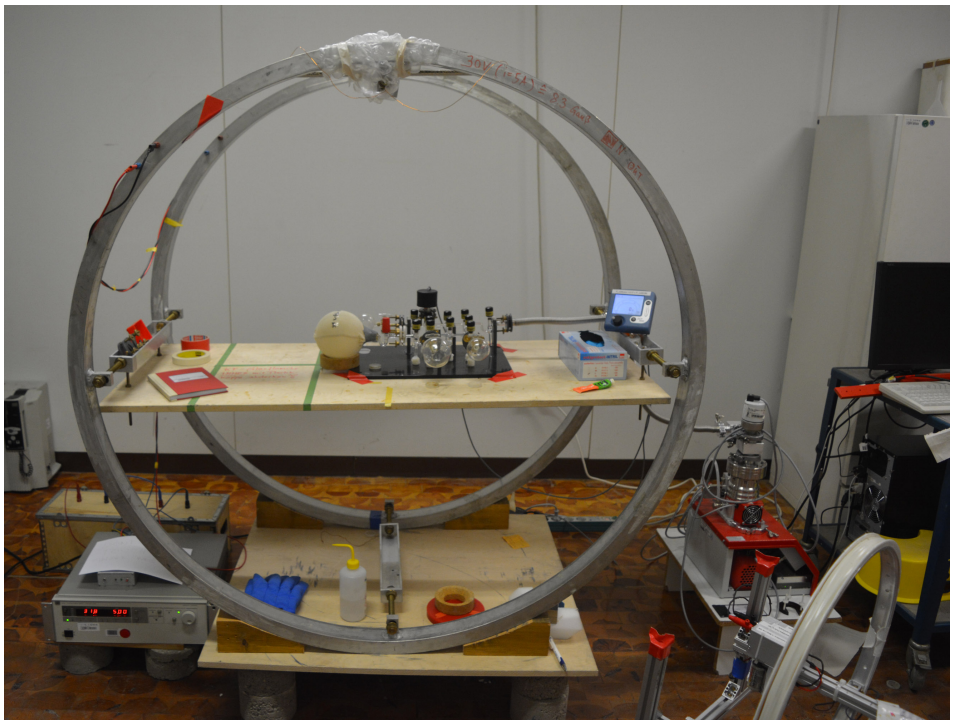

Figure 4.5.: Total view of the mixing system. The system of glass tubes and valves with the connected storage cells for the gases and a pressure sensor is located on a wooden plate inside a pair of Helmholtz coils. The turbo pump provides a vacuum inside the glass system of $< 10^{-7}\,\mathrm{mbar}$. A field of $B_0 \approx 8.5\,\mathrm{G}$ is generated by current source at 5 A. An emergency battery guarantees a failure free operation. The transport coil for carrying the transport cell to the filling station at the MSR can be seen at the bottom right corner.

Figure 4.6 shows a sketch of the gas manipulation unit. In order to extract defined quantities of gas from the respective storage vessels, three sluice valves (a, b) are used with preset volumes V_1, V_2, and V_3 of their respective connection lines. This way small portions of gas, e.g. ^{3}He, can be extracted, buffered and then released into the small

transport cell. This process has to be operated as quick as possible, concerning the relatively short $T_{1,\mathrm{wall}}$ relaxation time inside a thin glass tube (cf. equation 2.32). This procedure is repeated until the required amount of gas is collected in the transport cell.

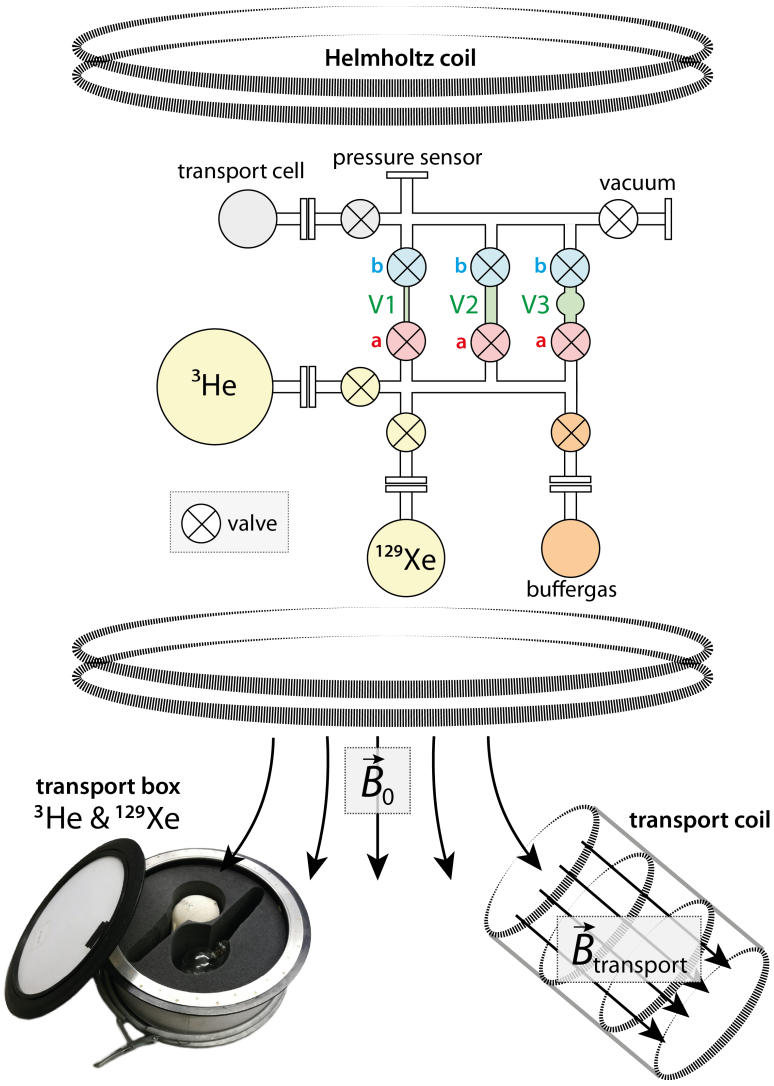

Figure 4.6.: Scheme of the gas mixing system. The respective transport/storage vessels with the polarized ^{3}He and ^{129}Xe gas are attached as well as the buffer gas vessel. The typical gas pressures are between $0.7\,\mathrm{bar} < p < 1.5\,\mathrm{bar}$, higher than the final partial pressures of the gases in the mixture $\approx 0.5\,\mathrm{bar}$. In this way an additional compression of gases is not necessary; the buffered gases are allowed to expand into the volume of the small transport cell. For this purpose we use the sluice valves $V_{1-3\mathrm{a/b}}$. After the mixing procedure the small transport cell is removed and brought to a second gas manipulation unit right at the MSR. A transport coil provides a homogeneous field and adopts the quantization axis for the sample spins. The magnetized transport box is used to transport the hyperpolarized gases from the polarizers to the mixing system.

V_1 has a volume of about 0.6 ml, V_2 about 2.4 ml and V_3 about 5.0 ml. With the well known volumes of the storage vessels for the gases V_{storage}, of the transport cell V_{cell} and of the glass tubes V_{tubes} between the cell and the volumes V_n, it is possible to calculate the exact amount of gas added to the transport cell for each portion of V_n. This mixing system with the defined volumes was designed to get the required amounts of gases in a reasonable number of operation steps. The pressure $P_{\text{cell,i+1}}$ inside the transport cell - after operating the valves of the volume V_n - can be calculated with the following equation:

$$P_{\text{cell,i+1}} = \frac{P_{\text{cell,i}} \cdot (V_{\text{cell}} + V_{\text{tubes}}) + P_{\text{storage}} \cdot V_n}{V_{\text{cell}} + V_{\text{tubes}} + V_n} \quad . \tag{4.3}$$

Here, $P_{\text{cell,i}}$ is the pressure inside the transport cell before this operation and P_{storage} is the pressure inside the storage vessel for the particular gas[4]. In addition, the pressure in the transport cell is monitored by a non-magnetic pressure sensor.
The size of the transport cell was chosen according to the following consideration: In order to avoid wasting gases[5], as little gas as possible should remain in the transport cell after the filling process. In other words, as much gas as possible from the transport cell should be filled into the EDM cell. This can be achieved by keeping the volume of the transport cell as small as possible. However, since a certain pressure is required in the EDM cell ($p \sim 100$ mbar) and no compression unit is used when mixing the gases, the pressure in the transport cell cannot be arbitrarily high. Transport cells with an inner diameter of 5 cm offer a good compromise. With these cells we have a volume ratio

$$V_{\text{transport}} : (V_{\text{transport}} + V_{\text{filling line}} + V_{\text{EDM cell}}) \sim 1 : 7 \quad . \tag{4.4}$$

The inverse ratio applies to the respective pressure, for example a pressure of $V_{\text{transport}} = 700$ mbar in the transport cell leads to a pressure of approximately $V_{\text{EDM cell}} = 100$ mbar in the EDM cell. The relatively high pressure in the transport cell reduces the influence of gradient relaxation during the transport. The wall relaxation time for the chosen cells is in the order of several hours for both Xe and He.

A theoretical and purely statistical optimization of the required partial pressures of hyperpolarized ^{129}Xe and ^{3}He with the addition of SF_6 for quenching (high voltage, cf. section 4.5), as well as with the additional buffer gases CO_2, SF_6, N_2 or ^{4}He is presented

[4]Since the pressure inside the particular storage vessel gets lower after each operation, P_{storage} has to be corrected for the exact calculation of $P_{\text{cell,i}}$. If only small amounts of gases are needed ($P_{\text{cell}} \cdot V_{\text{cell}} \ll P_{\text{storage}} \cdot V_{\text{storage}}$), a correction is not necessary to roughly estimate the required operation steps.
[5]Considering the economics of long term measurements: The price of ^{3}He is about 3000 €/bar·l.

in appendix A.3. For the prevailing experimental conditions (such as the magnetic field gradients), the best EDM sensitivity could be achieved with the following gas mixture:

$p_{\mathrm{Xe}} = 109\,\mathrm{mbar}$	$p_{^3\mathrm{He}} = 55\,\mathrm{mbar}$	$p_{\mathrm{SF_6}} = 5\,\mathrm{mbar}$	$p_{^4\mathrm{He}} = 327\,\mathrm{mbar}$

In general, however, there are deviations from this optimized mixture for an actual measurement. This is on the one hand due to the fact that additional operational boundary conditions have to be taken into account (e. g. dead times) and on the other hand due to experimental limitations. For example, if the polarization of ^{3}He is low, it is reasonable to increase its partial pressure. Furthermore, the total pressure in the transport cell with the optimized partial pressure would be way to high to achieve due to the high partial pressure of ^{4}He. Usually, we used much smaller buffer gas pressures for our experiments. Also, the ideal composition of the gas mixture has to be validated for each run to adapt the current experimental situation. The individual pressures that were used for the EDM measurement runs are listed in the particular sections for March (section 6.1) and July 2017 (section 6.2).

4.3.2. Gas Transport

The Helmholtz coils of the gas mixing station produce a strong stray field. In direct vicinity to the MSR the magnetic shielding factor of the mu-metal can change. Besides, a local magnetic field source next to MSR induces a more asymmetric residual field inside the shielding with higher field gradients. Therefore, the mixing station has to be located in a distance of about ten meters away from the magnetic shielded room to keep this influence low. To move the transport cell with the applicable gas sample from the mixing station to the MSR, a transport system - presented in figure 4.7 - is required.

Realized as a battery operated coil system, it is consisting of four coaxial air coils mounted on an aluminum frame. Each coil is made out of 1 mm isolated copper wire wound up on aluminum wheel rims with a diameter of 390 mm. The windings and the distances between the coils are chosen to optimize the magnetic field homogeneity inside. The relative magnetic field gradients in the center area of the coil system are in the order of $dB_0/d_z \cdot B_0^{-1} \approx 10^{-3}\,\mathrm{cm}^{-1}$ with a mean magnetic field of $B_0 = 200\,\mu\mathrm{T}$. The resulting relaxation time due to the gradients is in the order of $T_{1,\mathrm{grad,He}} \approx 4\,\mathrm{h}$ for ^{3}He at $p_{\mathrm{transport,He}} = 100\,\mathrm{mbar}$ and $T_{1,\mathrm{grad,Xe}} > 100\,\mathrm{h}$ for ^{129}Xe, also at $p_{\mathrm{transport,Xe}} = 100\,\mathrm{mbar}$.

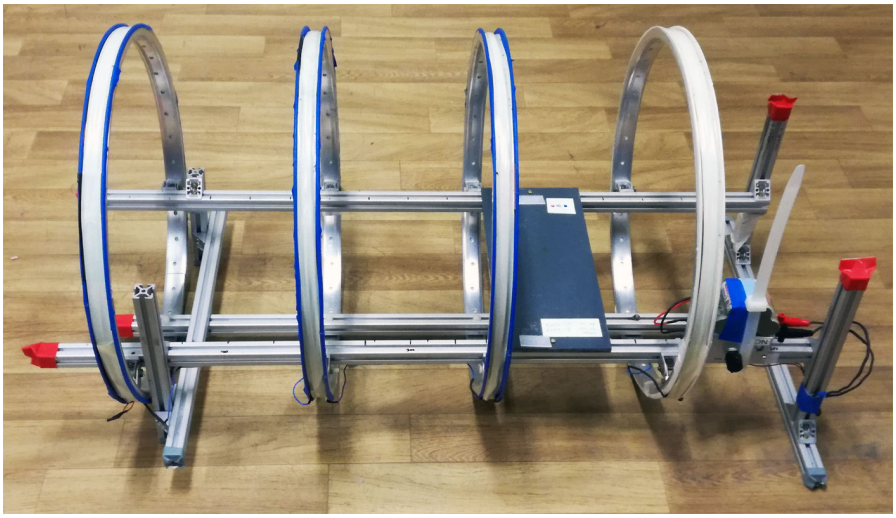

Figure 4.7.: Picture of the battery powered transport coil system.

These values are sufficient for the purpose of carrying the transport cell with the hyperpolarized gases to the filling system at the MSR and filling the mixture into the EDM cell, since this procedure requires about 10-15 minutes. [126]

4.3.3. Gas Filling

For the polarized gases, the only reasonable access to the MSR (except for the door) is a straight hole through the magnetic shields next to the door on the bottom left side with a diameter of $\sim 5\,\text{cm}$. Furthermore, the pneumatic valve which is connected to the EDM cell provides a flange-connection for the gas in-/output. Inspired by similar investigations in the dissertation of A. Kraft [129] a transfer line between the EDM cell and a connection outside of the MSR is implemented as a bent copper tube with an inner diameter of 6 mm. To maintain the polarization during the filling process, the magnetic guiding field must point in a predefined direction all the time. Therefore, the transfer line is placed inside different solenoids and a transverse coil[6]. Inside the mu-metal cylinder and the cos-coil, the copper tube is connected to a glass tube, spanning the vertical distance between the cos-coil entrance and the EDM cell to prevent Johnson noise. Outside of the MSR, the transfer line is connected to a four-port valve-system made out of glass. Two outlets are connected to a vacuum line and a pressure sensor. Once prepared and filled with the gas mixture and transported to the MSR, the transport cell can be connected to the

[6]Detailed discussion in [126].

remaining outlet of filling system (see figure 4.8b). Then the transport coil, introduced in the previous section 4.3.2, surrounds the whole filling system (see figure 4.8a) and provides the guiding field until the gas mixture is filled. The magnetic field of the first solenoid 1, that just fits through the hole of the MSR, and the field of the transport coil are matched to prevent a possible zero passing of the overall field. Along the transfer line the magnitude of the guiding field steadily decreases from $B_{\mathrm{sol}\,1} \approx 200\,\mu\mathrm{T}$ outside the MSR to $B_{\mathrm{cos}} \approx 1\,\mu\mathrm{T}$ inside the cos-coil. After the filling process, the transport coil and the transfer coils are slowly ramped down to avoid magnetic disturbances, i.e. sudden change of the working point of the SQUID gradiometers and magnetization of the mu-metal. First tests demonstrated the functionality of the system regarding the polarization conserving transfer of the gas mixture and the fact that the mixing ratio of the components does not change during the filling process [126].

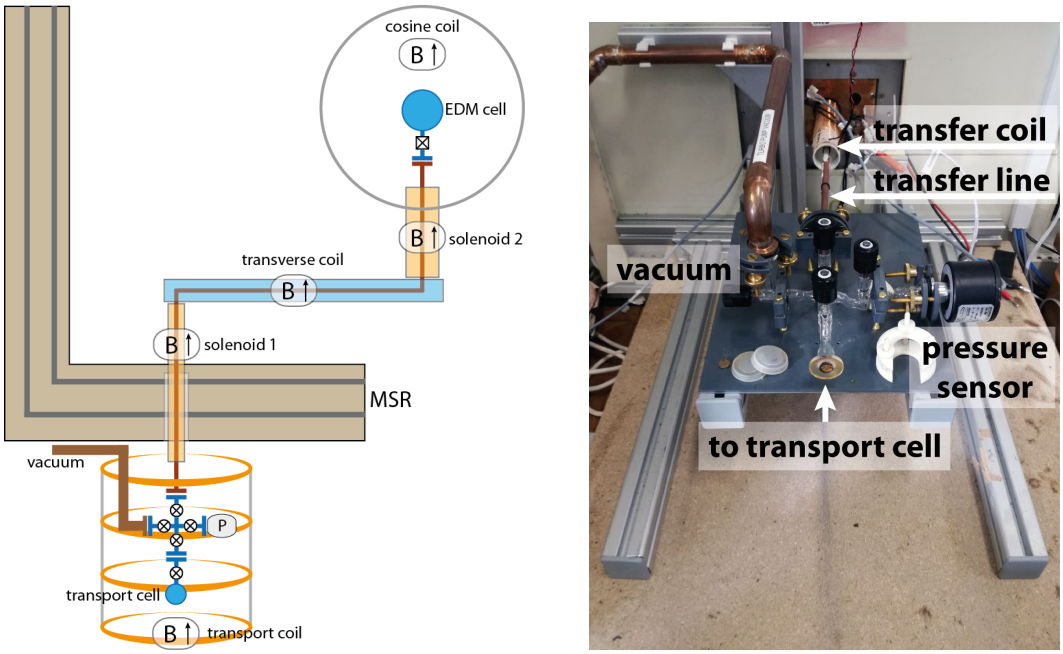

(a) Filling system: schematic overview **(b)** Filling station: detailed view

Figure 4.8.: The filling system provides the possibility to transfer the mixture of polarized gases from the transport cell into the EDM cell without substantial polarization losses. The schematic overview (a) shows the different coils that guarantee a fixed direction of the magnetic guiding field - from the transport coil through the MSR and into the cos-coil. The filling line, a copper tube, is placed inside the solenoid 1 that goes through the MSR, inside the transverse coil that goes on the perpendicular track and inside the solenoid 2 that goes into the cos-coil. A detailed view of the attached four-port valve-system with the connected vacuum line, a pressure sensor and the connection for the transport cell is shown in (b).

4.4. Spin Manipulation & Data Acquisition

During an EDM measurement the spin precession of both gas species ^{3}He and ^{129}Xe is defined by the field direction $\hat{e}_x$ of the cos-coil. For the following considerations it is assumed that the gas mixture has been filled into the EDM cell and the magnetic guiding field is still predetermined by the cos-coil (cf. previous section 4.3.3). With the different coils of our setup we have two possibilities to start the spin precession:
a) To flip the spins of both species simultaneously: The magnetic holding field is adiabatically rotated from the cos-coil field to the one of the solenoid. A non-adiabatic switch back to the field of the cos-coil starts the precession. The flipping angle α is defined by the angle of the adiabatic rotation. To put it plainly, the direction of the field changes from the x-direction to the z-direction, like

$$\vec{B}_0 = B_{\cos} \cdot \hat{e}_x \ \cos(\alpha) + B_{\mathrm{sol}} \cdot \hat{e}_z \ \sin(\alpha) \quad . \tag{4.5}$$

The magnitude of the solenoid field should be in the same order as the one of the cos-coil field. To start a spin precession of the hyperpolarized He and Xe, the field has to be switched instantaneously back to the x-direction. Typically the magnetic field is rotated with $\mathrm{d}\alpha/\mathrm{d}t \approx 0.5°/\mathrm{s}$. So a full $\pi/2$-rotation takes approximately three minutes. Depending on α it is possible to flip only a part of the magnetization (in the macroscopic sense). A useful example for this is the measurement of the T_1 relaxation time by use of spoiler gradients. For this only a tiny part of the magnetization is excited by choosing a small flip angle and the amplitude of the signal is determined. Afterwards the magnetization is destroyed by spoiler gradients and the measurement is be repeated several times to derive the longitudinal relaxation time. Because α is well-known, the loss in the signal for each measurement can be corrected (flip-angle correction).
b) Another technique to start the spin precession uses a resonant excitation pulse, a so-called RF-pulse[7]. Hereby only one species is flipped while the other one is not influenced by the excitation. The resonant frequency of the RF-pulse has to be matched to the Larmor frequency of the specific sample. Because of magnetic field drifts and resulting changes in the frequency it is reasonable to irradiate a sinc-shaped pulse[8] which equates a rectangular function in frequency space. This assures the matching of the pulse to the resonance of the particular species. The amplitude and the duration of the pulse define the flipping angle α, according to equation 2.22.

[7] RF, from radio frequency. This common term from NMR experiments is used, although we work with frequencies in the order of 10 Hz.
[8] cardinal sine function: $\mathrm{sinc}(x) = \sin(x)/x$ for $x \neq 0$, $\mathrm{sinc}(0) := 1$

The benefit of this method is the possibility to observe the spin precession of one species **A** while the other one **B** is "in rest". Thereby it is practically possible to study the mutual influence of the spins of the species, in this example of **B** on the precessing species **A** (so-called cross-talk, cf. section 5.2.4, Ramsey-Bloch-Siegert shift).

For each species the measured exponentially damped sinusoidal signal with N data points can be expressed as

$$s[n] = A \cdot e^{-\beta n} \cdot \cos\left(\frac{\omega}{r_s} n + \Phi\right) + \epsilon[n], \qquad n = 0, 1, \ldots, N-1 \tag{4.6}$$

with the precession frequency ω, the amplitude A, the damping factor $\beta = (r_s T_2^*)^{-1}$ due to the transverse relaxation and the phase Φ. Furthermore the signal is superimposed by the noise $\epsilon[n]$, e.g. white Gaussian noise. The detected signal of our SQUID system is acquired in sub-cuts of $\Delta t = 4\,\mathrm{s}$ with a sampling rate of $r_s = 250\,\mathrm{Hz}$ (1000 data points per sub-cut). Such a raw subset data is plotted in figure 4.9. For this measurement the cell was filled with hyperpolarized Xe with $p_{\mathrm{Xe}} \approx 45\,\mathrm{mbar}$ and He with $p_{\mathrm{He}} \approx 11\,\mathrm{mbar}$ and with additional buffer gases, and the spins are excited by 90°.

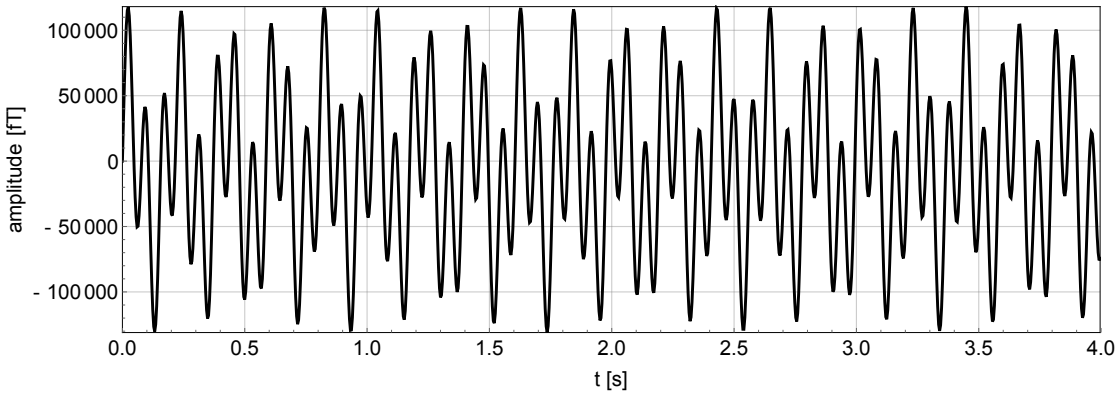

Figure 4.9.: Gradiometer signal of a ^{3}He and ^{129}Xe spin precession. The plot shows a $\tau = 4\,\mathrm{s}$ sub-cut of the acquired raw-data with a sampling rate of $r_s = 250\,\mathrm{Hz}$. The beat of the individual frequencies $\nu_{\mathrm{He}} \approx 13.8\,\mathrm{Hz}$ and $\nu_{\mathrm{Xe}} \approx 5.0\,\mathrm{Hz}$ is clearly evident.

The following plot in figure 4.10 shows the amplitude spectral density, accumulated from four consecutive sub-cuts of the raw-data. The two sharp peaks of the precessing spins of Xe and He are prominent at 5.0 Hz and 13.8 Hz. The noise level in this measurement is about $\rho \approx 12\,\mathrm{fT}/\sqrt{\mathrm{Hz}}$. Most likely the structures at around 15 Hz and 18 Hz stem from mechanical vibrations of the experimental setup. The strong increase of the noise below $\approx 1\,\mathrm{Hz}$ represents the $1/f$-noise. The noise beyond 3 Hz is essentially white noise.

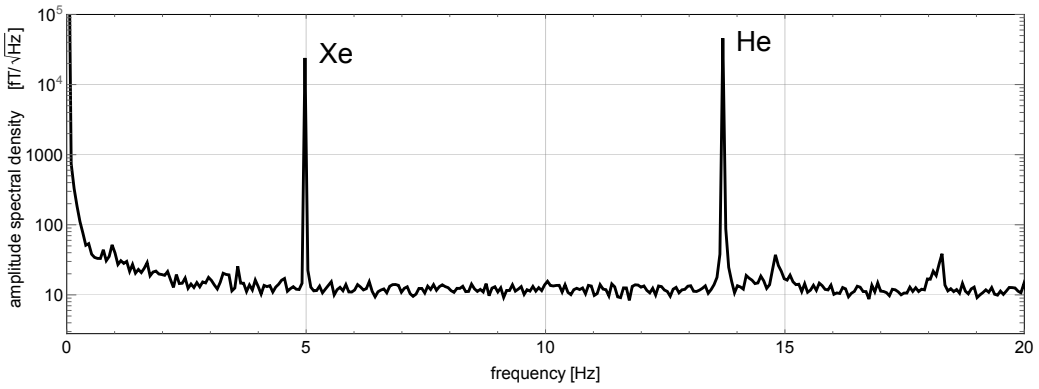

Figure 4.10.: Amplitude spectral density, accumulated from four consecutive sub-cuts of the raw-data. The spectrum shows the sharp peaks at the precession frequencies of the ^{3}He and ^{129}Xe spins in the EDM cell with a fully assembled setup, with $\nu_{\mathrm{Xe}} \approx 5.0\,\mathrm{Hz}$ and $\nu_{\mathrm{He}} \approx 13.8\,\mathrm{Hz}$. The magnetic holding field in this case was about $B_0 = 425\,\mathrm{nT}$. The noise floor in the region of interest is about $\rho \approx 12\,\mathrm{fT}/\sqrt{\mathrm{Hz}}$.

By determining the amplitudes A of the He- and Xe-precession signal (cf. equation 4.6) the signal-per-pressure ratio can be calculated. For this particular case - shortly after filling the gases and starting the spin precession - the achieved values are

$$\frac{A_{\mathrm{Xe}}}{p_{\mathrm{Xe}}} = \frac{53\,\mathrm{pT}}{45\,\mathrm{mbar}} = 1.2\,\frac{\mathrm{pT}}{\mathrm{mbar}} \qquad \text{and} \qquad \frac{A_{\mathrm{He}}}{p_{\mathrm{He}}} = \frac{73\,\mathrm{pT}}{11\,\mathrm{mbar}} = 6.6\,\frac{\mathrm{pT}}{\mathrm{mbar}} \quad . \tag{4.7}$$

These ratios are directly proportional to the actual polarization of the spin species in the EDM cell and a measure of this with a given distance d from the cell to the SQUID (cf. equation 2.43). Since the polarization can change - due the changing polarizer performances, transport losses, etc. - the A/p values are used to investigate these loss mechanisms to obtain optimal signal-to-noise ratios.

4.5. HV Appliance & Leakage Currents

According to equation 2.59, the achievable EDM sensitivity δd_{Xe} is inversely proportional to the applied electric field E. Tests with the setup presented in section 3.1.4 specify boundaries concerning the applicable high voltage. A high voltage larger than $U = \pm 4.5\,\mathrm{kV}$ leads to an exceedingly increasing leakage current between the electrodes and the casing up to $I_{\mathrm{leak}} \approx \mu\mathrm{A}$. It is standing to reason that discharge effects [130] between the casing and/or the HV connections cause a surge of the electric conductivity. Below

this critical voltage, the leakage current between the connections and the casing, as well as between the electrodes is reliably below $I_{\text{leak}} \approx 10\,\text{pA}$ - by deducting of the offset of the electronics. However, it is reasonable, but especially necessary for small xenon partial pressures $p_{\text{Xe}} \sim 20 - 40\,\text{mbar}$, to add SF_6 as quenching gas to the gas mixture to achieve this value. A partial pressure of $p_{SF_6} \approx 5\,\text{mbar}$ has proven to be effective. The offset of the leakage current determination (current with no applied voltage) varies between $I_{\text{leak, off}} \approx -50\,\text{pA}$ and $-70\,\text{pA}$. Depending on the condition of the inert gas atmosphere inside the casing, this value can differ significantly. As soon as the leakage currents start increasing significantly, the casing is flushed with fresh and clean SF_6. To be on the safe side, a voltage of $U = \pm 4\,\text{kV}$ is set for the EDM measurements. With a distance of $d \approx 10\,\text{cm}$ between the electrodes, this relates to an electric field of $E = \pm 800\,\text{V/cm}$.
A measurement of the leakage current with the pico-amperemeter during the first 10000 s of an EDM run is presented in figure 4.11.

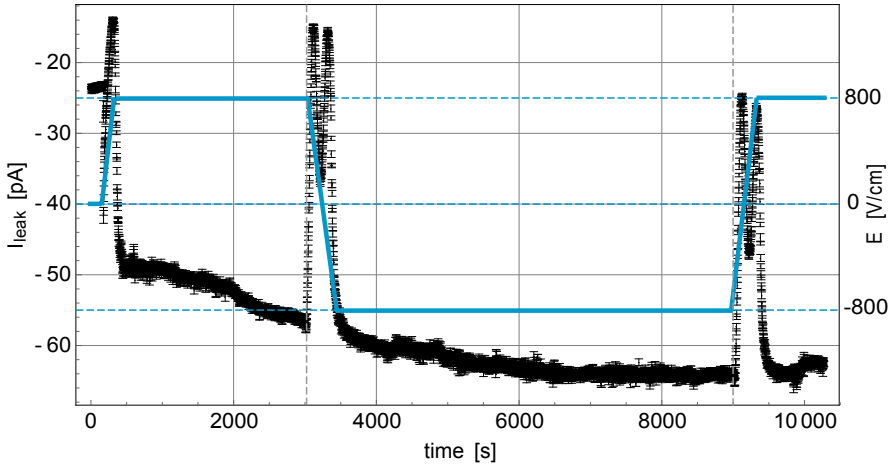

Figure 4.11.: Observation of the leakage current between the two electrodes overlaid by the settings of the high voltage, or rather the electric field (blue). The analysis of the data is described below.

The overall drift, starting at around $I_{\text{leak}} \approx -50\,\text{pA}$, stems mainly from an offset drift which stabilizes at around $I_{\text{leak}} \approx -65\,\text{pA}$. A significant leakage current would manifest as a jump in the curve before and after the switching. For instance the switching at around 9000 s shows no difference in the measured current before and after the polarity reversal procedure. The reversal of the electric field from $E = 800\,\text{V/cm}$ to $E = -800\,\text{V/cm}$ - indicated in blue - is performed with an accuracy of $\Delta U \approx \pm 1\,\text{V}$ [120]. The first switching is initiated after 50 min of data taking. After that, the field is reversed every 100 min. The distinct peaks are effects during the polarity change of the HV.

5

Systematics

5.1. Data Analysis

Short recap: To measure a potential EDM of ^{129}Xe $\vec{d}$, the spin precession of ^{3}He and ^{129}Xe in a magnetic holding field B_0 is observed. Additionally, an electric field E is applied - reversible between a parallel and anti-parallel alignment to B_0. An finite EDM would cause a shift of the weighted frequency difference, $\Delta\omega_{\mathrm{EDM}}$, or rather of the accumulated weighted phase difference, $\Delta\Phi_{\mathrm{EDM}}$, depending on the applied electric field (cf. equation 2.32):

$$\Delta\Phi_{\mathrm{EDM}}(t) = \int \Delta\omega_{\mathrm{EDM}}(t)\, dt = \int \frac{4}{\hbar}\vec{d}\cdot\vec{E}(t)\, dt \tag{5.1}$$

The electric field reversal and the corresponding potential EDM phase shift $\delta\Phi$ is exemplified in figure 5.1.

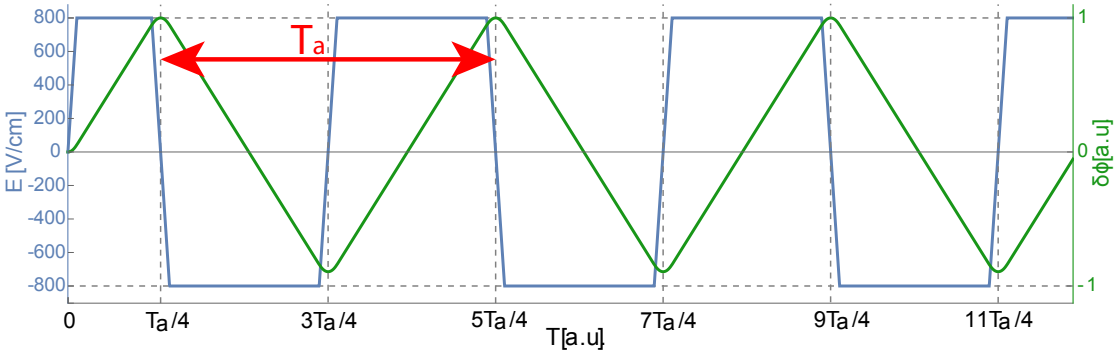

Figure 5.1.: The HV $U = \pm 4\,\mathrm{kV}$ is applied symmetrically to the electrodes with respect to the ground potential and changed periodically in polarity with the time constant T_a. The resulting electric field is $E = U/d = \pm 800\,\mathrm{V/cm}$, where $d = 10\,\mathrm{cm}$ is the distance between the electrodes. Except for the first polarity change after $T_a/4$, the polarity is always inverted after $T_a/2$. Then the accumulated EDM phase shift is symmetric around 0, characterized by the normalized triangular wave function $h(t, T_a)$ (green graph). Due to the non-instant ramp, the reversal points of this function are parabolically rounded.

By changing the polarity of the applied high voltage, the electric field is reversed (rectangular function) and therefore the sign of the accumulated phase shift is modulated (triangular function). The switching time is described by the time constant T_a. It quantifies the periodic time from setting the electric field from $+E$ to $-E$ and back to $+E$ (and vice versa). The normalized triangular wave function, characterizing the modulation of the phase shift, is from now on called EDM-function $h(t, T_a)$. A more detailed description of the EDM-function is presented in appendix A.1.

5.1.1. Phase Determination

In order to extract the accumulated EDM phase it is necessary to pre-analyze the raw data of a measurement. For this purpose the combined signal of He and Xe for each data sub-cut i (cf. equation 4.6) is evaluated by the fit function

$$\begin{aligned} f^i(t) = A^i_{\mathrm{He}} \cdot \cos\left(\omega^i_{\mathrm{He}} \cdot t\right) + B^i_{\mathrm{He}} \cdot \sin\left(\omega^i_{\mathrm{He}} \cdot t\right) \\ + A^i_{\mathrm{Xe}} \cdot \cos\left(\omega^i_{\mathrm{Xe}} \cdot t\right) + B^i_{\mathrm{Xe}} \cdot \sin\left(\omega^i_{\mathrm{Xe}} \cdot t\right) + C^i_0 + C^i_1 \cdot t \quad . \end{aligned} \tag{5.2}$$

The fit parameters $A_{\mathrm{He/Xe}}$ and $B_{\mathrm{He/Xe}}$ represent the signal amplitudes of the respective spin species in the superimposed signal. Accordingly $\omega_{\mathrm{He/Xe}}$ are the Larmor frequencies. C_0 and C_1 are the fit parameters for a constant offset and a linear drift of the signal. All parameters are estimated with their correlated and uncorrelated uncertainty and the goodness of the fit χ^2. From the fit amplitudes A and B, the magnitude a of the He and Xe signals can be calculated for each sub-cut by

$$a^i_{\mathrm{He/Xe}} = \sqrt{\left(A^i_{\mathrm{He/Xe}}\right)^2 + \left(B^i_{\mathrm{He/Xe}}\right)^2} \quad . \tag{5.3}$$

The time constants $T^*_{2,\mathrm{He/Xe}}$ of the exponentially decaying signals can be derived from a starting point $a_{0,\mathrm{He/Xe}}$ by

$$a_{\mathrm{He/Xe}}(t_i) = a_{0,\mathrm{He/Xe}} \cdot e^{\frac{-t_i}{T^*_{2,\mathrm{He/Xe}}}} \quad . \tag{5.4}$$

The phases $\phi^i_{\mathrm{He/Xe}}$ of each sub-cut are calculated by the relation of $A^i_{\mathrm{He/Xe}}$ and $B^i_{\mathrm{He/Xe}}$ by means of the atan2 function, an arctangent with two arguments:

$$\mathrm{atan2}\,(y, x) = \begin{cases} \arctan(\frac{y}{x}) & x > 0 \\ \arctan(\frac{y}{x}) + \pi & x < 0,\ y \geq 0 \\ \arctan(\frac{y}{x}) - \pi & x < 0,\ y < 0 \end{cases} \quad . \tag{5.5}$$

This function leads to the phases $\phi^i_{\mathrm{He/Xe}}$ by

$$\phi^i_{\mathrm{He/Xe}} = \mathrm{atan2}\left(B^i_{\mathrm{He/Xe}}, A^i_{\mathrm{He/Xe}}\right) + \pi \quad , \tag{5.6}$$

where ϕ is in the range of $[0, 2\pi)$. Additionally, the right amount of full periods $\Delta n^i_{\mathrm{He/Xe}}$ during this sub-cut has to be added. To find $\Delta n^i_{\mathrm{He/Xe}}$ of a particular sub-cut i it is reasonable to use the fitted precession frequencies $\omega^i_{\mathrm{He/Xe}}$. Thus it follows the dependency

$$\Delta n^i_{\mathrm{He/Xe}} = \frac{\omega^i_{\mathrm{He/Xe}} \cdot \Delta t - \left(\phi^i_{\mathrm{He/Xe}} - \phi^{i-1}_{\mathrm{He/Xe}}\right)}{2\pi} \quad , \tag{5.7}$$

where $\Delta t = 4\,\mathrm{s}$ is the length of a single sub-cut. The correct multiples of 2π after the m^{th} sub-cut, $n^m_{\mathrm{He/Xe}}$, are therefore calculated by the sum of the full periods after each sub-cut i, $\Delta n^i_{\mathrm{He/Xe}}$, like

$$n^m_{\mathrm{He/Xe}} = \sum_{i=1}^{m} \Delta n^i_{\mathrm{He/Xe}} \quad . \tag{5.8}$$

Now, the accumulated phases $\Phi^m_{\mathrm{He/Xe}}$ after the m^{th} sub-cut are determined by adding the right amount of full periods $n^m_{\mathrm{He/Xe}} \cdot 2\pi$, like

$$\Phi^m_{\mathrm{He/Xe}} = 2\pi \cdot n^m_{\mathrm{He/Xe}} + \phi^m_{\mathrm{He/Xe}} \quad . \tag{5.9}$$

Analogous to equation 2.51, this leads directly to the accumulated weighted phase difference after the m^{th} sub-cut

$$\Delta\Phi^m = \Phi^m_{\mathrm{Xe}} - \frac{\gamma_{\mathrm{Xe}}}{\gamma_{\mathrm{He}}} \cdot \Phi^m_{\mathrm{He/e}} \quad . \tag{5.10}$$

Theoretically $\Delta\Phi$ is constant if the spin precession is solely depending on the magnetic holding field B_0. In practice, however, there are deterministic phase drifts that lead to linear and exponential shifts of the weighted phase difference. These shifts will be discussed in detail in the next section 5.2. The fit function

$$\begin{aligned} \Delta\Phi_{\mathrm{fit}}(t) = \Phi_0 + \Delta\omega_{\mathrm{lin}} \cdot t + E_{\mathrm{He}} \cdot e^{\frac{-t}{T^*_{2,\mathrm{He}}}} + E_{\mathrm{Xe}} \cdot e^{\frac{-t}{T^*_{2,\mathrm{Xe}}}} \\ + F_{\mathrm{He}} \cdot e^{\frac{-2t}{T^*_{2,\mathrm{Xe}}}} + F_{\mathrm{Xe}} \cdot e^{\frac{-2t}{T^*_{2,\mathrm{He}}}} + g \cdot h(t, T_a) \end{aligned} \tag{5.11}$$

takes into account the various deterministic contributions that shift the effective weighted phase difference. These shifts have to be determined as accurately as possible in order to extract the accumulated EDM-phase shift (cf. equations 5.1)

$$\Delta\Phi_{\mathrm{EDM}}(t) = \int \frac{4}{\hbar} \vec{d} \cdot \vec{E}(t)\, dt =: g \cdot h(t, T_a) \quad . \tag{5.12}$$

To come back to the initial argument of this chapter, the reason for the reversal of the electric field is to minimize the correlation of $\Delta\Phi_{\mathrm{EDM}}(t)$, described by the normalized (triangular wave-) function $h(t, T_a)$ with the amplitude g and the globally accumulated weighted phase difference $\Delta\Phi$. From the amplitude g, including its uncertainty, a potential finite Xe-EDM can be determined, or rather an upper limit can be specified.
The data analysis is performed with the Mathematica package "DatFit" of U. Schmidt, collaboration member from the University of Heidelberg.

5.2. Deterministic Frequency/Phase Shifts

In this section the deterministic frequency/phase shifts that are occurring in the experiment are analyzed. In this context "deterministic" means that the time dependency of the respective phase drift is known. A comparison of the effects and their consequences is summarized in table 5.3.

5.2.1. Chemical Shift

The chemical shift is a well known effect in NMR spectroscopy, where it is used diagnostically to investigate, inter alia, the structure of molecules [131]. It quantifies the shift of the Larmor frequency caused by the reduction of the magnetic holding field B_0 due to the diamagnetic shielding of the nucleus. In the case of the He/Xe-comagnetometer, the induced magnetic field of the moving electrons of helium and xenon B_i leads to an effective precession frequency of

$$\omega_{\mathrm{eff}} = \gamma \cdot (B_0 - B_i) \quad . \tag{5.13}$$

Considering the weighted frequency difference, this diamagnetic shielding can be expressed by a reduction of the ratio of gyromagnetic ratios γ from their literature values [53, 55]

$$\frac{\gamma_{\mathrm{He}}}{\gamma_{\mathrm{Xe}}} = 2.754175973(126) \quad , \tag{5.14}$$

since ^{129}Xe, as the heavier atom, has a much stronger chemical shift than ^{3}He. The chemical shift is depending on the specific gas mixture and the interactions of the gas molecules with each other [132] and with the environment (the other gas species [133] and the wall of the cell [134]). Pressure and temperature changes can be neglected during a measurement, which is why this effect can be assumed to be constant. Such constant

and non-correlated (regarding the reversal of the electrical field) changes in the weighted frequency difference are covered by the applied fit-function with the consideration of (a constant and) a linear shift of the weighted phase difference.

5.2.2. Earth Rotation

To be precise, the laboratory system of the experimental setup is no inertial system. Since the laboratory, and therefore the detector (SQUIDs) and the magnetic field, is stationary located on the surface of Earth with a fixed orientation towards Earth rotation axis, the SQUIDs rotate with a certain frequency with respect to the precessing spins. As a result the measured Larmor precession of each species in the laboratory system is shifted from the actual Larmor frequency ω_L by the frequency ω_{det}. As visualized in figure 5.2, the laboratory system is defined by the latitude Θ of the location of the experiment and by the orientation of the magnetic field ρ (with respect to north direction).

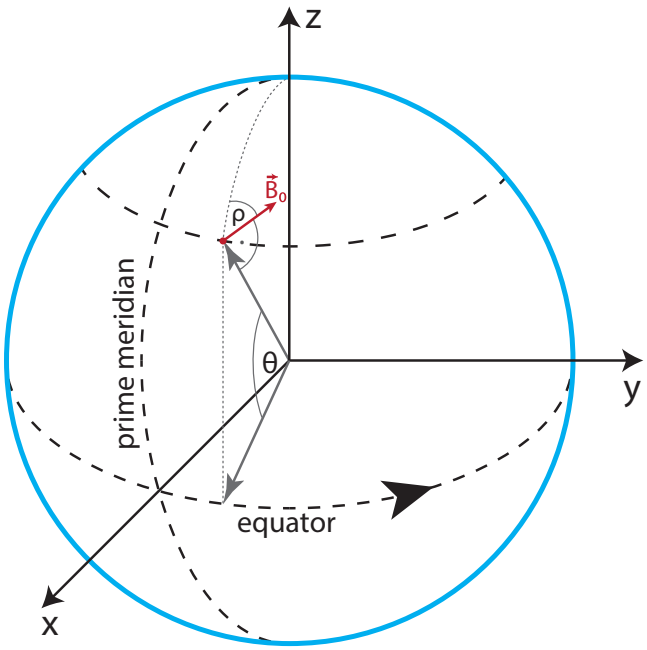

Figure 5.2.: Illustration of the rotating laboratory system on Earth. The latitude Θ is determined by the geographic position of the MSR on the surface of Earth, whereas the direction of the magnetic holding field $\vec{B}_0$, at a tangent to the surface, is described by ρ with respect to the north direction.

Assuming the x-axis as the vernal equinox and the z-axis as the axis of Earth rotation (axis from the center of Earth to the north pole), the conversion of the Cartesian co-

ordinates of the laboratory system to the geocentric equatorial coordinates of Earth is given by the following relation:

$$\begin{pmatrix} \hat{e}_x \\ \hat{e}_y \\ \hat{e}_z \end{pmatrix} = \begin{pmatrix} \sin\Theta\cos\rho \\ \sin\rho \\ \cos\Theta\cos\rho \end{pmatrix} \tag{5.15}$$

The resulting shift depends on the angular velocity of Earth $\vec{\Omega}_{\oplus} = \Omega_{\oplus} \begin{pmatrix} 0 \\ 0 \\ 1 \end{pmatrix}$, as

$$\omega_{\text{det}} = \Omega_{\oplus} \cdot \cos(\Theta) \cdot \cos(\rho) \quad . \tag{5.16}$$

$\Omega_{\oplus}$ can be calculated from the duration of a sidereal day $T_{\oplus} = 86164.099\,\text{s}$ [135] to

$$\Omega_{\oplus} = \frac{2\pi}{T} = 7.2921151 \cdot 10^{-5}\ \frac{\text{rad}}{\text{s}} \quad . \tag{5.17}$$

The latitude of the MSR at the research center Jülich is $\Theta = 50.9035°$ [136] and the angle between the magnetic holding field and the north direction is approximately $\rho = 43°$, resulting in a constant rotation of the detector with $\omega_{\text{det}} = 3.36 \cdot 10^{-5}\,\text{rad/s}$. Therefore, the measured shift in the weighted frequency difference is

$$\begin{aligned} \Delta\omega_{\oplus} &= \omega_{\text{Xe}} + \omega_{\text{det}} - \frac{\gamma_{\text{Xe}}}{\gamma_{\text{He}}}(\omega_{\text{He}} + \omega_{\text{det}}) \\ &= \left(1 - \frac{\gamma_{\text{Xe}}}{\gamma_{\text{He}}}\right) \cdot\ \omega_{\text{det}} \\ &= 5.90 \cdot 10^{-5}\ \frac{\text{rad}}{\text{s}} \quad . \end{aligned} \tag{5.18}$$

The accuracy in the determination of ρ is approximately $\Delta\rho \approx 1°$, leading to an uncertainty in $\Delta\omega_{\oplus}$ of about $\delta\Delta\omega_{\oplus} \approx 0.10 \cdot 10^{-5}\,\text{rad/s}$, since the other values $\Omega_{\oplus}$, Θ and $\gamma_{\text{Xe}}/\gamma_{\text{He}}$ are known much more accurately. However, the fit model considers such a constant shift in the weighted frequency difference, or rather a linear shift in the weighted phase difference.

5.2.3. Shifts Induced by Magnetic Field Gradients

The influence of magnetic field gradients on the relaxation of the (longitudinal and transverse) magnetization where already discussed in section 2.3.2. Another important phenomenon induced by magnetic field gradients that has to be taken into account is a shift in the Larmor frequency [73, 137]. With static magnetic field gradients in addition

to the magnetic holding field B_0 pointing in z-direction, the resulting shift is given by

$$\delta\omega_{\mathrm{grad}} = R^2\gamma^3 B_0 \cdot \sum_n \frac{|\vec{\nabla}B_{1,\mathrm{x}}|^2 + |\vec{\nabla}B_{1,\mathrm{y}}|^2}{x_{1,\mathrm{n}}^2(x_{1,\mathrm{n}}^2-2)(\gamma^2B_0^2 + D^2x_{1,\mathrm{n}}^4R^{-4})} \tag{5.19}$$

where $x_{1,n}$ with $n = 1, 2, 3, ...$ are the zeros of the derivative of the spherical Bessel function $\frac{d}{dx}j_1(x_{1,n}) = 0$ and R is the radius of the spherical EDM cell. Oscillating magnetic field gradients can be neglected in first order calculations. Under experimental conditions of the measurements (cf. section 2.3.2.1, paragraph Gradient Relaxation) the equation simplifies to [73]

$$\delta\omega_{\mathrm{grad,He/Xe}} = \frac{R^2\gamma_{\mathrm{He/Xe}}}{10B_0} \cdot \left(|\vec{\nabla}B_{1,\mathrm{x}}|^2 + |\vec{\nabla}B_{1,\mathrm{y}}|^2\right) \tag{5.20}$$

and becomes independent of the pressure, or rather on the diffusion coefficient D. It is evident that in this approximation the particular frequency shifts of He and Xe drop out in the weighted frequency difference. However, the following paragraphs a) - c) present deterministic effects that also depend on magnetic field gradients. Especially if gradient changes are correlated with the electrical field reversal, or rather the EDM-function $h(t, T_a)$, this has to be thoroughly investigated.

a) Gravitational Shift

The motivation for comagnetometry is based on the principle that two nuclear spin polarized species, which precess in the same volume, experience the same magnetic field. A closer look reveals that this is not entirely true if it is taken into account that the centers of mass $\bar{z}$ of the particular species inside the containment is not identical due to a vertical pressure gradient. For a spherical volume with a radius R the equation

$$\bar{z} = \frac{\int_{-R}^{R} dz\; z\; p(z)\; (R^2 - z^2)}{\int_{-R}^{R} dz\; p(z)\; (R^2 - z^2)} \tag{5.21}$$

prevails. Assuming an isothermal atmosphere, the barometric formula leads to the pressure $p(z)$ at a height z (with respect to the center of the cell $z = 0 \rightarrow p_0$) and can be simplified to

$$p(z) = p_0 \cdot e^{\frac{-z}{H}} \tag{5.22}$$

by the component-specific scale height $H = \bar{R}TM^{-1}g^{-1}$. Here $\bar{R}$ is the ideal gas constant. The result is the difference between the center of the mass to the center of the container $z = 0$. In this case the molar masses are $M_{^3\mathrm{He}} = 3.016\,\mathrm{g/mol}$ and

$M_{^{129}\mathrm{Xe}} = 128.904\,\mathrm{g/mol}$ [138] and the temperature in the cell with $R = 5\,\mathrm{cm}$ is approximately at room temperature $T = 300\,\mathrm{K}$. The literature value of the molar gas constant is $\bar{R} = 8.314\,\mathrm{J/mol{\cdot}K}$ [53] and the conventional standard value of the gravitational acceleration on the surface of earth is $g = 9.81\,\mathrm{m/s^2}$. The resulting centers of mass $\bar{z}$ for ^{3}He and ^{129}Xe can now be calculated to $\bar{z}_{^{129}\mathrm{Xe}} = -2.51 \cdot 10^{-7}\,\mathrm{m}$ and $\bar{z}_{^{3}\mathrm{He}} = -0.06 \cdot 10^{-7}\,\mathrm{m}$. The center of mass difference $\Delta\bar{z}$ results in

$$\Delta\bar{z} = \bar{z}_{^{129}\mathrm{Xe}} - \bar{z}_{^{3}\mathrm{He}} = -2.45 \cdot 10^{-7}\,\mathrm{m} \quad . \tag{5.23}$$

Based on equation 2.45 the resulting shift of the weighted frequency difference due to the magnetic field gradients in z-direction is

$$\begin{aligned}
\Delta\tilde{\omega}_{\mathrm{grav}} &= \omega_{\mathrm{Xe}} - \frac{\gamma_{\mathrm{Xe}}}{\gamma_{\mathrm{He}}} \cdot \omega_{\mathrm{He}} \\
&= \gamma_{\mathrm{Xe}} \cdot B_0(\bar{z}_{^{129}\mathrm{Xe}}) - \frac{\gamma_{\mathrm{Xe}}}{\gamma_{\mathrm{He}}}\gamma_{\mathrm{He}} \cdot B_0(\bar{z}_{^{3}\mathrm{He}}) \\
&= \gamma_{\mathrm{Xe}} \cdot B_0(\bar{z}_{^{129}\mathrm{Xe}}) - \gamma_{\mathrm{Xe}} \left(B_0(\bar{z}_{^{129}\mathrm{Xe}}) + \frac{dB_0}{dz} \cdot \Delta\bar{z} \right) \\
&= \gamma_{\mathrm{Xe}} \cdot \frac{dB_0}{dz} \cdot \Delta\bar{z} \\
&\approx 2.7 \cdot 10^{-8}\,\frac{\mathrm{rad}}{\mathrm{s}}
\end{aligned} \tag{5.24}$$

with a conservative estimation of the gradients of $dB_0/dz \approx 15\ \mathrm{pT/cm}$ (cf. section 4.2.2). Here it is assumed that the field gradients are constant during a measurement. Otherwise we should observe $\Delta\tilde{\omega}_{\mathrm{grav}}(t)$ which could lead to non-deterministic phase shifts. In this case a false-EDM would arise if the change of the field gradients and the resulting phase shift is correlated with the electric field reversal, or rather the EDM-function $h(t, T_a)$. However, if the gradients are constant the resulting linear phase shift is considered in the fit-function.

b) Leakage Currents

A leakage current I_{leak} close to the EDM cell, that depends on the applied electric field $\vec{E}$ causes an additional magnetic field which results in a shift of the spin precession frequency of He and Xe. This shows the benefit of comagnetometry, where this additional contribution to the Hamiltonian drops out in the weighted frequency difference (cf. equation 2.45). Nevertheless, the associated gradients of this additional magnetic field lead to frequency shifts, regarding the difference in the centers of mass of the two gas species due to the previously mentioned gravitational shift. Since leakage currents and

the induced magnetic field gradients change direction when the electric field is reversed, the correlated shift of the weighted frequency difference $\Delta\omega_{\text{leak}}$ is indistinguishable from a real EDM-effect, due to the correlation with the EDM-function $h(t, T_a)$.
As mentioned in section 4.5 the leakage current between the electrodes as well as between the electrodes and the EDM casing is continuously monitored during an EDM measurement. Under experimental conditions ($U = \pm 4\,\text{kV}$ with the specified gas mixture) the leakage current is below $I_{\text{leak}} = 10\,\text{pA}$ in steady state. Charging currents are subject in the next paragraph. Let's assume a leakage current that goes between the electrodes on a straight way on the surface outside of the glass cell. Inside the cell, with a wall thickness of $d \approx 2\,\text{mm}$, the magnetic field can be estimated by means of the Biot-Savart law for a current-carrying conductor (first order approximation)

$$B_{\text{leak}}(r) = \mu_0 \cdot \frac{I_{\text{leak}}}{2\pi \cdot r} \quad . \tag{5.25}$$

With the distance $r \geq d$ from the current path, the magnetic field gradients due to the leakage current are

$$\nabla B_{\text{leak}} = \frac{dB_{\text{leak}}(r)}{dr} < 5.0 \cdot 10^{-3}\,\frac{\text{pT}}{\text{cm}} \quad . \tag{5.26}$$

If the current path were to draw an entire loop, the gradients would be in the same order. Considering the difference in the centers of mass $\Delta\bar{z} = -2.45 \cdot 10^{-7}\,\text{m}$ the resulting shift of the weighted frequency difference is about $\Delta\omega_{\text{leak}} < 9.1 \cdot 10^{-12}\,\text{rad/s}$ (cf. equation 5.24). In this case and with the experimental parameters the false-EDM can be (quite conservatively) estimated from equation 2.50 to $\Delta d_{\text{leak}} < 1.9 \cdot 10^{-30}\,e\text{cm}$. In addition to this an influence of these induced gradients on the transverse relaxation time T_2^* is insignificant, since the gradients of the magnetic holding field are much higher ($\nabla B_0 \approx 15\,\text{pT/cm}$). To quantify this systematic effect and its influence on the weighted frequency difference a large leakage current could be simulated by use of a non-magnetic wire with a defined current, wound around the EDM cell. Then the effect of a real, smaller leakage current could be determined.

c) Charging Currents

Currents during the charging of the electrodes generate a magnetic field. This magnetic field should be low because of two reasons: First, sudden high magnetic field could lead to a loss of the phase of the spins, with regard to the phase determination, section 5.1.1. Second, it could leave an imprint on the magnetic shielding or magnetize environmental components. The latter would have an EDM-like behavior since it is also correlated with the electric field reversal, or rather the EDM-function $h(t, T_a)$. The potential false EDM effect is investigated in this paragraph.

The setup of the electrodes can be treated as a plate capacitor in good approximation. With a diameter of $D = 11.5\,\mathrm{cm}$ and a distance between the electrodes of $d = 10\,\mathrm{cm}$ the plate capacitor has a capacitance of about

$$C = \varepsilon_0 \varepsilon_r \frac{A}{d} \approx 10^{-12}\,\mathrm{F} \tag{5.27}$$

with the area of an electrode $A = \pi \cdot D^2/4$, the vacuum permittivity $\varepsilon_0 = (\mu_0 \cdot c^2)^{-1}$ and the relative permittivity ε_r. The glass cell with the gas mixture between the electrodes, as well as the SF_6 atmosphere inside the casing are neglected ($\varepsilon_r = 1$) for this estimation. When ramping up the electrodes to a certain voltage U within a defined time t, the charging current is given by

$$I_c = C\,\frac{dU}{dt} \quad . \tag{5.28}$$

Hence, ramping a voltage of $U = \pm 4\,\mathrm{kV}$ with $dU/dt = 25\,\mathrm{V/s}$ results in a charging/displacement current of $I_c \approx 23\,\mathrm{pA}$. The magnetic field generated by the displacement current between the capacitor electrodes is

$$B_c(r \geq R) = \mu_0 \cdot \frac{I_c}{2\pi} \cdot \frac{1}{r} \tag{5.29}$$

and

$$B_c(r < R) = \mu_0 \cdot \frac{I_c}{2\pi} \cdot \frac{r}{R^2} \tag{5.30}$$

where $R = 5\,\mathrm{cm}$ is the cell's radius. Accordingly, the magnetic field due to the displacement current inside the EDM cell is

$$B_c(r < R) < \mu_0 \frac{I_c}{2\pi} \cdot \frac{1}{R} \approx 9.2 \cdot 10^{-8}\,\mathrm{nT} \quad . \tag{5.31}$$

The corresponding magnetic field gradients inside the cell are

$$\nabla B_c = \frac{dB_c(r < R)}{dr} \approx 1.8 \cdot 10^{-5}\,\frac{\mathrm{pT}}{\mathrm{cm}} \quad . \tag{5.32}$$

If a permanent and correlated[1] imprint of the magnetic field gradients generated by the charging current is considered (conservative evaluation), the effective shift of the weighted frequency difference is $\Delta\tilde{\omega}_c \approx 3.3 \cdot 10^{-14}\,\mathrm{rad/s}$, regarding the gravitational shift (cf. equation 5.24). According to equation 2.50 and with the experimental parameters, the induced false-EDM due to charging currents is $\Delta d_c \approx 6.7 \cdot 10^{-33}\,e\mathrm{cm}$.

[1] with the switching of the electric field

5.2.4. Ramsey-Bloch-Siegert Shift

If a nuclear spin sample is exposed to an off-resonant[2] oscillating magnetic field B_1 the Larmor frequency is shifted. This effect was first described by F. Bloch and A. Siegert [139] in the context of NMR experiments using the rotating wave approximation to quantify the transitions of a two-level system coupled to a linear polarized resonant RF-field. The generalization to any non-resonant field by N. Ramsey [140] is known as the Ramsey-Bloch-Siegert (RBS) shift

$$\delta\omega_{\mathrm{RBS}}(t) = \pm\left(\sqrt{\Delta\omega^2 + \gamma^2 B_1^2(t)} - \Delta\omega\right) \tag{5.33}$$

with $\Delta\omega = |\omega_{\mathrm{L}} - \omega_1|$. As before, $\omega_{\mathrm{L}} = \gamma B_0$ is the Larmor frequency and ω_1 is the frequency of the off-resonant field with the amplitude B_1. If $\omega_1/\omega_{\mathrm{L}} < 1$ the plus sign applies, whereas if $\omega_1/\omega_{\mathrm{L}} > 1$ the minus sign applies, as shown in figure 5.3.

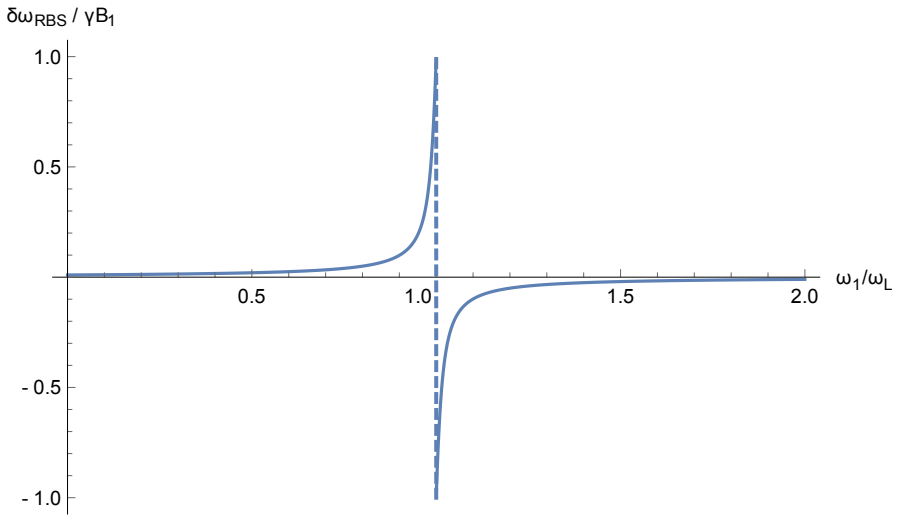

Figure 5.3.: Behavior of the RBS shift $\delta\omega_{\mathrm{RBS}}$ normalized to the driving field B_1. The dependency on the driving frequency ω_1 is normalized to the mean Larmor frequency ω_{L}. In this case γB_1 is set to 0.02 rad/s, which is reasonable, considering a magnetization of the spin sample in the order of $B_1 \approx 100\,\mathrm{pT}$ (cf. equation 4.7). For $\Delta\omega = |\omega_{\mathrm{L}} - \omega_1| = 0$ (vertical dashed line) the RBS shift vanishes.

The RF-field does not have to be necessarily irradiated from outside but can also stem from the precessing magnetization of the polarized spins themselves. In this case the amplitude B_1 of the RF-field amplitude is proportional to the signal amplitude (cf. equation 4.7) and therefore has to show an exponential behavior due to the relaxing polarization.

[2]Resonant irradiations (RF-pulses) are used to flip the magnetization, according to equation 2.22.

For the ^{3}He/^{129}Xe-comagnetometer two contributions can be identified. The first contribution is the effect of one species to the other and vice versa - ^{3}He $\longleftrightarrow$ ^{129}Xe - the so-called **cross-talk**. The second effect - the so-called **self-shift** - comes from the interaction of the precessing spin sample with its own field. This effect strongly depends on the geometry of the sample and the actual magnetic field gradients across the sample.

a) Cross-Talk

The cross-talk contribution describes the shift of the precession frequency of He due to the precessing magnetization of Xe and vice versa. The strength of the resulting B_1-field is much smaller than the magnetic holding field B_0. The B_1-field strength can be approximated by the magnetic field created by the nuclear spins of a spherical spin sample at its surface (cf. equation 4.7); $B_{1,\mathrm{He/Xe}} \approx 100\,\mathrm{pT} \ll 400\,\mathrm{nT} \approx B_0$. The Taylor expansion of equation 5.33 gives:

$$\begin{aligned}
\delta\omega_{\mathrm{RBS,ct}}(t) &= \pm\left(\sqrt{\Delta\omega^2 + \gamma^2 B_1^2(t)} - \Delta\omega\right) \\
&= \pm\left(\Delta\omega \cdot \sqrt{1 + \frac{\gamma^2 B_1^2(t)}{\Delta\omega^2}} - \Delta\omega\right) \\
&= \pm\left(\Delta\omega \cdot \left[1 + \frac{\gamma^2 B_1^2(t)}{2\Delta\omega^2} - \frac{\gamma^4 B_1^4(t)}{8\Delta\omega^4}\cdots\right] - \Delta\omega\right) \\
&\approx \pm\frac{\gamma^2 B_1^2(t)}{2\Delta\omega}, \qquad \text{for } \Delta\omega \gg \gamma B_1 \\
&= \pm\frac{\gamma^2 B_1^2(0)}{2\Delta\omega} \cdot e^{-\frac{2t}{T^*_{2,(1)}}} \quad .
\end{aligned} \tag{5.34}$$

Here $\Delta\omega = |\omega_{\mathrm{He/Xe}} - \omega_{\mathrm{Xe/He}}| \approx 2\pi \cdot 8\,\mathrm{Hz}$ and the different cases $\pm$ depend on the respective species that is under consideration:

i) + sign for He, because $\omega_1/\omega_\mathrm{L} < 1$

ii) − sign for Xe, because $\omega_1/\omega_\mathrm{L} > 1$

By integrating over time, the accumulated RBS-phases are

$$\begin{aligned}
\delta\Phi_{\mathrm{RBS,ct}}(t) &= \int_0^t \delta\omega_{\mathrm{RBS}}(t')dt' \\
&= const. \mp \frac{\gamma^2 B_1^2(0)}{2\Delta\omega} \cdot \frac{T^*_{2,(1)}}{2} \cdot e^{-\frac{2t}{T^*_{2,(1)}}}
\end{aligned} \tag{5.35}$$

where now + applies for Xe and − for He. The resulting deterministic phase shift of the weighted phase difference (cf. equation 2.45) induced by the cross-talk is

$$\begin{aligned}\Delta\Phi_{\mathrm{RBS,ct}}(t) &= \frac{\gamma_{\mathrm{Xe}}^2 B_{1,\mathrm{He}}^2(0)\cdot T_{2,\mathrm{He}}^*}{4\Delta\omega}\cdot e^{-\frac{2t}{T_{2,\mathrm{He}}^*}} + \frac{\gamma_{\mathrm{He}}\gamma_{\mathrm{Xe}} B_{1,\mathrm{Xe}}^2(0)\cdot T_{2,\mathrm{Xe}}^*}{4\Delta\omega}\cdot e^{-\frac{2t}{T_{2,\mathrm{Xe}}^*}} \\ &=: F_{\mathrm{Xe}}\cdot e^{-\frac{2t}{T_{2,\mathrm{He}}^*}} + F_{\mathrm{He}}\cdot e^{-\frac{2t}{T_{2,\mathrm{Xe}}^*}} \quad .\end{aligned} \tag{5.36}$$

The constant phase terms from equation 5.35 are not included to the exponential RBS contribution of the fit parameters $F_{\mathrm{He/Xe}}$ because the global fit-function takes them already into account by Φ_0 (cf. equation 5.11). An precise estimation of $F_{\mathrm{He/Xe}}$ is difficult, because the magnetic field inside the cell is not exactly known, mainly for geometric reasons.

b) Self-Shift

Now we consider the Larmor frequency of only one species. If all the spins are precessing coherently, the RBS shift vanishes because the peak values are $\pm\gamma B_1$ for $\Delta\omega = |\omega_{\mathrm{L}} - \omega_1| = 0$, as we can see in figure 5.3. Nevertheless, this is just the special case. In a real experiment, two effects contribute to the fact that the spins of one species see each other at all: Magnetic field gradients - in other words different magnetic fields in different inner-cell positions - are always distributed over the sample. Atoms in different spatial positions have therefore different Larmor frequencies. The resulting driving frequency ω_1 is much closer to the mean Larmor frequency ω_{L} than for the cross-talk. Considering an amplitude of $B_1 \approx 100\,\mathrm{pT}$ as before, then $\gamma_{\mathrm{He}} B_1 \approx 0.02\,\mathrm{rad/s}$.
Compared to the cross-talk dependency the Taylor expansion of $\delta\omega_{\mathrm{RBS,ss}}(t)$ is now

$$\begin{aligned}\delta\omega_{\mathrm{RBS,ss}}(t) &= \pm\left(\sqrt{\Delta\omega^2 + \gamma^2 B_1^2(t)} - \Delta\omega\right) \\ &= \pm\left(\gamma B_1(t)\cdot\sqrt{1 + \frac{\Delta\omega^2}{\gamma^2 B_1^2(t)}} - \Delta\omega\right) \\ &= \pm\left(\gamma B_1(t)\cdot\left[1 + \frac{\Delta\omega^2}{2\gamma^2 B_1^2(t)} - \frac{\Delta\omega^4}{8\gamma^4 B_1^4(t)} + \cdots\right] - \Delta\omega\right) \\ &\approx \pm\gamma B_1(t), \qquad \text{for } \Delta\omega \ll \gamma B_1 \\ &= \pm\gamma B_1(0)\cdot e^{-\frac{t}{T_2^*}} \quad .\end{aligned} \tag{5.37}$$

Again, the different cases ± correspond to:

i) + sign for He, because $\dfrac{\omega_1}{\omega_{\mathrm{L}}} < 1$

ii) − sign for Xe, because $\dfrac{\omega_1}{\omega_{\mathrm{L}}} > 1$

Certainly the approximation $\Delta\omega \ll \gamma B_1$ is not necessarily fulfilled. For example for strong gradients or low magnetizations (e.g. due to relaxation) can change the relation. Nonetheless, the deterministic phase shift in the weighted phase difference due to the self-shift can be expressed analogously to the cross-talk

$$\begin{aligned}\Delta\Phi_{\mathrm{RBS}}(t) \Bigg(&= \gamma_{\mathrm{Xe}} B_{1,\mathrm{Xe}}(0) \cdot T^*_{2,\mathrm{Xe}} \cdot e^{-\frac{t}{T^*_{2,\mathrm{Xe}}}} + \gamma_{\mathrm{Xe}} B_{1,\mathrm{He}}(0) \cdot T^*_{2,\mathrm{He}} \cdot e^{-\frac{t}{T^*_{2,\mathrm{He}}}} \Bigg) \\ &=: E_{\mathrm{Xe}} \cdot e^{-\frac{t}{T^*_{2,\mathrm{Xe}}}} + E_{\mathrm{He}} \cdot e^{-\frac{t}{T^*_{2,\mathrm{He}}}} \quad .\end{aligned} \tag{5.38}$$

Note that the term in brackets is only valid for the strict approximation of equation 5.37. An exact prediction of the fit parameters E is not possible because the experimental conditions mainly the (distribution of the) gradients can not be determined with the required precision, since the volume containing the spins is not a perfect sphere. The appendix and the not absolutely exact spherical shape lead to additional magnetization effects, regarding B_1. Hence, the shift is strongly depending on the complexion of the gradients (non-linear higher order gradients) and the diffusion of the gas inside the cell. An illustration of the RBS shift is shown in the summary of the chapter in figure 5.4.

To conclude, RBS contributions are not expected to contribute to a false EDM. Unfortunately it is not possible to predict the particular parameters $E_{\mathrm{Xe,He}}$ and $F_{\mathrm{Xe,He}}$, which is why they have to be set as free fit parameters. Furthermore, it has to be ensured, that the value of T_2^* is determined adequately, to describe the time dependency of the signal amplitudes as good as possible. Otherwise, a non-statistical behavior of the phase residuals may occur as a result of the global fit.

5.2.5. Motional Magnetic Field

A particle moving in a static electric field $\vec{E}$ with a velocity $\vec{v}_{\mathrm{m}}$ sees a magnetic field $\vec{B}_{\mathrm{m}}$ in its moving frame

$$\vec{B}_{\mathrm{m}} = \frac{1}{c} \cdot \vec{v}_{\mathrm{m}} \times \vec{E} \quad . \tag{5.39}$$

Due to the collisions of the gas atoms with each other and with the wall, the motional magnetic field is randomly fluctuating. Considering a small angle Θ_{EB} between the electric field $\vec{E}$ and the magnetic holding field $\vec{B}_0$, the resulting effective magnetic field in the particles inertial reference frame is

$$\vec{B} = \vec{B}_0 + \Theta_{\mathrm{EB}} \vec{B}_{\mathrm{m}} + \frac{1}{2} \frac{\vec{B}^2_{\mathrm{m}}}{\vec{B}_0} \quad , \tag{5.40}$$

which leads directly to a shift in the Larmor frequency [141]. Since this shift is correlated to the alignment of the electric field it mimics the same structure as an actual EDM would show (false-EDM). The respective contributions of $\vec{B}_{\mathrm{m}}$ are examined below.

a) linear term

The angle between the mean electric and magnetic field can be estimated to about $\Theta_{\mathrm{EB}} \approx 1 - 2°$. Because the electric field is not perfectly homogeneous (cf. section 3.1.4.1) the angle has to be assumed slightly larger ($\Theta_{\mathrm{EB}} < 5°$). The mean velocity $\langle v_{\mathrm{m}} \rangle$ of the hyperpolarized gases inside the spherical cell can be assumed to be zero because there is no preferred direction of the diffusing atoms - in contrast to beam or beam-like experiments, e.g. [50]. Furthermore, spin diffusion inside the cell due to relaxing hot spots (e.g. ferromagnetic impurities in the bulk material of the glass cell) can be neglected. Therefore the particles velocity is root mean square (RMS) speed $v_{\mathrm{m}} = v_{\mathrm{RMS}}$. As a result, the linear term in equation 5.40 does not contribute to a deterministic phase shift and therefore does not generate a false-EDM.

b) quadratic term

In contrast to the linear term, the quadratic dependency $B_m^2 \propto v_{\mathrm{m}}^2 E^2$ is independent on the angle between the electric and the magnetic holding field. However, this contribution does not average to zero due to the square dependency with the RMS speed $\left\langle v_{\mathrm{m}}^2 \right\rangle = \left\langle v_{\mathrm{RMS}}^2 \right\rangle$. Therefore, the corresponding shift of the weighted frequency difference is correlated with the switching of the electric field (with the EDM-function $h(t, T_a)$).
The following calculation steps are used to determine the mean free paths of He and Xe to finally calculate the resulting shift due to this effect in equation 5.46: The mean free path of a species m diffusing in a gas mixture with N different species i is [142]

$$\lambda_{m,i} = \left[\sum_{i=1}^{N} \frac{n_i \sigma_{m,i}^2}{\pi} \sqrt{1 + \frac{M_1}{M_i}} \right]^{-1} \tag{5.41}$$

with the number density n_i of the species i

$$n_i = \frac{p_i}{kT} \tag{5.42}$$

which depends on the particular partial pressure p_i and the temperature T.

Additionally the mean free path depends on the molar mass M_i of the species i and the scattering cross section

$$\sigma_{m,i} = \frac{\pi}{2}(d_m + d_i) \quad . \tag{5.43}$$

The kinetic diameter d_i of the species i is an indication of the size of the particle as a collision partner. In table 5.1 you can find an overview of the values for ^{3}He, ^{129}Xe and for the buffer gases ^{4}He, CO_2, N_2 and SF_6:

species	kinetic diameter d_i	molar mass M_i
^{3}He	260 pm [143]	3.02 g/mol [138]
^{129}Xe	396 pm [144]	128.90 g/mol [138]
^{4}He	260 pm [145]	4.00 g/mol [145]
CO_2	330 pm [146]	44.01 g/mol [146]
N_2	364 pm [146]	28.01 g/mol [146]
SF_6	606 pm [144]	146.05 g/mol [144]

Table 5.1.: Comparison of the kinetic diameters d_i and molar masses M_i of the relevant species i in our Xe-EDM experiment.

The RMS speed depends on the temperature T according to the Maxwell-Boltzmann distribution:

$$v_{\mathrm{RMS},i} = \sqrt{\frac{3RT}{M_i}} \tag{5.44}$$

with the ideal gas constant R and the molar mass M. The correlation time $\tau_{\mathrm{c},i} = \lambda_{m,i}/v_{\mathrm{RMS},i}$ quantifies the mean free time between collisions of the particles. The calculated parameters are listed below in table 5.2 for a temperature of $T = 300K$.

species	mean free path $\lambda_{m,i}$	RMS speed $v_{\mathrm{RMS},i}$	correlation time $\tau_{\mathrm{c},i}$
^{3}He	5.5 μm	1575.2 m/s	3.5 ns
^{129}Xe	1.2 μm	240.9 m/s	5.0 ns

Table 5.2.: Calculated values of the mean free paths λ_i, the RMS speeds $v_{\mathrm{RMS},i}$ and the correlation times $\tau_{\mathrm{c},i}$ of ^{3}He and ^{129}Xe in a gas mixture without buffer gases and a partial pressure $p_i = 10$ mbar of each species i at a temperature $T = 300$ K

The values of the mean free path are calculated for a He and Xe gas mixture without buffer gases and with partial pressure of $p = 10$ mbar, each. This is a conservative lower estimation of the partial pressures. In general the experimental values are consistently larger, cf. chapter 6. For the following calculations, this gives a conservative upper

estimation of respective deterministic effects.
With $\omega_{\mathrm{L}}\tau_{\mathrm{c}} \ll 1$ - which is the case for our experimental conditions - the additional frequency shift gets [141]

$$\delta\omega_{\mathrm{m}} = \frac{(2\pi)^2}{6} \cdot \left(\frac{\gamma}{c^2} v_{\mathrm{RMS}} E\right)^2 \omega_{\mathrm{L}}\tau_{\mathrm{c}} \quad . \tag{5.45}$$

The resulting linear shift of the weighted frequency difference due to the quadratic term with an electric field of $E = 800\,\mathrm{V/cm}$ and a magnetic holding field of about $B_0 \approx 400\,\mathrm{nT}$ is approximately

$$\begin{aligned} \Delta\omega_{\mathrm{m}} &= \delta\omega_{\mathrm{m,Xe}} - \frac{\gamma_{\mathrm{Xe}}}{\gamma_{\mathrm{He}}} \cdot \delta\omega_{\mathrm{m,He}} \\ &\approx 1.9 \cdot 10^{-16}\,\frac{\mathrm{rad}}{\mathrm{s}} \quad . \end{aligned} \tag{5.46}$$

However, this effect only results in a false-EDM if it is correlated with the switching of the electric field. This is only the case if the amplitude of the electrical field changes during switching. The reversal of the high voltage is performed with an accuracy of $\Delta U \approx \pm 1\,\mathrm{V}$ (cf. section 4.5), which means $\Delta E = \Delta U/d \approx \pm 0.1\,\mathrm{V/cm}$ for the given distance between the electrodes of $d = 10\,\mathrm{cm}$. Substituting E with ΔE in equation 5.45 results in a correlated shift of the weighted frequency difference of

$$\begin{aligned} \Delta\tilde{\omega}_{\mathrm{m}} &= \Delta\omega_{\mathrm{m}} \cdot \frac{(\Delta E)^2}{E^2} \\ &\approx 3.0 \cdot 10^{-24}\,\frac{\mathrm{rad}}{\mathrm{s}} \quad . \end{aligned} \tag{5.47}$$

According to equation 2.50 the false-EDM from this effect is $\Delta d_{\mathrm{m}} \approx 6.2 \cdot 10^{-43}\,e\mathrm{cm}$. Because $\delta\omega_{\mathrm{m}} \propto \tau_{\mathrm{c}}^2 \propto \lambda^2 \propto p^2$ this is a sufficient upper estimation of this systematic effect.

c) Geometric phases:

Another deterministic effect comes from the motion of the particles in a not completely uniform magnetic field. In the frame of any particle a magnetic field gradient looks like a moving magnetic field. As a result the spin precession can have additional so-called geometric phases.
Assuming a cylindrical cell with radius R and its cylindrical axis in z-direction, the RMS speed of the particles in the xy-plane is $v_{\mathrm{xy}} = \sqrt{2/3} \cdot v_{\mathrm{RMS}}$. Under consideration of a

uniform particle distribution in the cell and isotropic velocities, it was shown in [147] that the resulting angular speed ω_r of the additional moving magnetic field B_{xy} is

$$\omega_r^2 = 0.65 \cdot \left(\frac{v_{\mathrm{xy}}}{R}\right)^2 \quad . \tag{5.48}$$

in an approximation where the pressure is assumed to be zero. In this approximation there are no collisions of particles with each other, only reflections from the wall of the cylindrical cell. With magnetic field gradients in z-direction $\partial B_{0,z}/\partial z$ and the electric field E, this results in a shift of the precession frequency for each species of [147]

$$\delta\tilde{\omega}_{\mathrm{geo}} = \frac{1}{2} E \left(\frac{\partial B_{0,z}}{\partial z}\right) \frac{\gamma^2 R^2}{c^2} \left[1 - \frac{\omega_0^2}{\omega_r^2}\right]^{-1} \quad . \tag{5.49}$$

Since this equation is independent on the height of the cylinder it is a proper upper estimation for a spherical cell with radius R. As we work with a finite pressure, this shift is additionally suppressed by the factor [147]

$$S = \left[1 + \left(\frac{4R^2\omega_0}{2\pi v_{\mathrm{xy}} \lambda_{m,i}}\right)^2\right]^{-1} \quad . \tag{5.50}$$

Here, $\lambda_{m,i}$ is again the mean free path of a species m in a gas mixture with additional species i, cf. equation 5.41. With $\delta\omega_{\mathrm{geo}} = S \cdot \delta\tilde{\omega}_{\mathrm{geo}}$, a magnetic holding field of $B_0 = 400\,\mathrm{nT}$, magnetic field gradients of $\partial B_{0,z}/\partial z \approx 15\,\mathrm{pT/cm}$, and the cell radius $R = 5\,\mathrm{cm}$ the resulting shift of the weighted frequency difference is

$$\begin{aligned} \Delta\omega_{\mathrm{geo}} &= \delta\omega_{\mathrm{geo,Xe}} - \frac{\gamma_{\mathrm{Xe}}}{\gamma_{\mathrm{He}}} \cdot \delta\omega_{\mathrm{geo,He}} \\ &\approx -7.5 \cdot 10^{-11}\,\frac{\mathrm{rad}}{\mathrm{s}} \quad . \end{aligned} \tag{5.51}$$

The negative sign indicates that the individual effect is stronger for ^{3}He. This is easy to understand because the suppression for helium is much smaller than for xenon; in the particular case $S_{\mathrm{Xe}} \approx 120 \cdot S_{\mathrm{He}}$. To further suppress this value, higher pressures and buffer gases are used in the EDM experiment. Because of the pressure dependency (of λ and therefore of S), the true values of the false-EDM are actually much smaller.
Nevertheless, a proper upper estimation of the false-EDM from the geometric phase effect is $\Delta d_{\mathrm{geo}} \approx -1.5 \cdot 10^{-29}\,e\mathrm{cm}$, according to equation 2.50.

5.2.6. Summary

The following table 5.3 summarizes the deterministic shifts of the weighted frequency difference $\Delta\omega$ which were investigated in this chapter. It is indicated if the particular shift is covered by the fit function. Associated false-EDM contributions Δd are calculated with equation 2.50 taking an electric field of $E = 800\,\mathrm{V/cm}$.

origin		equation	fit	shift of $\Delta\omega$	false-EDM Δd
chemical shift			✓	$\sim$	–
earth rotation		5.18	✓	$5.9 \cdot 10^{-5}\,\mathrm{rad/s}$	–
constant magnetic field gradients			✓	–	–
gravitational shift ($\Delta B_{\mathrm{const}}$)		5.24	✓	$5.4 \cdot 10^{-8}\,\mathrm{rad/s}$	–
leakage current		5.26	×	$9.1 \cdot 10^{-12}\,\mathrm{rad/s}$	$1.9 \cdot 10^{-30}\,e\mathrm{cm}$
charging current		5.32	×	$3.3 \cdot 10^{-14}\,\mathrm{rad/s}$	$6.7 \cdot 10^{-33}\,e\mathrm{cm}$
RBS shift			✓	$\sim$	–
motional magnetic field B_{m}			✓	–	–
mot. magnetic field B_{m}^2	uncorr.	5.46	✓	$1.9 \cdot 10^{-16}\,\mathrm{rad/s}$	–
	corr.	5.47	×	$3.0 \cdot 10^{-24}\,\mathrm{rad/s}$	$6.2 \cdot 10^{-43}\,e\mathrm{cm}$
geometric phase		5.51	×	$7.5 \cdot 10^{-11}\,\mathrm{rad/s}$	$1.5 \cdot 10^{-29}\,e\mathrm{cm}$

Table 5.3.: Overview of deterministic shifts of the weighted frequency difference and false-EDMs. The contributions of the chemical shift and the RBS shift vary for each measurement because of the strong dependency on the particular pressures, the signals and the magnetic field gradients. The calculated false-EDM contributions are conservative upper estimations.

Please note that these considerations are preliminary checks of expectable systematic effects. As a matter of fact, the individual measurements have to be evaluated carefully to find possible deviations. Only if the fit model takes all deterministic phase and frequency shifts into account, it is plausible to evaluate EDM contributions. Problems can arise if our model for describing deterministic phases in the fit function does not cover all observable phase shifts. This concerns in particular any kind of magnetic field related effects like (changing) magnetic field gradients. The discussion of the measurement results in the following chapter 6 reveals exactly such kinds of issues.

A suitable check for systematic effects can be performed by studying the residuals of the weighted phase difference after applying the fit model, including the expected deterministic contributions. Deviations from a statistical distribution around zero indicate unconsidered effects. Furthermore, this is also reflected in the Allan-Standard-Deviation (ASD) of the phase residuals, as it is explained in section 2.4.2.
To visualize the importance of a proper fit of the measurement data, the following figure shows two plots of the weighted phase difference residuals. On the left side only linear phase drifts of equation 5.11 were included in the fit model. On the right side, the whole fit model - including the RBS terms - was applied. The plot on the left side shows a parabolic shape of the phase residuals which is caused by the RBS shift.

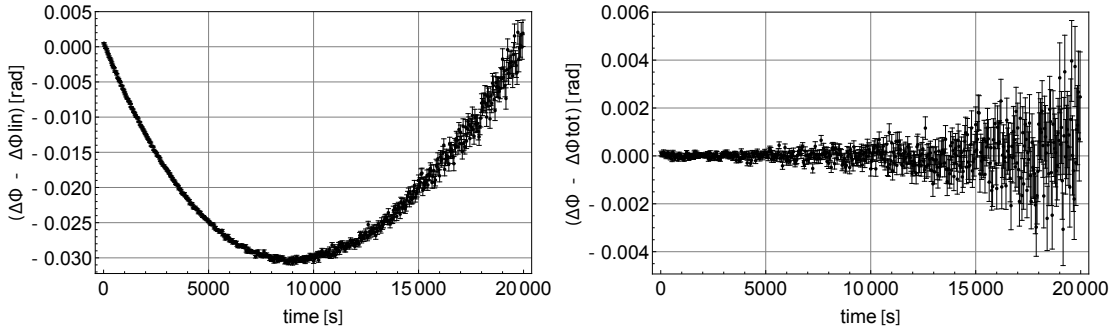

Figure 5.4.: Comparison of the residuals of the weighted phase difference (data of measurement run #2 of July 2017). The plot on the left side shows the residuals after subtracting only the linear contributions $\Delta\Phi_{\mathrm{lin}}$ of equation 5.11. The parabolic shape is a result from the RBS shift. The plot on the right side shows the phase residuals after including all deterministic phase drifts $\Delta\Phi_{\mathrm{tot}}$. The residuals are now statistically distributed around zero; all deterministic drifts are taken into account, at least up to the achieved sensitivity of this measurement run. The increase of the residual phase noise $\sigma_{\Phi,\mathrm{res}}$ over time is mainly due to the exponential decay of the Xe signal amplitude $\left(T^*_{2,\mathrm{Xe}} < T^*_{2,\mathrm{He}}\right)$ during data acquisition $\sigma_{\Phi,\mathrm{res}}(t) \propto \exp\left(t/T^*_{2,\mathrm{Xe}}\right)$ [95].

6

Analysis & Preliminary Results

In this chapter the preliminary results of two measurement campaigns in March 2017 and July 2017 are presented. During each campaign, several measurement runs were performed. These runs are analyzed in the subsequent sections 6.1 and 6.2 with the following approach:

First, the experimental conditions during the measurement campaign are briefly outlined, referring to the procedures described in chapter 4. Thereby the determining factors, such as the signal amplitudes and the relaxation times of the individual runs, are presented and interpreted, with regard to the applied gas mixtures.
Afterwards the particular measurement data is analyzed, regarding the statistical behavior of the weighted phase difference residuals (subsequently short: phase residuals). Run #4 of the campaign in March 2017 shows non-statistical effects and is exemplary analyzed further on.
The quality of the phase residuals of the individual measurement runs with regard to the statistical nature of the phase noise was used as a selection criterion for our final Xe-EDM analysis.

The evaluated plots of the phase residuals as well as the corresponding Allan Standard Deviation plots are moved to the appendix A.2 to give a detailed overview of the data analysis. Specially selected plots are presented in the following text.

6.1. March 2017

In this section, the EDM measurements from March 2017 are presented. These measurements were performed with the setup and procedure, as introduced in chapter 3 and 4. Four EDM runs were performed in total. The applied gas mixture is composed of hyperpolarized ^{3}He and ^{129}Xe, as well as CO_2 and SF_6 as buffer gases. This measurement

campaign was performed before an optimal buffer gas mixture was found. Details of this optimization can be found in appendix A.3. The following table 6.1 gives an overview of the individual runs with the particular partial pressures.

EDM run	$p_{^3\mathrm{He}}$ [mbar]	$p_{^{129}\mathrm{Xe}}$ [mbar]	$p_{\mathrm{CO_2}}$ [mbar]	$p_{\mathrm{SF_6}}$ [mbar]
#1 @ 03-28-2017 14:19	38	20	20	5
#2 @ 03-28-2017 20:22	22	18	20	3
#3 @ 03-29-2017 18:33	12	42	21	3
#4 @ 03-30-2017 15:00	70	36	36	0

Table 6.1.: Overview of the four EDM runs in March 2017, regarding the gas mixture inside the spherical EDM cell. The listed partial pressures are known with an uncertainty of about $\Delta p = \pm 1\,\mathrm{mbar}$.

The high voltage is set to $U = \pm 4\,\mathrm{kV}$, resulting in an electric field of $E = 800\mathrm{V/cm}$. For all runs the initial polarity HV_0 of the high voltage was set to have the electric parallel aligned to the magnetic field, $\vec{E} \parallel \vec{B}_0$. The switching period of the high voltage is set to $T_a = 12.000\,\mathrm{s}$ for all of the runs. The exact procedure for applying the high voltage and reversing its polarity is described in the appendix A.1. The determining factors of each run, such as the initial signal amplitudes $A(t = 0)$, the relaxation times T_2^* for both hyperpolarized species, and the total measurement time T are listed in table 6.2.

EDM run	$A_{^3\mathrm{He}}$ [pT]	$A_{^{129}\mathrm{Xe}}$ [pT]	$T^*_{2,\mathrm{He}}$ [h]	$T^*_{2,\mathrm{Xe}}$ [h]	T [s]	T_a [s]	HV_0 [kV]
#1	18	12	3.0	1.8	20044	12000	+/– 4
#2	6	9	4.4	2.4	38564	12000	+/– 4
#3	12	20	3.7	1.7	36396	12000	+/– 4
#4	18	24	2.5	1.7	16172	12000	+/– 4

Table 6.2.: Overview of the four EDM runs in March 2017, regarding the experimental parameters. The achievable T_2^* relaxation times vary between the individual runs, as well as the particular signal amplitudes A of helium and xenon at the start of the spin precession.

An essential characteristic of these measurements is the extraordinarily small signal amplitude, especially of He. Before this measurement campaign, values of the signal-per-pressure ratio of $A_{\mathrm{He}}/p_{\mathrm{He}} = 6.6\,\mathrm{pT/mbar}$ and $A_{\mathrm{Xe}}/p_{\mathrm{Xe}} = 1.2\,\mathrm{pT/mbar}$ were usually achieved, as stated in section 4.4. The values of these measurements vary between 0.3 and 1.0 pT/mbar for He and 0.5 and 0.7 pT/mbar for Xe. The reason for the modest He signal

was found to be caused by unforeseen short relaxation times T_1 of the helium transport and storage cell. Since the He-polarizer is located in Mainz the obvious polarization losses during transport and storage could not be solved during this measurement campaign. After this campaign, a leak was found at the buffer cell of the polarizer, which caused this issue. Concerning the Xe-polarizer, the optical pumping cell was exchanged[1] shortly before the March 2017 campaign. Apparently, the quality of the new cell was not as good as the previous one. All in all, one had to be satisfied with this situation for this campaign.
The differences of the total measurement time T have various reasons. Usually, the runtime of a measurement is aimed to be $T = 3 \cdot T^*_{2,\mathrm{Xe}}$ (cf. section 2.4.2), which is the case for run #1. If a run lasts longer (run #2 and #3), the measurement runs overnight without interruption. Reasons to end a run (or cut the raw data) earlier can be, for instance, external effects like strong noise enhancement, sudden magnetic field changes, or dwindling liquid helium in the cryostat.

Before globally fitting the data, it is reasonable to first check the resulting phase residuals without the EDM-function $g \cdot h(t, T_a)$ of equation 5.11:

$$\begin{aligned}\Delta\Phi_{\mathrm{fit}}(t) = \Phi_0 + \Delta\omega_{\mathrm{lin}} \cdot t + E_{\mathrm{He}} \cdot e^{\frac{-t}{T^*_{2,\mathrm{He}}}} + E_{\mathrm{Xe}} \cdot e^{\frac{-t}{T^*_{2,\mathrm{Xe}}}} \\ + F_{\mathrm{He}} \cdot e^{\frac{-2t}{T^*_{2,\mathrm{Xe}}}} + F_{\mathrm{Xe}} \cdot e^{\frac{-2t}{T^*_{2,\mathrm{He}}}} \cancel{+ g \cdot h(t, T_a)} \quad .\end{aligned} \tag{6.1}$$

Obvious temporal correlations between the EDM-function $h(t, T_a)$ and the time structure of the phase residuals would be an indicator for either an EDM or systematic contributions. Plots of the phase residuals are put together in the appendix A.2 in figure A.2. The red triangular EDM-function with arbitrary units for g is superimposed on the black data points. A check of the statistical nature of the residual phase noise is provided by the calculated Allan Standard Deviation (ASD) plots in figure A.3. As mentioned in section 2.4.2, if the phase noise is purely statistical, the ASD sensitivity follows the CRLB power law $\sigma_\Phi(\tau) \propto \tau^{-1/2}$.
The following figure 6.1 shows exemplary the fit result of a dataset (run #2) which shows a statistical distribution of the phase residuals around zero for all integration times τ. Accordingly, the corresponding ASD shows the $\propto \tau^{-1/2}$ behavior. In contrast to this, run #4 shows a non-statistical behavior of the phase residuals. The corresponding ASD deviates from the statistical behavior for $\tau > 100\,\mathrm{s}$, which indicates phase drifts that are not covered by the fit function (equation 6.1).

[1] The rubidium used for the spin exchange inside the optical pumping cell must be replaced from time to time due to oxidation.

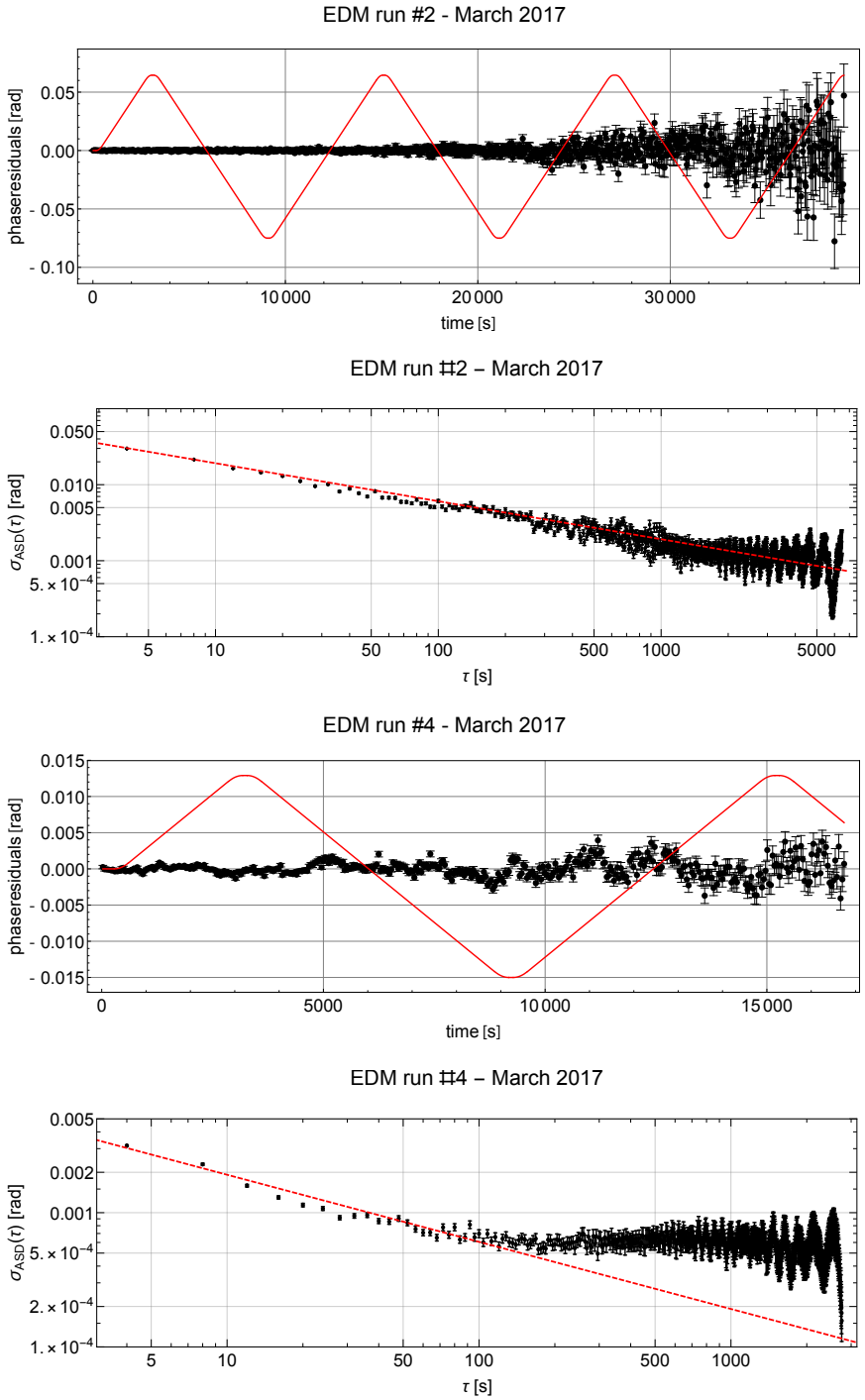

Figure 6.1.: Residuals of the weighted phase difference and ASD plots of the runs #2 and #4 of March 2017. The residuals of run #2 are statistically distributed around zero for all integration times as we can tell from the $\tau^{-1/2}$-behavior of the corresponding ASD plot ($\tau^{-1/2}$-slope: superimposed dashed red line). False-EDM structures in the phase residuals should be correlated to the triangular wave EDM-function (red, superimposed to the data with arbitrary units). Run #4 shows discrepancies from this statistical behavior.

The distribution of the phase residuals of the first three runs shows the expected statistical behavior of the phase noise around zero, more prominently evident in the respective ASD plots. By all appearances there are no correlations to the EDM function.
A close look at the distribution of the phase residuals of run #4 reveals some considerable variances, in comparison to the previous runs $\#1 - 3$. An actual correlation to the EDM-function is not evident (by eye). The evaluation of the phase residuals and the corresponding ASD plots including the EDM-function in the fit in figure A.4 show nearly the same structure. The residual phase noise is still non-statistically distributed. Accordingly, this measurement cannot be evaluated with the given fit routine in terms of an EDM due to the systematic effects that are not taken into account.

6.1.1. Considerations regarding the Observed Residual Phase Noise

A solution, as the ASD plot of run #4 in figure 6.1 would suggest, would be to subdivide the run in short data sets of about 100 s. For integration times $\tau < 100\,\mathrm{s}$ the residuals are statistically distributed. The problem, however, is that the predefined switching sequence (T_a) of the field polarity was much longer than 100 s. If only the short data sets were analyzed, the EDM-function for this short period would be essentially linear (not triangular) and it would be highly correlated, or rather indistinguishable from the linear deterministic shifts of the weighted phase difference that are taken into account in the fit function (cf. equation 5.11). To avoid this problem, the field polarity could be changed much more frequently. However, a statistical analysis shows that this would drastically reduce our EDM measurement sensitivity. A simple example:
Let T_m be the total measurement time of coherent spin precession. The EDM sensitivity scales according to the CRLB (equation 2.54) $\sigma_\omega \propto T_m^{-3/2}$. If we divide the data into n data sets, each with a measurement time of $T = T_m/n$, the total EDM sensitivity is

$$\sigma_\omega \propto \frac{T^{-3/2}}{\sqrt{n}} = \frac{T_m^{-3/2}}{\sqrt{n}} \cdot n^{3/2} = T_m^{-3/2} \cdot n = T_m^{-3/2} \cdot \frac{T_m}{T} \quad . \tag{6.2}$$

In other words, if we take $T = 100\,\mathrm{s}$ for the sets of the data with a total measurement time of $T_m \approx 16000\,\mathrm{s}$, the EDM sensitivity is impaired by a factor 160. Furthermore, the effective measurement time of each data set would be additionally reduced due to the dead time of the electric field reversal.

In the following it will be analyzed, where the disturbances during run #4 could stem from. For this it is useful to analyze the time courses of the Larmor frequency of ^{3}He (and ^{129}Xe) in figure 6.2 which indicate the time course of the absolute magnetic field during the runs #4 and #2.

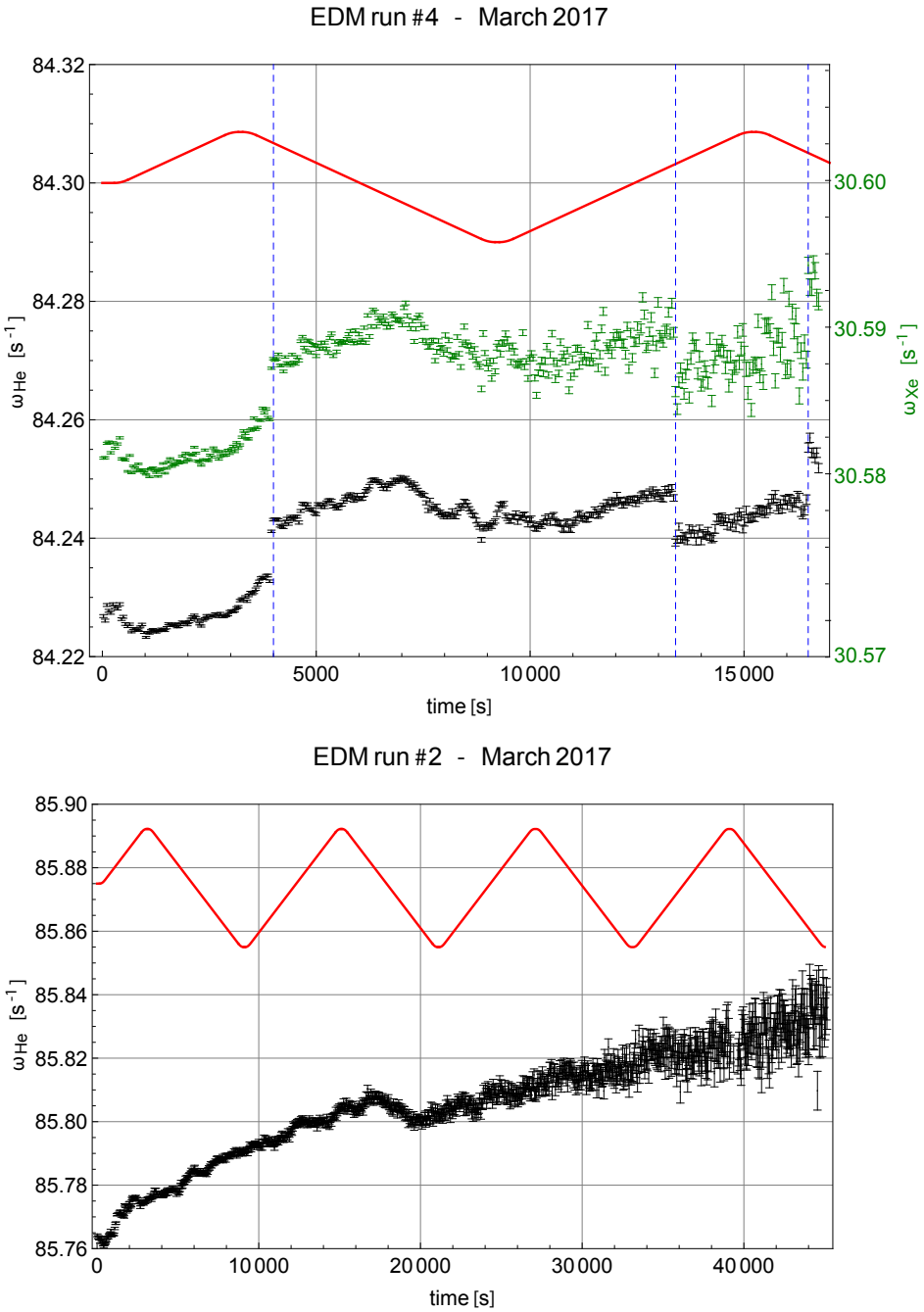

Figure 6.2.: Comparison of the Larmor frequencies of run #4 and #2 in March 2017. The determined frequencies (He: black data points, Xe: green data points) are plotted together with the EDM-function (red, arbitrary units). The dashed blue lines mark jumps of the frequency - related to magnetic field jumps - during the measurement. In run #4, such jumps at $t \approx 4000\,\mathrm{s}$, $t \approx 13300\,\mathrm{s}$, and $t \approx 16500\,\mathrm{s}$ are clearly evident, for He as well as for Xe. Please note the different plot ranges, especially the higher uncertainties in run #2. In plot of run #2 the data of Xe has been excluded for clarity reasons. In both runs there are no major structures that are apparently correlated with the switching of the electric field.

The dashed blue lines indicate major magnetic field changes. In run #4 three jumps of the frequency/field are evident at $t \approx 4000\,\mathrm{s}$, $t \approx 13300\,\mathrm{s}$ and $t \approx 16500\,\mathrm{s}$, for He as well as for Xe. For instance, the He-frequency change of the first jump is $\Delta\omega_{\mathrm{He}} \approx (84.244 - 84.234)\,\mathrm{rad/s} = 10\,\mathrm{mrad/s}$. This is equivalent to a jump of the absolute magnetic field of $\Delta B_0 \approx 50\,\mathrm{pT}$ with a mean magnetic field of $B_0 \approx 400\,\mathrm{nT}$, according to equation 2.5. Furthermore, a strong drift of the magnetic field is noticeable between $t \approx 7000\,\mathrm{s}$ and $8000\,\mathrm{s}$. A similar drift is evident in the frequency plot of run #2. It is standing to reason that these instabilities lead to the non-statistical fluctuations of the phase residuals of run #4. Due to comagnetometry magnetic field changes (even jumps) should not be a problem at all (at least to higher order). However, an indirect effect associated with field changes, i. e. changes in field gradients, has a strong influence on the phase residuals. It is necessary to have a deeper look into the correlated effects:

1) regarding the Ramsey-Bloch-Siegert shift:
Since the RBS contributions are depending on T_2^*, it is reasonable to determine this value sufficiently well. If the gradients do not change drastically during a measurement, it is possible to set T_2^* as constant. If the decay of the signal amplitudes is not well described by a constant T_2^*, it has to be interpolated and treated as time dependent $T_2^*(t)$ in the fit with equation 6.1. For comparison, the residual signal amplitudes of ^{3}He of run #4 (after subtracting the fitted exponential decay) and #2 are plotted in figure 6.3. The red data shows the amplitude residuals of He of run #4 with a constant T_2^* fit. For the same run, the green data corresponds to a fit with a time depending $T_2^*(t)$. The blue data shows the results of run #2 with a constant T_2^*. The phase noise of run #4 with a fit that takes into account the interpolated amplitudes is shown in figure 6.4.

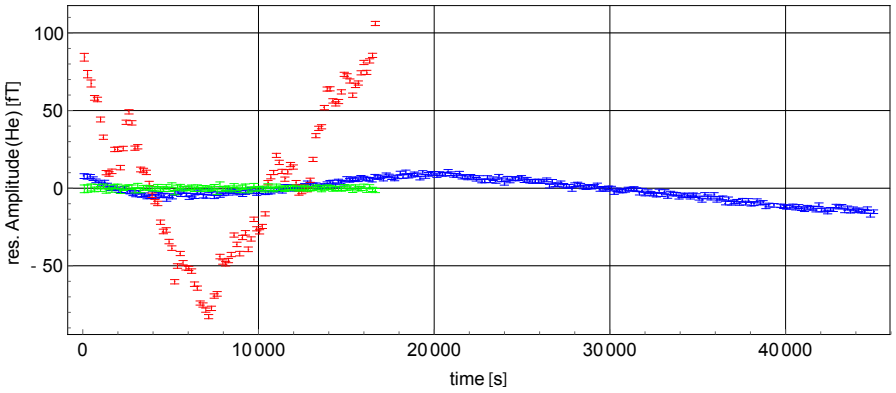

Figure 6.3.: Comparison of the residual ^{3}He signal amplitudes of run #4 and #2. The data points of run #4 are the results of a fit with a constant (red) and a time depending (green) T_2^*. The exponential decay of run #2 is fitted with a constant T_2^* (blue). This fit of run #2 is significantly better than the corresponding (constant) fit of run #4.

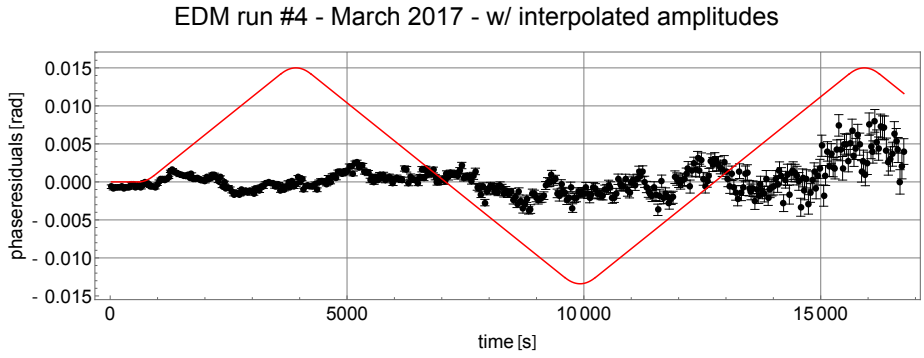

Figure 6.4.: The residuals of the weighted phase difference of run #4 of March 2017 in consideration of a time depending $T_2^*(t)$ of He and Xe in the RBS contribution of the fit function 6.1. There is no significant improvement compared to the fit residuals with constant T_2^* (cf. figure 6.1). The EDM-function (red) is shown again in arbitrary units.

Figure 6.3 shows clearly that the amplitudes of the He-signal of run #4 can be described much better with a time depending $T_2^*(t)$. Since the residuals are even better than of run #2 with a constant T_2^*, it can be assumed that the global fit, i.e. the time dependence of the RBS is sufficiently improved. However, despite the more accurate determination of the time dependence of the RBS shift by the improved fit function, the resulting distribution of the weighted phase residuals did not improve much; the non-statistical fluctuations of the phase noise are still evident as it can be deduced from the corresponding plot in figure 6.4. Actually, the effects are now more pronounced. The cause of this must consequently depend on other sources.

2) regarding sensor movements:

If the SQUID sensor moves with respect to the EDM cell in the precession plane of the polarized spins (perpendicular to $\vec{B}_0$), for example due to temperature changes, the frequency detected by this sensor varies during the movement. It does not matter whether sensor or cell are moving. In general, the movement (rotation) can be described by an angle β_2, as shown in figure 6.5. In case 2a) the sensor rotates around the cell, in case 2b) the cell rotates around the sensor; both cases are equivalent. The results would differ, if the sensor would not rotate together with the cell in case 2b), because the projection of the magnetization or rather the signal amplitude would decrease. This can be neglected for small angles.

For better understanding let's assume an exaggerated case where the sensor moves around the cell with the Larmor frequency of Xe. Then the detected frequency of Xe is $\omega'_{\mathrm{Xe}} = 0$ and the one of He is $\omega'_{\mathrm{He}} = \omega_{\mathrm{He}} - \omega_{\mathrm{Xe}}$.

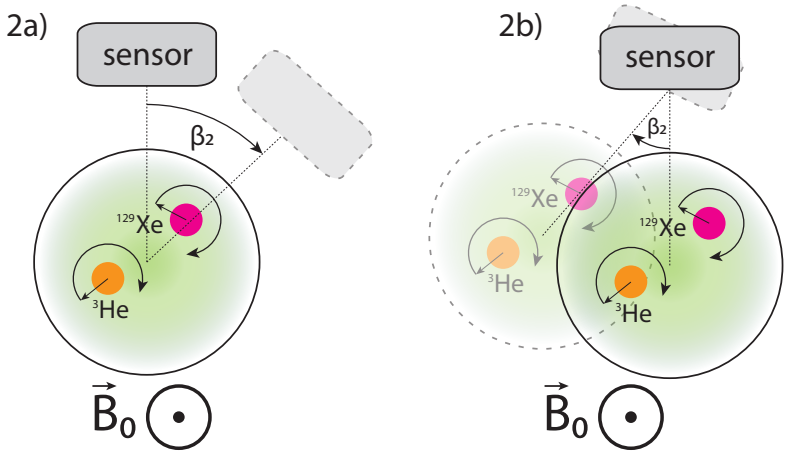

Figure 6.5.: Schematic illustration of 2a) a rotation of the sensor around the cell, and 2b) a rotation of the cell around the sensor. The magnetic holding field points out of the drawing plane. In both cases, the rotation angle β_2 describes the rotation in the precession plane, or rather perpendicular to $\vec{B}_0$. As a result, the sensor detects a change in the Larmor frequency during the rotation.

Considering the weighted frequency difference, the general case is

$$\Delta\omega_{\mathrm{rot2}} = \omega_{\mathrm{Xe}} - \omega_{\mathrm{det}} - \frac{\gamma_{\mathrm{Xe}}}{\gamma_{\mathrm{He}}}\left(\omega_{\mathrm{He}} - \omega_{\mathrm{det}}\right) \tag{6.3a}$$

$$= \left(1 - \frac{\gamma_{\mathrm{Xe}}}{\gamma_{\mathrm{He}}}\right) \cdot \omega_{\mathrm{det}} \tag{6.3b}$$

and the weighted phase difference

$$\Delta\Phi_{\mathrm{rot2}} = \left(1 - \frac{\gamma_{\mathrm{Xe}}}{\gamma_{\mathrm{He}}}\right) \cdot \Phi_{\mathrm{det}} \quad . \tag{6.4}$$

Although the cryostat with the SQUIDS, and the EDM setup are reinforced against each other, small movements must be considered possible. For a realistic case let's assume a movement of the sensor of $10\,\mu$m, the cell stays in position. With a distance of $d \approx 10\,$cm between the SQUIDs and the center of the cell, this movement corresponds to an angle change of $\beta_2 = \Phi_{\mathrm{det}} \approx 10^{-4}\,$rad. The accumulated weighted phase difference of this movement is $\Delta\Phi_{\mathrm{rot2}} \approx 6 \cdot 10^{-5}\,$rad. Regarding the phase noise of run #4 in figure 6.1, this effect alone is not enough to explain the variations of the residuals. However, although it is difficult to quantify how much the individual components move relative to each other, this effect must definitely be taken into account in the (future) experimental routine / data analysis.

3) regarding changes in the magnetic field orientation:
A rotation/tilting of the magnetic field with respect to the SQUID sensors results also in an additional shift of the weighted phase difference:
Let's consider a single spin species. The magnetization $\vec{M}$ of the polarized spins is precessing around the magnetic holding field $\vec{B}_0 = B_0 \cdot \hat{e}_z$ with the Larmor frequency ω_L (cf. equation 2.23). If the detector sees only the y-component the signal is $S(t) = \kappa M \cdot \sin(\omega_\mathrm{L} \cdot t)$ and the detected precession frequency is equal to the Larmor frequency $\omega = \omega_\mathrm{L}$. The constant factor κ considers the distance between the center of the cell and the detector among other parameters. In this case the detector frame and the frame of the magnetic field are the same.
Now let's assume that the magnetic field frame is not the same, the magnetic field points no longer only in z-direction in the detector frame, e.g. $\vec{B'}_0 = B_0 \cdot (\cos(\beta_3)\hat{e}_z + \sin(\beta_3)\hat{e}_x)$. The detected signal is accordingly reduced due to the projection angle β_3 between the detector and the new precession plane xy of the magnetization; $S'(t) = \kappa M \cdot \sin(\omega_\mathrm{L} \cdot t) \cdot \cos(\beta_3)$. It is evident, that the detected precession frequency is still equal to the Larmor frequency $\omega' = \omega_\mathrm{L}$. However, this is only true in the static case. During the rotation of the magnetic field the detected signal gets an additional geometric phase, the so-called Berry phase. According to [148], this effect leads to a change in the effective detected frequency $\omega \to \tilde{\omega}$, which is depending on the rotation angle β_3 and the angular velocity of this rotation $d\beta_{3,\tau}/d\tau$. Here $\beta_{3,\tau}$ is the rotation angle at time τ. In the adiabatic case $d\beta_{3,\tau}/d\tau \ll \omega_\mathrm{L}$ it holds

$$\tilde{\omega} = \omega_\mathrm{L} - \omega_\mathrm{rot3} = \omega_\mathrm{L} - \frac{d\beta_{3,\tau}}{d\tau}(1 - \cos\beta_3) \quad . \tag{6.5}$$

It is evident the contribution of the Larmor frequency of both species drops out in the weighted frequency difference. Small changes in the absolute value of the magnetic field do not contribute in this approximation. Therefore, the following equation applies for the resulting shift of the weighted frequency difference:

$$\Delta\omega_\mathrm{rot3} = \left(1 - \frac{\gamma_\mathrm{Xe}}{\gamma_\mathrm{He}}\right) \cdot \omega_\mathrm{rot3} \tag{6.6}$$

However, this shift of the weighted frequency difference, and accordingly the drift of the accumulated weighted phase difference

$$\Delta\Phi_\mathrm{rot3} = \left(1 - \frac{\gamma_\mathrm{Xe}}{\gamma_\mathrm{He}}\right) \cdot \omega_\mathrm{rot3} \cdot t \tag{6.7}$$

lasts only as long as the rotation of the field t. Therefore it follows that $d\beta_{3,\tau}/d\tau = \Delta\beta_{3,\tau}/\Delta\tau = \beta_3/t$. As a result the accumulated weighted phase difference

$$\Delta\Phi_{\mathrm{rot3}} = \left(1 - \frac{\gamma_{\mathrm{Xe}}}{\gamma_{\mathrm{He}}}\right) \cdot \beta_3(1 - \cos\beta_3) \tag{6.8}$$

is independent on the dynamics and only depending on the rotation angle β_3. In other words: for the accumulated weighted phase difference it does not matter whether the rotation of the magnetic field is fast (jump) or slow (drift).
At this point it should be mentioned that there is no difference whether the magnetic field rotates and the sensor is fix (case 3a) or the sensor rotates and the magnetic field is fixed (case 3b). Both cases are shown in the following figure 6.6.

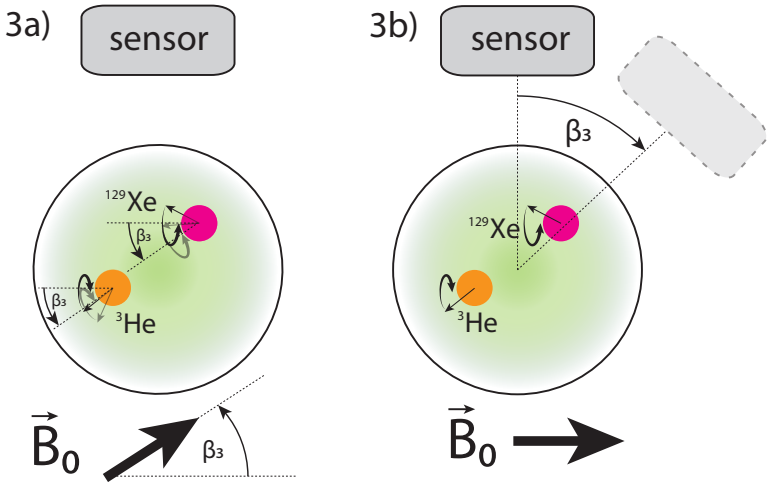

Figure 6.6.: Schematic illustration of 3a) a rotation of the magnetic field direction towards the sensor with β_3, and 3b) a rotation of sensor around the EDM cell towards the direction of $\vec{B}_0$ with β_3. As a result, the sensor detects a change in the Larmor frequency during the rotation.

To estimate a usual value of β_3 it is reasonable to have a look at the jumps in the He frequency of run #4. The first jump in figure 6.2 for example is in the order of $\Delta\omega_{\mathrm{He}} \approx 10\,\mathrm{mrad/s}$. This corresponds to a change in the absolute value of the magnetic field of $\Delta B_0 = \Delta\omega_{\mathrm{He}}/\gamma_{\mathrm{He}} \approx 50\,\mathrm{pT}$. Assuming that this change is associated with a rotation of the magnetic field $B_0 = 400.00\,\mathrm{nT}$ by an angle β_3, like

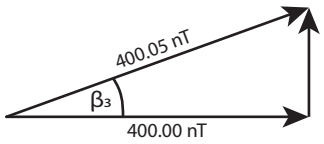

then the rotation is in the order of $\beta_3 \approx 1° \approx 0.017\,\text{rad}$. For this estimation the signal change due to the change of the projection angle to the sensor can be neglected, since $\cos(\beta_3) \approx 1$.
This rotation can also occur if there is no frequency jump, or rather no change of the absolute magnetic field. The field can rotate by an angle β_3' without changing its absolute value, like

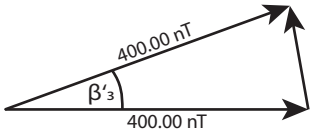

Such a rotation can occur if the whole setup changes its orientation, for example if the holding frame of the mu-metal cylinder gets tilted, which would change the magnetic field (orientation). As a result, phase residual changes are not correlated with frequency jumps and the causal analysis gets more complicated. Sensor movements (case 3b) do not seem to be the main origin of this effect, since the rotation is in the same order as estimated for effect 2). However, it is not expected that such rotations are much larger than 1°. If this value is used in equation 6.8 the resulting shift of the weighted phase difference is $\Delta\Phi_{\text{rot3}} \approx 2 \cdot 10^{-6}\,\text{rad}$. Similar as for the second effect 2), this third effect is not sufficient to explain the variations of the phase residuals, as they are evident in the phase noise of run #4 in March 2017 in figure 6.1.

4) regarding changes in the magnetic field orientation and Earth rotation:
As described in section 5.2.2, the shift of the weighted frequency difference due to Earth rotation $\Delta\omega_{\pm}^{\circlearrowleft}$ is depending on the angle ρ between the magnetic field and the north direction of Earth (cf. equation 5.16). Hence, if the direction of the magnetic field changes it results in a change of the frequency shift due to Earth rotation. The angle of this rotation/change can therefore be regarded as the uncertainty of the angle between the magnetic field $\vec{B}_0$ and the north orientation $\beta_4 = \Delta\rho$. It follows $\Delta\omega_{\pm}^{\circlearrowleft} \rightarrow \Delta\omega_{\pm}^{\circlearrowleft} \pm \Delta\omega_{\pm,\text{rot4}}^{\circlearrowleft}$. From the discussion of the previous effect 3) we can estimate an angular change of the magnetic holding field of $\beta_4 = \beta_3 \approx 1°$. If we use $\rho = (43 \pm 1)°$ in equations 5.16 and 5.18 the resulting change of the weighted frequency difference due to the rotation of the magnetic field regarding the Earth rotation is $\Delta\omega_{\pm,\text{rot4}}^{\circlearrowleft} = 10^{-6}\,\text{rad/s}$.
It is important to understand that the frequency shift exists as long as the angle is changed, which is a huge difference compared to the previous effects 2) and 3). Assuming a fast rotation (jump) of the magnetic field the result is not a constant phase shift but a

constant frequency shift. In the worst case, if this frequency shift is correlated with the reversal of the electric field (T_a), this contributes to a false-EDM. Also, comparing the strength of both effects with the same rotation of the magnetic field $\beta_4 = \beta_3$

$$\Delta\Phi_{\mathrm{rot3}} \approx 2 \cdot 10^{-6}\,\mathrm{rad} \quad \longleftrightarrow \quad \Delta\Phi_{\overset{+}{\circlearrowleft},\mathrm{rot4}} = \int \Delta\omega_{\overset{+}{\circlearrowleft},\mathrm{rot4}} dt \approx t \cdot 10^{-6}\,\mathrm{rad/s}$$

the shift due to Earth rotation considerably exceeds the phase shift which is directly linked to the magnetic field rotation after a short time. For example after 1000 s the resulting shift of the weighted phase difference gets $\Delta\Phi_{\overset{+}{\circlearrowleft},\mathrm{rot4}} \approx 10^{-3}\,\mathrm{rad}$. Considering the time scales of residual phase noise in figure 6.1, this effect is certainly a possible cause.

5) regarding the fit routine:
Parallel to the analysis presented in this thesis, a revised fit routine has been developed [120]. At the end of 2017 it turned out that the observed non-statistical noise of the phase residuals are mainly due to high correlations of the fit parameters in the original fit routine. A re-analysis of the data with orthogonalized fit-parameters resulted in a considerable improvement of statistical sensitivity. Due to time constraints the analysis of the following measurement campaign in July 2017 was performed by F. Allmendinger from the University of Heidelberg.

Nevertheless, the previous considerations allow to further analyze the data from runs #1 − 3 with the original fit routine. The average statistical frequency sensitivity obtained for the three runs is $\sigma_\omega \approx 3 \cdot 10^{-8}\,\mathrm{rad/s}$. The results of the EDM term g after including the EDM-function to the fit (cf. equation 5.11) and recalculating with equation 2.50, are presented in table 6.3 with one statistical standard error.

EDM run	d_{Xe} $[10^{-27}\,e\mathrm{cm}]$
#1	-14.47 ± 9.81
#2	3.36 ± 7.52
#3	6.33 ± 8.08

Table 6.3.: Overview of the three evaluable EDM runs in March 2017 regarding the experimental results. The corresponding uncertainties are the statistical errors.

A conclusion of these results is presented together with the results of the measurement campaign of July 2017 in the following section 6.2.

6.2. July 2017

Several improvements were made after the measurement campaign in March 2017. The T_1 relaxation time of the hyperpolarized ^{3}He in the transport cells was improved and the optical pumping of the Xe-polarizer was optimized. In July 2017, six EDM measurements were performed, moreover with the same setup as in March. Furthermore, the optimization of the gas mixture, as calculated in the appendix section A.3, was considered. At the beginning of the July measurement campaign it was observed that either the ^{4}He or the SF_6 reservoir was contaminated with oxygen, which resulted in low T_2^* relaxation times. Therefore we decided to continue from run #3 on to work without buffer gases but with increased partial pressures of ^{3}He and ^{129}Xe instead. This measure was also required to prevent gas discharges and corresponding leakage currents inside the EDM cell. The following table 6.4 gives an overview of the six runs with the individual partial pressures.

EDM run	$p_{^3\mathrm{He}}$ [mbar]	$p_{^{129}\mathrm{Xe}}$ [mbar]	$p_{^4\mathrm{He}}$ [mbar]	$p_{\mathrm{SF_6}}$ [mbar]
#1 @ 07-18-2017 12:00	12	24	49	4
#2 @ 07-18-2017 19:56	25	53	44	5
#3 @ 07-19-2017 15:17	45	96	0	0
#4 @ 07-19-2017 22:08	20	100	0	0
#5 @ 07-20-2017 11:28	27	91	0	0
#6 @ 07-20-2017 22:46	31	103	0	0

Table 6.4.: Overview of the six EDM runs in July 2017, regarding the gas mixture inside the spherical EDM cell. The listed partial pressures are known with an uncertainty of about $\Delta p = \pm 1\,\mathrm{mbar}$.

The method of operation is the same as in March 2017 (cf. section 6.1). The high voltage is again set to $U = \pm 4\,\mathrm{kV}$, resulting in an electric field of $E = 800\mathrm{V/cm}$. The reversal time of the electric field T_a was altered for the individual runs. This adjustment was a reaction to the change in the T_2^* relaxation times, as mentioned above. In addition, the start polarity HV_0 was altered between the runs to check for systematic effects.
The determining factors of each run are listed in table 6.5. It is evident that the T_2^* relaxation times increased for both species after the omission of additional buffer gases. This fact clearly indicates a relaxation effect due to impurities - most likely oxygen - in (one of) the buffer gases.

EDM run	$A_{^3\mathrm{He}}$ [pT]	$A_{^{129}\mathrm{Xe}}$ [pT]	$T^*_{2,\mathrm{He}}$ [h]	$T^*_{2,\mathrm{Xe}}$ [h]	T [s]	T_a [s]	HV_0 [kV]
#1	30	22	4.7	2.1	22968	16000	$^-/_+\,4$
#2	59	53	3.2	1.6	20000	12000	$^-/_+\,4$
#3	128	113	18.9	2.9	23460	12000	$^-/_+\,4$
#4	77	102	20.8	2.8	40356	18000	$^+/_-\,4$
#5	96	123	20.0	2.9	34948	18000	$^+/_-\,4$
#6	105	117	18.0	2.8	24396	18000	$^-/_+\,4$

Table 6.5.: Overview of the six EDM runs in July 2017, regarding the experimental parameters. The achievable T_2^* relaxation times vary between the individual runs, as well as the particular amplitudes A of helium and xenon at the start of the experiment.

In this measurement campaign in July 2017, the statistical sensitivity is considerably enhanced, compared to the measurements in March 2017. The main reasons for this are the longer relaxation times - for both ^{3}He and ^{129}Xe - as well as the higher signal amplitudes, also for both species. This is especially evident in the plots of the phase residuals and the corresponding ASD plots, evaluated with the original fit routine, which are shown in appendix A.2. As mentioned before, this original fit routine that was used for the evaluation of the EDM runs in March 2017 resulted in high correlations of the fit parameters. This in turn led to a high non-statistical noise of the phase residuals, as it is evident from the plots in appendix A.2, figures A.5 and A.6, especially from the ASD plots of runs $\#3-6$, figure A.7 and A.8. Apart from runs #1 and #2, all runs show significant deviations from statistical behavior. Therefore, the analysis was performed again with the revised fit routine [120], as explained in section 6.1.1 paragraph 5). With this re-analysis, the phase residuals of all six EDM runs are distributed statistically around zero and the runs can be further evaluated [120]. A statistical frequency sensitivity of $\sigma_\omega \approx 6 \cdot 10^{-10}\,\mathrm{rad/s}$ can be achieved. The calculated EDM values are presented in the table 6.6.

EDM run	d_{Xe} [$10^{-28}\,e$cm]
#1	-27.6 ± 53.7
#2	-23.8 ± 30.5
#3	5.1 ± 19.8
#4	-7.6 ± 5.6
#5	10.3 ± 7.7
#6	-4.2 ± 11.0

Table 6.6.: Overview of the six EDM runs in July 2017, regarding the experimental results [120]. The corresponding uncertainties are the statistical errors.

Figure 6.7 gives a compilation of the nine calculated EDM values from the measurements of March and July 2017, which are distributed statistically around their weighted mean. The weighted mean of all EDM values is $d_{\mathrm{Xe}} = (2.0 \pm 4.0_{\mathrm{stat}} \pm 0.2_{\mathrm{sys}}) \cdot 10^{-28}\, e\mathrm{cm}$ and it is compatible with zero within its error bar. The given systematic error is a conservative estimation from the calculated false-EDM effects in table 5.3.
To conclude, the present upper limit $|d_{\mathrm{Xe}}| < 7.3 \cdot 10^{-27}\, e\mathrm{cm}$ (95% CL) [3] (cf. table 1.3) could be lowered to $|d_{\mathrm{Xe}}| < 1.0 \cdot 10^{-27}\, e\mathrm{cm}$ (95% CL). Please note that this value is preliminary. A final analysis will be published soon.

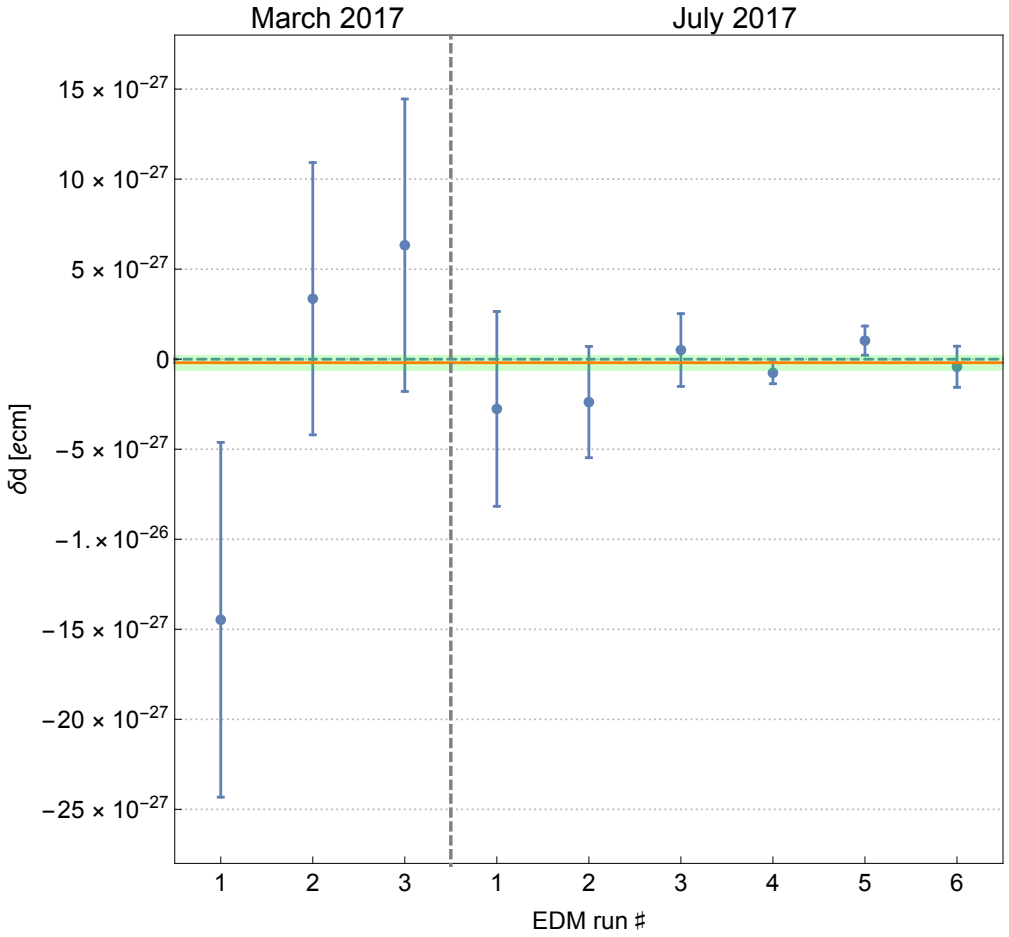

Figure 6.7.: Summary of the calculated EDM values of the nine evaluated runs of March and July 2017. The orange line represents the weighted mean of the nine values; the green shading represents the corresponding one standard error uncertainty of the weighted mean. The individual data points with the respective uncertainties are statistically compatible with the weighted mean, which in turn is compatible with zero.

7

Conclusion

In this final chapter, the thesis is concluded by a summary of the achieved experimental results, followed by an outlook with a discussion about ongoing and scheduled improvements of the experiment.

Summary

The experimental setup, which was developed within this thesis, has proven to be fully operational. Within our MIXeD-collaboration we were able to lower the current upper limit of the Xe-EDM. A short summary of the developments taken so far is presented in the following paragraphs:

The conceptional design of the Xe-EDM setup and the operating procedures to run this experiment at the MSR in Jülich were developed and implemented into a functioning apparatus. Considering the MSR, the temporal and spatial characteristic of the residual magnetic field inside the shielding was thoroughly characterized. An additional mu-metal cylinder had to be added to the setup to further reduce the magnetic field gradients and to obtain a better total shielding factor.
All components of the EDM spectrometer had to fit into the mu-metal cylinder whose maximum diameter was predetermined by the width of the door of the MSR. A sophisticated cos-coil system together with gradient coils was designed, constructed and examined to provide a homogeneous magnetic guiding field for the precessing spin samples inside the limited space of the cylinder. Combined with the elaboration of a suitable demagnetization routine for the mu-metal shield, we were able to keep the magnetic field gradients in the order of $\nabla B \approx 10\,\mathrm{pT/cm}$ across the volume of the EDM cell - one of the key objectives in this experiment.
In parallel, the actual EDM setup was developed and constructed. Under consideration and intensive checks of the particular materials and components, the final setup consists

of the EDM casing - an electro-conductive glass T-piece - which contains the EDM cell, adapted high voltage supply lines, as well as a specially designed non-magnetic, pneumatic valve for the hyperpolarized gas mixtures.
Another aspect was the practicability of the experimental operation. The possibility to replace individual components - for example to recover the relaxation properties of the EDM cell - and to perform long term measurements were an important consideration. For this purpose, much effort was put in the mechanical suspension and the frame construction of the setup.

Step by step, the restricting parameters of the setup were checked and optimized. Regarding the achievable EDM sensitivity, the most important aspects are:

- The obtainable relaxation time T_2^* was optimized primarily by improving the magnetic field gradients.
- The optimization of the signal-to-noise ratio: Possible sources of polarization losses were searched for consistently and extensively eliminated and the system noise was reduced as far as possible.
- The electric field: since the EDM sensitivity is directly proportional to the applied electric field, it is an experimental challenge to make this as high as possible without suffering from increased leakage currents. Besides the HV-supply should not produce too much system noise going along with the increase of the electric field strength. The chosen $E = \pm 800\,\mathrm{V/cm}$ was a first conservative setting.
- Correlated systematic effects had to be carefully inhibited.

The results from the measurement campaigns of March and July 2017 are a proof of principle of the whole setup, the experimental procedures and the analysis of the data. Although some conditions were not yet optimized at that time, we lowered the former experimental upper limit of the Xe-EDM to a preliminary value of $|d_{\mathrm{Xe}}| < 1.0 \cdot 10^{-27}\,e\mathrm{cm}$ (95% CL).
Furthermore, the measurements of July 2017 revealed the high potential of the setup and the method of operation. The statistical limits from March to July were improved again by an order of magnitude, mostly due to higher signal-to-noise ratios and longer coherence times. Though we had to deal with strong correlations of the fit parameters, a revised fit-routine allowed us to evaluate the measurements in an appropriate way. Nevertheless, because the system is now much more sensible on the experimental conditions - most of all on magnetic field changes during a measurement - the data analysis has to be further checked to ensure to cover these kind of deterministic effects.

Outlook

After the successful proof of principle the next step is to improve the determining factors to achieve even better sensitivities, in order to put more stringent limits on CP violating low energy parameters. Also, special attention must be paid in order to avoid the previously mentioned systematic effects beforehand. Afterwards, long term measurements are scheduled to improve the statistics further on. There are three main aspects that can be further improved:

1. The signal-to-noise ratio SNR. Especially the polarization of Xe and the electromagnetic noise are the limiting factors.

Polarization tests and analytic studies of the Xe-polarizer with a newly installed online NMR system revealed sources of polarization loss during the polarization process of the Xe. It's assumed that the achievable polarization can be increased significantly by optimizing this process. Additionally we intend to minimize polarization losses, including the filling of the polarized xenon in the polarizer unit, the mixing of the gases, and the transport and filling process to transfer the gas mixture into the EDM cell. To be realistic, the aim is to increase the effective polarization of Xe by a factor of two.
Furthermore, the electromagnetic noise in the frequency range between 3 Hz and 20 Hz is crucial for the SNR. It is planned for the future to install a new mu-metal shield, which should further decrease the noise level. In this context it will also be ensured that disturbances of the magnetic field - as they are elaborated in the discussion of the experimental results - are suppressed. Also the EDM components, such as the HV connection and the conductive casing will be revised, regarding the Johnson noise. Hereby, an improvement by factor of two is aspired, too. Therefore, the resulting signal-to-noise ratio could be enhanced in total by realistic a factor of four.

2. The measurement time T, which is essentially related to T_2^*. Currently the measurement time is limited mainly by the wall relaxation $T_{1,\mathrm{wall}}$ of xenon and the gradient relaxation time $T_{2,\mathrm{grad}}$.

To extend the effective measurement time it is necessary to keep relaxation effects, mainly $T_{1,\mathrm{wall,Xe}}$, of the hyperpolarized gases low. In the current setup, the wall relaxation of xenon was evaluated to be $T_{1,\mathrm{wall,Xe}} \approx 8.6\,\mathrm{h}$. Usually, similar cells have wall relaxation times that are about a factor of two longer. Since we have the possibility to remove the EDM cell from the setup, it is planned to recover the glass cell or exchange it for future measurement runs.

With regard to the first point: once the SNR is increased we have the possibility to decrease the partial pressures of the gases and therefore extend the transverse gradient relaxation time $T_{2,\mathrm{grad}}$ of the gases. An additional improvement of $T_{2,\mathrm{grad}}$ is planned by moving the EDM setup into a superior magnetically shielded room. A new MSR with a higher shielding factor and a lower and more homogeneous residual magnetic field is already in development and will be installed at the University of Heidelberg. It is to be expected that this will considerably extend the obtainable measuring time of coherent spin precession and thus significantly improve the achievable EDM sensitivity. However, we then reach again the extrinsic disturbances regarding the residual phase noise, i.e. changes in the magnetic field orientation, among others. For this reason, we must make every effort to reduce these effects in the future. Considerations on this will be incorporated into the planning and design of the new MSR, as well as into an improvement of the experimental setup itself.

3. The high voltage. A higher electric field would immediately improve the achievable EDM sensitivity.

At the moment the electric field is limited by the performance of the HV power supply. For future measurement runs the power supply will be replaced by other devices with a higher voltage. Here, the challenge is to find HV power supplies which do not increase the system noise even at higher HV settings when the HV is applied on the electrodes. In this respect, improvements are also planned with regard to the leakage currents. An advanced electrode configuration of the EDM cell, as well as optimized surfaces of all HV components are already designed and in construction.

With regard to the improvements of all these aspects, we expect to enhance the experimental sensitivity by an overall factor of at about ten in the coming period.
As soon as the setup works under optimized conditions it is aspired to perform long term measurements to reduce statistical limitations. The planned timetable considers 100 days of data taking. To perform such an extensive schedule it is inevitable to automate the experimental procedure as much as possible. This includes mainly the optical pumping of xenon, the mixing of the gases, the gas transfer into the EDM cell and the actual process of measurement. The latter is already automated to a great extend. The processes concerning the handling of the gases will be integrated in one apparatus. Only the hyperpolarization of helium will be performed as usual. First measures are already in preparation.

A

Appendix

A.1. Detailed Description of the EDM-Function

The EDM-function of the fit routine is part of the global fit function of the measurement data. Because it is necessary to describe this function as accurate as possible, this section provides a detailed overview of the order of events, regarding the reversal of the electric field.

In general, the switching time T_a of the electric field is depending on the achievable T_2^* relaxation time. A well-established setting is $T_a = 2 \cdot T_2^*$. Because the high voltage of the electrodes can not be switched instantaneously, the procedure consists of several timing contributions.
As an example, a gas mixture with a xenon relaxation time of $T_{2,\mathrm{Xe}}^* \approx 1.7\,\mathrm{h}$ is observed. Accordingly, the switching time is set to $T_a = 12000\,\mathrm{s}$. The EDM measurement (beginning of data taking) should start at $t = 0$. After a desired waiting time of 280 s the high voltage of the electrodes around the cell is ramped with 25 V/s to $U = \pm 4\,\mathrm{kV}$. As a reminder, the distance between the electrodes is $d = 10\,\mathrm{cm}$. Thus, the electric field of $E = +800\,\mathrm{V/cm}$ is fully provided after a ramping time of $4\,\mathrm{kV}/25\mathrm{V/s} = 320\,\mathrm{s}$, and therefore at $t = 280\,\mathrm{s} + 320\,\mathrm{s} = 600\,\mathrm{s}$. From this point, the time until the opposite electric field $E = -800\,\mathrm{V/cm}$ is fully provided, is $T_a/4 = 3000\,\mathrm{s}$, thus at $t = 3000\,\mathrm{s} + 600\,\mathrm{s} = 3600\,\mathrm{s}$. These 3000 s include the time of a constant voltage $\pm 4\,\mathrm{kV}$, the ramp down to 0 V, a waiting time of 100 s, as well as the ramp to $\mp 4\,\mathrm{kV}$. The total time of field reversal is therefore $2 \cdot 320\,\mathrm{s} + 100\,\mathrm{s} = 720\,\mathrm{s}$. The waiting time of 100 s is always implemented at the reversal point at 0 V. Now, the opposite high voltage $\mp 4\,\mathrm{kV}$ is fully applied. The time until the field is again fully reversed is $T_a/2 = 6000\,\mathrm{s}$, thus at $t = 3600\,\mathrm{s} + 6000\,\mathrm{s} = 9600\,\mathrm{s}$. As before, this includes the constant voltage $\mp 4\,\mathrm{kV}$, the ramp down to 0 V, a waiting time of 100 s, as well as the ramp to $\pm 4\,\mathrm{kV}$. From now on, the switching time of 6000 s is maintained and the scheme of field reversal stays the same.

A schematic diagram of the applied electric field (blue) and the resulting EDM-function (yellow, arbitrary units) is presented in the following figure A.1. As a reminder, the EDM function h is the integral over the electric field function. It describes the accumulated phase an EDM would induce.

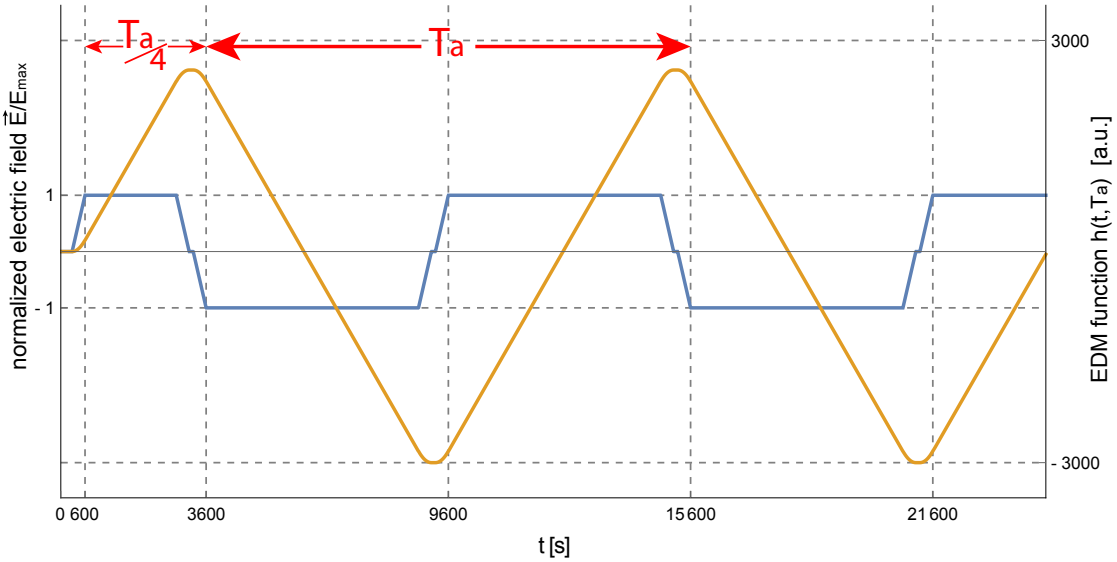

Figure A.1.: Schematic diagram of the normalized electric field function (blue) and the resulting EDM-function $h(t, T_a)$ (yellow, arbitrary units). The switching time is set to $T_a = 12000\,\mathrm{s}$. After 280 s the field is ramped for 320 s. The ramp is completed at $t = 600\,\mathrm{s}$. After an additional $T_a/4 = 3000\,\mathrm{s}$, the field is completely reversed, including the ramping with $2 \cdot 320\,\mathrm{s}$ and a waiting time of 100 s. From this on, the field is reversed every $T_a/2 = 6000\,\mathrm{s}$.

The graphic shows that the resulting EDM-function is more or less symmetric around zero, due to the fact that the first setting of the high voltage has a duration only half as long as the following settings. A perfectly symmetric function could be achieved, if the first setting is performed slightly longer. The symmetric shape is crucial to differentiate the EDM-function as much as possible from (global) linear phase drifts. This is to prevent strong correlated errors between the fit-parameter g and mainly the linear fit parameter $\Delta\omega_{\mathrm{lin}}$ (cf. equation 5.11).

This most accurate specification of the EDM-function is used for the data analysis of the EDM measurements, presented in chapter 6. The switching time and the respective waiting time at the beginning are adjusted if necessary.

A.2. Concerning the Analysis of the EDM Measurements

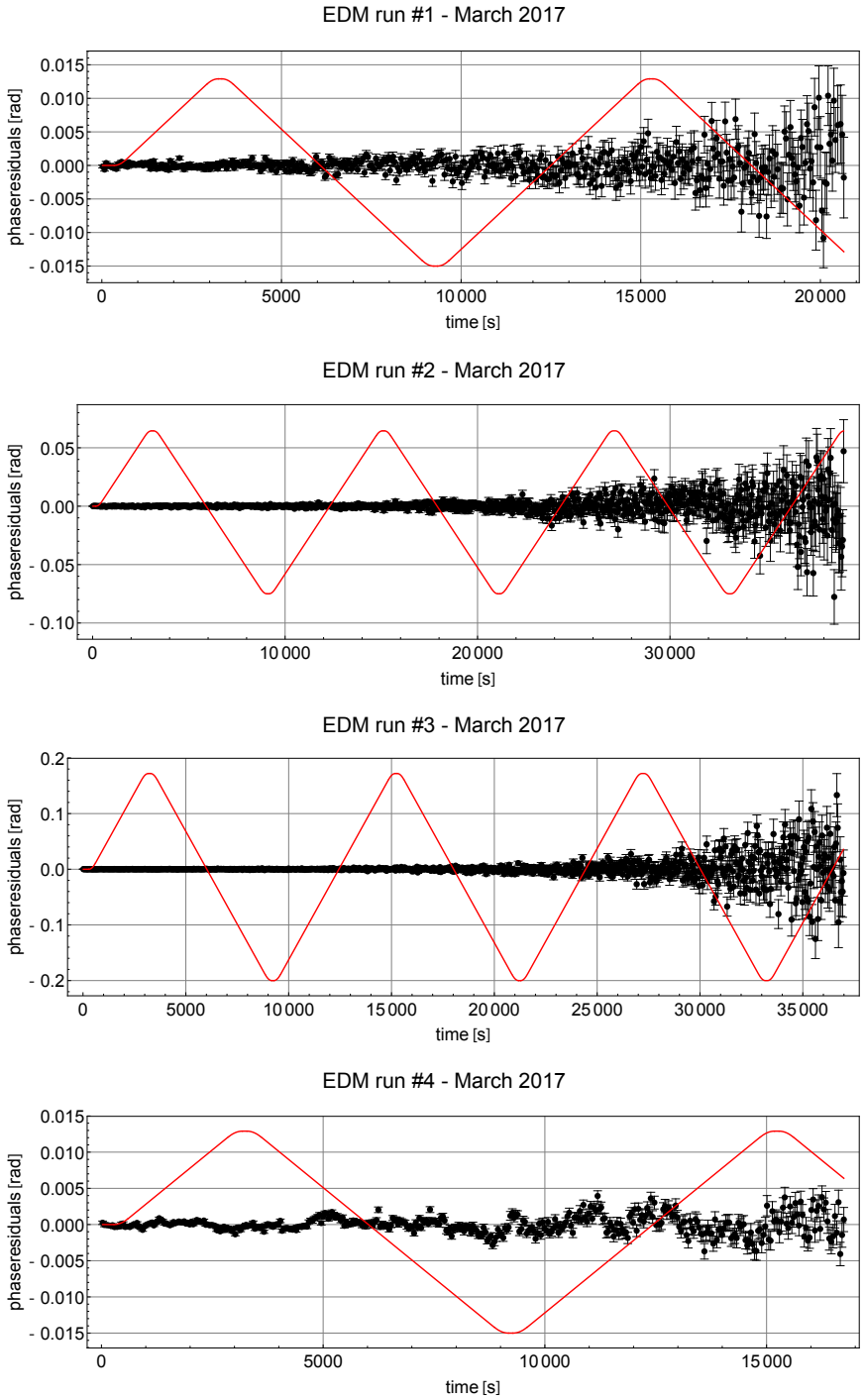

Figure A.2.: Phase residuals of the runs #1 − 4 of March 2017 using the fit function of equation 6.1. Visualization of the EDM-function h (red) in arbitrary units. Apart from run #4, the other runs show a statistical distribution of the phase residuals.

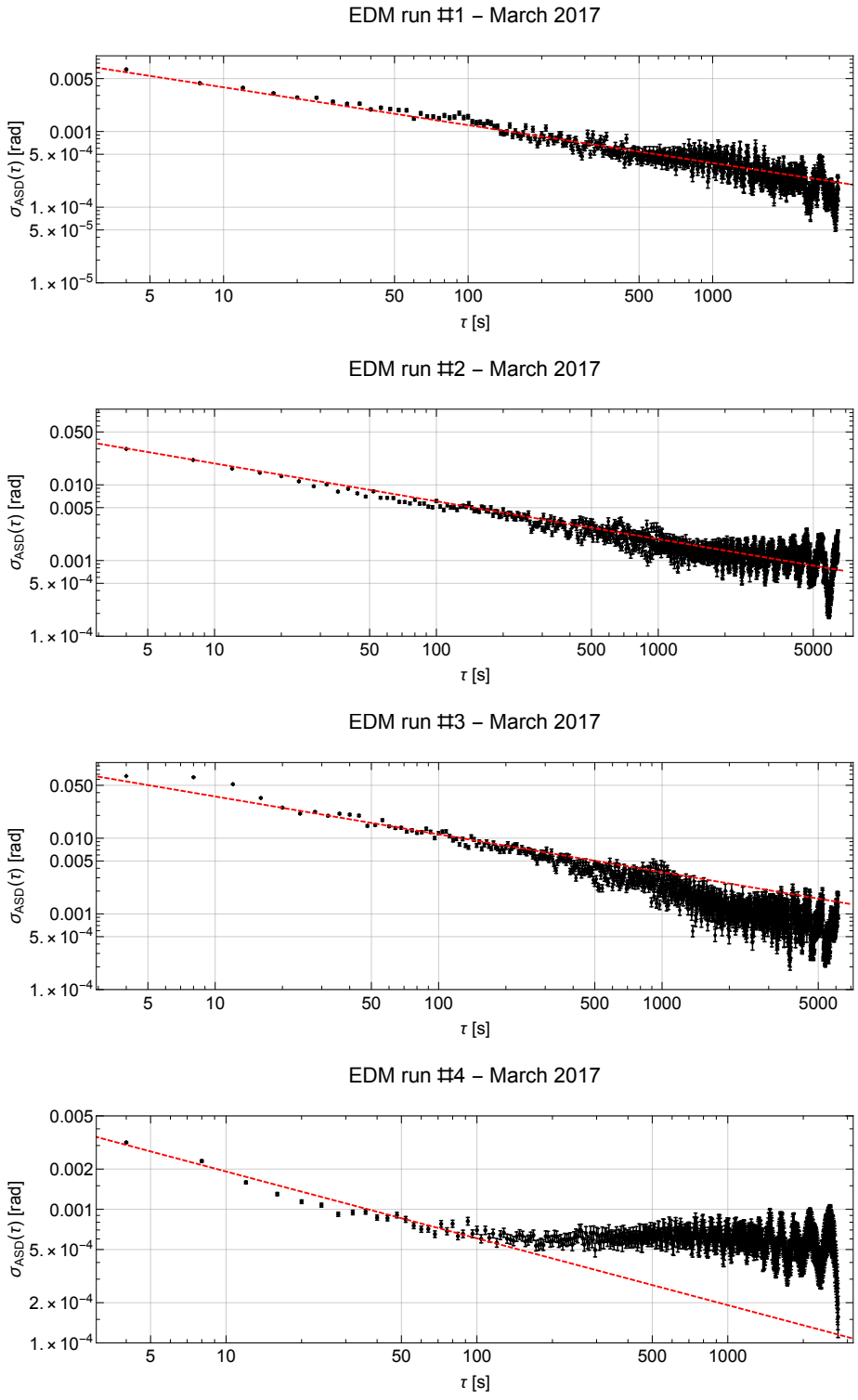

Figure A.3.: ASD plots of the runs $\#1-4$ of March 2017. The ASD plots for the runs $\#1-3$ show a fairly good $\tau^{-1/2}$ dependency, whereas run #4 deviates from the expected statistical behavior from $\tau \approx 100\,\mathrm{s}$ on.

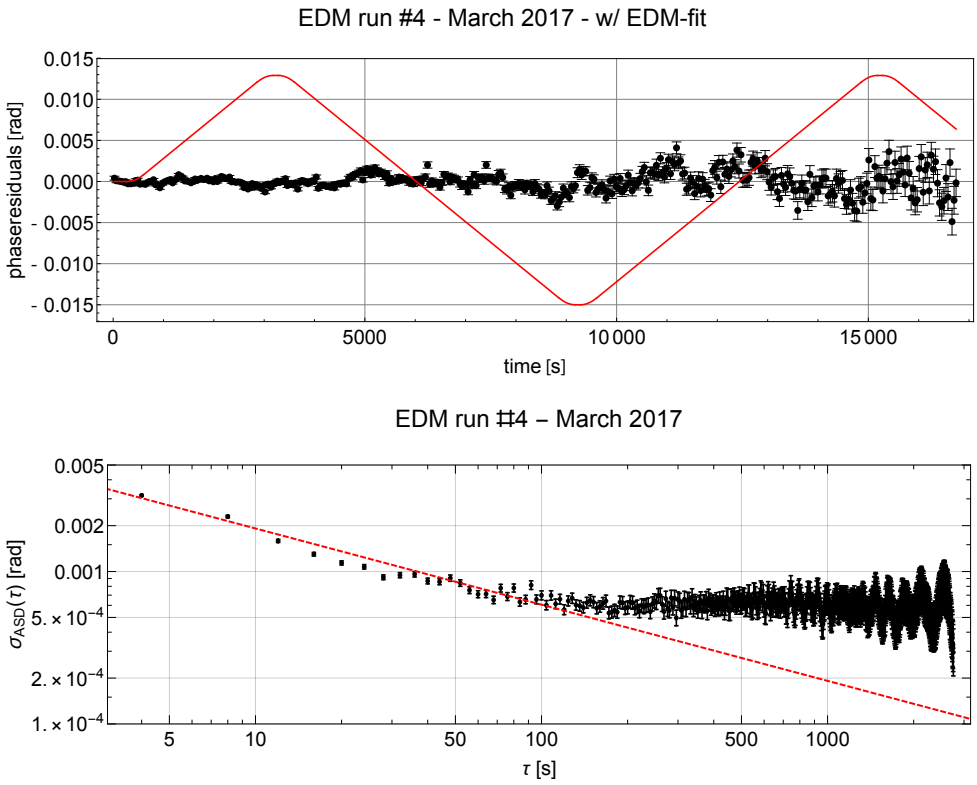

Figure A.4.: The phase residuals and ASD plot of run #4 of March 2017, **including the EDM-function** in the fit, using the fit function of equation 5.11. Visualization of the EDM-function h (red) in arbitrary units. The non-statistical phase noise is still evident. This is a clear indication that the non-statistical behavior does not stem from an actual EDM. A detailed study of possible causes for this is discussed in section 6.1.1.

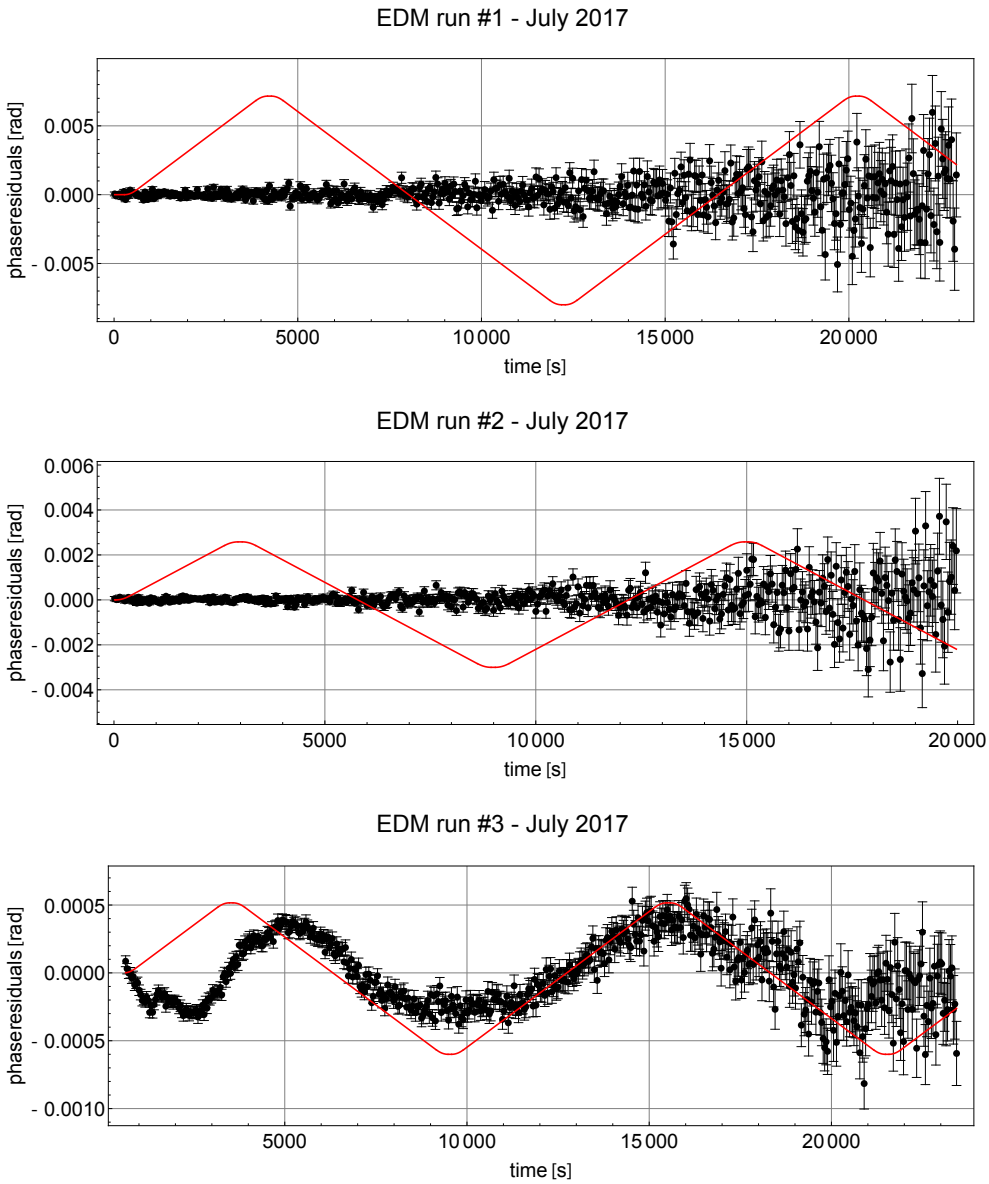

Figure A.5.: Phase residuals of the runs #1 – 3 of July 2017. Visualization of the EDM-function h (red) in arbitrary units. The phase residuals of run #1 and 2 are statistically distributed around zero. The residuals of run #3 show clearly a non-statistical behavior, which is also (seemingly) correlated with the switching of the electrical field. It has to be noted, however, that the phase sensitivity is greatly improved compared to the previous runs. Effects that are responsible for the non-statistical behavior, could have been simply suppressed in the other runs.

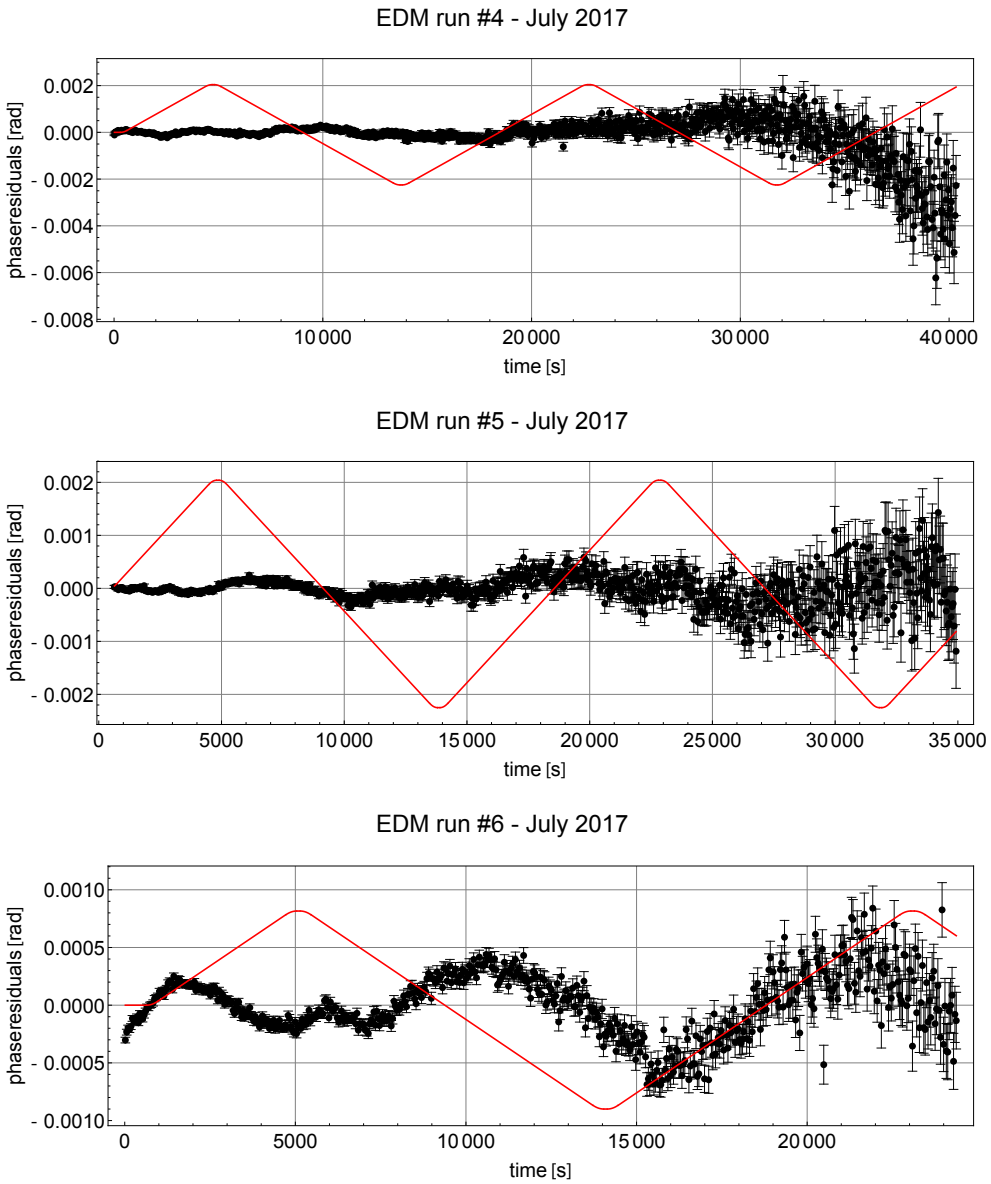

Figure A.6.: Phase residuals of the runs #4 – 6 of July 2017. Visualization of the EDM-function h (red) in arbitrary units. These runs also show a non-statistical behavior of the phase residuals, similar to run #3 in figure A.5.

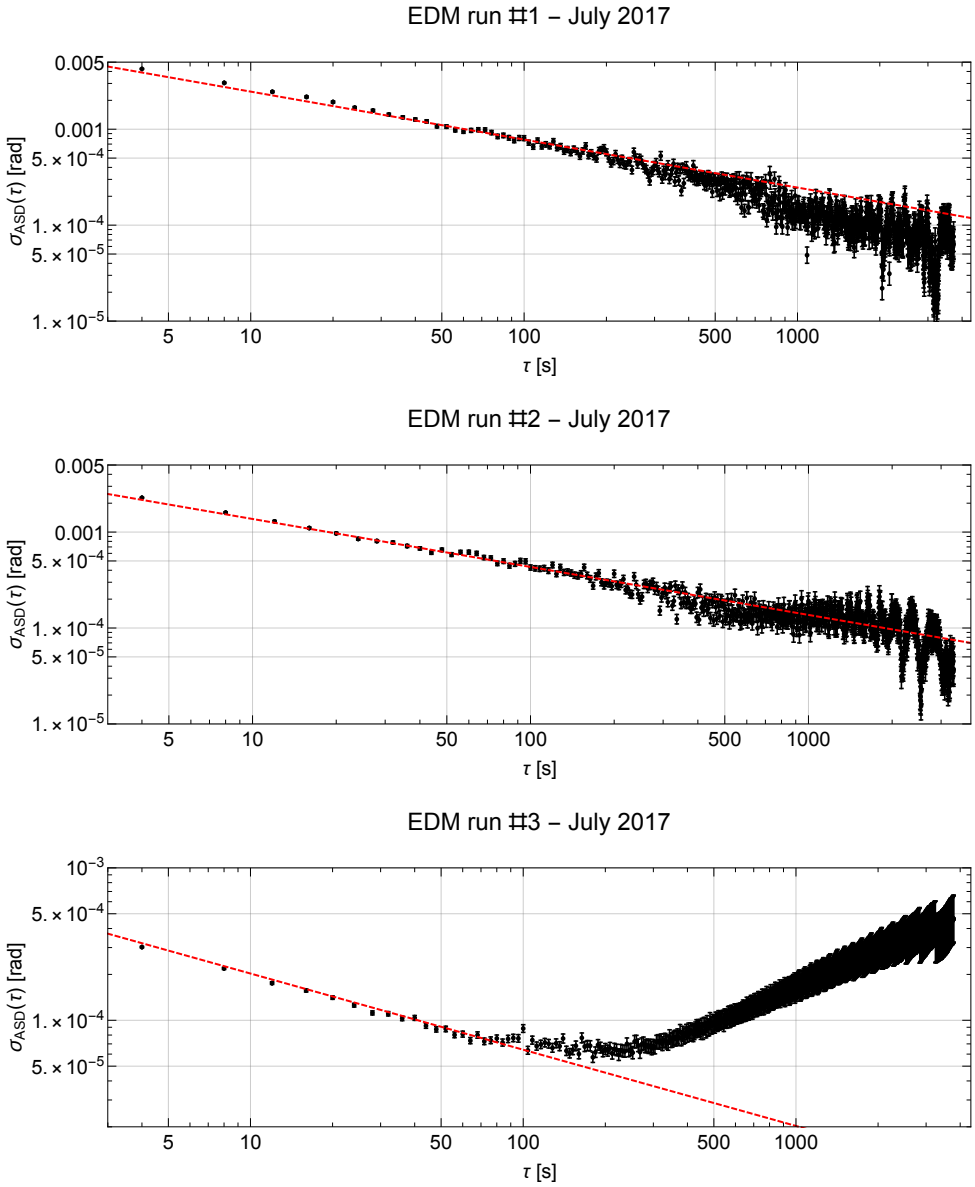

Figure A.7.: ASD plots of the runs $\#1 - 3$ of July 2017. In accordance with the findings from the distribution of the phase residuals in figure A.5, the ASD plots for the runs $\#1 - 2$ show a fairly good $\tau^{-1/2}$ dependency, whereas run #3 deviates from the expected statistical behavior from $\tau \approx 100\,\mathrm{s}$ on.

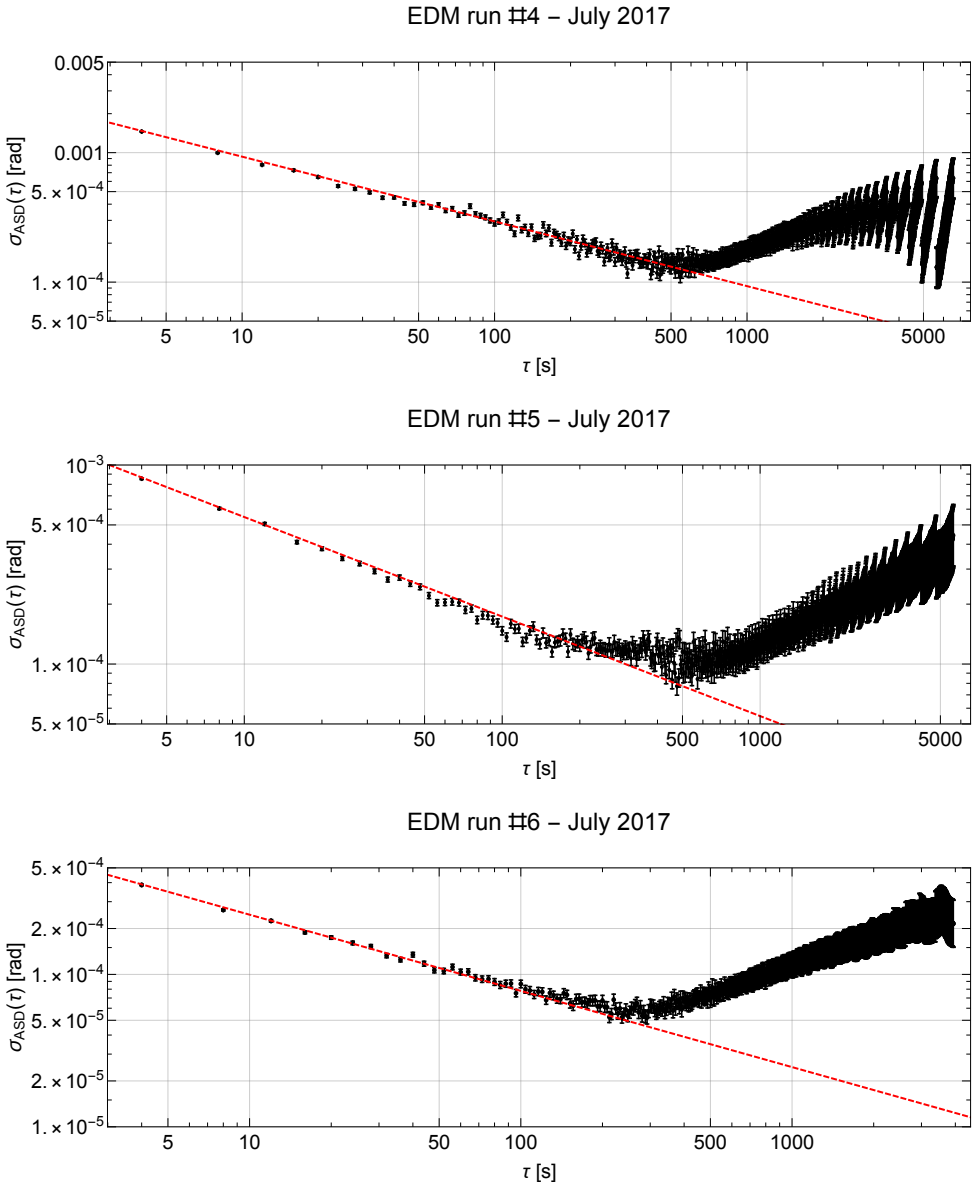

Figure A.8.: ASD plots of the runs $\#4 - 6$ of July 2017. Again the deviation from the $\tau^{-1/2}$ dependency of all runs is in accordance with the findings from the distribution of the phase residuals in figure A.6

All runs of July 2017 have been re-analyzed by F. Allmendinger from the University of Heidelberg with regard to the reduction of fit-routine-related correlations of the fit parameters. The calculations of the preliminary EDM values are based on this very evaluation with a revised fit function. The resulting phase residuals now have a statistical behavior [120]. A detailed discussion and final results will be published soon.

A.3. Optimization of the Gas Mixture

In this section, an optimization of the achievable sensitivity of the Xe-EDM with regard to the gas mixture used in the EDM cell is presented. According to the CRLB (equation 2.54), the frequency sensitivity is depending on the signal-to-noise ratio (SNR) A/ρ and the effective measurement time T. As described in section 2.4.2, equation 2.58, we make use of the substitution

$$T^{-3/2} \cdot \sqrt{C(T, T_2^*)} =: f(r) \cdot (T_2^*)^{-3/2} \quad , \tag{A.1}$$

with r being the ratio of the measurement time T and the relaxation time T_2^* (cf. equation 2.56). T_2^* is a combination of the longitudinal relaxation times $T_{1,\text{wall}}$, $T_{1,\text{vdW}}$, T_{1,O_2}, $T_{1,\text{bin}}$ and the gradient relaxation time $T_{2,\text{grad}}$. For the further considerations T_{1,O_2} and $T_{1,\text{bin}}$ will be neglected (as explained in section 2.3.2.1). Also, the wall relaxation time $T_{1,\text{wall}}$ will be treated as constant ($T_{1,\text{wall}} = 8.4\,\text{h}$, cf. section 3.1.3) for the optimization. Now, the contributions of interest are the van-der-Waals relaxation $T_{1,\text{vdW}}$ and the gradient relaxation $T_{2,\text{grad}}$. Starting with $T_{1,\text{vdW}}$ it is directly proportional to ratio of the partial pressures of a buffer gas B and Xe

$$\alpha_\text{B} = \frac{p_\text{B}}{p_\text{Xe}} \tag{A.2}$$

for a given destruction rate coefficient r_B, as in equation 2.35. So, for this contribution only α_B has to be optimized, independently on the absolute values of p_Xe and p_B.
$T_{2,\text{grad}}$ is inversely proportional to the diffusion coefficient D (resp. the diffusion coefficient of xenon in the gas mixture D_Xe^GM, cf. equation 2.28). The diffusion coefficient for xenon in the gas mixture in terms of α_B is

$$\begin{aligned} \frac{1}{D_\text{Xe}^\text{GM}} &= \left(\frac{p_\text{Xe}}{D_\text{Xe}} + \frac{p_{^3\text{He}}}{D_{\text{Xe in } ^3\text{He}}} + \frac{\tilde{p}_{\text{SF}_6}}{D_{\text{Xe in SF}_6}} + \frac{p_\text{B}}{D_{\text{Xe in B}}} \right) \cdot \frac{1}{p_0} \cdot \frac{T_0^{3/2}}{T^{3/2}} \\ &= \left(\frac{p_\text{Xe}}{D_\text{Xe}} + \frac{p_{^3\text{He}}}{D_{\text{Xe in } ^3\text{He}}} + \frac{\tilde{p}_{\text{SF}_6}}{D_{\text{Xe in SF}_6}} + \frac{\alpha_\text{B} \cdot p_\text{Xe}}{D_{\text{Xe in B}}} \right) \cdot \frac{1}{p_0} \cdot \frac{T_0^{3/2}}{T^{3/2}} \quad . \end{aligned} \tag{A.3}$$

The gases ^{3}He and SF_6 in the final mixture have a special role in the experiment, which is why they are already listed in the equation for the gas mixture A.3[1]. Starting with SF_6, it is used as a quenching gas for the applied high voltage to prevent leakage currents and discharges in the EDM cell at a certain partial pressure $\tilde{p}_{\text{SF}_6}$. ^{3}He is required at a certain

[1] In the first approximation the binary diffusion coefficient for Xe in ^{3}He is assumed to be the one of Xe in ^{4}He, justified by [74]

partial pressure $p_{^3\mathrm{He}}$ because of comagnetometry. The SNR is mainly depending on the amplitude of the precessing xenon magnetization A and the detected noise ρ. Usually there are no limitations due the signal amplitude of helium, because of the generally higher polarization and the greater magnetic moment. For an EDM measurement it is therefore expedient to regulate the helium pressure to the xenon pressure, e.g. $p_{^3\mathrm{He}} = 0.5 \cdot p_{\mathrm{Xe}}$. For a given polarization, the signal amplitude is solely direct proportional to p_{Xe} in the gas mixture. Common values are: $A = \varepsilon \cdot p_{\mathrm{Xe}} = 1\,\mathrm{pT/mbar} \cdot p_{\mathrm{Xe}}$, where ε is the measured signal, recalculated for 1 mbar of Xe (cf. equation 4.7).
If the EDM sensitivity is optimized, the electric field E must also be included. With regard to the gas mixture, however, an actual optimization of E is not necessary, since there is no immediate correlation between the gas mixture and E. However, we must keep in mind that to avoid leakage currents, we need a buffer gas in the EDM cell.
Now it is possible to derive an expression for the achievable sensitivity δd_{Xe} with the dependencies on the particular partial pressures of the gas mixture components:

$$
\begin{aligned}
\delta d_{\mathrm{Xe}} &= \frac{\pi\hbar}{2E} \cdot \sigma_\nu \qquad\qquad (\mathrm{A.4})\\
&= \frac{\pi\hbar}{2E} \cdot \frac{\sqrt{3}}{\pi} \cdot \frac{\rho}{A} \cdot T^{-3/2} \cdot \sqrt{C(T, T_2^*)} \quad , \qquad \text{with } T^{-3/2}\cdot\sqrt{C(T,T_2^*)} =: f(r)\cdot(T_2^*)^{-3/2}\\
&= f(r) \cdot \frac{\sqrt{3}\,\hbar}{2E} \cdot \frac{\rho}{\varepsilon \cdot p_{\mathrm{Xe}}} \cdot (T_2^*)^{-3/2}\\
&= f(r) \cdot \frac{\sqrt{3}\,\hbar}{2E} \cdot \frac{\rho}{\varepsilon \cdot p_{\mathrm{Xe}}} \cdot \left(\frac{1}{T_{1,\mathrm{wall}}} + \frac{1}{T_{1,\mathrm{vdW}}} + \frac{1}{T_{2,\mathrm{grad}}}\right)^{3/2}\\
&= f(r) \cdot \frac{\sqrt{3}\,\hbar}{2E} \cdot \frac{\rho}{\varepsilon \cdot p_{\mathrm{Xe}}} \cdot\\
&\qquad \cdot \left[\frac{1}{T_{1,\mathrm{wall}}} + \frac{1}{4.6}\left(1 + r_{\mathrm{He}}\frac{p_{^3\mathrm{He}}}{p_{\mathrm{Xe}}} + r_{\mathrm{SF_6}}\frac{\tilde{p}_{\mathrm{SF_6}}}{p_{\mathrm{Xe}}} + r_{\mathrm{B}}\frac{p_{\mathrm{B}}}{p_{\mathrm{Xe}}}\right)^{-1} + \frac{8R^4\gamma_{\mathrm{Xe}}^2}{175 D_{\mathrm{Xe}}^{\mathrm{GM}}}\left(|\nabla B_z|^2\right)\right]^{3/2}\\
&= f(r) \cdot \frac{\sqrt{3}\,\hbar}{2E} \cdot \frac{\rho}{\varepsilon \cdot p_{\mathrm{Xe}}} \cdot\\
&\qquad \cdot \left[\frac{1}{T_{1,\mathrm{wall}}} + \frac{1}{4.6}\left(1 + r_{\mathrm{He}}\frac{p_{^3\mathrm{He}}}{p_{\mathrm{Xe}}} + r_{\mathrm{SF_6}}\frac{\tilde{p}_{\mathrm{SF_6}}}{p_{\mathrm{Xe}}} + r_{\mathrm{B}}\,\alpha_{\mathrm{B}}\right)^{-1} + \frac{8R^4\gamma_{\mathrm{Xe}}^2}{175 D_{\mathrm{Xe}}^{\mathrm{GM}}}\left(|\nabla B_z|^2\right)\right]^{3/2}
\end{aligned}
$$

For further considerations, the parameters E, ε, ρ and ∇B_z as well as $T_{1,\mathrm{wall}}$ and the radius R of the cell are set as constant to reasonable values determined in previous test measurements. Also, for the SF_6 partial pressure $\tilde{p}_{\mathrm{SF_6}}$ (and ^{3}He see above) we take empirically established values. All fixed values are listed in table A.1. Now, the achievable sensitivity δd_{Xe} is only dependent on the variable parameters p_{Xe}, α_{B} and r_{B}.

	parameter	value
$T : T_2^*$	r	3
	$f(r{=}3)$	0.857
noise level	ρ	$10\,\mathrm{fT}/\sqrt{\mathrm{Hz}}$
signal per pressure	ε	$1\,\mathrm{pT/mbar}$
electric field	E	$800\,\mathrm{V/cm}$
wall relaxation time	$T_{1,\mathrm{wall}}$	$8.4\,\mathrm{h}$
inner cell radius	R	$4.8\,\mathrm{cm}$
magnetic field gradients	$\lvert\nabla B_z\rvert$	$15\,\mathrm{pT/cm}$
min. partial pressure of SF_6	$\tilde{p}_{\mathrm{SF_6}}$	$5\,\mathrm{mbar}$
partial pressure of ^{3}He	$p_{^3\mathrm{He}}$	$0.5 \cdot p_{\mathrm{Xe}}$

Table A.1.: Summary of empirically established values of the parameters, on which the achievable EDM sensitivity is depending on, regarding an optimization of the partial pressures of the gas mixture components.

For the following optimization of p_{Xe}, α_{B} and r_{B}, four expedient buffer gases are available: CO_2, SF_6, N_2 and ^{4}He. A mixture with a total pressure p_{tot} is always composed like

$$p_{\mathrm{tot}} = [p_{\mathrm{Xe}} + p_{^3\mathrm{He}} + \tilde{p}_{\mathrm{SF_6}}] + p_{\mathrm{B}} \quad . \tag{A.5}$$

The values in parentheses are fully determined by p_{Xe} with the information in table A.1. A mixture without any additional buffer gas ($p_{\mathrm{B}} = 0$) is from now on called *minimum mixture*. Please note that the total partial pressure of SF_6 should never fall below $p_{\mathrm{tot,SF_6}} = \tilde{p}_{\mathrm{SF_6}} + p_{\mathrm{SF_6}} = 5\,\mathrm{mbar}$.

To find the optimal settings for p_{Xe} and α_{B} it is useful to determine a certain minimum relaxation time in advance. Because of the unavoidable loss in statistics due to the required reversal of the electric field (dead time, cf. section A.1) it has been concluded that the relaxation time should not be significantly below $T_2^* < 2\,\mathrm{h}$. This consideration is based on the expertise of previous test measurements. The optimization for single measurements with the different buffer gases results in the following plots A.9 to A.12, which show the achievable statistical EDM sensitivity δd_{Xe}, depending on p_{Xe} and α_{B}. The red line in those plots represents the settings of p_{Xe} and α_{B} for which $T_2^* = 2\,\mathrm{h}$, whereas the purple line represents the settings for which $T_2^* = 3\,\mathrm{h}$. The green markings show the respective best "T_2^*"-setting, regarding the best achievable sensitivity. The values for a *minimum mixture* result from $p_{\mathrm{B}}/p_{\mathrm{Xe}} = 0$, separately shown in figure A.13. The results of the achievable sensitivities for the different cases and dependencies, comparing $T_2^* = 2\,\mathrm{h}$ and $3\,\mathrm{h}$ are summarized in table A.2.

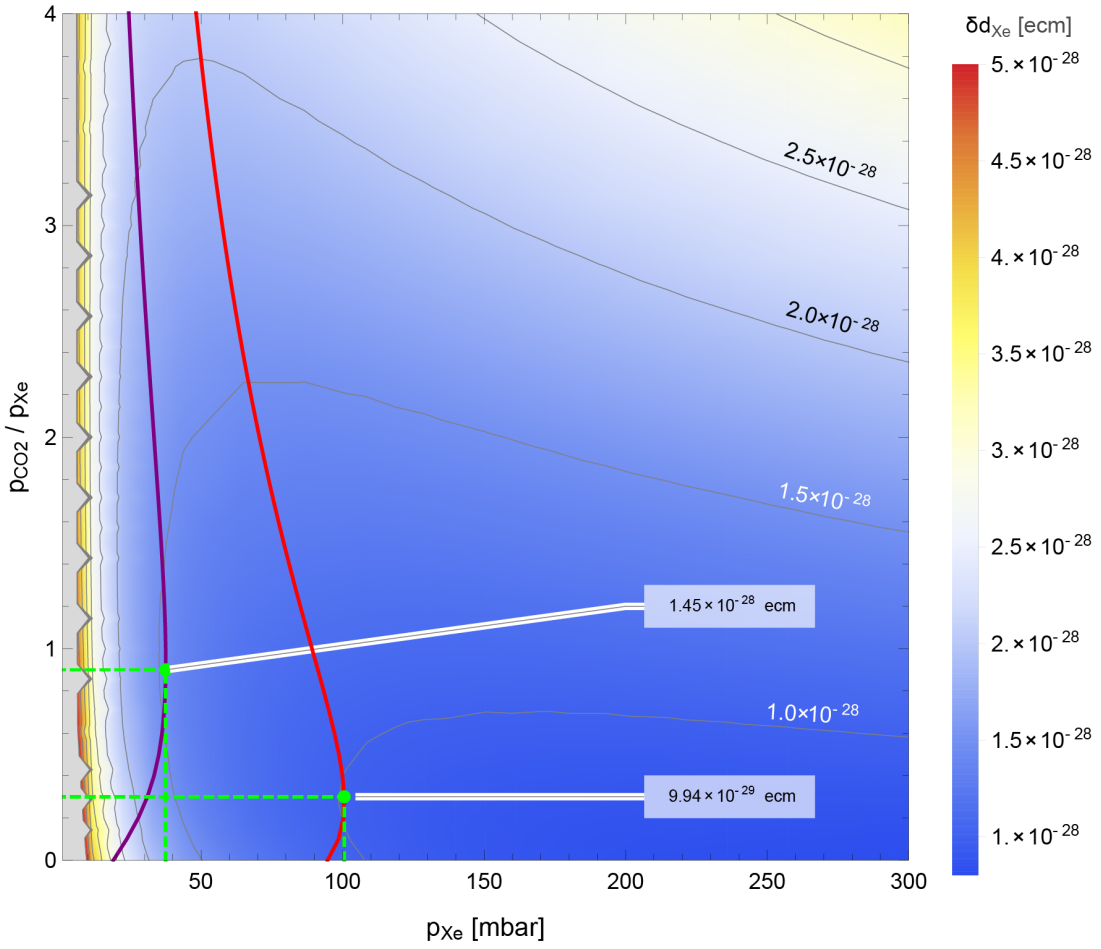

Figure A.9.: Density plot of the achievable EDM sensitivity with CO_2 as a buffer gas, depending on the partial pressure of Xe and the ratio α_{CO_2} of CO_2 and Xe. The color coding represents the achievable sensitivity, where the gray color means worse sensitivity than the red region. The red contour shows the settings for the values leading to $T_2^* = 2\,\mathrm{h}$. The purple contour shows the settings for the values leading to $T_2^* = 3\,\mathrm{h}$. The green markings show the respective optimum. The optimal settings for $T_2^* = 2\,\mathrm{h}$ are $p_{\mathrm{Xe}} = 100\,\mathrm{mbar}$, $\alpha_{CO_2} = 0.3$, resulting in $\delta d_{\mathrm{Xe,\,opt}} = 0.99 \cdot 10^{-28}\,e\mathrm{cm}$. For $T_2^* = 3\,\mathrm{h}$ they are $p_{\mathrm{Xe}} = 37\,\mathrm{mbar}$ and $\alpha_{CO_2} = 0.9$, resulting in $\delta d_{\mathrm{Xe,\,opt}} = 1.45 \cdot 10^{-28}\,e\mathrm{cm}$

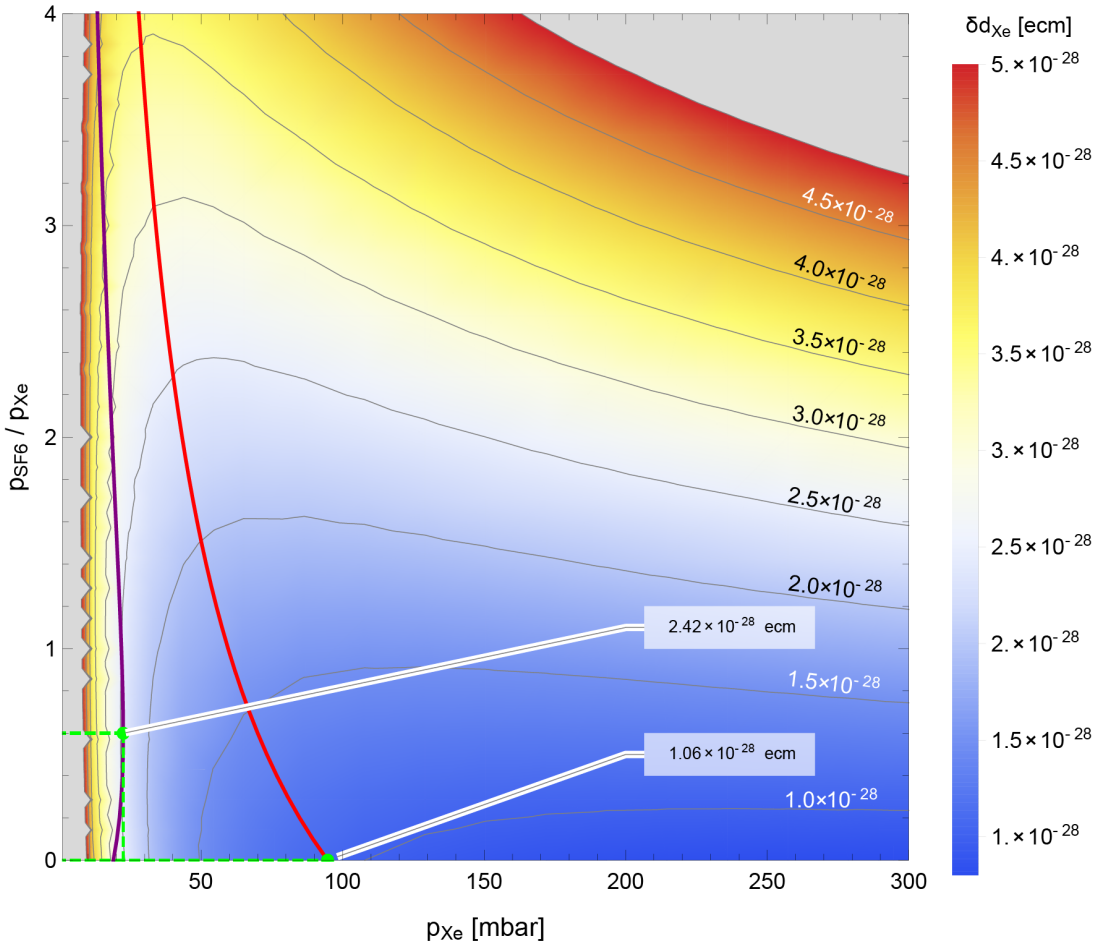

Figure A.10.: Density plot of the achievable EDM sensitivity with SF_6 as a buffer gas, depending on the partial pressure of Xe and the ratio α_{SF_6} of SF_6 and Xe. The color coding represents the achievable sensitivity, where the gray color means worse sensitivity than the red region. The red contour shows the settings for the values leading to $T_2^* = 2\,\mathrm{h}$. The purple contour shows the settings for the values leading to $T_2^* = 3\,\mathrm{h}$. The green markings show the respective optimum. The optimal settings for $T_2^* = 2\,\mathrm{h}$ are $p_{Xe} = 94\,\mathrm{mbar}$ with no additional SF_6, resulting in $\delta d_{Xe,\,opt} = 1.06 \cdot 10^{-28}\,e\mathrm{cm}$. For $T_2^* = 3\,\mathrm{h}$ they are $p_{Xe} = 22\,\mathrm{mbar}$ and $\alpha_{SF_6} = 0.6$, resulting in $\delta d_{Xe,\,opt} = 2.42 \cdot 10^{-28}\,e\mathrm{cm}$

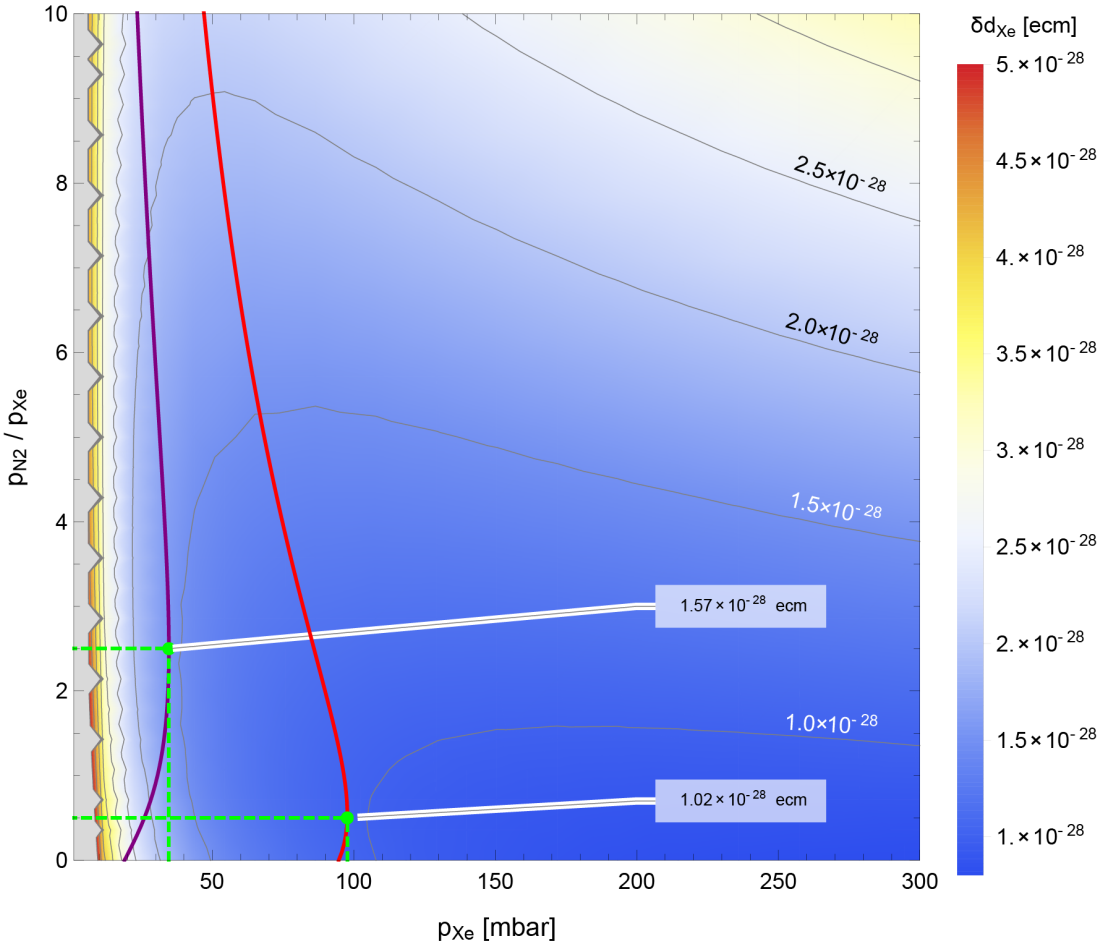

Figure A.11.: Density plot of the achievable EDM sensitivity with N_2 as a buffer gas, depending on the partial pressure of Xe and the ratio α_{N_2} of N_2 and Xe. The color coding represents the achievable sensitivity, where the gray color means worse sensitivity than the red region. The red contour shows the settings for the values leading to $T_2^* = 2\,\mathrm{h}$. The purple contour shows the settings for the values leading to $T_2^* = 3\,\mathrm{h}$. The green markings show the respective optimum. The optimal settings for $T_2^* = 2\,\mathrm{h}$ are $p_{Xe} = 97\,\mathrm{mbar}$ and $\alpha_{N_2} = 0.5$, resulting in $\delta d_{\mathrm{Xe,\,opt}} = 1.02 \cdot 10^{-28}\,e\mathrm{cm}$. For $T_2^* = 3\,\mathrm{h}$ they are $p_{Xe} = 34\,\mathrm{mbar}$ and $\alpha_{N_2} = 2.5$, resulting in $\delta d_{\mathrm{Xe,\,opt}} = 1.57 \cdot 10^{-28}\,e\mathrm{cm}$

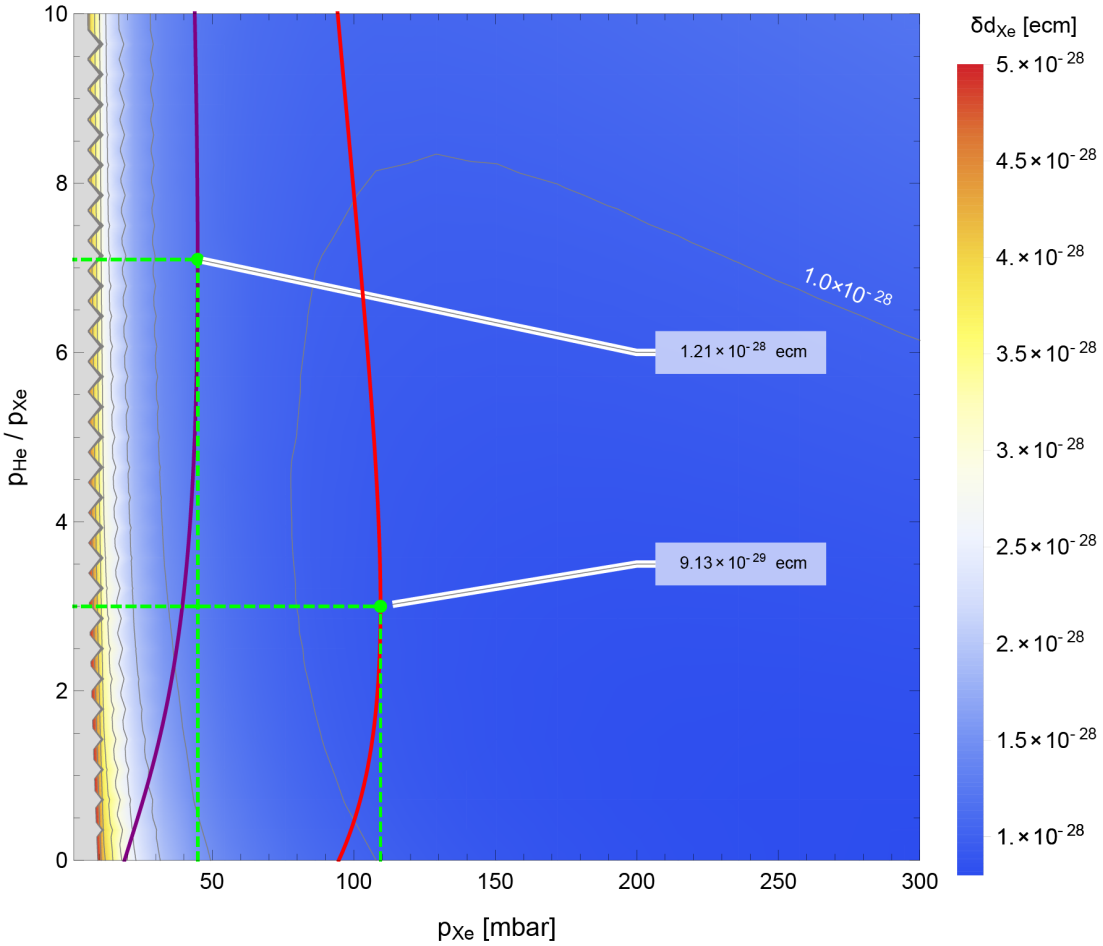

Figure A.12.: Density plot of the achievable EDM sensitivity with ^{4}He as a buffer gas, depending on the partial pressure of Xe and the ratio $\alpha_{^4\mathrm{He}}$ of ^{4}He and Xe. The color coding represents the achievable sensitivity, where the gray color means worse sensitivity than the red region. The red contour shows the settings for the values leading to $T_2^* = 2\,\mathrm{h}$. The purple contour shows the settings for the values leading to $T_2^* = 3\,\mathrm{h}$. The green markings show the respective optimum. The optimal settings for $T_2^* = 2\,\mathrm{h}$ are $p_{\mathrm{Xe}} = 109\,\mathrm{mbar}$, $\alpha_{^4\mathrm{He}} = 3.0$, resulting in $\delta d_{\mathrm{Xe,\,opt}} = 0.91 \cdot 10^{-28}\,e\mathrm{cm}$. For $T_2^* = 3\,\mathrm{h}$ they are $p_{\mathrm{Xe}} = 44\,\mathrm{mbar}$ and $\alpha_{\mathrm{SF_6}} = 7.1$, resulting in $\delta d_{\mathrm{Xe,\,opt}} = 1.21 \cdot 10^{-28}\,e\mathrm{cm}$

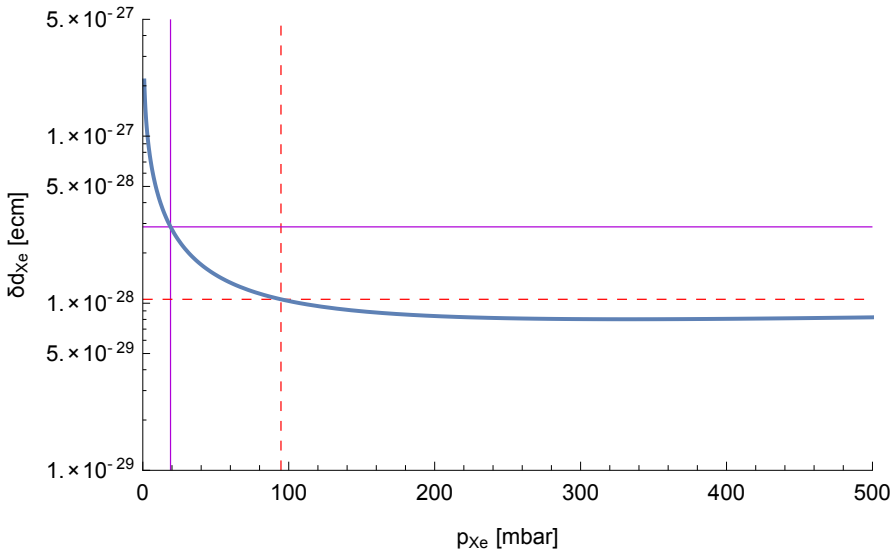

Figure A.13.: Dependency of the achievable EDM sensitivity with a *minimum mixture* on the partial pressure of xenon. The dashed red line marks p_{Xe} leading to $T_2^* = 2\,\mathrm{h}$. The solid purple line marks p_{Xe} leading to $T_2^* = 3\,\mathrm{h}$. The optimal setting for $T_2^* = 2\,\mathrm{h}$ is $p_{\mathrm{Xe}} = 94\,\mathrm{mbar}$, resulting in $\delta d_{\mathrm{Xe,\,opt}} = 1.06 \cdot 10^{-28}\,e\mathrm{cm}$. For $T_2^* = 3\,\mathrm{h}$ it is $p_{\mathrm{Xe}} = 19\,\mathrm{mbar}$, resulting in $\delta d_{\mathrm{Xe,\,opt}} = 2.86 \cdot 10^{-28}\,e\mathrm{cm}$

buffer gas	$p_{\mathrm{Xe,\,opt}}$ [mbar]	α_{opt}	T_2^* [h]	$\delta d_{\mathrm{Xe,\,opt}}$ [$e$cm]
CO_2	100	0.3	2.0	$0.99 \cdot 10^{-28}$
	37	0.9	3.0	$1.45 \cdot 10^{-28}$
SF_6	94	0.0	2.0	$1.06 \cdot 10^{-28}$
	22	0.6	3.0	$2.42 \cdot 10^{-28}$
N_2	97	0.5	2.0	$1.02 \cdot 10^{-28}$
	34	2.5	3.0	$1.57 \cdot 10^{-28}$
^4He	109	3.0	2.0	$0.91 \cdot 10^{-28}$
	44	7.1	3.0	$1.21 \cdot 10^{-28}$
minimum mixture	94	×	2.0	$1.06 \cdot 10^{-28}$
(no buffer gas)	19	×	3.0	$2.86 \cdot 10^{-28}$

Table A.2.: Summary of achievable sensitivities for the different buffer gas additions at the specific optimized values of p_{Xe} and α_{B} with $T_2^* = 2$ and 3 h. In the case of SF_6 for $T_2^* = 2\,\mathrm{h}$, the best sensitivity is achieved by not adding SF_6, i.e. *minimum mixture* with $p_{\mathrm{B}} = p_{\mathrm{SF_6}} = 0$.

It turns out that the achievable sensitivity for a single measurement is generally better if the partial pressures of the gas mixture are set to values that lead to shorter relaxation times T_2^*. This is mainly due to the increase in the xenon partial pressure and the resulting higher signal amplitudes in these cases. Now, the benefit from this is that the total sensitivity can be further improved by multiple measurements N in the same total measuring time of coherent spin precession $T_{\mathrm{tot}} = N \cdot 3 \cdot T_2^*$, apart from the statistical improvement that is already evident, like $1/\sqrt{N}$ (cf. equation 2.59). If we compare measurements with $T_2^* = 2\,\mathrm{h}$ and $3\,\mathrm{h}$, we can theoretically gain an additional "statistical" factor of $1/\sqrt{3\,\mathrm{h}/2\,\mathrm{h}}$, simply by performing more measurements in the same total measurement time. In practice, however, the dead time during (electric field reversal) and between the individual measurements prevents that this value can be actually achieved.

Based on the calculations it is evident that for the preset parameters in table A.1 SF_6 is not an adequate buffer gas for the experiment. It is actually more advantageous to measure without any addition (besides $\tilde{p}_{\mathrm{SF_6}} = 5\,\mathrm{mbar}$). On the other hand, ^{4}He is the most suitable buffer gas under the given conditions in terms of the best achievable sensitivity, even though it possesses the lowest destruction rate coefficient of the investigated buffer gases (cf. table 2.2). Since we have a shallow sensitivity optimum, as it is evident from the blue colored area in figure A.12, the sensitivity does not depend much on the actual $p_{^4\mathrm{He}}/p_{\mathrm{Xe}}$ ratio, at least in the range $1 < \alpha_{^4\mathrm{He}} < 10$. That may be advantageous in practice since we do not rely on an exact gas mixing ratio. However, in the same context it turns out that the *minimum mixture* results in a similar good achievable sensitivity, at least for $T_2^* = 2\,\mathrm{h}$.

In order to interpret the results of this chapter especially in the context of practicability, it should be mentioned that there is of course a deviation from the theoretical preconditions. This concerns on the one hand the fixed "constant" parameters (cf. table A.1), which are varying in reality. Most of all the magnetic field gradients are in general not the same for each measurement. On the other hand, it is a purely statistical optimization. All kinds of systematic, organizational and procedural factors, as well as the actual comagnetometry signal with ^{3}He are not taken into account for the most part. In individual cases, it is always necessary to consider the present circumstances of the experiment. Nonetheless, the presented optimization routine gives a good indication of how the achievable sensitivity depends on the used gas mixture.

A.4. Degaussing with "Ludwig van Beethoven"

For our experimental routine we developed a degaussing routine, which allows us to demagnetize our mu-metal cylinder. A detailed description of the routine was presented in section 4.2.1. This *standard routine* is characterized by a sequence of exponentially decaying sines with frequencies of 3 Hz and 1 Hz, which modulate the current of the degaussing coil, according to equation 4.1. The time constant is set to $\tau = 30\,\mathrm{s}$. With this routine we were able to achieve small magnetic field gradients in the order of $10\,\mathrm{pT/cm}$. In this section we present a non-standard routine (no exponentially decaying wave function) with significantly higher frequencies. The motivation for this approach was originally not meant to demagnetize, but to show how well our standard routine works, once the mu-metal is magnetized. As a signal for the (de-)magnetization current we have chosen the first 3:14 (π) minutes of Ludwig van Beethoven's first movement of Symphony No. 5 in C minor: Allegro con brio, Op. 67 [149]. The waveform of the signal is visualized in figure A.14.

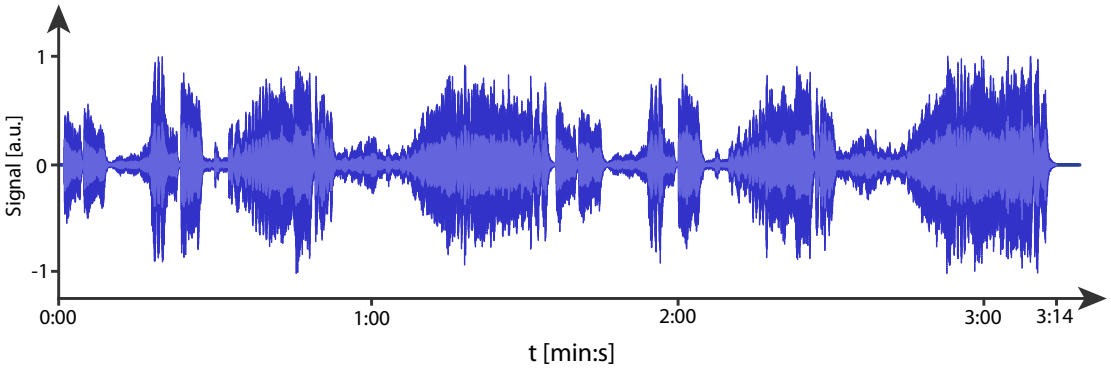

Figure A.14.: Signal waveform of the first 3:14 min of Ludwig van Beethoven's first movement of Symphony No. 5 in C minor: Allegro con brio, Op. 67

Many peaks at maximum intensity, in particular close to the end of the waveform, disagree with the common understanding of an adequate degaussing routine (c.f. section 4.2.1 and [124]). Apart from that it is most likely that the high frequencies of the applied waveform have a substantial influence on surface magnetizations of the mu-metal. This can be explained by the skin-effect of the mu-metal. The skin-depth [70]

$$\delta = \sqrt{\frac{2\rho}{\omega\mu}} \tag{A.6}$$

describes how well a certain electromagnetic wave with a frequency ω enters a bulk material with the electrical resistivity ρ and the permeability $\mu = \mu_0 \cdot \mu_r$. Mu-metal has a resistivity of $\rho \approx 0.6\,\Omega\cdot$m and a relative permeability[2] at 50 Hz of about $\mu_r = 50000$ [116]. A frequency analysis of the waveform of Beethoven's 5th in figure A.15 shows that the most prominent frequencies are between 50 Hz and 1 kHz. The skin-depth at 50 Hz is about $\delta \approx 0.02$ mm. It seems reasonable that some surface effects of the mu-metal could be affected (neutralized) more efficiently by frequencies much higher than the ones of the *standard routine*.

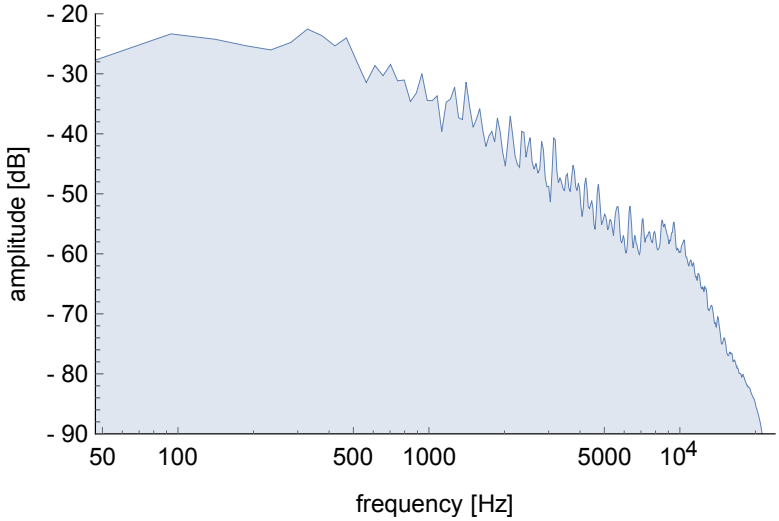

Figure A.15.: Frequency analysis of the waveform of Beethoven's 5th. The most prominent frequencies are between 50 Hz and 1 kHz.

The residual magnetic field gradients of the mu-metal cylinder are a good indicator for a well-demagnetized material, as it was before with our so far *standard routine* described in section 4.2.1. Because it was impossible without further ado to rebuilt the setup for the gradient measurement, as it was used for the analysis in section 4.2.1, another method for estimating the quality of the demagnetization was chosen: Since a measurement of the best achievable T_2^* time would have been too time-consuming at that moment, the amplitude spectral density was analyzed. If the mu-metal would be magnetized it could become visible in the amplitude density spectrum due to vibration modes of the setup if thereby the magnetic field gradients at the SQUIDs position change. Another cause could be spontaneous domain flips of the mu-metal.

[2]Please note that the permeability of a material strongly depends on the irradiation frequency and the saturation magnetization.

As a starting point, a measurement of the amplitude spectral density taken from an EDM run just before performing the unusual degaussing routine is presented in figure A.16. This graph shows a typical spectrum as achieved after a standard demagnetization routine with 3 Hz and 1 Hz. The Xe and He signals at about 5 Hz and 13 Hz are clearly evident. For clarification, the dashed red line marks the mean amplitude spectral density between 5 Hz and 40 Hz. It drops from circa 15 fT/$\sqrt{\text{Hz}}$ to about 12 fT/$\sqrt{\text{Hz}}$. Besides the peak at 50 Hz from the power grid and some small peaks around 18, 28 and 32 Hz the rest of the spectrum is free from other spectral lines which lift up from the noise floor.

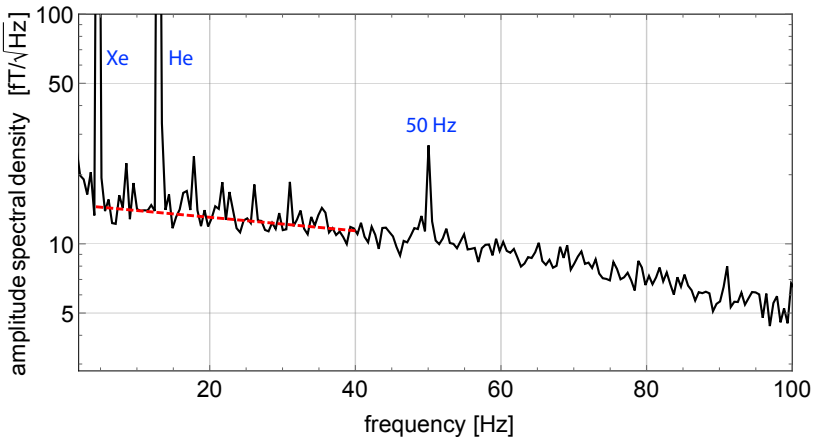

Figure A.16.: Amplitude spectral density during an EDM measurement with He and Xe, just before testing the degaussing routine with Beethoven's 5th. The noise level, indicated by the dashed red line drops from around 15 fT/$\sqrt{\text{Hz}}$ to about 12 fT/$\sqrt{\text{Hz}}$ between 5 Hz and 40 Hz.

The following spectrum in figure A.17 was measured without He and Xe, after degaussing with Beethoven's 5th subsequently to the measurement in figure A.16. The degaussing signal was put out by a 24 bit sound card and amplified to about 8 A maximum current in the degaussing coil of the mu-metal cylinder inside the MSR. The waveform shown in figure A.14 was clearly visible in the SQUID-signal.
As expected, several high peaks appear in the spectrum, stemming apparently from a magnetization of the mu-metal. Especially at around 20 Hz an enormously increased signal is observed. Unquestionably this degaussing routine is not suitable on its own to properly prepare the mu-metal. Nevertheless, it is evident that besides the strong peaks the noise floor is lower than before. Estimated by the placement of the dashed red line, the amplitude spectral density drops from around 12 fT/$\sqrt{\text{Hz}}$ at 5 Hz to about 7 fT/$\sqrt{\text{Hz}}$ at 40 Hz.

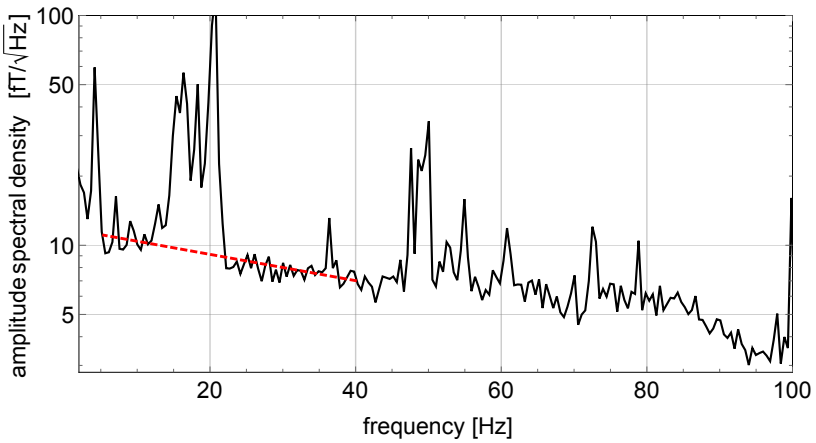

Figure A.17.: Amplitude spectral density right after degaussing with Beethoven's 5th, without He and Xe. The strong peaks indicate a magnetized material. The frequency distribution could stem from vibration modes of the experimental setup or from domain flips of the mu-metal.

To get rid of the magnetization of the mu-metal, as the numerous high peaks indicate, the cylinder was subsequently degaussed with the *standard routine* with 3 Hz and 1 Hz. The following figure A.18 shows the resulting spectrum.

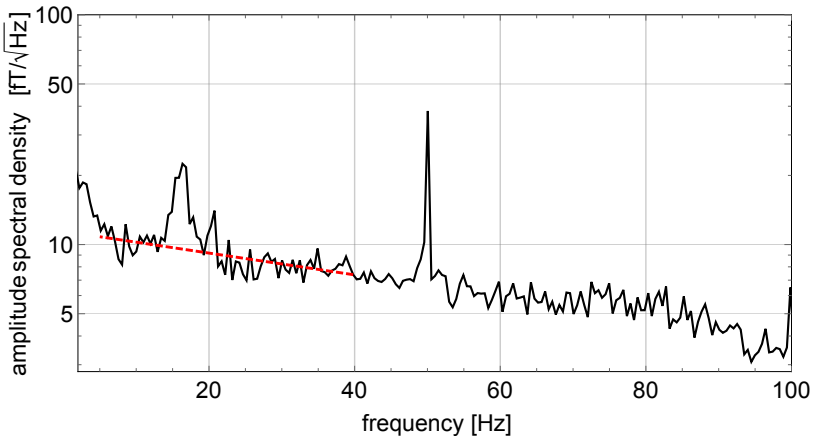

Figure A.18.: Amplitude spectral density after degaussing with Beethoven's 5th and subsequently performing a *standard routine* with 3 Hz and 1 Hz.

As usual the *standard routine* demagnetizes the bulk material which manifests in the smoothed amplitude spectral density. Solely a rather wide frequency distribution at around 18 Hz is still present. It is a well known fact that the mu-metal undergoes a kind of relaxation phase after a demagnetization. A possible explanation is that spontaneous

domain flips of the bulk material lead to an increased noise. The effect decreases if the mu-metal is at rest for some time. The noise in the same region before, indicated by the dashed red line, did not change significantly, meaning it is still lower than without degaussing with Beethoven's 5th.
A last check was performed about three hours after the last step of demagnetization. The spectrum in figure A.19 was measured during an EDM run under the same experimental conditions (again with He and Xe) as in the run from figure A.16.

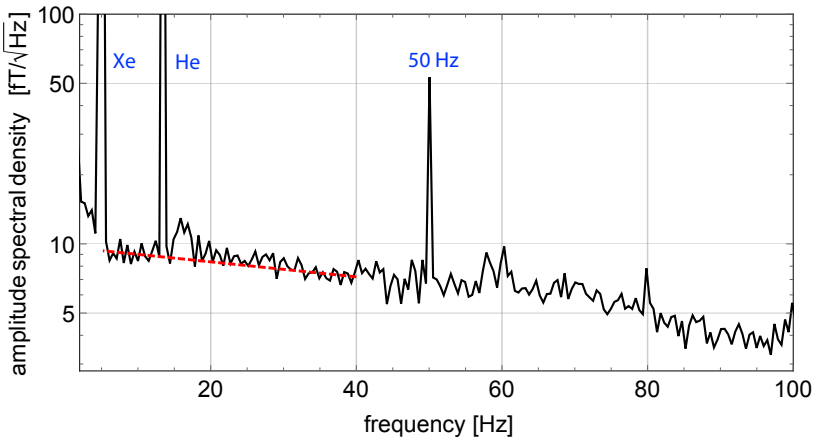

Figure A.19.: Amplitude spectral density during an EDM measurement with He and Xe, about three hours after the measurement from figure A.18.

Clearly, the overall amplitude spectral density, or rather the noise floor is now significantly smaller than before. The noise level is between $9\,\mathrm{fT}/\sqrt{\mathrm{Hz}}$ and $7\,\mathrm{fT}/\sqrt{\mathrm{Hz}}$. This is an improvement of more than 50%. However, the 50 Hz peak is slightly increased. This could be caused by electronic devices in the laboratory, like the air condition or vacuum pumps. Furthermore, the peak at around 18 Hz is considerably reduced. This confirms the hypothesis of the relaxing mu-metal. Beyond that it cannot be finally concluded if this peak stems from the demagnetization because it is possible that the same peak is superimposed by stronger, external effects in the measurement from figure A.16.

In conclusion the demagnetization with Beethoven's 5th symphony seems to have a positive effect on the condition of the mu-metal. The exact cause of this improvement cannot be finally clarified. It is possible that the improvement is merely a coincidence. Compared with an earlier measurement, e.g. in figure 4.2, the noise level is definitely not constant, but varies from day to day. A reliable conclusion can not be considered until further tests are performed. However, in contrast to the improved noise floor the achievable field gradients did not change due to this procedure.

List of Figures

List of Tables

Bibliography

[1] Sakharov, A. D., *Violation of* CP *invariance,* C *asymmetry, and baryon asymmetry of the universe*. Soviet Physics Uspekhi, **34**, 5, 392, 1991.

[2] Pauli, W., *Über den Zusammenhang des Abschlusses der Elektronengruppen im Atom mit der Komplexstruktur der Spektren*. Zeitschrift für Physik, **31**, 1, 765–783, 0044-3328, 1925.

[3] Rosenberry, M. A. and Chupp, T. E., *Atomic Electric Dipole Moment Measurement Using Spin Exchange Pumped Masers of* ^{129}Xe *and* ^{3}He. Phys. Rev. Lett., **86**, 22–25, 2001.

[4] Riotto, A. and Trodden, M., *RECENT PROGRESS IN BARYOGENESIS*. Annual Review of Nuclear and Particle Science, **49**, 1, 35-75, 1999.

[5] Aguilar, M., Alcaraz, J., Allaby, J., Alpat, B., Ambrosi, G., Anderhub, H., Ao, L., Arefiev, A., Azzarello, P., Babucci, E., Baldini, L., Basile, M., Barancourt, D., Barao, F., Barbier, G., Barreira, G., Battiston, R., Becker, R., Becker, U., Bellagamba, L., Béné, P., Berdugo, J., Berges, P., Bertucci, B., Biland, A., Bizzaglia, S., Blasko, S., Boella, G., Boschini, M., Bourquin, M., Brocco, L., Bruni, G., Buénerd, M., Burger, J., Burger, W., Cai, X., Camps, C., Cannarsa, P., Capell, M., Casadei, D., Casaus, J., Castellini, G., Cecchi, C., Chang, Y., Chen, H., Chen, H., Chen, Z., Chernoplekov, N., Chiueh, T., Cho, K. et al., *The Alpha Magnetic Spectrometer (AMS) on the International Space Station: Part I - results from the test flight on the space shuttle*. Physics Reports, **366**, 6, 331 - 405, 0370-1573, 2002.

[6] Canetti, L., Drewes, M. and Shaposhnikov, M., *Matter and antimatter in the universe*. New Journal of Physics, **14**, 9, 095012, 2012.

[7] Cyburt, R. H., Fields, B. D. and Olive, K. A., *Primordial nucleosynthesis in light of WMAP*. Physics Letters B, **567**, 3-4, 227 - 234, 0370-2693, 2003.

[8] Minamizaki, A. and Sugamoto, A., *Can the baryon number density and the cosmological constant be interrelated?*. Physics Letters B, **659**, 3, 656 - 660, 0370-2693, 2008.

[9] Spergel, D. N., Bean, R., Doré, O., Nolta, M. R., Bennett, C. L., Dunkley, J., Hinshaw, G., Jarosik, N., Komatsu, E., Page, L., Peiris, H. V., Verde, L., Halpern, M., Hill, R. S., Kogut, A., Limon, M., Meyer, S. S., Odegard, N., Tucker, G. S., Weiland, J. L., Wollack, E. and Wright, E. L., *Three-Year Wilkinson Microwave Anisotropy Probe (WMAP) Observations: Implications for Cosmology*. The Astrophysical Journal Supplement Series, **170**, 2, 377, 2007.

[10] Fixsen, D. J., *The Temperature of the Cosmic Microwave Background*. The Astrophysical Journal, **707**, 2, 916, 2009.

[11] Hill, T., *An Introduction to Statistical Thermodynamics*. Dover Publications, 2012.

[12] Plouffe, S., *The Value of Zeta(3) to 1,000,000 Places*. Createspace Independent Publishing Platform, 2017.

[13] Bennett, C. L., Halpern, M., Hinshaw, G., Jarosik, N., Kogut, A., Limon, M., Meyer, S. S., Page, L., Spergel, D. N., Tucker, G. S., Wollack, E., Wright, E. L., Barnes, C., Greason, M. R., Hill, R. S., Komatsu, E., Nolta, M. R., Odegard, N., Peiris, H. V., Verde, L. and Weiland, J. L., *First-Year Wilkinson Microwave Anisotropy Probe (WMAP) Observations: Preliminary Maps and Basic Results*. The Astrophysical Journal Supplement Series, **148**, 1, 1, 2003.

[14] Kobayashi, M. and Maskawa, T., CP-*Violation in the Renormalizable Theory of Weak Interaction*. Progress of Theoretical Physics, **49**, 2, 652-657, 1973.

[15] Farrar, G. R. and Shaposhnikov, M. E., *Baryon asymmetry of the Universe in the standard model*. Phys. Rev. D, **50**, 774–818, 1994.

[16] Cohen, A. G., Kaplan, D. B. and Nelson, A. E., *Progress in Electroweak Baryogenesis*. Annual Review of Nuclear and Particle Science, **43**, 1, 27-70, 1993.

[17] Lide, D., *CRC Handbook of Chemistry and Physics, 84th Edition*. Taylor & Francis, 2003.

[18] Wirzba, A., *Electric dipole moments of the nucleon and light nuclei*. Nuclear Physics A, **928**, Supplement C, 116 - 127, 0375-9474, 2014.

[19] Christenson, J. H., Cronin, J. W., Fitch, V. L. and Turlay, R., *Evidence for the* 2π *Decay of the* K_2^0 *Meson*. Phys. Rev. Lett., **13**, 138-140, 1964.

[20] Pospelov, M. E. and Khriplovich, I. B., *Electric dipole moment of the W boson and the electron in the Kobayashi-Maskawa model.* Sov. J. Nucl. Phys., **53**, 638-640, 1991.

[21] Baluni, V., CP*-nonconserving effects in quantum chromodynamics.* Phys. Rev. D, **19**, 2227–2230, 1979.

[22] Pendlebury, J. M., Afach, S., Ayres, N. J., Baker, C. A., Ban, G., Bison, G., Bodek, K., Burghoff, M., Geltenbort, P., Green, K., Griffith, W. C., Grinten, M., Grujić, Z. D., Harris, P. G., Hélaine, V., Iaydjiev, P., Ivanov, S. N., Kasprzak, M., Kermaidic, Y., Kirch, K., Koch, H.-C., Komposch, S., Kozela, A., Krempel, J., Lauss, B., Lefort, T., Lemière, Y., May, D. J. R., Musgrave, M., Naviliat-Cuncic, O., Piegsa, F. M., Pignol, G., Prashanth, P. N., Quéméner, G., Rawlik, M., Rebreyend, D., Richardson, J. D., Ries, D., Roccia, S., Rozpedzik, D., Schnabel, A., Schmidt-Wellenburg, P., Severijns, N., Shiers, D., Thorne, J. A., Weis, A., Winston, O. J., Wursten, E., Zejma, J. and Zsigmond, G., *Revised experimental upper limit on the electric dipole moment of the neutron.* Phys. Rev. D, **92**, 092003, 2015.

[23] Tullney, K., *Search for a Spin-Dependent Short-Range Force between Nucleons with a* ^{3}He/^{129}Xe *Clock-Comparison Experiment.* Dissertation, University of Mainz, 2013.

[24] Arnowitt, R., Dutta, B. and Santoso, Y., *Supersymmetric phases, the electron electric dipole moment and the muon magnetic moment.* Phys. Rev. D, **64**, 113010, 2001.

[25] Helaine, V., *Neutron Electric Dipole Moment measurement: simultaneous spin analysis and preliminary data analysis.* Dissertation, Université de Caen, 2014.

[26] Kirch, K., Pretz, J. and Wirzba, A., *Elektrische Dipolmomente gesucht.* Physik Journal, Wiley-VCH Verlag, **16**, 11, 41-46, 2017.

[27] Graner, B., Chen, Y., Lindahl, E. G. and Heckel, B. R., *Reduced Limit on the Permanent Electric Dipole Moment of* ^{199}Hg. Phys. Rev. Lett., **116**, 161601, 2016.

[28] Rathmann, F., Saleev, A. and Nikolaev, N. N., *Search for electric dipole moments of light ions in storage rings.* Physics of Particles and Nuclei, **45**, 1, 229–233, 1531-8559, 2014.

[29] Bennett, G. W., Bousquet, B., Brown, H. N., Bunce, G., Carey, R. M., Cushman, P., Danby, G. T., Debevec, P. T., Deile, M., Deng, H., Deninger, W., Dhawan, S. K., Druzhinin, V. P., Duong, L., Efstathiadis, E., Farley, F. J. M., Fedotovich, G. V., Giron, S., Gray, F. E., Grigoriev, D., Grosse-Perdekamp, M., Grossmann, A., Hare, M. F., Hertzog, D. W., Huang, X., Hughes, V. W., Iwasaki, M., Jungmann, K., Kawall, D., Kawamura, M., Khazin, B. I., Kindem, J., Krienen, F., Kronkvist, I., Lam, A., Larsen, R., Lee, Y. Y., Logashenko, I., McNabb, R., Meng, W., Mi, J., Miller, J. P., Mizumachi, Y., Morse, W. M., Nikas, D., Onderwater, C. J. G., Orlov, Y., Özben, C. S., Paley, J. M., Peng, Q. et al., *Improved limit on the muon electric dipole moment*. Phys. Rev. D, **80**, 052008, 2009.

[30] Adelmann, A., Kirch, K., Onderwater, C. J. G. and Schietinger, T., *Compact storage ring to search for the muon electric dipole moment*. Journal of Physics G: Nuclear and Particle Physics, **37**, 8, 085001, 2010.

[31] Schiff, L. I., *Measurability of Nuclear Electric Dipole Moments*. Phys. Rev., **132**, 2194–2200, 1963.

[32] Ginges, J. and Flambaum, V., *Violations of fundamental symmetries in atoms and tests of unification theories of elementary particles*. Physics Reports, **397**, 2, 63 - 154, 0370-1573, 2004.

[33] Khriplovich, I. and Lamoreaux, S., CP *Violation Without Strangeness: Electric Dipole Moments of Particles, Atoms, and Molecules*. Springer Berlin Heidelberg, 2012.

[34] Ghosh, D. and Sato, R., *Lepton electric dipole moment and strong* CP *violation*. Physics Letters B, **777**, 335 - 339, 0370-2693, 2018.

[35] Balazs, C., White, G. and Yue, J., *Effective field theory, electric dipole moments and electroweak baryogenesis*. Journal of High Energy Physics, **2017**, 3, 30, 1029-8479, 2017.

[36] Chupp, T. and Ramsey-Musolf, M., *Electric dipole moments: A global analysis*. Phys. Rev. C, **91**, 035502, 2015.

[37] Sandars, P., *The electric dipole moment of an atom*. Physics Letters, **14**, 3, 194 - 196, 0031-9163, 1965.

[38] Commins, E. D., *Electric Dipole Moments of Leptons.* Advances In Atomic, Molecular, and Optical Physics, **40**, 1 - 55, 1049-250X, 1999.

[39] Sushkov, O. and Flambaum, V., *Parity breaking effects in diatomic molecules.* JETP, **48**, 4, 608, 1978.

[40] Baron, J., Campbell, W. C., DeMille, D., Doyle, J. M., Gabrielse, G., Gurevich, Y. V., Hess, P. W., Hutzler, N. R., Kirilov, E., Kozyryev, I., O'Leary, B. R., Panda, C. D., Parsons, M. F., Petrik, E. S., Spaun, B., Vutha, A. C. and West, A. D., *Order of Magnitude Smaller Limit on the Electric Dipole Moment of the Electron.* Science, **343**, 6168, 269–272, 0036-8075, 2014.

[41] Flambaum, V. V. and Ginges, J. S. M., *Nuclear Schiff moment and time-invariance violation in atoms.* Phys. Rev. A, **65**, 032113, 2002.

[42] Sushkov, O., Flambaum, V. and Khriplovich, I., *Possibility of investigating* P- *and* T-*odd nuclear forces in atomic and molecular experiments.* Sov. Phys. - JETP (Engl. Transl.); (United States), **60:5**, 1984.

[43] https://www.psi.ch/nedm/ *Search for the neutron electric dipole moment (nEDM) at PSI*, Accessed 04. September 2017.

[44] http://hepwww.rl.ac.uk/edm/index_files/cryoedm.htm *A cryogenic experiment to search for the EDM of the neutron at ILL*, Accessed 04. September 2017.

[45] http://nedm.ph.tum.de/index.html *A next generation measurement of the electric dipole moment of the neutron at the FRM-II*, Accessed 04. September 2017.

[46] Dzuba, V. A., Flambaum, V. V. and Ginges, J. S. M., *Atomic electric dipole moments of* He *and* Yb *induced by nuclear Schiff moments.* Phys. Rev. A, **76**, 034501, 2007.

[47] Flambaum, V., Khriplovich, I. and Sushkov, O., *On the* P- *and* T-*nonconserving nuclear moments.* Nuclear Physics A, **449**, 4, 750 - 760, 0375-9474, 1986.

[48] Flambaum, V., Khriplovich, I. and Sushkov, O., *Limit on the constant of* T-*nonconserving nucleon-nucleon interaction.* Physics Letters B, **162**, 4, 213 - 216, 0370-2693, 1985.

[49] Baker, C., Doyle, D., Geltenbort, P., Green, K., van der Grinten, M., Harris, P., Iaydjiev, P., Ivanov, S., May, D., Pendlebury, J., J.D. Richardson, J., Shiers, D. and Smith, K., *Improved Experimental Limit on the Electric Dipole Moment of the Neutron*. Phys. Rev. Lett., **97**, 13, 131801, 2006.

[50] Parker, R. H., Dietrich, M. R., Kalita, M. R., Lemke, N. D., Bailey, K. G., Bishof, M., Greene, J. P., Holt, R. J., Korsch, W., Lu, Z.-T., Mueller, P., O'Connor, T. P. and Singh, J. T., *First Measurement of the Atomic Electric Dipole Moment of* ^{225}Ra. Phys. Rev. Lett., **114**, 233002, 2015.

[51] Allmendinger, F., Heil, W., Karpuk, S., Kilian, W., Scharth, A., Schmidt, U., Schnabel, A., Sobolev, Y. and Tullney, K., *New Limit on Lorentz-Invariance- and* CPT*-Violating Neutron Spin Interactions Using a Free-Spin-Precession* ^{3}He-^{129}Xe *Comagnetometer*. Phys. Rev. Lett., **112**, 110801, 2014.

[52] Tullney, K., Allmendinger, F., Burghoff, M., Heil, W., Karpuk, S., Kilian, W., Knappe-Grüneberg, S., Müller, W., Schmidt, U., Schnabel, A., Seifert, F., Sobolev, Y. and Trahms, L., *Constraints on Spin-Dependent Short-Range Interaction between Nucleons*. Phys. Rev. Lett., **111**, 100801, 2013.

[53] Mohr, P. J., Newell, D. B. and Taylor, B. N., *CODATA recommended values of the fundamental physical constants: 2014*. Rev. Mod. Phys., **88**, 035009, 2016.

[54] http://physics.nist.gov/cuu/constants/ *The NIST Reference on Constants, Units, and Uncertainty*, Accessed 29 November 2016.

[55] Pfeffer, M. and Lutz, O., *129*Xe *Gas NMR Spectroscopy and Imaging with a Whole-Body Imager*. Journal of Magnetic Resonance, Series A, **108**, 1, 106 - 109, 1064-1858, 1994.

[56] Gemmel, C., *Test of Lorentz Symmetry with a* ^{3}He/^{129}Xe *Clock-Comparison Experiment*. Dissertation, University of Mainz, 2010.

[57] Mrozik, C., *Konstruktion und Inbetriebnahme eines kompakten* ^{3}He*-Polarisators*. Dissertation, University of Mainz, 2014.

[58] Courtade, E., Marion, F., Nacher, P., Tastevin, G., Kiersnowski, K. and Dohnalik, T., *Magnetic Field Effects on the* 1083 nm *Atomic Line of Helium*. Eur. Phys. J. D, **21**, 25-55, 2002.

[59] Rosner, S. D. and Pipkin, F. M., *Hyperfine Structure of the* 2^3S_1 *State of* He^3. Phys. Rev. A, **1**, 571–586, 1970.

[60] Wolf, M., *Erzeugung höchster* ^{3}He*-Kernspinpolarisation durch metastabiles optisches Pumpen*. Dissertation, University of Mainz, 2004.

[61] http://www.saespuregas.com/products/gas-purifier/helium/home.html *Helium Gas Purifier Overview | SAES Pure Gas*, Accessed 02 April 2017.

[62] Hiebel, S., Grossmann, T., Kiselev, D., Schmiedeskamp, J., Gusev, Y., Heil, W., Karpuk, S., Krimmer, J., Otten, E. and Salhi, Z., *Magnetized boxes for housing polarized spins in homogeneous fields*. Journal of Magnetic Resonance, **204**, 1, 37 - 49, 1090-7807, 2010.

[63] Repetto, M., *Improvements in production and storage of HP-*^{129}Xe. Dissertation, University of Mainz, 2015.

[64] Happer, W., Miron, E., Schaefer, S., Schreiber, D., Wijngaarden, W. A. and Zeng, X., *Polarization of the nuclear spins of noble-gas atoms by spin exchange with optically pumped alkali-metal atoms*. Phys. Rev. A, **29**, 3092–3110, 1984.

[65] Ramsey, N., Miron, E., Zeng, X. and Happe, W., *Formation and breakup rates of* RbXe *van der Waals molecules in* He *and* N*2 gas*. Chemical Physics Letters, **102**, 4, 340 - 343, 0009-2614, 1983.

[66] Ruth, U., Hof, T., Schmidt, J., Fick, D. and Jänsch, H., *Production of nitrogen-free, hyperpolarized* ^{129}Xe *gas*. Applied Physics B, **68**, 1, 93–97, 1432-0649, 1999.

[67] Haynes, W., *CRC Handbook of Chemistry and Physics, 92nd Edition*. CRC Press, 2011.

[68] Raich, H. and Blümler, P., *Design and construction of a dipolar Halbach array with a homogeneous field from identical bar magnets: NMR Mandhalas*. Concepts in Magnetic Resonance Part B: Magnetic Resonance Engineering, **23B**, 1, 16–25, 1552-504X, 2004.

[69] Repetto, M., Zimmer, S., Allmendinger, F., Blümler, P., Doll, M., Grasdijk, J., Heil, W., Jungmann, K., Karpuk, S., Krause, H.-J., Offenhäusser, A., Schmidt, U., Sobolev, Y. and Willmann, L., *HP-Xe to go: Storage and transportation of hyperpolarized* ^{129}*Xenon*. Journal of Magnetic Resonance, **265**, 197 - 199, 1090-7807, 2016.

[70] Jackson, J., *Classical electrodynamics*. Wiley, 1975.

[71] Bloch, F., *Nuclear Induction*. Phys. Rev., **70**, 460–474, 1946.

[72] Koch, H.-C., *An accurate combined* ^{3}He/Cs *magnetometer with* fT *sensitivity for the* n*EDM experiment at PSI*. Dissertation, University of Fribourg and University of Mainz, 2015.

[73] Cates, G. D., Schaefer, S. R. and Happer, W., *Relaxation of spins due to field inhomogeneities in gaseous samples at low magnetic fields and low pressures*. Phys. Rev. A, **37**, 2877–2885, 1988.

[74] Acosta, R. H., Agulles-Pedros, L., Komin, S., Sebastiani, D., Spiess, H. W. and Blümler, P., *Diffusion in binary gas mixtures studied by NMR of hyperpolarized gases and molecular dynamics simulations*. Phys. Chem. Chem. Phys., **8**, 4182-4188, 2006.

[75] Ding, X., Kennedy, B. M., Molins, S., Kneafsey, T. and Evans, W. C., *Experimental studies and model analysis of noble gas fractionation in low-permeability porous media*. Geochimica et Cosmochimica Acta, **205**, 149 - 167, 0016-7037, 2017.

[76] Mair, R. W., Hoffmann, D., Sheth, S., Wong, G., Butler, J. P., Patz, S., Topulos, G. P. and Walsworth, R. L., *Reduced xenon diffusion for quantitative lung study - the role of* SF_6. NMR IN BIOMEDICINE, **13**, 229-233, 0952-3480, 2000.

[77] Hasson, K. C., Cates, G. D., Lerman, K., Bogorad, P. and Happer, W., *Spin relaxation due to magnetic-field inhomogeneities: Quartic dependence and diffusion-constant measurements*. Phys. Rev. A, **41**, 3672–3688, 1990.

[78] http://galileo.phys.virginia.edu/research/groups/spinphysics/glass_properties.html *Selected List of Glass Properties*, Accessed 02 November 2016.

[79] Schmiedeskamp, J., *Weiterentwicklung einer Produktionsanlage und der Speicherungs- bzw. Transportkonzepte für hochpolarisiertes* ^{3}He. Dissertation, University of Mainz, 2004.

[80] Scharth, A., *Entwicklung des Messaufbaus für das* Xe-*EDM Experiment*. Diploma thesis, University of Mainz, 2013.

[81] Repetto, M., Babcock, E., Blümler, P., Heil, W., Karpuk, S. and Tullney, K., *Systematic* T_1 *improvement for hyperpolarized* ^{129}*xenon*. Journal of Magnetic Resonance, **252**, 163 - 169, 1090-7807, 2015.

[82] Chann, B., Nelson, I. A., Anderson, L. W., Driehuys, B. and Walker, T. G., ^{129}Xe – Xe *Molecular Spin Relaxation.* Phys. Rev. Lett., **88**, 113201, 2002.

[83] Saam, B., Happer, W. and Middleton, H., *Nuclear relaxation of* ^{3}He *in the presence of* O_2. Phys. Rev. A, **52**, 862–865, 1995.

[84] Jameson, C. J., Jameson, A. K. and Hwang, J. K., *Nuclear spin relaxation by intermolecular magnetic dipole coupling in the gas phase.* ^{129}Xe *in oxygen.* The Journal of Chemical Physics, **89**, 7, 4074-4081, 1988.

[85] Hahn, E. L., *Spin Echoes.* Phys. Rev., **80**, 580–594, 1950.

[86] Cussler, E., *Diffusion.* Cambridge University Press, 1997.

[87] Allmendinger, F., Blümler, P., Doll, M., Grasdijk, O., Heil, W., Jungmann, K., Karpuk, S., Krause, H.-J., Offenhäusser, A., Repetto, M., Schmidt, U., Sobolev, Y., Tullney, K., Willmann, L. and Zimmer, S., *Precise measurement of magnetic field gradients from free spin precession signals of* ^{3}He *and* ^{129}Xe *magnetometers.* The European Physical Journal D, **71**, 4, 98, 1434-6079, 2017.

[88] Clarke, J. and Braginski, A., *The SQUID Handbook: Fundamentals and Technology of SQUIDs and SQUID Systems.* Wiley, 2006.

[89] Clarke, J. and Braginski, A., *The SQUID Handbook: Applications of SQUIDs and SQUID Systems.* Wiley, 2006.

[90] http://physics.nist.gov/cgi-bin/cuu/value?flxquhs2e *CODATA value: magnetic flux quantum*, Accessed 03 February 2017.

[91] Josephson, B., *Possible new effects in superconductive tunnelling.* Physics Letters, **1**, 7, 251 - 253, 0031-9163, 1962.

[92] Allmendinger, F., *Precise Tests of Fundamental Symmetries at Low Energies using a* ^{3}He $-^{129}$ Xe *Comagnetometer.* Dissertation, University of Heidelberg, 2015.

[93] Heisenberg, W., *Über den anschaulichen Inhalt der quantentheoretischen Kinematik und Mechanik.* Zeitschrift für Physik, **43**, 3, 172–198, 0044-3328, 1927.

[94] Kay, S. M., *Fundamentals of Statistical Signal Processing, Volume I: Estimation Theory.* Prentice Hall, 1993.

[95] Gemmel, C., Heil, W., Karpuk, S., Lenz, K., Ludwig, C., Sobolev, Y., Tullney, K., Burghoff, M., Kilian, W., Knappe-Grüneberg, S., Müller, W., Schnabel, A., Seifert, F., Trahms, L. and Baessler, S., *Ultra-sensitive magnetometry based on free precession of nuclear spins*. The European Physical Journal D, **57**, 3, 303–320, 1434-6079, 2010.

[96] Barnes, J. A., Chi, A. R., Cutler, L. S., Healey, D. J., Leeson, D. B., McGunigal, T. E., Mullen, J. A., Smith, W. L., Sydnor, R. L., Vessot, R. F. C. and Winkler, G. M. R., *Characterization of Frequency Stability*. IEEE Transactions on Instrumentation and Measurement, **IM-20**, 2, 105-120, 0018-9456, 1971.

[97] http://www.technoplast-onlineshop.de/inhalt,mein_shop,de/medium.inhalt_datenblatt_pom *TECHNOPLAST V.TRESKOW GMBH - POM Datenblatt*, Accessed 29 June 2017.

[98] http://www.magnicon.com *Magnicon GmbH*, Accessed 21 June 2017.

[99] http://cryoton.org *CRYOTON Co. Ltd.*, Accessed 21 June 2017.

[100] Johnson, J. B., *Thermal Agitation of Electricity in Conductors*. Phys. Rev., **32**, 97–109, 1928.

[101] http://www.agarscientific.com/fr/colloidal-graphite-aquadag.html *Colloidal graphite (Aquadag): Agar Scientific*, Accessed 26 June 2017.

[102] http://www.boedeker.com/esdmatls.htm *Boedeker Plastics: Anti- & Conductive Plastics*, Accessed 26 June 2017.

[103] Nikiel, A., Blümler, P., Heil, W., Hehn, M., Karpuk, S., Maul, A., Otten, E., Schreiber, L. M. and Terekhov, M., *Ultrasensitive* ^{3}He *magnetometer for measurements of high magnetic fields*. The European Physical Journal D, **68**, 11, 330, 1434-6079, 2014.

[104] Zimmer, S., *Optimierung und Charakterisierung eines* ^{3}He*-Magnetometers für nEDM-Experimente*. Diploma thesis, University of Mainz, 2013.

[105] Murari, A., Vinante, C. and Monari, M., *Comparison of PEEK and VESPEL ®SP1 characteristics as vacuum seals for fusion applications*. Vacuum, **65**, 2, 137 - 145, 0042-207X, 2002.

[106] http://iseg-hv.com *High Voltage Power Supply (HVPS) - iseg Germany*, Accessed 18 August 2017.

[107] Tipler, P., *College Physics*. p. 467, Worth Publishers, 1987.

[108] Zinke, O. and Seither, H., *Widerstände, Kondensatoren, Spulen und ihre Werkstoffe*. Springer Berlin Heidelberg, 2013.

[109] Christophorou, L., *Insulating gases*. Nuclear Instruments and Methods in Physics Research Section A: Accelerators, Spectrometers, Detectors and Associated Equipment, **268**, 2, 424 - 433, 0168-9002, 1988.

[110] https://www.rct-online.de/en/shopware.php?sviewport=hmswglossar&saction=detail&id=32 *SI - Silikon-Kautschuk | Reichelt Chemietechnik*, Accessed 20. February 2018.

[111] http://www.carbon-vertrieb.com/carbon-fasern/index.html *Carbon-Vertrieb - Carbon-Fasern * Carbon-Technik * Carbon-Modellbau*, Accessed 20. February 2018.

[112] *CRC Handbook of Chemistry and Physics, 2009-2010, 90th ed.*. Journal of the American Chemical Society, **131**, 35, 2009.

[113] http://www.fz-juelich.de/pgi/pgi-8/en/research/biosensing/magnetocardiography/_node.html *Forschungszentrum Jülich - Magnetocardiography*, Accessed 22 June 2017.

[114] https://www.ptb.de/cms/en/ptb/fachabteilungen/abt8/ag-821/bmsr-8210.html *Magnetically super-shielded room (BMSR-2) - PTB.de*, Accessed 26 June 2017.

[115] http://www.stefan-mayer.com/en/products/magnetometers-and-sensors/fluxmaster.html *Stefan Mayer Instruments: Fluxgate Magnetometer Fluxmaster*, Accessed 14 February 2017.

[116] http://www.sekels.de/werkstoffe-und-halbzeuge/mumetall-vacoperm/ *Sekels GmbH: MUMETALL Werkstoffeigenschaften*, Accessed 14 February 2017.

[117] Sumner, T. J., Pendlebury, J. M. and Smith, K. F., *Convectional magnetic shielding*. Journal of Physics D: Applied Physics, **20**, 9, 1095, 1987.

[118] Volk, K. and Ergang, R., *Nickel und Nickellegierungen: Eigenschaften und Verhalten*. Springer Berlin Heidelberg, 2013.

[119] Jansen, J., *Optimierung einer Entgaußungsroutine zur Entmagnetisierung von Mumetall-Zylindern im Rahmen des* Xe-*EDM-Experiments*. Bachelor Thesis, University of Mainz, 2014.

[120] Allmendinger, F., *Private discussion*. 2017.

[121] Grasdijk, O., *Dissertation within the context of the* Xe-*EDM experiment (MIXed$\vec{d}$-collaboration)*. University of Groningen, to be published.

[122] Bernstein, M., King, K. and Zhou, X., *Handbook of MRI Pulse Sequences*. Elsevier Science, 2004.

[123] Ashcroft, N. W. and Mermin, N. D., *Solid state physics*. Holt, Rinehart and Winston, 1976.

[124] Thiel, F., Schnabel, A., Knappe-Grüneberg, S., Stollfuss, D. and Burghoff, M., *Demagnetization of magnetically shielded rooms*. Review of Scientific Instruments, **78**, 3, 035106, 2007.

[125] Nelder, J. A. and Mead, R., *A Simplex Method for Function Minimization*. The Computer Journal, **7**, 4, 308-313, 1965.

[126] Doll, M., *Untersuchung von Spintransfer und Relaxationsmechanismen im Rahmen des* Xe-*EDM Experiments*. Masters thesis, University of Mainz, 2016.

[127] https://www.vacuubrand.com/en/page794.html *Set DCP 3000 + VSK 3000 Vacuum gauge - VACUUBRAND*, Accessed 26. February 2018.

[128] Ludwig, C., *Voruntersuchungen zu Lorentzinvarianz-Tests mit Hilfe eines* ^{3}He $-^{129}$ Xe-*Komagnetometers*. Diploma thesis, University of Mainz, 2008.

[129] Kraft, A., *Aufbau und Inbetriebnahme eines hochsensitiven* ^{3}He-*Magnetometers für ein zukünftiges Experiment zur Bestimmung eines elektrischen Dipolmoments des freien Neutrons*. Dissertation, University of Mainz, 2012.

[130] Little, P. F., *Secondary Effects - Handbuch der Physik*. Springer Berlin Heidelberg, 1956.

[131] Silverstein, R., Webster, F., Kiemle, D. and Bryce, D., *Spectrometric Identification of Organic Compounds*. Wiley, 2014.

[132] Segebarth, N., Aïtjeddig, L., Locci, E., Bartik, K. and Luhmer, M., *Novel Method for the Measurement of Xenon Gas Solubility Using* ^{129}Xe *NMR Spectroscopy*. The Journal of Physical Chemistry A, **110**, 37, 10770-10776, 2006.

[133] Jameson, A. K., Moyer, J. W. and Jameson, C. J., *Variation of chemical shielding with intermolecular interactions and rovibrational motion. IV. 11*B *and 13*P *nuclei in* BF*3 and* CH*4*. The Journal of Chemical Physics, **68**, 6, 2873-2877, 1978.

[134] Raftery, D., Reven, L., Long, H., Pines, A., Tang, P. and Reimer, J. A., *Spin-polarized xenon-129 NMR study of a polymer surface.* The Journal of Physical Chemistry, **97**, 8, 1649-1655, 1993.

[135] Aoki, S., Kinoshita, H., Guinot, B., Kaplan, G. H., McCarthy, D. D. and Seidelmann, P. K., *The new definition of universal time.* Astron. Astrophys., **105**, 359-361, 1982.

[136] https://www.google.de/maps/place/forschungszentrum+jülich/ *Forschungszentrum Jülich - Google Maps*, Accessed 02 June 2017.

[137] Cates, G. D., White, D. J., Chien, T.-R., Schaefer, S. R. and Happer, W., *Spin relaxation in gases due to inhomogeneous static and oscillating magnetic fields.* Phys. Rev. A, **38**, 5092–5106, 1988.

[138] Audi, G., Wapstra, A. and Thibault, C., *The Ame2003 atomic mass evaluation.* Nuclear Physics A, **729**, 1, 337 - 676, 0375-9474, 2003.

[139] Bloch, F. and Siegert, A., *Magnetic Resonance for Nonrotating Fields.* Phys. Rev., **57**, 522–527, 1940.

[140] Ramsey, N. F., *Resonance Transitions Induced by Perturbations at Two or More Different Frequencies.* Phys. Rev., **100**, 1191–1194, 1955.

[141] Lamoreaux, S. K., *Additional motional-magnetic-field considerations for electric-dipole-moment experiments.* Phys. Rev. A, **53**, R3705–R3708, 1996.

[142] Chapman, S. and Cowling, T., *The Mathematical Theory of Non-uniform Gases: An Account of the Kinetic Theory of Viscosity, Thermal Conduction and Diffusion in Gases.* Cambridge University Press, 1970.

[143] Bondi, A., *van der Waals Volumes and Radii.* The Journal of Physical Chemistry, **68**, 3, 441-451, 1964.

[144] Breck, D., *Zeolite molecular sieves: structure, chemistry, and use.* Wiley, 1973.

[145] Matteucci, S., Yampolskii, Y., Freeman, B. D. and Pinnau, I., *Materials Science of Membranes for Gas and Vapor Separation, Chapter 1: Transport of Gases and Vapors in Glassy and Rubbery Polymers.* John Wiley & Sons, Ltd, 2006.

[146] Ismail, A., Khulbe, K. and Matsuura, T., *Gas Separation Membranes: Polymeric and Inorganic.* Springer International Publishing, 2015.

[147] Pendlebury, J. M., Heil, W., Sobolev, Y., Harris, P. G., Richardson, J. D., Baskin, R. J., Doyle, D. D., Geltenbort, P., Green, K., Grinten, M. G. D., Iaydjiev, P. S., Ivanov, S. N., May, D. J. R. and Smith, K. F., *Geometric-phase-induced false electric dipole moment signals for particles in traps.* Phys. Rev. A, **70**, 032102, 2004.

[148] Bohm, A., Mostafazadeh, A., Koizumi, H., Niu, Q. and Zwanziger, J., *The Geometric Phase in Quantum Systems: Foundations, Mathematical Concepts, and Applications in Molecular and Condensed Matter Physics.* Springer Berlin Heidelberg, 2003.

[149] https://archive.org/details/lvb_5_1 *Ludwig van Beethoven (1770-1827) Symphony No 5 in C-minor, Op 67, First movement: Allegro con brio*, Accessed 01 June 2017.